

UNIVERSITY COLLEGE LONDON

**Towards patient-specific modelling of
cerebral blood flow using
lattice-Boltzmann methods**

by

Gary Mark Doctors

A thesis submitted in partial fulfillment for the
degree of Doctor of Philosophy

in the

Department of Chemistry

December 2011

Declaration of Authorship

I, GARY MARK DOCTORS, declare that this thesis titled, 'TOWARDS PATIENT-SPECIFIC MODELLING OF CEREBRAL BLOOD FLOW USING LATTICE-BOLTZMANN METHODS' and the work presented in it are my own. I confirm that:

- This work was done wholly or mainly while in candidature for a research degree at this University.
- Where any part of this thesis has previously been submitted for a degree or any other qualification at this University or any other institution, this has been clearly stated.
- Where I have consulted the published work of others, this is always clearly attributed.
- Where I have quoted from the work of others, the source is always given. With the exception of such quotations, this thesis is entirely my own work.
- I have acknowledged all main sources of help.
- Where the thesis is based on work done by myself jointly with others, I have made clear exactly what was done by others and what I have contributed myself.

Signed:

Date:

“If this is coffee, please bring me some tea; but if this is tea, please bring me some coffee.”

Abraham Lincoln

Abstract

Department of Chemistry

Doctor of Philosophy

by Gary Mark Doctors

Patient-specific Computational fluid dynamics (CFD) studies of cerebral blood flow have the potential to help plan neurosurgery, but developing realistic simulation methods that deliver results quickly enough presents a major challenge. The majority of CFD studies assume that the arterial walls are rigid. Since the lattice-Boltzmann method (LBM) is computationally efficient on multicore machines, some methods for carrying out lattice-Boltzmann simulations of time-dependent fluid flow in elastic vessels are developed. They involve integrating the equations of motion for a number of points on the wall. The calculations at every lattice site and point on the wall depend only on information from neighbouring lattice sites or wall points, so they are suitable for efficient computation on multicore machines.

The first method is suitable for three-dimensional axisymmetric vessels. The steady-state solutions for the wall displacement and flow fields in a cylinder at realistic parameters for cerebral blood flow agree closely with the analytical solutions. Compared to simulations with rigid walls, simulations with elastic walls require 13% more computational effort at the parameters chosen in this study.

A scheme is then developed for a more complex geometry in two dimensions, which applies the full theory of linear elasticity. The steady-state wall profiles obtained from simulations of a Starling resistor agree closely with those from existing computational studies. I find that it is essential to change the lattice sites from solid to fluid and *vice versa* if the wall crosses any of them during the simulation. Simple tests of the dynamics show that when the mass of the wall is much greater than that of the fluid, the period of oscillation of the wall agrees within 7% of the expected period. This method could be extended to three dimensions for use in cerebral blood flow simulations.

Acknowledgements

This thesis would not have been possible without the support, encouragement and assistance provided by many people and I would like to express my appreciation here. Firstly, I would like to express my gratitude to my family and especially my parents Ashley and Karen Doctors for their love and support, which have been very much appreciated.

I thank my supervisors, Peter Coveney and Nick Ovenden for their guidance, feedback on my work and helpful discussions. I am grateful to my colleagues in the Centre for Computational Science for their support and helpful hints. In particular, I thank Rupert Nash and Marco Mazzeo for interesting and helpful discussions on simulation methods, Steven Manos for useful discussions on blood flow simulations, Radhika Saksena and James Suter for discussions on the geometry of complex systems, and Simon Clifford, Owain Kenway, David Wright and Tom Hewer for generous general technical support and assistance with the use of software.

Thanks are due to our collaborators, Dr. Stefan Brew and Dr. Fergus Robertson at the National Hospital for Neurology and Neurosurgery for taking the time to explain how information about blood flow is used during neurosurgery and for permission to observe neurosurgery.

I would also like to show my appreciation for the encouragement I have received from my friends and the pleasure of their company. I would particularly like to thank Jonathan Worthington, Peter Inglesby, Clare Hammond, Hannah Davies, Dan Drodge, Tom Rosoman, Claire White, Adam Stevens, Ben White, Karen Eyre, John Noble, Jude Eyre, James Aitcheson, Cerys and Adam Harmon, Amy New, Jessica Arnold, Nicola Abrams, Freya Grimwood, Rosie Bloxsom, Edwin Law, Jonathan Watson-Lee, David Barclay and Simeon and Emily Dry for their kindness, generosity and friendship.

I acknowledge EPSRC for funding my PhD studentship, associated with the RealityGrid project and Peter Coveney for additional assistance.

Contents

Declaration of Authorship	2
Abstract	4
Acknowledgements	5
List of Figures	10
List of Tables	15
Abbreviations	17
Physical Constants	19
Symbols	20
Introduction	24
1 Haemodynamics	27
1.1 Structure of the blood vessels	28
1.2 Cardiovascular diseases of the blood vessels	30
1.3 Treatment of cardiovascular diseases	33
1.4 Use of simulation for surgical planning	36
1.5 Typical simplifications and assumptions of the models	41
1.6 Specifying simulation parameters	43
1.7 Methods of imaging of cerebral vasculature	49
1.7.1 Magnetic Resonance Angiography	49
1.7.2 X-ray Angiography	50
1.7.3 Computed Tomography Angiography	52
1.7.4 Ultrasound imaging	52
1.7.5 Phase contrast Magnetic Resonance Angiography	53
1.7.6 Segmentation, postprocessing and visualisation	56
1.7.7 Accuracy	59
1.8 Three dimensional fluid dynamics simulation of blood flow	61

1.9	Other models of cerebral blood flow	72
1.10	Inclusion of arterial elasticity	88
2	Lattice-Boltzmann methods	96
2.1	Summary of the lattice-Boltzmann method	97
2.2	Advantages of the lattice-Boltzmann method	99
2.3	LBM simulations of blood flow	100
2.4	Development from Lattice Gas Automata	103
2.5	Detailed Theory of the lattice-Boltzmann method	107
2.5.1	Derivation of the lattice-Boltzmann equation from the Boltzmann equation	117
2.6	Incompressible models	120
2.7	Conversion of parameters into lattice units	123
2.7.1	The law of similarity	125
2.8	Simulation accuracy of lattice-Boltzmann method	127
2.9	Boundary condition methods	134
2.9.1	Bounce back	135
2.9.2	Consistent methods	143
2.9.3	Comparison of body force with pressure boundary conditions	149
2.9.4	Equilibrium schemes	149
2.9.5	Extrapolation methods	149
2.9.6	Methods involving extrapolation in time	153
2.9.7	Grid refinement	154
2.10	Further applications of the lattice-Boltzmann method	155
2.11	Application to non-Newtonian fluids	156
3	A new method for lattice-Boltzmann simulations of fluid flow through axially symmetric elastic systems	163
3.1	Summary of lattice-Boltzmann fluid flow simulations in elastic pipes	165
3.2	Theoretical background	169
3.2.1	Equations of motion for the elastic walls	169
3.2.2	The lattice-Boltzmann model	171
3.3	Choice of boundary condition methods for simulations of a 3D cylinder	172
3.3.1	A new method for pressure and velocity boundary conditions	173
3.3.2	Simulation method	175
3.3.3	Stability of the simulations	177
3.3.4	Comparison of the accuracy of the simulations	178
3.3.5	Discussion	178
3.4	Choice of boundary condition methods for simulations of a 2D channel	181
3.4.1	Combination of a velocity and pressure condition at the corner sites	183
3.4.2	Stability of the simulations	184
3.4.3	Comparison of the accuracy of the simulations	185
3.4.4	Discussion	185
3.5	Simulation method	188
3.5.1	Method for avoiding the creation and destruction of fluid nodes as the wall moves over a lattice site	191
3.5.2	Oscillation of the walls	191

3.5.3	Solving the equation of motion	193
3.5.4	Comparison of numerical and analytical solutions	195
3.6	Results	196
3.7	Discussion	200
3.8	Conclusions	202
4	A new method for simulating fluid flow through elastic systems with a general geometry	204
4.1	Theory of Linear Elasticity in Two and Three Dimensions	205
4.1.1	The Strain Tensor	205
4.1.2	The stress tensor	207
4.1.3	Calculating the Free Energy	208
4.1.4	Hooke's law	209
4.1.5	Expressing Hooke's law in terms of the Young's modulus and Poisson's ratio	210
4.1.6	Equations of motion and its boundary conditions for an isotropic elastic medium	212
4.2	Scheme for simulating fluid flow through an elastic vessel in a general geometry	213
4.2.1	Simulation setup	214
4.2.2	Procedure at each time step	214
4.2.3	Finding the Derivatives of Displacement	216
4.3	The choice of neighbouring points	220
4.4	Calculation of the surface normals, normalised cut distances and stress tensor	223
4.5	Work required to extend the simulation method to three dimensions	225
4.6	Review of studies of a Starling resistor	226
4.7	Comparisons with the study by Lowe and Pedley	233
4.7.1	The wall parameters	234
4.7.2	The flow parameters	236
4.7.3	Convergence of the simulation	237
4.7.4	Results and Discussion	238
4.8	Conclusions	244
5	Dynamic simulations of fluid flow through elastic systems	247
5.1	The density of the wall	248
5.1.1	Limitations on the density of the wall caused by the temporal resolution	248
5.1.2	Subdivision of the lattice-Boltzmann timesteps	251
5.1.3	Testing the dynamics of a Starling resistor with subdivision of the timesteps.	256
5.2	Setting up a comparison of the dynamics of the Starling resistor simulation with previous computational studies	259
5.3	Change to the method for calculation of the normalised cut distances	261
5.4	Initial spacing between the points on the elastic wall	264
5.5	Causes and effects of negative or undefined normalised cut distances	267
5.6	Adaptations of the simulation method when fluid nodes are created or destroyed	271
5.6.1	Algorithm for updating the site types	272

5.6.2	Algorithm for calculating the normalised cut distances	277
5.6.3	Extrapolation of the stress	277
5.6.4	Conservation of mass	278
5.7	Results for a Starling resistor with a large wall displacement	282
5.8	Computational cost of the simulation	283
5.9	Computational issues regarding simulations of fluid flow through large elastic systems on multicore machines	287
5.10	Change to the method for applying velocity boundary conditions to the fluid	292
5.11	Inclusion of viscoelastic behaviour	296
5.12	Comparison of the dynamics with results from a previous study	299
5.13	Conclusions	302
6	Conclusions and Future Work	306

List of Figures

1.1	Main systemic arteries and arteries in the Circle of Willis	29
1.2	A saccular, or bubble aneurysm	31
1.3	A fusiform aneurysm	31
1.4	Regions of an aneurysm	32
1.5	An arterio-venous malformation, which is a direct connection between an artery and a vein.	32
1.6	Packing an aneurysm with coils causes the blood to clot inside it.	34
1.7	A stent redirects the flow through the parent artery.	35
1.8	A typical pressure waveform at the ICA [1].	47
1.9	Change in blood pressure down the arterial tree [2].	47
1.10	Volumetric flow rate waveform for the right ICA [3] measured using phase-contrast Magnetic Resonance Angiography.	48
1.11	A digital subtraction angiogram of a giant aneurysm near the PComA.	51
1.12	Time resolved 3D particle traces illustrating blood flow in parts of the Circle of Willis.	55
1.13	Phase-Contrast Magnetic Resonance angiography measurements of volumetric flow rate waveforms can provide boundary conditions for the whole Circle of Willis.	56
1.14	Procedure for image reconstruction used by Hassan et al. [4].	59
1.15	Wall shear stress distribution and flow velocities obtained in simulations of aneurysms with different characteristics.	60
1.16	Pressure and velocity flow fields obtained from a simulation of an adult Vein of Galen Aneurysm Malformation. Image taken from Hassan et al. [4].	67
1.17	A model of half of the CoW, as studied by Hillen et al. [1]. The arrows show the normal directions of blood flow.	76
1.18	A model of the CoW, as studied by Hillen et al. [5]. The arrows show the positive directions of blood flow. See also figure 1.1.	77
1.19	Flow rate through the left and right posterior communicating artery (PcomA) and anterior communicating artery (AcomA) with respect to the diameter of the right PcomA obtained in [5]	78
1.20	Relationships between flux through an artery vs resistance (top row) and flux vs radius.	81
1.21	The Wheatstone bridge.	82
1.22	The sector model for blood vessels, by Alastruey et al. [6].	83
1.23	Resistance-capacitance-resistance model for the vessels beyond the outflow boundaries.	90
2.1	Lattice velocities for the D2Q9 and D3Q15 models.	109

2.2	Checkerboard colouring of the lattice structures of D3Q19 and D3Q15 models.	134
2.3	Illustration of the bounce-back method on a hexagonal lattice.	135
2.4	Computational grid and location of the non-slip wall for a simulation of an inclined channel.	136
2.5	Details of the bounceback of the distribution functions used in the method by Bouzidi et al. [7] and the cells surrounding the lattice sites for the method by Verberg and Ladd [8].	139
2.6	Representation of an inclined boundary for the method proposed by Verberg and Ladd [8].	142
2.7	2D lattice geometry for the flow over a backward facing step. The arrow shows the direction of flow.	146
3.1	Balance of transmural pressure and tensile stress in the arterial wall.	170
3.2	Minimum values of τ for which simulations of flow in a channel with the ZouHe+GZS method are stable for half widths R of $5.0\Delta x$ to $5.9\Delta x$ and $10.0\Delta x$ to $10.8\Delta x$	185
3.3	Maximum Reynolds numbers for which simulations of flow in a channel that use the pressure boundary condition by Zou and He [9] and the velocity boundary condition by Zhao-Li et al. [10] are stable for half widths R of $5.0\Delta x$ to $5.9\Delta x$ and $10.0\Delta x$ to $10.8\Delta x$	186
3.4	Diagram showing the configuration of fluid sites in a quarter of one layer of a circular cylinder.	189
3.5	Difference between the numerical and analytical displacement in a simulation of fluid flow in a 3D elastic cylinder with $\Delta R = 1.0$ lattice unit at the inlet and $Re = 120$	197
3.6	Difference between the numerical and analytical pressure in a simulation of fluid flow in a 3D elastic cylinder with $\Delta R = 1.0$ lattice unit at the inlet and $Re = 120$	198
3.7	Velocity profiles obtained at four locations in a 3D elastic cylinder with $\Delta R = 1.0$ lattice unit at the inlet and $Re = 120$ and comparison with the analytical solution.	198
4.1	A volume element at the boundary of the elastic body.	208
4.2	Configuration of points on the wall and nearby lattice sites.	215
4.3	A possible selection of the four neighbours that are used to calculate the spatial derivatives of displacement at a point on the wall. This selection gives rise to instability.	221
4.4	This elastic rectangle (the dotted line) is unstable with respect to the shape defined by the continuous lines if, for each point represented by a square, an unsuitable combination of neighbouring points is used to calculate the spatial derivatives of displacement there.	221
4.5	The final selections of the four neighbours that are used to calculate the spatial derivatives of displacement at a point on the wall. This is stable with respect to the situation in figure 4.4.	223
4.6	Diagram of a 2D Starling resistor.	227
4.7	Setup of simulations of the Starling resistors for which the wall profiles were compared to those obtained by Lowe and Pedley [11].	235

4.8	Comparison of the wall profiles obtained in the present study with those obtained by Lowe and Pedley [11] under three different external pressures.	240
4.9	Wall profiles obtained in the present study for $\frac{TD}{\eta Q} = 10^5$ and $\Delta p^* = (p_e - p_d) \left(\frac{D^2}{\eta Q}\right) = 24$ at different lattice resolutions and wall thicknesses.	241
4.10	Wall profiles obtained in the present study for $\frac{TD}{\eta Q} = 10^5$ and $\Delta p^* = (p_e - p_d) \left(\frac{D^2}{\eta Q}\right) = 84$ at different lattice resolutions and wall thicknesses.	241
4.11	Wall profiles obtained in the present study for $\frac{TD}{\eta Q} = 10^5$ and $\Delta p^* = (p_e - p_d) \left(\frac{D^2}{\eta Q}\right) = 224$ at different lattice resolutions and wall thicknesses.	242
4.12	Comparison of the wall profiles near the wall's right hand end obtained in the present study with those obtained by Lowe and Pedley [11] at external pressures either side of that at which the wall is expected to undergo a transition from a fully to partially distended state.	243
4.13	Comparison of the wall profiles near the wall's left hand end obtained in the present study with those obtained by Lowe and Pedley [11] at external pressures either side of that at which the wall is expected to undergo a transition from a partially to fully collapsed state.	244
5.1	Modulus of the amplitude of the dominant frequency of oscillation of the separation in the y -direction between each point on the lower surface and its corresponding point on the upper surface, for simulations of the elastic sections of the walls of two Starling resistors with length $L_e = 5\Delta x$.	252
5.2	Modulus of the amplitude of the dominant frequency of oscillation of the separation in the y -direction between each point on the lower surface and its corresponding point on the upper surface, for simulations of the elastic sections of the walls of two Starling resistors with length $L_e = 8\Delta x$.	253
5.3	Modulus of the amplitude of the dominant frequency of oscillation of the separation in the y -direction between each point on the lower surface and its corresponding point on the upper surface, for simulations of the elastic sections of the walls of two Starling resistors with length $L_e = 10\Delta x$.	254
5.4	y -displacement of the central point on the inner surface of the elastic wall in a stable simulation of a Starling resistor with the parameters used in [12] except that $\rho_w = 3896.968603\rho_f$.	257
5.5	y -displacement of the central point on the inner surface of the elastic wall in a simulation of the same Starling resistor as in figure 5.4 except that the density of the wall is lower, which causes the simulation to be unstable because the period of oscillation of the wall is too short.	258
5.6	Example of the setup for simulations of a Starling resistor in which the wall is not flat to begin with.	262
5.7	Initial inner surface of the elastic wall for the simulations started close to the steady state found in figure 4 of [13].	264
5.8	Configuration of lattice sites and points on the wall for which one of the normalised cut distances becomes undefined.	265
5.9	Diagram to show why it is inappropriate to approximate the surface between a point and its neighbours as a circle.	265

5.10	Profiles of the elastic wall at different times for a simulation of a Starling resistor that becomes unstable because the points were not sufficiently evenly spaced at the beginning of the simulation.	267
5.11	Profiles of the elastic wall in a simulation of the same Starling resistor as in figure 5.10, but with more evenly spaced initial points.	268
5.12	Configuration of lattice sites and their points on an elastic segment on the inner surface of the wall if the wall slope is gentle.	268
5.13	Configuration of lattice sites around a region of the inner surface of the wall that is initially concave, but becomes convex, which causes a normalised cut distance from one of the lattice sites to become undefined.	270
5.14	Configuration of lattice sites that could occur around a region of the inner surface of the wall that is convex if the rules in Fang et al. [14] are applied. A normalised cut distance from one of the lattice sites is undefined.	270
5.15	Lattice sites immediately surrounding a segment of the inner surface of the wall, for which their normalised cut distances and nearest points on the wall need to be updated.	273
5.16	The first nine of seventeen tests for the algorithm that changes lattice sites from fluid to solid or <i>vice versa</i>	274
5.17	The last eight of seventeen tests for the algorithm that changes lattice sites from fluid to solid or <i>vice versa</i>	275
5.18	Test case for which the algorithm that changes lattice sites from fluid to solid or <i>vice versa</i> will fail.	276
5.19	Configuration of the wall for which the calculation of the stress at a point on the inner surface of the wall, using the method described in section 4.4, will fail because the normalised cut distance that it requires is undefined.	278
5.20	Possible combinations of a boundary site's neighbouring fluid sites.	281
5.21	Displacement of the central point on the inner surface of the wall over time for a simulation of a Starling resistor with the parameters used in [11], except for the external pressure, which is much greater.	284
5.22	Wall profiles for a Starling resistor with the same parameters as those used for figure 5.21 during the first period of oscillation of the wall.	285
5.23	Wall profiles for a Starling resistor with the same parameters as those used for figure 5.21 during the fourth period of oscillation of the wall.	285
5.24	L^1 norms of the fluid velocity and wall displacement during a simulation of a Starling resistor.	293
5.25	Long-term velocity of the wall for a simulation of a Starling resistor at $t = 8002\Delta t$, calculated from equation (5.5), with the same parameters as figure 5.24.	294
5.26	Method for estimating the velocity of the wall at the point of intersection with a lattice link by interpolation.	295
5.27	L^1 norms of the fluid velocity and wall displacement during three simulations of a Starling resistor for which different methods involving spatial interpolation are used to calculate the velocity to impose at the boundary of the fluid domain.	297
5.28	Wall profile obtained by simulations of a Starling resistor with three different methods.	298
5.29	Diagram of a 2D Starling resistor for section 5.12.	300

5.30	Wall profiles obtained during a simulation of a Starling resistor with approximately the same parameters as those for the steady state solution used for figure 4 of [15].	303
5.31	Wall position y at $x = 3.5D$ as a function of time for a simulation of a Starling resistor with the parameters approximately equal to those used for figure 4 of [15].	304
5.32	Wall position y at $x = 3.5D$ as a function of time from figure 4 of [15]. . .	305

List of Tables

1.1	Anatomical and model dimensions. All anatomical dimensions are external diameters in fixed material.	46
2.1	Coefficients for the equilibrium distribution functions of various lattice-Boltzmann models [16–18].	111
3.1	Minimum values of τ and corresponding maximum Reynolds number for which simulations of flow in a cylinder at radius R are stable for three different boundary condition methods.	178
3.2	Comparison of the accuracy of simulations of flow in a cylinder at $Re = 1.0$, $\tau = 0.8$ for three different boundary condition methods.	179
3.3	Comparison of the accuracy of simulations of flow in a cylinder at $Re = 30.0$, $\tau = 0.53$ for the boundary condition methods described at the beginning of section 3.3.	180
3.4	Minimum values of τ and corresponding maximum Reynolds number for which simulations of flow in a channel are stable for three different boundary condition methods.	184
3.5	Comparison of the accuracy of simulations of flow in a channel at $Re = 31.2$, $\tau = 0.53$ for three different boundary condition methods.	187
3.6	Relative errors in velocity, pressure and wall displacement for simulations of fluid flow in 3D elastic and rigid cylinders at $Re = 120$	199
3.7	Comparison of computational cost between the simulation of fluid flow in a 3D elastic cylinder that includes a damping factor, with $\Delta R = 1.0$ lattice unit at the inlet, and the simulation for rigid walls with the same Reynolds number.	199
4.1	Unstrained positions of points, (x, y) , and their displacements, \mathbf{u} , from these positions for the piece of elastic material shown in figure 4.4.	222
4.2	Spatial derivatives of displacement at point C in figure 4.4 for both choices of neighbouring points.	223
5.1	Parameters of computations of the elastic section of the wall of a Starling resistor for which a constant pressure gradient is applied at the lower surface.	250
5.2	Comparison of observed and expected periods of oscillation of the elastic wall in simulations of a Starling resistor.	259
5.3	Positions of the ends of the line segments that form the inner surface of the elastic wall measured relative to its bottom left corner for the simulations started close to the steady state found in figure 4 of [13].	263

5.4 y -ordinate of the point on the wall at $x = 3.5D$, measured relative to the left-hand end of the elastic wall, for the steady state solutions obtained by [13, 19] at different values of the tension, $T = \frac{1.610245N}{\beta}$ 299

Abbreviations

2D	Two- D imensional
3D	Three- D imensional
3DRA	Three- D imensional Rotational Angiography
AAA	Abdominal A ortic A neurysm
ACA	Anterior C erebral A rtery
AcomA	Anterior c ommunicating A rtery
AVM	Arterio- V enous M alformation
BGK	B hatnagar- G ross- K rook
BOT	B alloon O cclusion T est
CCA	Common C arotid A rtery
CFD	Computational F luid D ynamics
CoW	Circle of W illis
CPP	Cerebral P erfusion P ressure
CSF	Cerebrospinal F luid
CTA	Computer T omography A ngiography
DSA	Digital S ubtraction A ngiography
ECA	External C arotid A rtery
ICA	Internal C arotid A rtery
IVUS	Intravascular U ltrasound
LBE	Lattice- B oltzmann E quation
LBGK	Lattice B hatnagar- G ross- K rook
LBM	Lattice- B oltzmann M ethod
MCA	Middle C erebral A rtery
MR	Magnetic R esonance
MRA	Magnetic R esonance A ngiography

MRI	M agnetic R esonance I magingy
PCA	P osterior C erebral A rtery
PCMRA	P hase- C ontrast M agnetic R esonance A ngiography
PcomA	P osterior co mmunicating A rtery
VA	V ertebral A rtery
VGAM	V ein of G alen A neurysm M alformation
WSS	W all S hear S tress

Physical Constants

Ideal gas constant $R_g = 8.314472 \text{JK}^{-1}\text{mol}^{-1}$

Boltzmann constant $k_B = 1.3806504 \times 10^{-23} \text{JK}^{-1}$

Symbols

A	Area	m^2
c	Lattice speed $\frac{\Delta x}{\Delta t}$	m s^{-1}
c_s	Speed of sound in fluid	m s^{-1}
C	Compliance constant	$\text{m}^2\text{kg}^{-1}\text{s}^2$ (2D), $\text{m}^4\text{kg}^{-1}\text{s}^2$ (3D)
D	Diameter	m
\mathbf{e}_i	Particle velocity	m s^{-1}
E	Young's modulus	kg s^{-2} (2D), Pa (3D)
f_i	Distribution function of particle density	kg m^{-2} (2D), kg m^{-3} (3D)
$f_i^{(eq)}$	Equilibrium distribution function	kg m^{-2} (2D), kg m^{-3} (3D)
$f_i^{(neq)}$	Nonequilibrium distribution function	kg m^{-2} (2D), kg m^{-3} (3D)
f_i^+	Postcollisional distribution function	kg m^{-2} (2D), kg m^{-3} (3D)
$f_i^{(1)}, f_i^{(2)}$	Chapman-Enskog components of distribution functions	kg m^{-2} (2D), kg m^{-3} (3D)
\mathbf{F}	Force per unit volume	$\text{kg m}^{-1}\text{s}^{-2}$ (2D), $\text{kg m}^{-2}\text{s}^{-2}$ (3D)
h	Thickness of vessel wall	m
Hct	Haematocrit	Dimensionless
K	Bulk modulus	kg s^{-2} (2D), Pa (3D)
l	Normalised distance along line segment	Dimensionless
L	Length	m
L_{entr}	Entrance length	m
L_d	Length of rigid section of vessel downstream of elastic section	m
L_e	Length of elastic section	m
L_u	Length of rigid section of vessel upstream of elastic section	m

m	Mass	kg	
m_m	Molar mass	kg	
Ma	Mach number	Dimensionless	
\mathbf{n}	Surface normal	Dimensionless	
N_D	Number of dimensions	Dimensionless	
p	Pressure	kg s^{-2} (2D),	Pa (3D)
p_0	Reference pressure	kg s^{-2} (2D),	Pa (3D)
p_d	Outlet pressure	kg s^{-2} (2D),	Pa (3D)
p_e	External pressure	kg s^{-2} (2D),	Pa (3D)
p_u	Inlet pressure	kg s^{-2} (2D),	Pa (3D)
Q	Flow rate	m^2s^{-1} (2D),	m^3s^{-1} (3D)
r	Radial ordinate	m	
R	Radius of vessel	m	
R_0	Reference radius of vessel	m	
Re	Reynolds number	Dimensionless	
St	Strouhal number	Dimensionless	
t	Time	s	
T	Tension	N	
T_0	Reference tension	N	
\mathbf{u}	Displacement	m	
\mathbf{v}	Velocity	m s^{-1}	
V	Volume	m^2 (2D),	m^3 (3D)
W	Helmholtz free energy per unit volume	kg s^{-2} (2D),	Pa (3D)
w_i	Weight of distribution function	kg m^{-2} (2D),	kg m^{-3} (3D)
\mathbf{x}	Position vector	m	
\mathbf{x}'	Position vector in strained solid	m	
x, y, z	Cartesian coordinates	m	
x', y', z'	Cartesian coordinates in strained solid	m	
Z_R	Resistance to flow	$\text{kg m}^{-2}\text{s}^{-3}$ (2D),	$\text{kg m}^{-4}\text{s}^{-3}$ (3D)
α	Womersley number	Dimensionless	
β	Tension reduction factor	Dimensionless	
γ	Time required for computation	s	

γ	Vorticity	s^{-1}	
Γ	Period of shortest mode of oscillation	s	
δ	Normalised cut distance	m	
Δm	Mass of fluid per lattice point	kg	
Δx	Lattice spacing	m	
Δt	Duration of one lattice timestep	s	
ϵ	Knudsen number	Dimensionless	
ϵ	Strain tensor	Dimensionless	
ζ	Kinematic bulk viscosity	m^2s^{-1}	
η	Dynamic viscosity	$kg s^{-1}$ (2D),	Pas (3D)
θ	Circumferential ordinate	Dimensionless	
Θ	Temperature	K	
λ	First Lamé coefficient	$kg s^{-2}$ (2D),	Pa (3D)
Λ	Period of oscillation	s	
μ	Shear modulus	$kg s^{-2}$ (2D),	Pa (3D)
ν	Kinematic viscosity	m^2s^{-1}	
ξ	Frequency for Fourier transform	s^{-1}	
ρ	density	$kg m^{-2}$ (2D),	$kg m^{-3}$ (3D)
ρ_0	Reference density	$kg m^{-2}$ (2D),	$kg m^{-3}$ (3D)
ρ_f	Density of fluid	$kg m^{-2}$ (2D),	$kg m^{-3}$ (3D)
ρ_w	Density of vessel wall	$kg m^{-2}$ (2D),	$kg m^{-3}$ (3D)
σ	Stress tensor	$kg s^{-2}$ (2D),	Pa (3D)
Φ	Ratio of computational costs	Dimensionless	
χ_i	Collision operator		
Ψ	Number of elastic wall timesteps per lattice timestep	Dimensionless	
τ	Relaxation parameter	Dimensionless	
τ	External stress	$kg s^{-2}$ (2D),	Pa (3D)
ω	Angular frequency	$rad s^{-1}$	
Ω	Poisson's ratio	Dimensionless	

Dedicated to my parents

Introduction

Cerebral blood flow behaviour, i.e. haemodynamics, plays a crucial role in the understanding, diagnosis and treatment of cerebrovascular disease, of which there are several types. For example, aneurysms are dilations of the arterial walls, which could grow and then rupture, atherosclerosis is the buildup of fatty deposits in arteries, which restricts blood flow, and an arterio-venous malformation is a direct connection between an artery and a vein, which may rupture or direct blood flow away from the surrounding vessels. Haemodynamics has been modelled extensively in the last thirty years, by simple one and two-dimensional computational models and, more recently, three-dimensional computational fluid dynamics (CFD) studies. Many of these CFD studies simulate blood flow in patient-specific vasculatures. The models have enhanced our understanding of haemodynamic phenomena. In particular, some of the work discussed in section 1.8 provides evidence of correlation between the behaviour of the blood flow and the development of neurovascular pathologies, such as the effect of the area over which the inflow jet impinges on the wall of an aneurysm on the risk of rupture of that aneurysm.

Patient-specific medicine is the adaptation of medical treatment to the characteristics of an individual patient. For example, simulations of cerebral blood flow could be used to help surgeons assess the risks of cerebrovascular disease in patients and the effects of surgical treatments on a patient before they are carried out. In the latter case, the results must be available within a few minutes. These simulations have a high computational cost due to the intricate geometry of the vessels. Therefore, it is essential that they run efficiently on multicore computers. It is difficult to develop high-performance codes for continuum solvers that satisfy this requirement. The lattice-Boltzmann method (LBM) has several advantages over continuum solvers. Most importantly, it is possible to achieve a linear

speed-up with the number of processors. Since 2007, the LBM has been used to simulate patient-specific blood flow in cerebral vasculatures.

Most CFD simulations of cerebral blood flow have, thus far, assumed that the arterial walls are rigid. However, the displacement of the wall could influence or be influenced by cardiovascular disease. Since 3D CFD studies have shown that the flow fields are sensitive to small changes in the geometry, as discussed in section 1.8, it is likely that the elasticity will have important effects on the pressure, velocity and stress flow fields. In this thesis, I first devise a method for carrying out time-dependent simulations of fluid flow through three-dimensional axisymmetric elastic vessels, then develop a somewhat similar method to deal with a more complex geometry. The LBM is used because of its computational efficiency on multicore machines and I attempt to minimise the increase in computational cost due to the inclusion of elasticity and to maintain the scalability characteristics of the LBM. The ultimate aim of this work is to simulate patient-specific cerebral blood flow realistically, including the effects of arterial elasticity, within a clinically useful timescale. Some modifications to the LBM have already been proposed to simulate fluid flow in elastic vessels. However, the majority of these studies only include simulations of flow through a simple two-dimensional channel in which the wall is divided into segments that move independently. The scheme that can deal with a more complex geometry places a restriction on one of the parameters of the elastic wall material, whereas the method developed in this study does not restrict that parameter.

This thesis begins with an overview of blood circulation, cerebrovascular disease, medical imaging techniques that are used for diagnosis of cerebrovascular disease, computational models of cerebral blood flow and the use of simulation for surgical planning. The importance of including arterial elasticity is also discussed in chapter 1 and some simple computational models that include arterial elasticity are reviewed. Chapter 2 describes theoretical and practical aspects of the lattice-Boltzmann method, which was used for all simulations of fluid flow in this thesis. That chapter includes a discussion of the accuracy of the LBM, its advantages over other CFD techniques, its limitations, and a review of methods for applying boundary conditions within the LBM. Lattice-Boltzmann simulations of cerebral blood flow are reviewed there. Chapter 2 also describes how the LBM can be used for simulations of non-Newtonian fluids.

Chapter 3 begins with a short discussion of systems other than blood vessels in which the effect of elasticity on fluid flow in systems is important. This is followed by a review of existing methods for including wall elasticity in lattice-Boltzmann models. A method for carrying out lattice-Boltzmann simulations of fluid flow through 3D axisymmetric vessels is proposed in chapter 3 and its accuracy, computational cost and suitability for cerebral blood flow simulations are evaluated. The accuracy of several different combinations of lattice-Boltzmann boundary condition methods and their suitability for computations of fluid flow through elastic vessels was also tested.

A method is developed for lattice-Boltzmann simulations of fluid flow through elastic vessels in a more general geometry in chapter 4. Experimental and computational work on an extensively studied system of fluid flow through compliant vessels is reviewed. The steady-state wall profiles resulting from simulations with the scheme developed in chapter 4 are compared with those from existing computational studies of the same system to validate the steady-state behaviour. In chapter 5, the scheme is improved so that it can cope with a wider range of wall densities and larger displacements of the wall.

Chapter 6 contains concluding remarks and a discussion about future work.

Chapter 1

Haemodynamics

Cerebral blood flow behaviour plays a crucial role in the understanding, diagnosis and treatment of cerebrovascular disease. This has been modelled extensively in both healthy and diseased blood vessels by simple one and two-dimensional models and three-dimensional computational fluid dynamics (CFD) studies. For these studies, the required models of the luminal geometry are usually extracted from 3D data sets acquired *in vivo*, such as magnetic resonance angiograms and computed tomography angiograms [20–22]. In this chapter, cerebrovascular diseases and their treatments are discussed, then the one, two and three dimensional models of blood flow are reviewed. The methods of extracting the geometry for the 3D simulations are also summarised.

In section 1.1, I describe the structure of the cerebral blood vessels. Diseases of blood vessels are discussed in section 1.2 and surgical treatment is described in section 1.3. Section 1.4 explains why it is important to understand the cerebral blood flow behaviour. The typical simplifications and assumptions of blood flow models are described in section 1.5. The physical parameters of blood flow are discussed in section 1.6. Section 1.7 describes some methods for medical imaging and how they are used to obtain data for CFD simulations. Three dimensional CFD simulations and simpler models are reviewed in sections 1.8 and 1.9 respectively. Finally, studies that include arterial elasticity are discussed in section 1.10.

1.1 Structure of the blood vessels

There is no effective storage of oxygen and glucose in the brain. 15% of total cardiac output goes to the brain and it consumes 25% of the oxygen supplied to the body. The vasculature of the brain differs from the rest of the body in several ways [23].

Firstly, the brain and spinal cord are surrounded by three membranes called meninges. The dura mater consists of two periosteal layers and is the outermost membrane. The arachnoid membrane is in the middle. The innermost meninx, the pia mater, follows the surface of the brain and penetrates the fissures. The subarachnoid space, which is between the pia mater and arachnoid membrane, contains cerebrospinal fluid (CSF), which cushions the brain. The arteries and veins are surrounded by CSF after they pierce the dura mater.

There are differences in the structures of the vessels. In the brain, the arteries have a thin endothelium, then a tunica media, consisting of the elastic fibres, then the tunica adventitia, which is a tough outer layer. Outside the brain, the elastic fibres take up the whole width of the arterial wall.

The brain also has some collateral circulation, which means that we have an arterial network which prevents focal disruption of blood flow when an artery is occluded. It allows distal branches of an occluded artery to fill in a retrograde fashion by providing alternative routes for blood flow. The small cortical branches of the cerebral arteries (arteries supplying the left and right cerebral cortices, which make up the majority of the brain) join across a vulnerable watershed or border zone on the surface of the brain. The most important collateral route is the circle of Willis, as shown in figure 1.1. It joins the left and right internal carotid arteries (ICAs), and the basilar artery. The ICAs and vertebral arteries, which join to form the basilar artery, supply the brain.

As well as providing alternative routes for blood flow when arteries are occluded, the CoW may also have a role in healthy subjects [1]. The flow in the vertebral artery and possibly the carotid artery is influenced by movements of the head. The posterior communicating artery (PcomA) may have a compensatory function in this case, so that the effects of a decrease in blood flow in one of the afferent (incoming) vessels of the CoW are reduced and a critically low level is not reached in any of the efferent (outgoing) vessels.

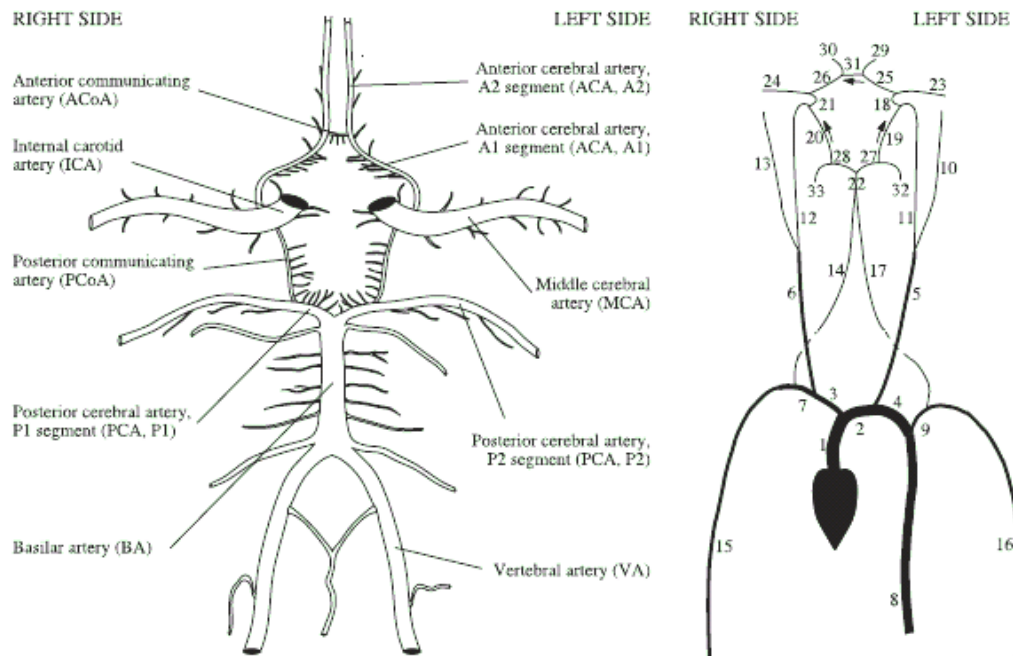


FIGURE 1.1: The left image shows the CoW and the right image shows the main systemic arteries. The arrows show the normal flow directions for blood. Image taken from [6].

The systemic arteries that supply the body are configured as shown in figure 1.1. The aorta (1) comes up from the heart and splits into the aortic arch (2) on the left and the brachiocephalic artery (3) on the right. The first branch of the brachiocephalic artery and aortic arch are the right and left common carotid arteries respectively (5 and 6). The common carotid arteries split into the external carotid arteries, which supply the face (10 and 13) and the ICAs (11 and 12), so the systemic arteries supplying the left and right ICAs are asymmetric. The brachiocephalic artery becomes the right subclavian artery (7) and the aortic arch reaches its maximum height and curves over and its next branch is the left subclavian artery (9). The first branch of each subclavian artery is the vertebral artery (14 and 17) The left and right subclavian arteries reach a maximum height and curve over to become the left and right brachial arteries (16 and 15).

The veins that drain the brain begin deep within the parenchyma of the brain and drain on the surface. All veins drain into cavities called dural venous sinuses, which force apart the two periosteal layers in the dura mater. The sinuses drain into the internal jugular vein. Dural sinuses are a feature unique to the brain. One of the largest veins is the Great

Cerebral Vein, or vein of Galen, which drains the deep cerebrum, which is the uppermost and largest part of the brain [23].

The arteries branch into smaller and smaller ones that become arterioles when the diameter is below approximately $50\mu\text{m}$ [24]. The capillaries are $4\text{--}7\mu\text{m}$ wide and one cell thick and are not surrounded by CSF.

1.2 Cardiovascular diseases of the blood vessels

The blood vessels also differ in their response to injury. If a subarachnoid haemorrhage occurs, blood leaks into the CSF. The presence of blood here may induce sustained vasoconstriction and compression of structures in the brain, which do not occur if blood is applied to the outside of extracranial arteries. Cerebral haemorrhage results from rupture of the wall of a blood vessel due to weakening by high blood pressure, in which case intracerebral haemorrhage is most likely, or the rupture of an aneurysm, in which case a subarachnoid haemorrhage is most likely. Aneurysms are dilations of the arterial wall that frequently form at arterial bifurcation sites [3, 23]. An aneurysm may be saccular, in which case it resembles a bubble (figure 1.2) or fusiform (figure 1.3), in which case the vessel bulges around the entire circumference without protrusion of the inner layers of the vessel [4]. A schematic diagram of the regions of an aneurysm is given in figure 1.4.

Ischaemia, or a reduction in blood supply, destroys the brain tissue. This may be caused by stenosis which is the partial occlusion of an artery. Stenosis is usually due to atherosclerosis, which is the buildup of fatty deposits. A deposit may serve as a nidus for the formation of a clot, called a thrombus. A clot may come from a distant site and lodge in a smaller vessel. In this case, it is called an embolus. A drop in cerebral perfusion pressure, which is the difference between arterial and venous pressure results in a smaller flow. The collateral circulation should reduce the chance of ischaemia. The term stroke refers to neurologic dysfunction resulting from a derangement of blood supply to the brain or spinal cord. A stroke may be haemorrhagic or ischaemic.

An arterio-venous malformation (AVM) occurs when there is a direct connection between an artery and a vein, as shown in figure 1.5. It is important to treat it in order to regain normal cerebral flow [4]. Atherosclerosis can cause the development of vessels in the



FIGURE 1.2: A saccular, or bubble aneurysm. Image taken from a presentation by Dr. Stefan Brew, National Hospital for Neurology and Neuroscience, Queen Square, London.

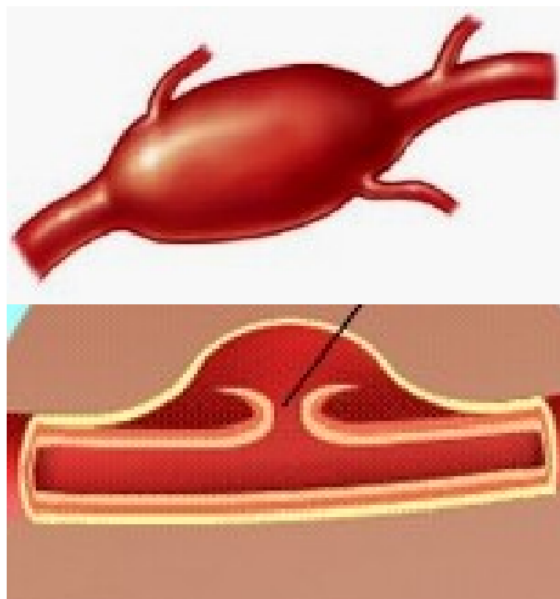


FIGURE 1.3: A fusiform aneurysm. Image taken from a presentation by Dr. Stefan Brew.

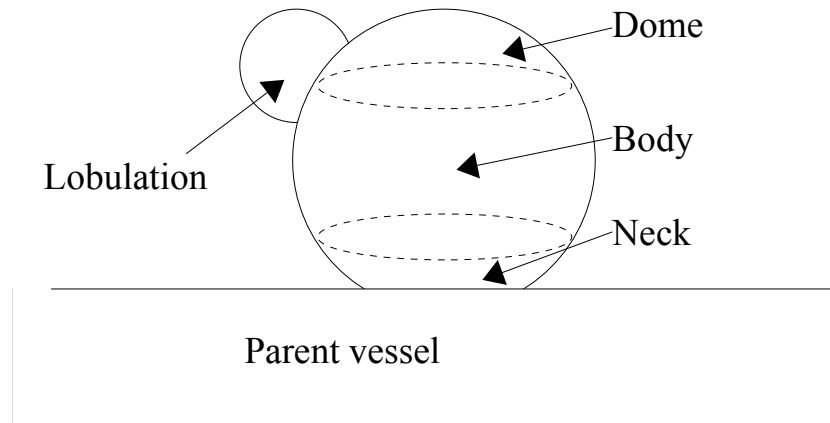


FIGURE 1.4: Regions of an aneurysm. Image based on [25].

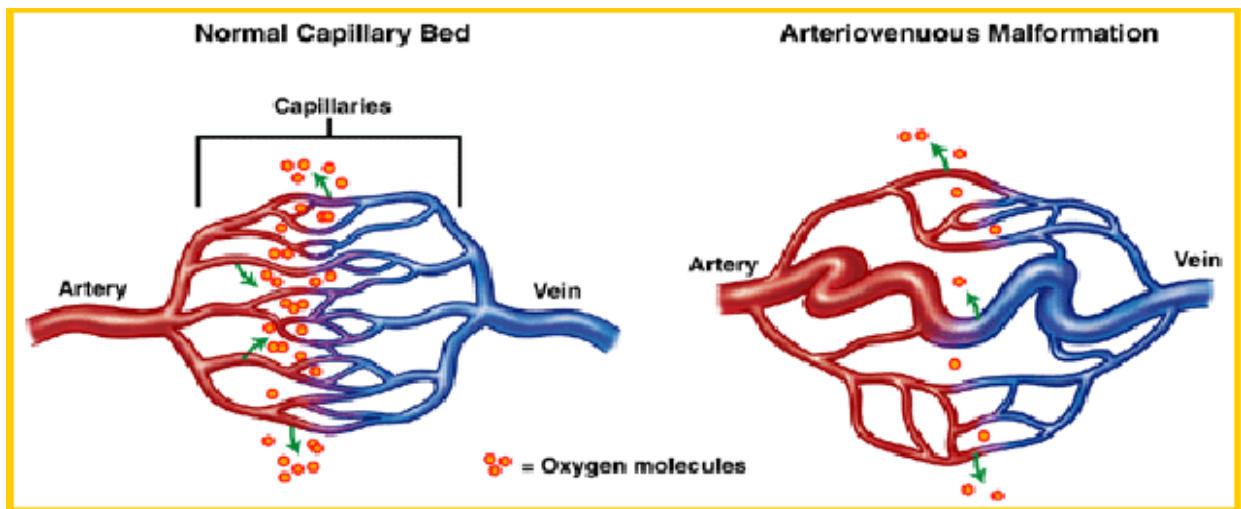


FIGURE 1.5: An AVM is a direct connection between an artery and a vein. Image taken from a presentation by Dr. Stefan Brew.

tunica adventitia (outer layer) of arteries. One type of AVM is a vein of Galen aneurysm malformation (VGAM) which, in adults is associated with a fusiform aneurysm. Hassan et al. [4] were treating a patient who had a VGAM supplied by a single feeder from the medial posterior choroidal artery, which is a branch of the PCA. It drained to an old sinus that usually would have closed after birth.

1.3 Treatment of cardiovascular diseases

The information in this subsection came from a talk and from watching operations by Dr. Stefan Brew, National Hospital for Neurology and Neuroscience, Queen Square, London. Other citations are indicated.

For ischaemic strokes, there are several methods of treatment. One can use thrombolytic agents, intravenously or intra-arterially to remove the thrombus if that causes the stroke. Anticoagulants may be injected. Alternatively, an arterial deposit can be surgically removed. One can mechanically recanalise the artery, that is, to place a bypass to allow blood to flow past an occluded segment of an artery. It may be treated by angioplasty, which is the widening of a blood vessel using folded balloons and inserting a stent, which is a cylindrical structure consisting of struts that cross one another.

A cerebral haemorrhage may be treated by occluding the aneurysm. A surgical clip may be used to stop blood flowing into the aneurysm. A coil may be inserted into it (figure 1.6) [26]. When an aneurysm is packed with one or more coils, the blood clots around it. Angioplasty may also be used to redirect the flow [6]. A stent may be used to support the coils [27]. Stents are increasingly being used to redirect the flow of blood through the parent artery and not the aneurysm (figure 1.7), rather than merely being a support device for the coils [28]. A blood clot may form on the spaces between the struts of the stent [28]. Alternatively, the parent artery may be occluded by injecting particles or glue. An artery may also be occluded if it supplies a tumour.

An AVM may be treated by embolisation of the abnormal blood vessels. In [4], the VGAM was treated by stenosis of the parent artery just before the aneurysm, after which the drainage pattern was normal.

If a coil, stent or balloon is inserted into an artery or an injection is needed in a specific place, this is done by catheterisation. The insertion of a coil like this is shown in figure 1.6. Stents or coils are made of a material with memory and they are kept inside the catheter as a long, thin rod of a material with memory [26–28]. An incision is made in the femoral artery and the catheter is guided up to the brain, then to the point where the treatment is needed. The stent or coil is then pushed through and it will assume the correct shape. A balloon will be inflated inside the vessel. X-ray angiographies, explained in section 1.7 are

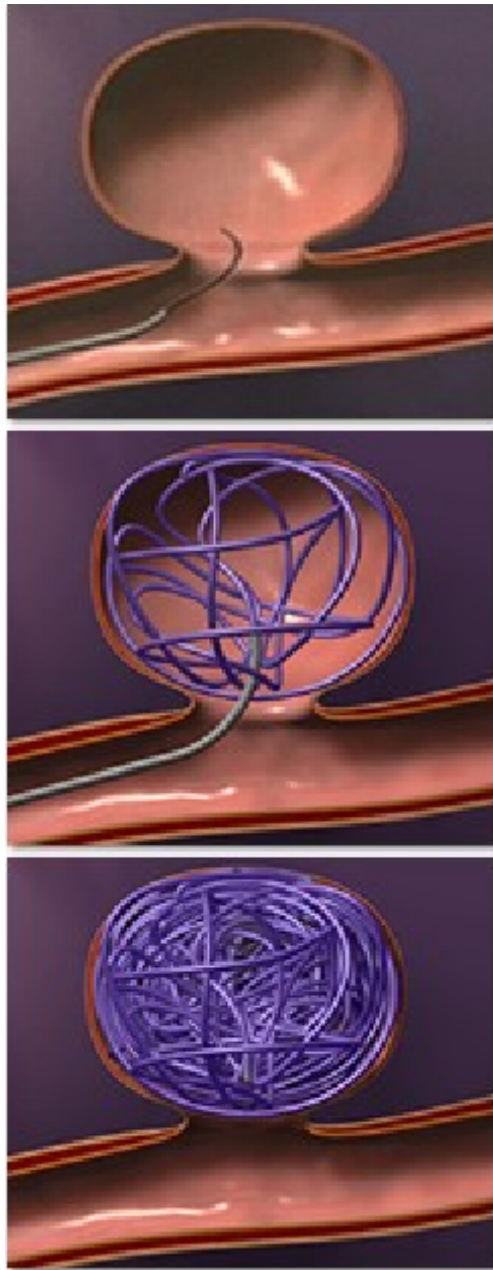


FIGURE 1.6: Packing an aneurysm with coils causes the blood to clot inside it. Image taken from a presentation by Dr. Stefan Brew.

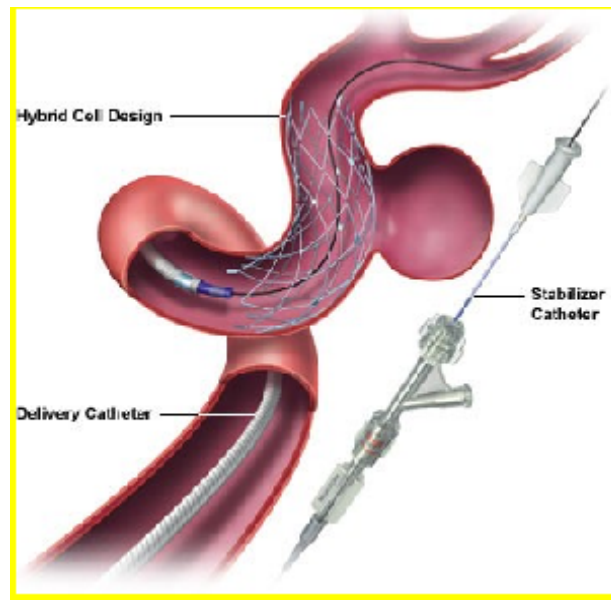


FIGURE 1.7: A stent redirects the flow through the parent artery. Image taken from a presentation by Dr. Stefan Brew.

taken at various times during the procedures to check the position of the catheter [26, 27] and check the flow of blood after treatment. They are not taken continuously during the entire operation due to the risks of x-rays to the patient and surgeon. The procedures described are called interventional neuroradiology and it is replacing conventional surgery due to improvements in imaging equipment, catheters, embolic agents and stents. However, there will always be some lesions (abnormal tissues) that are best treated by conventional surgery.

When treatment involves occluding a vessel, the treatments take advantage of the collateral circulation in the brain, so that blood will be supplied via a different route. However, 51% of people have an incomplete CoW or a hypoplastic (small and underdeveloped) artery in the CoW [6]. The most common anatomical variations are PcomA missing (9% of people), both PcomAs missing (9%), one P1 PCA missing (9%), one PcomA and the contralateral P1 PCA missing (9%), one A1 ACA missing (6%). These were included in the study by Alastruey et al. [6]. They also included the CoW with a missing AcomA, even though it occurs in only 1% of people because the AcomA is commonly recognised as the most important collateral route in the case of severe occlusion of an ICA. When neurosurgery is carried out, it is essential to check whether the patient will have an adequate supply of blood to all parts of the brain. A balloon occlusion test (BOT) is usually used in

the treatment of non-operable cerebral aneurysms [29]. The balloon makes a temporary occlusion of the vessel to test the effect of a permanent one.

The deployment of a stent to treat atherosclerosis injures the arterial wall. Smooth muscle cells regrow in response to this injury but excessive regrowth can cause restenosis of the artery.

1.4 Use of simulation for surgical planning

In all these treatments, it is difficult to assess whether the treatment will be successful before it is carried out and return the blood flow pattern to normal. Therefore, simulations of cerebral blood flow will be an essential tool for surgeons to assess the effects of treatments before they are carried out. It is essential to ensure that there will be a sufficient blood supply to all areas of the brain, that unwanted blood flow, for example in aneurysms or AVMs, has been stopped and that haemodynamic factors such as the wall shear stress and blood pressure are favourable and do not lead to complications such as the rupture of vessels. Currently, the effects of treatment are not known precisely before the treatment is carried out. Furthermore, the causes of growth and rupture of cerebral aneurysms, are not well understood, but are thought to depend on haemodynamic factors [30]. These factors, particularly wall shear stress (WSS) may also play a role in the onset and perhaps the progression of atherosclerotic plaques. Atherosclerosis usually develops in regions of complex flow. Simulations of blood flow in the brain will help to understand these factors.

Planned aneurysm surgery could benefit from a better understanding of the process of aneurysm formation, progression and rupture, so sound judgement in therapies could be exercised [3]. Haemodynamic factors should be important in the pathogenesis and thrombosis of aneurysms, so a correlation between patient-specific clinical events and haemodynamic patterns must be undertaken to better understand the relative importance of the haemodynamic forces.

Computational models are attractive for studying correlations between haemodynamic patterns and clinical events because they are able to model and study any possible geometry [3, 31]. They are capable of predicting the flow and pressure at any desired section in the vessel network [29]. They can estimate flow in normal and disease situations and

predict the result of treatment procedures [29]. By 2008, some tools had been developed to allow endovascular devices to be placed virtually inside patient-specific vascular geometries and to simulate the fluid dynamics before and after treatment [32–34]. Bernardini et al. [32] computed the flow fields in an artery harbouring an aneurysm before and after insertion of a stent, using several different models of stent deployment. Tahir et al. [35] modelled restenosis of arteries after stent deployment. These studies are discussed in more detail in section 1.8.

For a patient-specific simulation, the geometry must first be extracted from a medical image [3, 31]. This will be described in section 1.7. The geometry is converted into a numerical model by converting it into volumetric data and creating a tetrahedral grid in the fluid domain on which the incompressible Navier-Stokes equations [36] for unsteady incompressible flow in three dimensions are solved:

$$\nabla \cdot \mathbf{v} = 0 \quad (1.1)$$

$$\rho \left(\frac{\partial \mathbf{v}}{\partial t} + \mathbf{v} \cdot \nabla \mathbf{v} \right) = \nabla \cdot \sigma, \quad (1.2)$$

where ρ is the density, t is time, \mathbf{v} is velocity and σ is the stress tensor. For a Newtonian fluid:

$$\sigma_{ij} = \eta \left(\frac{\partial v_i}{\partial x_j} + \frac{\partial v_j}{\partial x_i} \right) - p \delta_{ij}, \quad (1.3)$$

where η is the dynamic viscosity, p is the pressure and \mathbf{x} is the position.

A finite-element formulation is usually used for cerebral blood flow simulations [3, 37]. At each fluid inlet and outlet, boundary conditions for the pressure and velocity must be specified. No slip boundary conditions are applied at the vessel walls, which means the velocity of the fluid parallel and perpendicular to the wall is zero. In contrast, Hassan et al. [4] used a finite-volume formulation and solved it using a software package called Fluent [38].

Many three dimensional computational fluid dynamics (CFD) studies have been carried out concerning the haemodynamics of cerebral aneurysms and how this relates to their formation, growth and rupture [37].

These studies usually only consider blood vessels immediately surrounding the aneurysm and not the whole brain. Studies on flow throughout the brain usually use alternative

models. It is difficult to quantitatively test the accuracy of CFD models because any of the flow parameters, such as the blood velocity at a certain point, or the phase difference between flow in places are difficult to measure *in vivo* and the measurement would involve significant patient risk [25, 39]. For example, intravascular probes can be used to measure the pressure, but they can only provide a small amount of information [40]. On the other hand, velocities can be measured accurately in some circumstances, as shown in section 1.7, and Cebal et al. [41] have used these measurements to validate their CFD simulations, as described in section 1.8. To assess the significance of assumptions and gain an understanding of the effects of changing the parameters, a sensitivity analysis is often conducted, in which only one parameter is changed in each simulation relative to the base case, and the behaviour is compared to that case [25, 37].

Another approach for understanding the blood flow is to create geometrical models. Tateshima et al. [30] constructed geometrically realistic models, from 3D Computer Tomography angiography. Stereolithography was used to create the models, from which female acrylic casts were made. The models included the parent artery and the arterial branches. An elevated reservoir tank and a servomotor generated velocity-controlled pulsatile flow at the inlets to the models. Laser-Doppler velocimetry was used to measure the velocity of the fluid. Titanium dioxide particles were added so that the velocity could be measured. The fluid used was sodium iodide, which has the same refractive index as acrylic, to eliminate optical distortion. The velocity as a function of time was ensemble averaged over many periods. The shear stress was calculated from the velocity measurement at the walls and 0.7mm away using equation (1.4).

$$\sigma = \eta \frac{\partial v}{\partial x}. \quad (1.4)$$

For accurate flow velocity simulation, not all parameters, such as kinematic viscosity and the duration of one pulsatile period, must be matched between the *in vitro* and *in vivo* states. It is sufficient to match dimensionless parameters and the waveform shape. In this study, the acrylic models were of a different size to the actual aneurysms and the fluid viscosity was different, but the Reynolds number, Re and Womersley number, α were

matched. They are given by:

$$Re = \frac{v_{max}D}{\nu}, \nu = \frac{\eta}{\rho} \quad (1.5)$$

$$\alpha = \frac{D}{2} \sqrt{\frac{\omega}{\nu}}, \quad (1.6)$$

where ω is the angular frequency in rad s^{-1} and ν is the kinematic viscosity. The velocity profile was arranged so that the maximum and minimum Reynolds number and the Womersley numbers matched the *in vivo* conditions.

This contrasts with most studies involving models, which often use idealised geometries, which allowed detailed measurement of haemodynamic variables but cannot be used easily for understanding the haemodynamic forces in an individual clinical case [25]. The creation of patient specific geometrical models is impractical for large population studies, but without them correlation between patient-specific events and haemodynamic patterns cannot be assessed. Computational based models provide the ability to model and study all possible geometries [25].

Hassan et al. [4] point out that it is important to minimise the region of interest to decrease computational time. Their simulations take one day for rigid walls and four days for elastic walls.

Studies of large areas of the intracranial vasculature, such as the whole CoW, are often carried out using a significantly simplified model of the blood flow, that is one dimensional, so that the velocity and pressure are averaged over the cross-section. These usually do not extract the vasculature from medical images, so they sometimes require the dimensions of arteries. In some cases, the Navier-Stokes equations are used in one dimension [24, 29], in which a conservation of mass relation is used to calculate the pressures and the Navier-Stokes momentum equation calculates the flows. In other studies, simpler equations involving mass and momentum conservation are used [1, 5, 6]. In Hillen et al. [39]’s 1988 study, the flow is assumed to be steady Poiseuille flow, so conservation of momentum is already satisfied by that and no further equations are needed.

Boundary conditions for the junctions consist of mass conservation, so the volume flow rate into the junction is equal to the volume flow rate away from it. The pressure at the end of one artery must be equal to that at the start of the next artery [1, 5, 6, 24, 29, 39].

Sometimes, the pressures are matched, taking into account the curvature in the arteries by adding a term proportional to ρv^2 , according to Bernoulli's law, to the pressure [1, 6]. Hillen et al. [1] tested the effect of this in the PCA and found that it was negligible. The use of this for junctions was discussed in [24], since the cross-sectional area changes. It typically increases, so the actual pressure (not including ρv^2) decreases. However, the change in area is discontinuous, so flow separation and vortex formation are expected downstream from any bifurcation and it was decided that pressure continuity was more appropriate. An appropriate pressure or velocity waveform must be applied at the inlet. Not all or even most of the arteries can be included in the model [29]. We must choose where to terminate the model. At the outlets, there are few measurements of pressure or velocity, so some assumptions must be made regarding the boundary conditions [29, 31].

In some models, some of the main systemic arteries are included as well as the cerebral ones [6, 29]. This could be because they play an important role in wave propagation and overall flow distribution [29] or because there may be a time delay between the inlet flow waves in the ICAs and VAs [6]. Clark et al. [29] comment that patient specific studies have not yet reached the clinical utilisation stage. A past study by the authors involved a generic model including 108 vessels that used patient-specific vessel sizes measured from digital subtraction angiography (DSA), which is described in section 1.7.2. The driving force was the pressure waveform in the aorta. The flow patterns were measured as well as simulated by single photon emission computerised tomography, electroencephalography, cerebral oxygen saturation and transcranial Doppler, which is described in section 1.7. Satisfactory accuracy was achieved for some, but not all flows. In this study, not only are the arteries in the model distensible, but also the outflow conditions take into account the elasticity of the arteries that are not simulated, by using a lumped resistance-capacitance resistance (RCR) model (see section 1.10). This was also applied by Alastruey et al. [6]. The RCR parameters are calculated on a patient-specific basis using Phase Contrast Magnetic Resonance Angiography (PCMRA) flow measurements of the velocities in some vessels.

Some 2D and 3D models have been used to simulate the CoW [6]. Some models have made the nonlinear 1D Navier-Stokes or mass and momentum conservation equations (equations (1.1), (1.2), (1.16) and (1.17)) linear.

1.5 Typical simplifications and assumptions of the models

Detailed haemodynamic information is not usually available in vivo, so ranges of parameters, such as mean flows, phase shifts and waveform shapes are usually estimated from measurements of healthy volunteers [3, 37, 42]. In the 3D CFD simulations, the walls are usually assumed to be rigid and blood is modelled as an incompressible, Newtonian fluid. This is due to a lack of information about arterial elasticity and wall thickness. At the inlet, the analytical solution by Womersley for pulsatile flow in a straight rigid pipe is usually applied to each Fourier mode of a volume flow rate waveform. However, [32] applied a parabolic flow with the correct flow rate at each time step.

Mihalef et al. [43] carried out 3D CFD simulations of the heart, for which moving boundaries must be included. Rather than solving the equations of motion for the wall, the wall motion was derived from a series of medical images taken at different instants of time, as discussed in section 1.7.6. A similar approach was also used by Jeays et al. [44] for simulating blood flow in the superior mesenteric artery, which is a branch of the aorta.

In the simplified models, the vessels are often assumed to be straight and to have a circular cross-section [1, 5, 6, 24, 29, 39]. The models of the CoW are also flat, whereas in reality the CoW is not confined to one plane.

A resistance model is usually used for the outflow boundaries. The idea of this is explained well in [39]. The pressure drop in an arterial segment is given by:

$$\Delta p = Z_R Q, \quad (1.7)$$

where Z_R is the resistance, Q is the volume flow rate and p is the pressure. For Poiseuille flow in a circular pipe, the resistance is:

$$Z_R = \frac{8\eta l}{\pi R^4} \quad (1.8)$$

At the outflow boundaries, one can calculate the flux, then the pressure is found from the venous pressure and the combined resistance of all arteries and capillaries beyond, but supplied by, the outflow arteries. This pressure can then be used as an outlet boundary condition. This peripheral resistance is often taken to be inversely proportional to the

brain masses irrigated by the vessels, so that if the pressure at the outlets is the same, the volume flow rate is proportional to the mass irrigated, which is reasonable. Then the resistance is inversely proportional to the volume flow rate. This idea was used in [6] to calculate the resistance of the brain from the total resistance. Castro et al. [37] assumed that the resistances of the distal vascular beds supplied by the outflow arteries were all equal, which may be valid if very small arteries are included, but not necessarily for models that only include a small number of vessels. The idea of resistance can be applied to any blood vessels.

Finding the correct peripheral resistance distribution is one of the major challenges to cerebral blood flow simulation [29]. The peripheral resistances may be calculated by running a simulation of steady flow and adjusting the resistances until the total flux through the brain agrees with values from the literature [1, 5]. The average volume flux under pulsatile flow with the same resistances is found to be only slightly higher [1]. If the model only takes into account large arteries, the pressure drop will be small compared to the total difference between arterial and venous pressure, so the total resistance will be approximately equal to the resistance of the efferent arteries combined in parallel using equation (1.9), and this can be compared to the literature.

$$\frac{1}{Z_{R,total}} = \sum_{i=1}^N \frac{1}{Z_{R,i}} \quad (1.9)$$

In contrast to the 3D CFD models, the simplified models usually use distensible walls [1, 5, 6, 24, 29], but these remain a challenge to model and assumptions have to be made about them. There is little information available about wall elasticity [3]. Models that include elasticity will be discussed in section 1.10. More recently, Zhang et al. [45] have developed a method of measuring the motion of aneurysm walls from 3D rotational angiography, which is discussed in section 1.7.2. From these measurements, it is possible to identify regions of an aneurysm with different mechanical properties. The accuracy of the wall motion estimates was tested by taking images of physical models and found to be accurate within 10% [40]. These methods could be used to measure the mechanical properties of the wall required for a patient-specific simulation.

Resistances are almost always kept constant in time, but Alastruey et al. [6] commented that time-varying resistances in the efferent vessels can account for vasoconstriction and

vasodilation.

1.6 Specifying simulation parameters

In order to simulate blood flow, one needs approximate physical parameters to put into the Lattice-Boltzmann simulation and the approximate output parameters we might expect, for example the WSS or velocity. This section reviews these parameters.

Many of the parameters depend on Haematocrit (Hct), which is defined as the ratio of the volume of erythrocytes (red blood cells) to the volume of whole blood [46, 47]. Any part of the blood that is not a red blood cell is called plasma. Hct is an important property on which the speed of sound, density and viscosity depend. It is typically 46% for men and 38% for women, except in certain disorders of the blood [46]. Kenner [48] gives a range of densities for arterial blood, which agrees with Purves et al. [46], except that it includes values intermediate between those typical of men and women. Kenner [48]'s data show that $Hct = 31\%$ for capillary blood. This either disagrees with Purves et al. [46] or Purves et al. [46] only show data for arterial blood.

It is necessary to know the speed of sound in order to match all parameters in the Lattice-Boltzmann simulation with the *in vivo* conditions (section 2.7). The speed of sound depends on Haematocrit, temperature and frequency. It may be measured by placing a sample of blood in a temperature controlled chamber. An 10MHz ultrasound transducer is placed below the container. The ultrasound waves reflect at both the bottom of the container and the interface of the blood with the air. The traces of the two echoes are displayed on an oscilloscope. Measurements at many different chamber heights give an accurate sound speed. At 37°C, I found the following values from the literature: 1590m s⁻¹ [49], 1580m s⁻¹ [50], 1591m s⁻¹ at a Hct of 51.6% [47], 1584.2m s⁻¹ [51], 1590m s⁻¹ [52], $(1541.82 + 0.98Hct)$ m s⁻¹, giving 1571 – 1591m s⁻¹ for typical $Hcts$ of 30% to 50%. These values agree within 1.3% of each other.

The density of plasma and erythrocytes depends only on temperature. The density of blood is given by Kenner [48]:

$$\rho = Hct\rho_{erythrocytes} + (1 - Hct)\rho_{plasma} \quad (1.10)$$

The density of plasma $(1017 \pm 2)\text{kg m}^{-3}$ and that of erythrocytes is $(1095 \pm 2)\text{kg m}^{-3}$. Using the typical *Hcts* quoted earlier and linear interpolation, the density of arterial blood is between 1045kg m^{-3} and 1055kg m^{-3} . It has been shown that measuring the density is an accurate way to find the *Hct* [48]. Hinghofer-Szalkay and Greenleaf monitored the density of blood continuously in six subjects and found that it varied between 1046kg m^{-3} and 1057kg m^{-3} , depending on whether the person's body position [53]. The density of blood may be measured using a mechanical oscillator [48]. We simply use the relationship between the resonant frequency and mass of the oscillator with blood for damped harmonic motion. In 3D CFD simulations of cerebral blood flow, the density is taken to be 1000kg m^{-3} (1982) [37], or 1050 to 1060kg m^{-3} [4–6, 54] [42], which may be more accurate.

The viscosity of blood depends on many factors. An empirical equation for viscosity in terms of *Hct* is

$$\eta = \frac{\eta_0}{1 - Hct} \quad (1.11)$$

The viscosity is $2.7 \times 10^{-3}\text{Pa s}$ for a *Hct* of 46%, implying that the viscosity of plasma is $1.25 \times 10^{-3}\text{Pa s}$ [55]. A good fit to this formula was found for in vivo measurements of blood viscosity.

The viscosity also depends on shear rate [56] ranging from $5.8 \times 10^{-3}\text{Pa s}$ at 1s^{-1} to $(3.43 \pm 0.33) \times 10^{-3}\text{Pa s}$ and $(3.20 \pm 0.49) \times 10^{-3}\text{Pa s}$ at 100s^{-1} for men and women respectively when normalised to a *Hct* of 45%. Men and women have similar viscosities for shear rates below 100s^{-1} . Above 150s^{-1} , Eckmann et al found that the viscosity is constant, but this was for blood that was haemodiluted with albumen to a *Hct* of 22.5% [57]. With a *Hct* of 45%, the behaviour with respect to shear rate should be the same for a *Hct* of 45% provided that the formula quoted in the previous paragraph holds.

When the red cells are at rest they tend to aggregate and stack together in a space efficient manner. In order for blood to flow freely, the size of these aggregates must be reduced. The forces that disaggregate the cells produce elastic deformation. With a 2Hz oscillation, the elastic modulus of the blood is $8 \times 10^{-3}\text{Pa s}$ at 1s^{-1} , but becomes negligible relative to the viscosity at 100s^{-1} for an oscillation at 2Hz at 22°C . The viscosity varies from $2 \times 10^{-2}\text{Pa s}$ at 1s^{-1} to $7 \times 10^{-3}\text{Pa s}$ at 1000s^{-1} [58], but this measurement was carried out at 22°C , not 37°C . Since viscosity and elasticity were measured separately, this cannot

be compared to a viscosity measurement alone [56]. To a fair approximation, blood can be treated as Newtonian in large blood vessels, where the typical shear rate exceeds 100s^{-1} . [59].

Red blood cells also line up behind each other in very narrow tubes. The viscosity at high shear rates, extrapolated to a *Hct* of 45% is constant at tube diameters above 1mm, it falls more and more rapidly, reaching a minimum at $7\mu\text{m}$, then rises very rapidly at diameters below this [60]. The comparison was done at all shear rates greater than 50s^{-1} .

The viscosity is usually measured with a viscometer that applies a certain strain rate by moving a pair of parallel plates. The force required to move them is measured, from which the stress can be calculated. The viscosity is calculated from equation (1.4). The elasticity and viscosity can be combined into a complex viscosity which depends on frequency. If an oscillation at a particular frequency is applied, the viscous and elastic components may be separated. Otherwise, only the apparent viscosity can be measured. The apparent viscosity can be determined by a method based on Poiseuille's law (equation (1.12)) [55]:

$$v = -\frac{1}{4\nu\rho}\nabla p(R^2 - r^2) \quad (1.12)$$

For flow in a narrow tube, a reservoir of fluid of a certain depth could be used to supply the tube. It will apply a certain pressure to the inlet. The fluid will then flow at a constant velocity if the depth is constant. This can be measured by working out the volume flow rate and dividing by the cross-sectional area of the tube. There is some range in the values of viscosity, which is perhaps due to its complexity.

The viscosity of blood used in simulation ranges from 0.003Pa s to 0.0046Pa s [1, 4-6, 24, 37, 42, 54]. These viscosities are slightly higher than the experimentally measured ones.

The equations in [24] do not require the density or dynamic viscosity. Instead they use a kinematic viscosity, $\nu = 4.6 \times 10^{-6}\text{m}^2\text{s}^{-1}$, which is slightly larger than in the other studies. A pulsatile period is almost always taken as 1s [1, 5, 6, 29, 39].

The dimensions of the arteries, when needed, are often taken from the literature. These dimensions are from Hillen et al [1]. They put the vertebral, basilar and P1 PCA together as one artery in their model, so the length of these individually in the table was taken from [5]. In [1], the diameter of the PcomA was varied from 0.06 to 0.14cm. It is not

clear why the internal diameters in the model were made slightly larger than the ones they quoted from the literature. They agree with the diameters used in [30]. Alastruey et al used slightly different internal diameters, but they were within the range given by table 1.1, except the ICA, which had an internal diameter of 4.0mm [6]. The diameters can be measured by MRA.

	Anatomical dimensions (cm)		Model dimensions (cm)	
	Diameter (mean)	Diameter (range)	Internal diameter	Length
ICA	0.32	0.16-0.38	0.4	25.0
MCA	0.32	0.16-0.38	0.4	7.0
Vertebral artery	0.29	0.08-0.42	0.3	20.0
Basilar artery	0.30	0.25-0.35	0.3	3.0
P1 PCA	0.21	0.07-0.30	0.3	2.0
P2 PCA	0.23	0.12-0.30	0.3	7.0
PcomA	0.12	0.05-0.33	0.1	2.0

TABLE 1.1: Anatomical and model dimensions. All anatomical dimensions are external diameters in fixed material.

For the 3D CFD simulations, two pulsatile periods are typically carried out. There are usually 100 timesteps per cycle [3, 37, 42], though [54] found that 40 timesteps per cycle gave a reasonable compromise of accuracy and computational time.

Timesteps of 8×10^{-4} s [5] to 1×10^{-3} s [1] are used to solve the differential equation for the one-dimensional models. Models use between 30 and 100 spatial points to solve the differential equation [1, 5], which is a rather coarse resolution. Some of the other articles did not state the spatial and temporal discretisation.

The pressure at the ICA or basilar artery is often taken to be periodic, with a systolic pressure of 120mmHg and a diastolic pressure of 80mmHg [1, 5, 39]. [2] used a systolic and diastolic pressure of 110mmHg and 80mmHg respectively. The waveform is sometimes smoothed slightly. The waveform is shown in figure 1.8 [1]. The blood pressure gradually decreases and becomes less pulsatile further down the arterial tree, as shown in figure 1.9. From simulations, the WSS we can expect is usually much smaller than the pressure, at 25Pa to 100Pa [54, 59].

The volume flow rate through the brain is 10 to 15mls⁻¹. A typical waveform is shown in figure 1.10. [6] used a flow rate waveform, with a peak volume flow rate of 485mls⁻¹. Though this appears to be very high, using the fact that this is the flow from the aorta and the brain uses 15% of the cardiac output (section 1.1) and integrating the volume flow

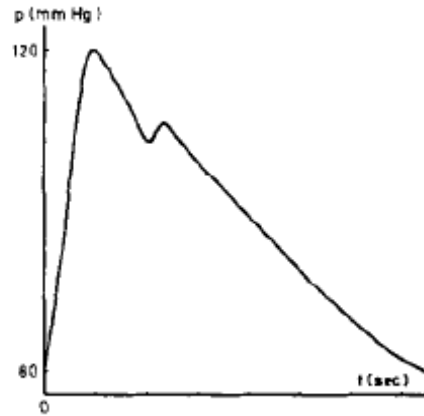


FIGURE 1.8: A typical pressure waveform at the ICA [1].

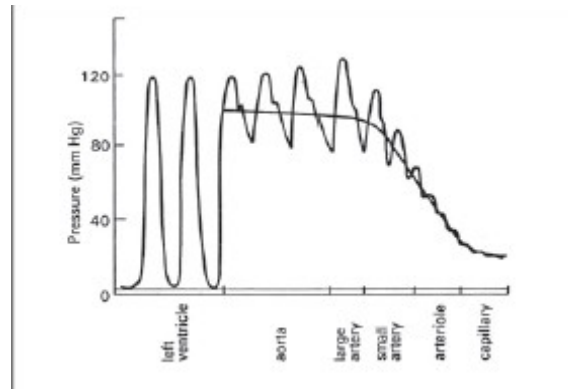


FIGURE 1.9: Change in blood pressure down the arterial tree [2].

rate over the period, the average over one pulsatile period is 15mls^{-1} . The flows in the efferent arteries from their data only add up to 7.8mls^{-1} , so it appears that something is not correct. The inlet boundary condition acts as a total reflector when the flow rate is zero, simulating the closure of the aortic valve.

$$Q(t) = \begin{cases} Q \sin \frac{\pi t}{t_1}, & t < t_1 \\ 0, & \text{otherwise} \end{cases} \quad (1.13)$$

Olufsen [24] used a flow rate measured from magnetic resonance. It peaked at 375mls^{-1} . Unusually, the period of oscillation was 1.25s. The total flow rate through the system was 4.03 litres per minute, so if 15% flows through the brain, this gives 10mls^{-1} . The waveforms for the left and right ICA are typically in phase and the flow in the ICAs may

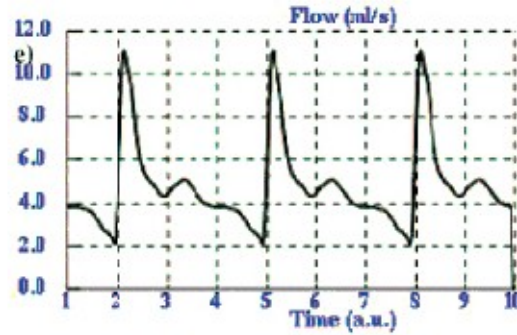


FIGURE 1.10: Volumetric flow rate waveform for the right ICA [3] measured using phase-contrast Magnetic Resonance Angiography, which is discussed in subsection 1.7.5.

lag that in the vertebral arteries by $17 \pm 8 \times 10^{-3}$ s, which is very slight [61].

The venous pressure is between 5mmHg and 20mmHg [1, 5, 6, 29, 39]. Hillen et al [1, 5] assumed a total flux of 12.5mls^{-1} . The efferents to the CoW, i.e. the ACAs, MCAs and PCAs have peripheral resistances in the ratios 6:3:4 under the assumption in section 1.5. The total resistance of the brain from literature is $1.375 \times 10^9\text{Nsm}^{-5}$ [1]. Alastruey et al [6] state that the total resistance of all arteries in the body is $1.34 \times 10^8\text{Nsm}^{-5}$. Combining the resistances of the brain and the rest of the system in parallel, assuming that the resistance of efferent arteries is inversely proportional to the volume flow rate and the brain uses 15% of the cardiac output, the resistances of the brain would be $8.93 \times 10^8\text{Nsm}^{-5}$, which is lower than the value used by Hillen et al. The resistances in the ACAs, MCAs and PCAs were also in a different ratio because they were calculated in a different way. They were $8.48 \times 10^9\text{Nsm}^{-5}$, $5.97 \times 10^9\text{Nsm}^{-5}$ and $8.48 \times 10^9\text{Nsm}^{-5}$ respectively.

Velocities are between 0.7 and 1m s^{-1} in the carotid arteries [62]. The flow rate in each ICA is approximately 4.8mls^{-1} . Flow rates are approximately 0.7m s^{-1} in the vertebral arteries [29], 0.4m s^{-1} in the efferent arteries of the CoW under normal conditions and can reach 1.5m s^{-1} when an artery is missing or occluded [6]. For the circle segments, the velocities can be higher. They are between 0.6 and 1.13m s^{-1} for the M1 MCA and 0.64 to 1.68m s^{-1} for the ACA [62].

1.7 Methods of imaging of cerebral vasculature

It is essential to be able to extract the vasculature from medical imaging in order to perform patient specific simulations of cerebral blood flow. Until recently, CFD modelling was only used to study blood flow in idealised geometries [3, 31, 42]. The study of cerebral blood flow requires that simulations begin to use actual clinical data. Medical imaging and reconstruction methods can provide accurate geometric information for the CFD simulations. The medical imaging methods described here are usually used routinely during medical procedures, as well as simulations.

1.7.1 Magnetic Resonance Angiography

In Magnetic Resonance Imaging, a static magnetic field is applied. There will be resonant absorption of radio waves due to the magnetic moments of nuclei aligning with or against the magnetic field. The contrast is achieved by differences in the density of nuclei or difference in the relaxation time for them or a mixture of these effects. The ability to choose different contrast mechanisms gives MRI great flexibility. In MRI scans, one slice is imaged at a time. Magnetic Resonance angiography (MRA) is the imaging of flowing blood in vessels using MRI.

The blood itself can be used as a contrast agent. The signal from flowing blood can be enhanced at the expense of signal from static surrounding tissue. These are called “bright blood” MR angiograms [31, 37]. However, they suffer from poor signal quality and low resolution compared to x-ray angiograms, and regions of slowly flowing or recirculating blood can induce signal loss. Therefore, they may not give a complete visualisation of flow in the aneurysm dome. “Bright-blood” MR angiograms can be enhanced with paramagnetic contrast agent. Hassan et al. [54] had a resolution of $700\mu\text{m}$ and an isotropic resolution of $600\mu\text{m}$ will soon be achieved with this technique. This may not be good enough for CFD models of aneurysms, particularly in the aneurysm neck. Recent refinements have made this contrast-enhanced MRA the noninvasive method of choice for large intra- and extracranial arteries and larger dural venous sinuses [23, 29]. Such angiograms may still not receive a signal in slow flow regions, so some arteries, including the PcomA and AcomA are often invisible when imaged by MR techniques, but they can be better visualised by performing the scan when the flux is maximal according to a simulation [6].

In “black-blood MRI”, the signal from flowing blood is suppressed rather than enhanced. The resolution of inner and outer boundaries of the vessel wall is $300\mu\text{m}$ in plane and there is a 1.5-2mm slice thickness [31]. This anisotropic resolution means that side vessels oriented parallel to the slices may not be imaged well. Limitations of this method are that imaging artifacts that arise from slow recirculating flow can mimic atherosclerotic plaques [63] and that the contrast at the outer vessel wall is poor, which degrades the reliability of wall thickness measurements [31].

1.7.2 X-ray Angiography

In x-ray angiography, the clinician uses a contrast agent, injected into an artery via a catheter [23, 31, 64]. The contrast agent absorbs x-rays while two x-ray scanners, one anterior to the head and one lateral, record the flow of blood through the vasculature. The images are projections of the vasculature on two planes. First, the blood in arteries is seen, then late arteries and early veins, then only veins [4]. When a run of images is taken, the first image can be subtracted or an image can be taken without contrast agent and subtracted from the rest of the images to remove bone and other unwanted tissue from the images. This is called digital subtraction angiography (DSA). Its predecessor was screen film catheter angiography [23]. The resolution and contrast is better than those in MRA and CT scans [31]. CFD simulations cannot be performed with these 2D images and three-dimensional reconstruction requires at least two (ideally orthogonal) projections and some assumptions about the shape of the lumen. A typical digital subtraction angiogram is shown in figure 1.11.

A recent development is 3D Rotational angiography (3DRA) [3, 4, 31, 37, 64]. A 3D model is built up through the acquisition of a series of 2D rotational projections at different angles on one axis of rotation[64]. Between 44 and 200 images are required, and the reconstruction has an isotropic resolution of $200\text{-}400\mu\text{m}$ [3, 4, 31, 37, 42, 54]. The contrast agent must be injected continuously so that complete filling of the selected artery is achieved. The scan can be finished in five to eight seconds, and requires 5ml of contrast agent, which is less than ordinary DSA [3, 64]. In [4] however, 17ml of contrast agent was used. In this study, a VGAM was visualised and the 3DRA images showed that the small arterial aneurysm was communicating with the venous aneurysm.

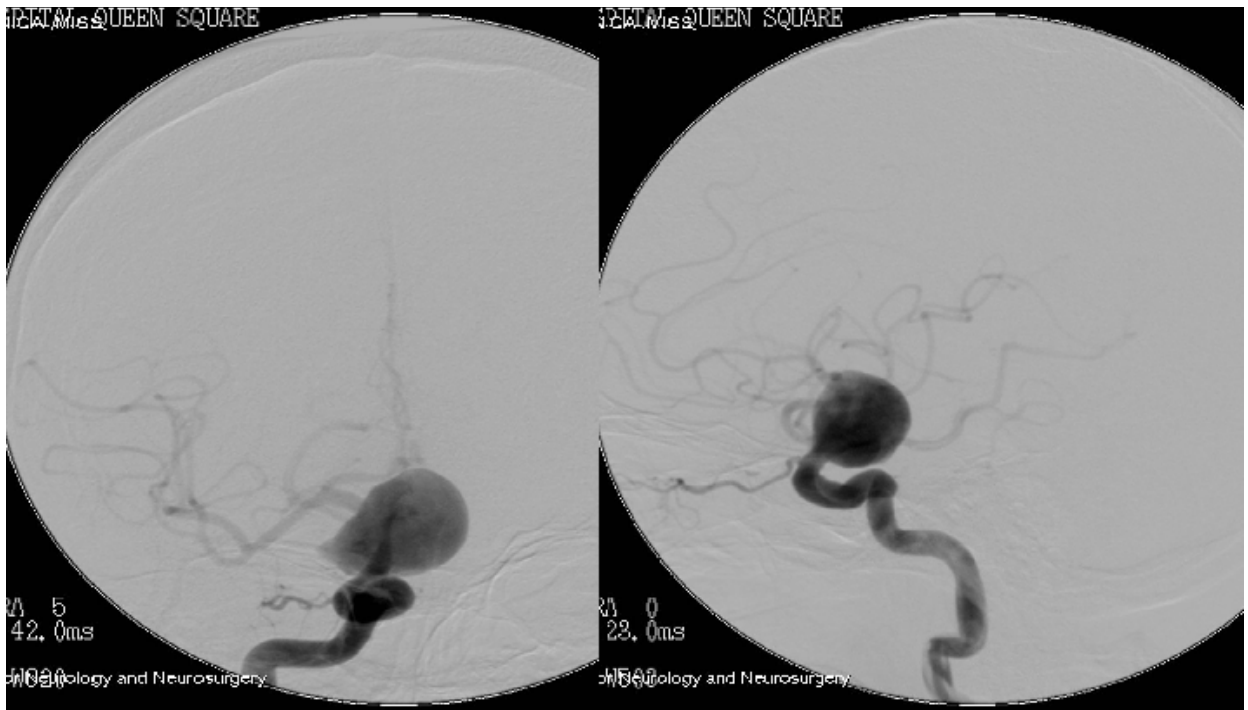


FIGURE 1.11: A digital subtraction angiogram of a giant aneurysm near the PComA. Image taken from a presentation by Dr. Stefan Brew.

Jiang et al. [64] compared 3DRA and digital subtraction angiography for the treatment of spinal cord vascular malformations in 12 patients. The method facilitated further treatment in two cases and modified therapeutic strategies in two cases. In one particular case, where the vasculature surrounding a spinal aneurysm was sufficiently complicated, 3DRA gave the clinician a better understanding of the connective vascular structure.

Zhang et al. [45] developed an algorithm for finding the displacement field over the wall of an aneurysm during the cardiac cycle from 3DRA. A physiological signal, such as the blood pressure is used to calculate the time between the start of the cardiac cycle and the acquisition of each 2D projection and the 2D projections are sorted by this time interval. For each time at which a 2D projection is available, the 3D model is iteratively deformed in order to maximise the similarities between the simulated and actual 2D projections. From the wall displacement field, it is possible to produce a strain map and hence identify regions of the aneurysm with different mechanical properties Villa-Uriol et al. [40]. The mechanical properties of an aneurysm could therefore be determined by running a simulation, then adjusting the properties until the resulting wall displacement field matches the wall displacement of the actual aneurysm.

The limitation of 3DRA and DSA is that they are unable to visualise an entire lesion fed by more than one artery because they rely on selective angiographic catheterisation. In 3DRA, the contrast agent is typically injected into one of the ICAs or VAs and it flows with the blood, so only the left or right side of the CoW is visualised at a time [37]. It is possible to image both sides with angiography of some kind with simultaneous injection of contrast agent in both ICAs or using an aortic arch injection, but this carries more risk for the patient [37]. Jiang et al. [64] say that this can be improved with refinement of image fusion techniques and Castro et al. [37, 42] have developed such a technique, so that the two sides are imaged independently, then fused together.

This technique is invasive, with a risk less than 1% of complications such as stroke as a result of catheterisation. It is only carried out when catheterisation is necessary for the patient. It also cannot measure the vessel wall thickness, so it cannot provide information about the plaque burden for assessing atherosclerosis [31].

1.7.3 Computed Tomography Angiography

Computer Tomography Angiography (CTA) uses x-rays to produce the images, but unlike DSA, the brain is scanned in slices. It can be used to construct 3D CFD models [30]. Slices are 1.0 mm apart but the data is reconstructed with a 0.5 mm interval by linear interpolation. The resolution was 0.35×0.35 mm. Hassan et al. [54] achieved a similar resolution. The mesh quality can be sufficient for a simulation, but one must remove the skull base bone. Sometimes a grid generator can allow construction of a triangular, prismatic, layered mesh that represents vascular walls of finite thickness. Though CTA can image both avenues of inflow into an AcomA, i.e. both sides of the CoW [37], this resolution may not be sufficient for 3D CFD models of aneurysms, particularly in the aneurysm neck.

1.7.4 Ultrasound imaging

Ultrasound images are produced by transmitting a 1-10MHz beam of sound and analysing the returned echoes. If the ultrasound is swept along a vessel, an image with resolution $0.2 \times 0.2 \times 0.6$ mm³ can be achieved in 10s, but the image quality is not yet sufficient for reliable CFD simulations [31]. 2D images are acquired manually without reference to a

fixed coordinate system, making it difficult to reconstruct a series of them in 3D. The image quality depends on the proximity of the transducer to the tissue of interest, so this method is usually limited to superficial vessels. Ultrasonography is also limited by its intrinsic variability and sound propagation problems around bone or air cavities [62]. With MRA scans and x-ray angiography, the patient lies in a supine position for practical reasons. Transcranial Doppler ultrasound has the ability to measure velocity of blood flow with the patient in different positions, which is an advantage for CFD studies because the effects of physiological variations, e.g. heart rate and cardiac output may be important [31]. This was used by [4] and [54] for inlet boundary conditions.

In contrast, Intravascular ultrasound (IVUS) is useful for CFD. It is the most sensitive of all imaging techniques. A transducer is introduced into the artery via a catheter. X-ray angiography is used with it to guide the placement of the transducer and orient the imaging planes. This is a highly invasive procedure and will not be carried out unless that patient has been referred for cardiac catheterisation. Doppler ultrasound can be used to measure blood velocities *in vivo*, either at the centreline of the vessel, or at a series of points at different radii. IVUS can also be used to measure the regional mechanical properties of the vessel wall, by measuring its thickness and displacement over time.

1.7.5 Phase contrast Magnetic Resonance Angiography

Phase-contrast MRA (PCMRA) can provide 2D and occasionally 3D images of one or more velocity components in a time-resolved manner [31]. Wetzel et al. [62] evaluated this technique in which velocities in three dimensions are encoded into the radio-frequency signal in reciprocal space. The PCMRA was synchronised with an electrocardiogram. Blood flow in three patients was studied to evaluate the technique. The resolution is 50ms in time and $1.5 \times 1.5 \times 1.5$ mm in space. Significant postprocessing was carried out in this study. Regions of low signal intensity, such as the air or ventricular system were excluded. Further noise reduction was achieved by comparing the standard deviation of the velocity-time course for each pixel, so that flowing blood could be separated from static tissue. The thresholds could be adjusted interactively for noise suppression. A particle-tracing technique was used to visualise the blood flow. The data was reformatted onto chosen 2D planes transecting the 3D data volumes. Imaginary particles were released from all points on these planes and the new positions of each particle after each timestep were calculated.

The progress of the particles up to a certain time could be viewed as a streamline, enabling the flow pattern to be visualised. The images were also colour-coded for velocity, as shown in figure 1.7.5. The scan takes 15-20 minutes and the entire processing time was 45-60 minutes. The most time-consuming part was placement of the 2D planes.

The flow was well visualised in the left and right ICA, M1 MCA and A1 ACA. Pulsatile forward flow directed downstream was observed, with no retrograde flow. No flow was visualised in a patient with an occluded left ICA from the point of the occlusion. On the non-occluded side, the flow appeared to be normal compared to that in healthy volunteers. One volunteer demonstrated a helical flow pattern in the carotid siphon when the visualisation covered the axial volume (figure 1.7.5B). This was consistent with the sagittal volume results. Such flow had been reported in previous numerical simulation. The peak systolic velocities were compared with Transcranial Doppler ultrasound, as explained in section 1.7.4. The velocities from PCMRA were 30.3% lower on average. However, velocity aliasing did not occur.

The study showed that 3D velocity fields for a single frame can be depicted in great detail and complex flow patterns can be detected. This shows that there have been improvements in PCMRA between 2002 and 2007, since Steinman commented that it can measure the flow in straight segments, but complex flow patterns can be distorted [31]. It probably underestimated the peak velocities because the temporal resolution was relatively low, which might lead to an underestimation of peak velocities due to low-pass filtering. It could also be due to attenuation and shift of the pressure and flow rate waveforms induced by the compliance or the vessel [31].

The limitations of the technique are that it requires significant manual processing. Late diastolic flow cannot be assessed. The advantage over CFD simulation is that no assumptions are made, such as using rigid walls and a Newtonian flow, but the resolution is not sufficient to calculate secondary flow parameters, such as WSS and will not be able to visualise secondary flow patterns. The velocity range must be predefined, so for patients with pathologies such as stenosis, an altered geometry can result in accelerated flow, causing velocity aliasing artifacts. Some suggestions for improvements are given, including sampling central k -space more frequently than peripheral k -space to improve temporal resolution and using partial Fourier acquisitions and parallel imaging to improve spatial resolution. Clark et al. [29] improved the accuracy of PCMRA by taking a 3D time of flight

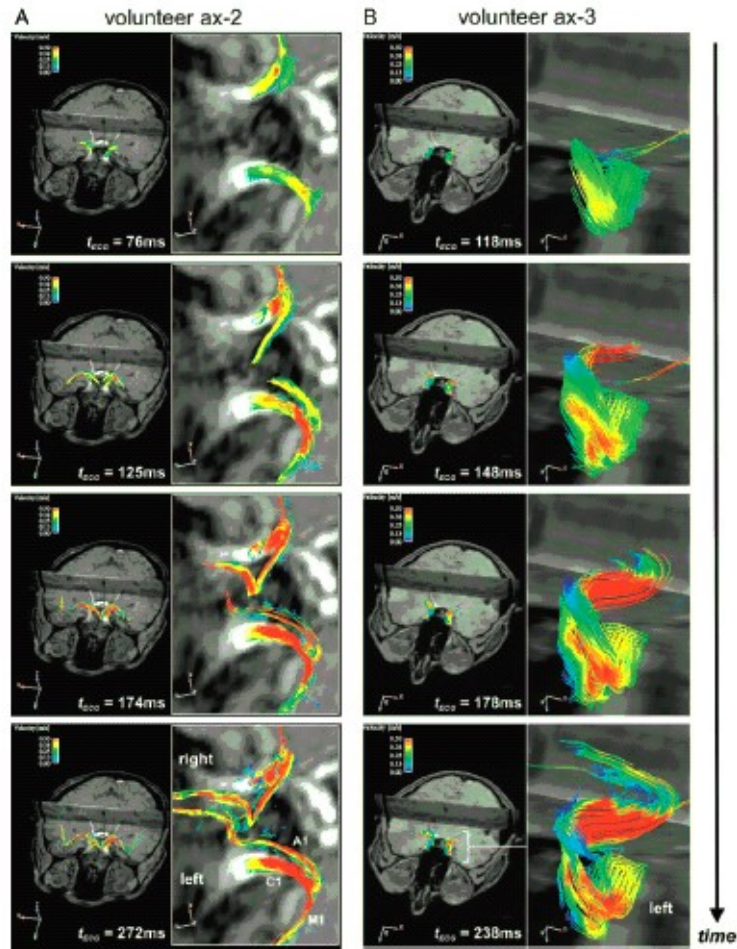


FIGURE 1.12: Time resolved 3D particle traces for 4 successive systolic timeframes illustrating blood flow in parts of the CoW in 2 healthy volunteers with axial slab orientations. The progress of the particles over time helps us to understand the flow field. Image from [62].

MRA scan, reconstructing the 3D surface rendering of the vasculature, then applying a new localisation algorithm to this rendering to specify the position for an oblique PCMRA scan. This scan produces images with 256×128 pixels over a 16cm field of view, giving a resolution of 1.25mm in one direction and 0.63mm in the other.

PCMRA is usually used in image-based CFD applications for providing flow-rate waveforms at straight segments [3, 6, 29] as boundary conditions, which allows cerebral circulation simulations to be more patient-specific [29]. With four optimally placed imaging planes, the boundary conditions at all afferent and efferent arteries to the CoW can be specified [3], as shown in figure 1.13. Womersley solutions are usually imposed at the inlets.

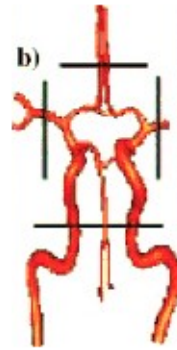


FIGURE 1.13: PC-MRA measurements of volumetric flow rate waveforms can provide boundary conditions for the whole CoW. Image taken from [3].

If a full velocity profile is required, the image must be interpolated onto the inlet nodes, requiring sophisticated postprocessing and higher quality images, which take more time to acquire [31]. Patient-specific boundary conditions can then be specified in a noninvasive way, whereas for patient-specific pressure boundary conditions, a transducer would need to be inserted via a catheter, which is invasive and dangerous for the patient. Though it would help CFD studies, there would be no benefit to that particular patient.

1.7.6 Segmentation, postprocessing and visualisation

When one has a series of 2D cross-sectional images, one can reconstruct boundaries of the lumen, then convert these to a 3D surface [54]. It is straightforward to connect points around the edge using splines or filtering techniques to achieve the desired smoothing. For bifurcating vessels, one may use this approach to reconstruct each branch separately, then merge them using solid modelling operations. When there are hundreds of vessels to be imaged, it is easier to extract from the 3D volumetric data 2D images distributed along and oriented normal to the centrelines of vessels of interest. An alternative approach is to operate on the 3D images directly by extending 2D contour detection algorithms to 3D. One can place a triangulated sphere in the lumen and refine it via the same internal and image-based forces as for the 2D dynamic contour, but this technique requires programming from scratch and it remains to be seen how it would perform for very complex geometries. This approach does not require operator intervention to reconstruct branches.

When the 3D geometry is reconstructed in terms of the boundaries of the vessels, the model must be discretised into finite elements or volumes for CFD simulation. For simple structures, one can divide the tube like structure into a fixed number of points around the circumference and along the tube axis. For bifurcating geometries, more effort is required to ensure the quality of the elements. The most popular method is unstructured meshes on which arbitrary distributions of tetrahedral, hexahedral or prismatic elements are generated using sophisticated algorithms. The approaches still need the user to identify complex regions where refinement is needed. Adaptive refinement can be used in which the simulation error is estimated, but to date this has only been applied to steady flows.

In some of the studies mentioned thus far [3, 25, 37, 42], a deformable model is used for some of the models. The image is smoothed by a combination of blurring and sharpening operations, then segmented with a region growing algorithm, then the isosurface is extracted. An alternative to this is the level-set approach [25], in which an image of a function, called the action map, is created. There is an abrupt jump in the time values in the neighbourhood of the edges of an aneurysm and the surrounding vessels. A pre-segmentation of the aneurysm is then extracted using threshold values of the action map. The grey values of this are modelled by a Gaussian distribution. Based on this, the surface is left to evolve and a level set algorithm is used to make the final image.

To generate the finite-element grid, an advancing front method may be used that first re-triangulates the surface, then marches into the domain, creating tetrahedral elements [25, 37]. In these studies, vessel branches were truncated and the vessels were extruded along their axes. Castro et al. [37, 42] also fused images from the two sides of the CoW together, in order to study the AcomAs. There are usually 1-3 million elements in a 3D CFD simulation [37, 42] and the resolution is usually finer than the original image, for example, [42] had a final resolution of 0.16mm. The inlet, outlet and wall boundaries are defined at this stage. If an inlet boundary is not defined, the simulation may assume it is a wall, so one would have a dead end.

Hassan et al. [4] used 3DRA to study a VGAM. In this study and their next one [54], the volumetric data from 3DRA are reformatted into 460 DICOM sections, with one file for each. This changes it from a set of rotational images to a set of slices. This number of slices is needed to obtain a good quality final mesh. The files were concatenated into a single file to be read by the DICOM reader, in binary or ASCII format. A raster (rectangular grid of

pixels) 3D image was produced, which included data such as the image size and patient's name. The region of interest was defined using AVS express. In this study, the basilar artery was cut out to reduce the computing time. This produced a Stereolithography file, with no extra information in it. ICEM CFD 4.1 was used to discretise the domain with an unstructured tetrahedral boundary-fitted mesh containing 77696 nodes and 384129 tetrahedrons. The grid generation allows us to cut out unnecessary parts like small vessels and to define inlet, outlet and wall boundaries. Mesh smoothing further improves the quality of the grid. The mesh generation takes about 30 minutes. Only minor manual manipulations are needed if the resolution is fine. The coarser the resolution, the more manipulations are needed, There is a penumbra effect as the boundaries are approached and correction for this is operator dependent. Figure 1.14 illustrates these stages in the image processing.

Mihalef et al. [43] used a series of CTA images taken at different times throughout the cardiac cycle such that the fluid boundaries moved. The surfaces were modelled by a number of parameters for the trajectories of specific landmarks on the heart and for the surface meshes. These parameters were fitted to the images. A machine-learning algorithm was used to avoid the need to explore the entire parameter space. The algorithm would explore a small subspace spanned by a few parameters to find approximate values for them, thereby eliminating the majority of the parameter space. This was repeated several times. Since it would have been difficult to generate a suitable finite-element mesh due to the large deformations of the heart, a level-set method was used for the CFD simulation, in which the level set function was used to create a sharp distinction between the fluid domain and the remainder of the space. While this is a simulation of blood flow in the heart, the same approach could be applied elsewhere in the cerebral vasculature.

The results of the simulation are usually visualised. The velocity may be shown as colour coded streamlines [4, 62] (see subsection 1.7.5 [37]), or as a colour map on a selected plane through the vasculature [3] or on the surface [4]. In that study, the pressure at the surface was also visualised. General purpose software, called Enight was used. The WSS is usually visualised as a colour map on the surface of an aneurysm or blood vessel, as shown in figure 1.15.

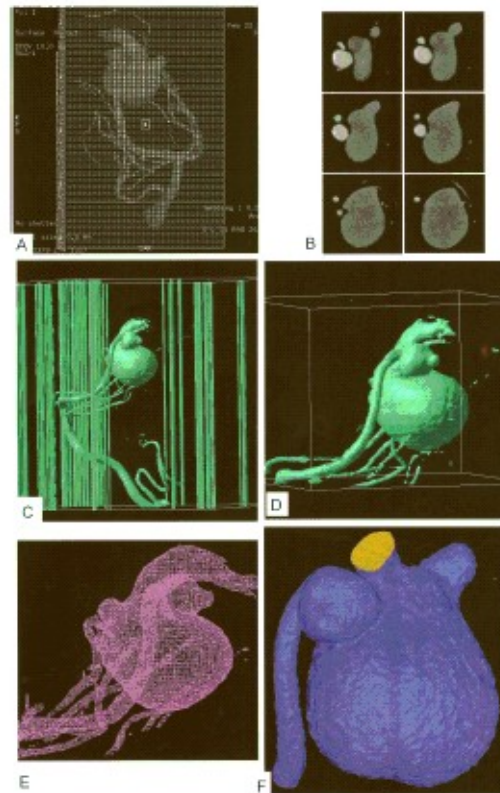


FIGURE 1.14: Detailed procedure of image reconstruction. A, Reformatting protocol of the angiographic image into DICOM sections. B, Examples of the sequential secondary DICOM sections. C, Raster greyscale 3D binary image output by (x) MedCon to AVS/Express. The columns around the image are the patient's data and image parameters. Under AVS/Express, image manipulation and cutting out of the region of interest is done as shown in panel D. The figure in panel D is the STL file output from AVS/Express to ICEM CFD. E demonstrates the STL file in its mesh form. Finally, mesh reconstruction, smoothing and closure of the inlet and outlet re done by a mesh generator before volume mesh generation and CFD calculation on the tetrahedral mesh illustrated in F. Image taken from [4].

1.7.7 Accuracy

Some studies have compared the flow fields obtained by CFD simulations of flow through blood vessels to experimentally measured flow fields in physical models of the same blood vessels with the same boundary conditions [65–67]. Perktold et al. [65] constructed physical and numerical models from the same cast of a human left coronary artery branch. They compared the velocity profiles obtained from a CFD simulation to those measured by laser-Doppler anemometry at several different locations and observed good agreement.

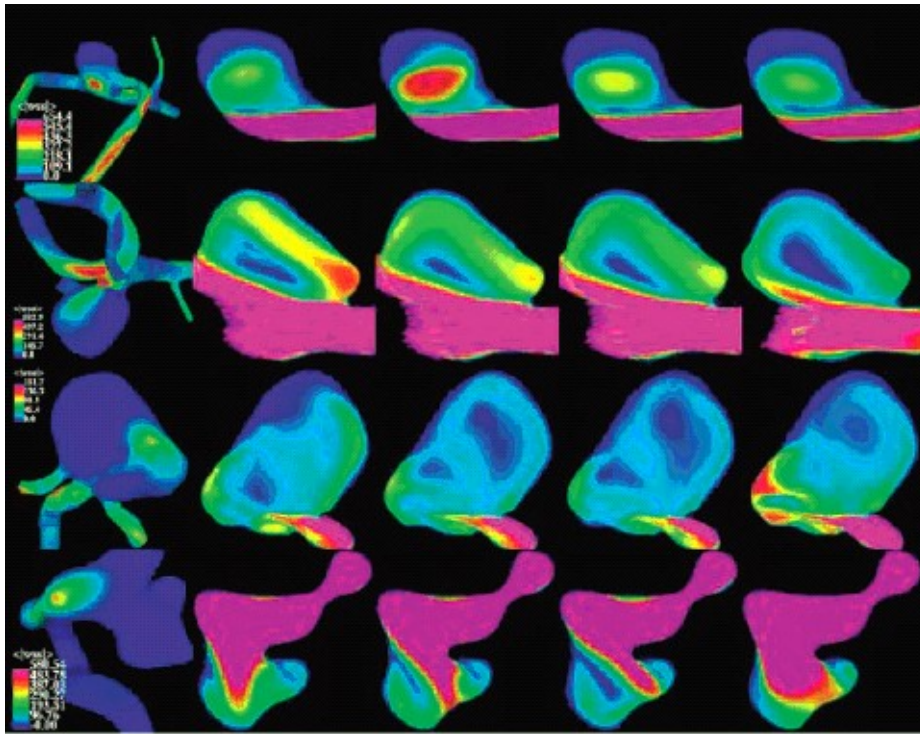


FIGURE 1.15: Examples of aneurysms where the inflow jet impacts the neck (top row of images), body (2nd row), dome (3rd row) or has a changing impingement zone (4th row). Images from left to right: mean wall shear stress distribution, then intra-aneurysmal flow velocity on a planar cut through the sac at 4 instants during the cardiac cycle. Taken from [3]

Botnar et al. [66] carried out a similar comparison for a carotid artery bifurcation. Phase-contrast MRI was used to measure the axial velocities at selected locations, as described in section 1.7.5. The differences between the corresponding simulated and experimentally measured axial velocities at each plane over which the velocity was compared were less than 10% of the maximum axial velocity over that plane. Myers et al. [67] compared the measured wall shear stress (WSS) in a model of the right coronary artery to the WSS calculated from their CFD simulation and observed reasonable quantitative agreement. Steinman [31] comments that while these studies show that the flow fields in physical models of blood vessels are accurately calculated by CFD methods, they cannot tell us whether a reconstructed model is faithfully reproducing the *in vivo* environment. Such direct validation is difficult in the absence of a perfect technique for measuring velocities *in vivo*. If there was such a technique, there would be no need for CFD simulations [3, 31]. Steinman [31] commented that the accuracy of PCMRA may provide a gold standard for measuring velocities *in vivo* in future.

In CFD studies, the geometry cannot be reconstructed perfectly. Steinman [31] compared a geometric model of the aortic bifurcation made of acrylic using CT data with an MRA scan. The geometric errors in the acrylic cast were within $150\mu\text{m}$, but there were differences of 15-35% in the simulated WSS and that measured in the cast, because MRA underestimated the dimensions immediately before the bifurcation.

A mesh is considered sufficiently resolved when a doubling of the element size induces little change in the velocity fields. Extremely fine mesh densities are required to resolve WSS to 10%, because WSS is the gradient of the velocity field and must be calculated from it. However, the patterns of WSS are reproduced. One other issue is the reproducibility of the models. A study showed that interoperator variability was only slightly higher than intra operator variability. If the same subject is imaged again, there is $< 300\mu\text{m}$ inaccuracy in geometry and less than 0.4Pa inaccuracy in WSS. Villa-Uriol et al. [40] have developed an automatic approach for segmenting the vascular tree and validated it by constructing vascular models from 3DRA and MRA images of a physical model of a vessel. The differences between the geometries of the physical models and the computed models were $200\mu\text{m}$ and $300\mu\text{m}$ for the models constructed from 3DRA and MRA images respectively, which are below the corresponding resolutions of the imaging methods.

It is hard to automatically extract the vasculature, measure the arterial diameters accurately and measure the flow rate and pressure [29]. The arterial diameters extracted from patients were used in [6].

1.8 Three dimensional fluid dynamics simulation of blood flow

In this section, I review the results of three dimensional computational fluid dynamics simulations of blood flow in the literature.

Many studies strongly suggest that the wall shear stress plays a particularly important role in the evolution of aneurysms. Jou et al. [21] studied two similar aneurysms in 2005, one of which was growing. A clear correlation between regions of growth and low WSS was visible in images of these in the growing aneurysm and this aneurysm had larger areas of low WSS than the stable one. In 2008, Boussel et al. [22] discovered a statistically

significant negative correlation between growth and time-averaged WSS by measuring these quantities in many tiny regions of seven aneurysms. This is counterintuitive, but the two aforementioned studies comment that low WSS leads to the death of endothelial cells (those at the inner surfaces of arteries) and changes their secretions, including vasodilators and vasoconstrictors. These processes may cause arterial wall remodelling. On the other hand, Shojima et al. [20] and Boussel et al. [22] cited animal studies in which a high WSS initiated an aneurysm. Shojima et al. [20] found a significant negative correlation between the spatially averaged wall shear stress and the aspect ratio, which had been linked to a greater risk of rupture in previous studies, but the ruptured aneurysms in [20] had a higher average WSS but regions of low WSS near the tip, so the conclusion is not entirely clear. The conclusions concerning WSS strongly suggest that one should consider the mechanisms for initiation, growth and rupture of aneurysms separately.

Cebral et al. [3, 25] characterised aneurysms according to the flow patterns inside, which allowed them to search for correlations with the risk of rupture. They concluded that rupture is significantly more likely in aneurysms which have an inflow jet with a smaller impingement zone on the wall. The WSS is elevated in the impingement zone [25]. The @neurIST project [68] aims to extend these studies by building a database of morphological, flow and structural characteristics for hundreds of aneurysms. The flow characteristics include vortex patterns and maximum, minimum and average velocities. The pressure on the surfaces of aneurysms may be less important than WSS [20, 68], since its spatial variation is usually much less than the difference between systolic and diastolic pressure. This is confirmed by the simulations in Shojima et al. [20]'s study.

In Cebral et al. [3]'s study, the geometry of the parent artery is included, but the surrounding vasculature is not, because it is impractical to do so. Since the smaller arteries were excluded, outflow velocity boundary conditions could be applied, without the need for a resistance model, as described in section 1.5. They comment that prior clinical studies had largely ignored the effects of the geometry of the parent artery and its relationship to the aneurysm. Extremes in parent artery configuration can cause large changes in the flow in the aneurysm. It can cause deflection of the inflow jet away from the typical location in the distal lip and cause it to impact the dome or proximal neck, which in effect converts a sidewall aneurysm to a flow pattern analogous to a terminal aneurysm. There were some other simplifications relating to the geometry. AcomA was not included, which may

introduce a bias. The geometry was also assumed not to be changed by the rupture of an aneurysm.

For the velocity boundary conditions in Cebral et al. [3, 25]’s studies, the velocity boundary conditions were given by PCMRA measurements of velocity were obtained on four planes around the CoW (Figure 1.13)(see subsection 1.7.5). At the outflow, traction-free boundary conditions were used, in which each flow rate is assumed to be proportional to the area of the outflow vessel. One further simplification in their study is that the input flow rate relied on pulse rates in healthy subjects.

To assess the significance of some of the modelling assumptions, Cebral et al. [25] carried out an analysis of the sensitivity of the results with respect to the mean flow, flow division in the outflow vessels, by raising and lowering the resistances where there was more than one outflow vessel, including non-Newtonian effects, as shown in section 2.11, closing off small vessels and varying the mesh size and reconstruction, in which other modellers were asked to construct new models from scratch. There were four aneurysms and in all cases, the location and shape of vortex structures were slightly different as the parameters were changed, but this did not change the classification of the aneurysms with respect to the complexity and stability of the flow pattern, or the impingement region or their WSS classification, if the WSS was measured. The WSS was measured with the changes to the mean flow and viscosity. It corresponded to the region of impingement of the flow on the wall of the aneurysm in all cases. The only large change in the flow behaviour happened in one remodelling case in which the segmentation algorithm wrongly joined an artery and an aneurysm due to the limited resolution, which showed that a small but important change in the geometry can cause a large difference in flow dynamics.

With flow rate, the magnitude of velocity or vortex intensity was affected. The size of the impingement region changed slightly. A non-Newtonian model produced smaller viscosity gradients than the Newtonian one because of an increase in the non-Newtonian viscosity in the regions of low flow and strain rate. The largest differences were seen in the artery with the lowest flow rate. They conclude that the precise flow conditions do not matter for qualitative studies. Hassan et al. [54] opine that simplifications such as neglecting gravity and the non-Newtonian nature of blood are of secondary importance.

Cebral et al. [3] highlight the feasibility of computational methods for clinical investigation. The findings suggest that the characteristics of the inflow jet and the interaction with the wall play an important role in the development and ultimate rupture of the aneurysm.

Castro et al. [37] investigated the effects of unequal flow conditions in the ICAs on the haemodynamics of AcomA aneurysms. A sensitivity analysis was conducted on the wall shear stress (WSS) in which a parameter was changed, then the flow conditions were swapped. The velocity was increased by 5% in one artery and decreased by 5% in the other, the volume flow rate waveform shapes were changed so that both ICAs had a different waveform from each other and from the base case and 2% and 4% phase leads of the waveform in one ICA relative to the other.

In one patient, the flow was symmetric and most of the blood stayed on the same side of the AcomA as it flowed from the A1 ICA to the A2 ICA. In the other patient, the AcomA was more superiorly located (higher) and the flow was more asymmetric, with significant cross over between the two arteries. In this patient, the jet flows meet closer to the neck of the aneurysm, resulting in a larger elevation of wall shear stress. This provides further evidence that the geometry can have large effects on the flow conditions.

They found that there is potential for rapid and severe shifts in flow if there are differences in flow between the ICAs or asymmetric changes in flow related to the pathology and geometry of the connecting intracranial arteries because AcomAs are a site of meeting and colliding pressure waves. The sensitivity to asymmetries can vary. Changing the velocities shifts the peaks of WSS towards the vessel with the larger mean flow. At selected regions, it can diffuse or concentrate the peaks in time depending on whether the inflow jets interfere constructively or destructively. In contrast, changing the relative phase or shape of the waveforms has a much more dramatic effect by making regions of elevated WSS travel along the surface.

They discuss whether the asymmetries exist. The different velocities could be caused by differences in the impedance of distal vascular beds. The phase and waveform differences may arise due to differences in the proximal carotid arteries. They carry out a calculation based on wave propagation effects and conclude that difference in length would cause a negligible difference in phase, but differences in thickness of the walls and the elastic modulus could cause a phase difference of 2.25%, as shown in section 1.10.

For improvements to the model, such as wall compliance and sensible outflow conditions at the boundary requires information that is unavailable, e.g. wall compliance, 4D information of vascular motion and flow or resistance information. Further work is needed to improve the models and characterise the errors.

Castro et al. [37]’s paper builds on previous work by Cebal et al. [3, 25] by analysing AcomA aneurysms, which had been excluded because of the potential of multiple avenues of inflow, which could not be imaged by 3DRA. In this study, they overcame the problem using a new technique in which two independently acquired rotational angiograms were combined.

The effect of a non-Newtonian viscosity was not tested in AcomA aneurysms, but from their previous studies, it is likely to have very little effect on the velocity and WSS.

Hassan et al. [4] studied a VGAM in an adult. This involves a small fusiform aneurysm on the artery, which communicated with a large aneurysm on the vein. They comment that fusiform aneurysms had been inadequately studied. Only three had been studied in Cebal *et al.*’s initial study [3]. A CFD simulation was carried out. The boundary condition was obtained by transcranial ultrasonography. The boundary condition at the outlet was that in the Fluent software [38], not a resistance model. Since the geometry can have a large effect on the flow fields, the boundary conditions were set as far as possible from the aneurysms or other complex parts, so that a Womersley flow profile at the inlet would be more accurate [4] and this is what physicians must do.

From a CFD simulation, they noticed that the venous aneurysm was washed out faster than the nearby normal veins. Inspection of the computational replica revealed a narrow hole between the aneurysms, through which the contrast agent passed. This might explain why the patient did not suffer the usual symptoms of a VGAM anomaly. The volume flow was low, so there was a normal venous drainage pattern. The artery was stenotic just before the aneurysm, so the Bernoulli effect was quite marked and the smaller segment resulted in much higher velocities, of $1.48 - 2.15 \text{ m s}^{-1}$. The jet subjected the wall to high shear stress and pressure, as it impinged on the wall, as shown in figure 1.16. In general, when blood impinges on an aneurysm wall, there is a stagnation point at which the pressure is maximal but the WSS is zero. The WSS was very high around it, caused by the bloodstream turning along the wall [4, 54]. The small aneurysm regulated a low shunt

volume of blood, so it was not high enough to cause venous reflux, i.e. some blood flowing backwards due to failure of valves. When the jet came near to the venous aneurysm, part of it went through the hole and the other part performed a whirling motion inside the arterial aneurysm, as shown in figure 1.16. The embolisation (see subsection 1.3) eliminated the whirling flow but did not terminate the blood flow completely. The artery was packed with many coils and the stenosis was sealed off. In the example, the CFD simulation helped to understand what was happening.

Hassan et al. [4, 54] used all the available modalities of cerebral angiography. Their CFD simulation was carried out using Fluent [38], including its outlet boundary conditions. They present a method of reconstructing cerebral grids as 3D numerical grids. Four examples of grid reconstruction and flow simulation for patients with ruptured aneurysms (three MCA aneurysms and one ICA-PcomA aneurysms) were validated with angiographic and operative findings. The rupture corresponded to the area facing the jet entering the aneurysm. Wall elasticity was simulated on two aneurysms using Fidap (see section 1.10). This confirmed that the area of maximum wall displacement is located at the angiographically determined bleb at the aneurysmal inflow zone. The points of rupture have a relatively high pressure and WSS.

A comparative blinded study should be conducted before the whole numerical procedure is proved correct and time-efficient.

The endothelium regulates vascular tone by producing vasodilator and vasoconstrictor substances. It is sensitive to changes in oscillating WSS which has stronger biologic influence on vessels than direct mechanical force. Increased WSS stimulates the release of nitrous oxide, which is a strong vasodilator and also a factor in arterial wall degeneration. Therefore, a local increase in WSS may cause local dilation and degeneration of arterial walls. The approach could be extended for AVM, AVM flow induced aneurysms and atherosclerosis. Patient specific computer modelling combined with information from other imaging modalities may provide important insights into flow dynamics before and after surgical or endovascular treatment.

They emphasise the importance of geometry, in particular the curvature of the parent artery. They point out that one must consider the errors and it may not make sense to compute the flow fields to 1% if the geometry is only known to 10%.

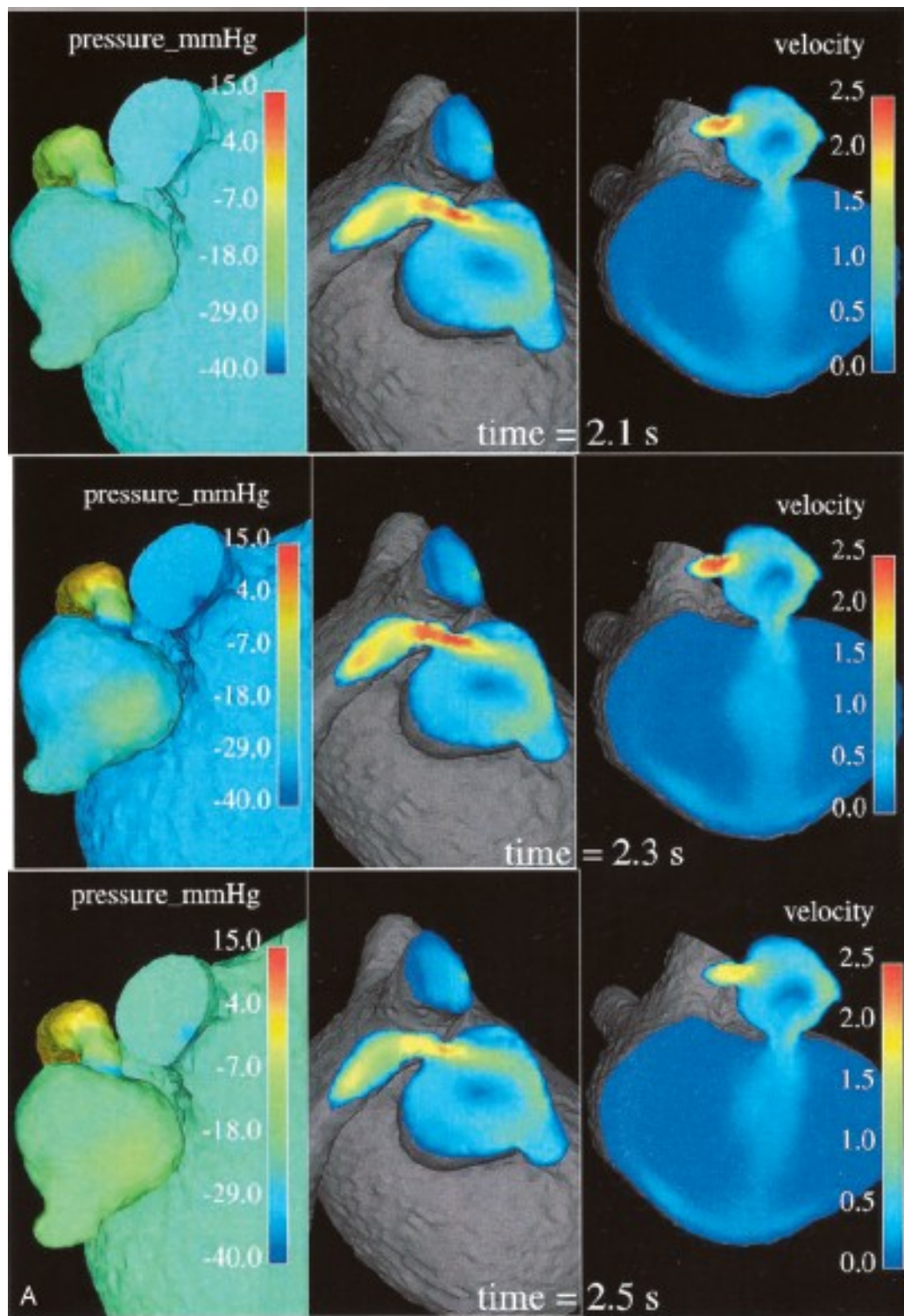


FIGURE 1.16: Simulation results for the blood flow in an adult Vein of Galen Aneurysm Malformation at three instants of time within a cardiac cycle. The left images are relative surface pressure maps, while the central and right images demonstrate the blood velocity maps in two cross-sections. The small and large aneurysms are the arterial and venous aneurysms respectively. Image taken from Hassan et al. [4].

Castro et al. [42] said that simulations had only been performed on idealised models. More recently, parent arteries have been used instead of straight ones. They carried out a CFD simulation to assess the effects of truncation of the parent artery in the flow rates in aneurysms. All distal vascular beds were assumed to have similar resistance to flow. They found that curvatures in the parent artery upstream to the aneurysm neck significantly influences the direction of the inflow jet. Truncation of the parent arteries causes the WSS to be lower and shifted towards the neck. Streamlines show that the flow has a simpler vortical pattern and is quieter in truncated models. The changes are more pronounced in cases with high degrees of upstream curvature. The inflow jet is parallel to the walls in truncated models, and therefore almost tangential to the aneurysm neck in sidewall aneurysm. Curvature may cause the flow to be directed into the aneurysm more. In the patient with the AcomA aneurysm, truncation changed the relative contributions to flow from the two ICAs. They say that there are two different theories on the effects of WSS. Low flow theories claim that domes are under low WSS states that trigger mechanobiologic processes that weaken the arterial wall. The theories were based on observations of low WSS in the dome made on idealised experiments or computer models. On the other hand, high flow theories indicate that a different set of mechanobiologic processes are triggered by high WSS at the aneurysm wall, particularly at flow impaction zones, that weaken vessel structure. The theories are not mutually exclusive, but the low flow theory might have to be reexamined. Generalizing from idealised models may be misleading.

A limitation of this study is the sample size is small and biased by their intention to show an effect. It is not clear how much of the parent artery is needed, but one could use theories about developing distance. The developing distance is given by:

$$L_{entr} = 0.06ReD \quad (1.14)$$

and

$$L_{entr} = 4.4Re^{0.25}D \quad (1.15)$$

for laminar and turbulent flow respectively [69, 70]. Each patient-specific anatomy has its own solution.

Radaelli et al. [71] analysed some mirror cerebral aneurysms, which are aneurysms within the same patient symmetrically located within the cerebral vasculature. Patient-specific

geometries were constructed from 3DRA images of the aneurysm. For the patients in which one of the aneurysms had ruptured, but not the other, there was significant asymmetry between the two sides of the COW and the ICA and this caused significant differences in the simulated haemodynamics. This shows that it is essential to include the parent artery and perhaps some of its branches in CFD simulations of cerebral aneurysms if the risk of rupture is to be assessed.

Steinman [31] reviewed the applications of image-based CFD for studying atherosclerosis progression. Studies show that low WSS promotes progression of atherosclerotic lesions. He underlines the importance of obtaining an accurate patient-specific geometry, since small changes can have large effects on the flow fields. It is possible to simultaneously reconstruct 3D maps of WSS and wall thickness in a patient-specific manner from black blood MRI images. A low or oscillating WSS leads to an increased wall thickness, but a statistically significant relationship was not obtained. Inability to resolve wall thickness or other sources of inaccuracy may have masked the relationship.

A study showed that distensibility in the carotid bifurcation caused the WSS to be lowered, but the WSS and velocity still kept the same pattern. In older subjects or patients with cardiovascular disease, there will be increased stiffness. Side branches are sometimes ignored, especially if they are oriented parallel to the (often thick) imaging slices but this has relatively minor effects on the flow patterns. It may be satisfactory to find flow fields qualitatively. One author pointed out that “errors in WSS should only be considered significant if they would lead to different conclusions regarding the likely cause or location of vascular disease”. CFD is improving, so it will soon be able to predict rather than confirm, the development, progression and perhaps even induced regression of atherosclerosis, and other cardiovascular diseases.

Villa-Uriol et al. [40] have reviewed some techniques for characterising and managing cerebral aneurysms. They discuss how personalised vascular models can be created and used to derive a collection of descriptors. The correlation between these descriptors and clinical events could be examined so that in future, the descriptors could provide more information to clinicians than they currently have when they assess the situation for a particular patient. The descriptors include characterisations of the shape of the aneurysms, their rate of growth, the pulsation of the walls of the aneurysms and the flow characteristics.

They discuss some studies that simulate the blood flow after coils or stents have been inserted into the vasculature.

Villa-Uriol et al. [40] also emphasise the importance of validating both the reconstruction of the vessels from medical images and of ensuring that the flow fields agree with those occurring *in vivo*. They cite Geers et al. [72], who studied the differences between models of four MCA aneurysms derived from 3DRA and CTA images and the subsequent differences in the flow fields. Since the contrast and resolution of the CTA images was lower than that of the 3DRA images, the aneurysm neck appeared to be wider in the models constructed from CTA images, which increased the flow rate into the aneurysm. Furthermore, some of the vessels that could be reconstructed from the 3DRA images could not be reconstructed from the CTA images, so they were not included in the models derived from the CTA images. Despite these differences, the main flow characteristics were well produced between the two sets of models.

Experimental measurements of the flow in physical models of blood vessels can be used to validate CFD simulations [73, 74] as well as to study the flow, as Tateshima et al. [30] did. Both Ford et al. [73] and Hoi et al. [74] measured the velocity of flow in a silicon phantom over selected planes using particle imaging velocimetry. A laser was used to illuminate a selected plane and the positions of the particles were measured from images taken by a camera at regular intervals. Ford et al. [73] found that the CFD simulations were able to capture the features of the flow in fine detail, although there were discrepancies between the simulated and measured flow fields in some places. They comment that this may be due to the slight distensibility of the physical phantom. Hoi et al. [74] also obtained good agreement between the simulated and measured velocity fields. Their physical phantom was almost spherical, but the velocity field simulated in an ideal spherical model disagreed with that measured from the phantom, which shows that a small change in the geometry can cause a large change in the flow fields.

Cebral et al. [41] compared the isovelocity surfaces extracted from their patient-specific CFD simulations with isointensity surfaces obtained from time-of-flight MRA images, which were discussed in section 1.7.5, and obtained good agreement in the aneurysmal flow region. In contrast to the sensitivity analyses discussed earlier in this section, this provides one of the few tests of whether a CFD model is reproducing the *in vivo* environment correctly.

Mihalef et al. [43] carried out a simulation of the blood flow in the heart. The motion of the walls was derived from a series of CTA images, as explained in section 1.7.6. Their computation resulted in right-handed helical motion of blood as it entered the aorta, which is a well known feature of healthy aortic flow. This occurred despite the fact that the torsional motion of the heart was not included, which provides evidence that the helical rotation is determined by the orientation of the aorta with respect to the mitral valve and the valve geometry. The time-dependent flow rate through the valves in the heart also agreed qualitatively with some typical data measured *in vivo*. While the model achieves some qualitatively correct results, a quantitative comparison with *in vivo* experiments has not been attempted. Jeays et al. [44] simulated blood flow in the superior mesenteric artery with moving walls and compared the velocity flow fields to those obtained using rigid walls. The largest difference in the WSS was 26% when compared with a global norm, but the average difference was 2%, despite expansion of the artery of order 10% of its radius and translation of order its radius.

Bernardini et al. [32] used a finite-element method to simulate the flow in an artery with an aneurysm before and after insertion of a stent in the parent artery. The mesh resolution was 0.3mm, except at the vessel and aneurysm walls and around the stent struts, where it was 0.02mm, which is much finer than the other simulations discussed in this section. Some methods of surgical treatment, such as occlusion of certain blood vessels, could be simulated by editing the vasculature and therefore a coarser resolution could be used. Bernardini et al. [32] compared the results obtained with five different models of the stent itself. The most complex model used the precise three-dimensional shape of the stent and took into account the material properties and its elasticity to determine the position it reaches after deployment, while the simplest model neglected the material properties and assumed that the stent was rigid with struts that had a uniform cross section. The velocity and wall shear stress were averaged over the volume and wall of the aneurysm respectively, then the ratio between the values of these averages in the treated and untreated vessels was calculated and averaged over time. The velocity and wall shear stress were reduced by approximately 50% in the aneurysm, but there was significant variation between the results for different stent deployment models. Nevertheless, the results are consistent with redirection of the blood flow through the parent artery, which gives some evidence that the model is behaving correctly. The tool is therefore promising for use in neurosurgery.

Villa-Uriol et al. [40] evaluated some recent techniques for simulating the effects of neurosurgery and explain that the performance of different stents can now be evaluated with CFD models. For example, Kim et al. [33] investigated the influence of two different stents in different axial orientations on the flow fields in an aneurysm. The geometry was extracted from 3DRA images of an aneurysm. The struts on the stents were assumed to be uniform and the stent position was calculated by iteratively solving an evolution equation for the points on the stent mesh. Both stents reduced the velocity in the aneurysm and the WSS on the aneurysm wall, but for one of the stents, the remaining WSS depended strongly on the position of the stent. Morales et al. [34] developed a virtual coiling method, in which a CFD simulation is carried out in the presence of coils. They found that the WSS increased near the aneurysm neck but decreased on the wall of the aneurysm. The haemodynamic differences owing to coil configurations were negligible when the coil packing rate was above 20%. They concluded that their technique has the potential to become a valid tool for evaluating post-treatment aneurysm haemodynamics.

Tahir et al. [35] modelled restenosis of arteries after stents had been deployed. The arterial wall was damaged based on hoop strain and longitudinal threshold criteria, which exposed the smooth muscle cells in the model to blood flow, causing them to proliferate. A biological solver controlled the progression of cell proliferation according to a set of rules. The probability that a smooth muscle cell divides was decreased by interactions with neighbouring cells, high wall shear stress and use of a drug-eluting stent. The blood flow was modelled with the lattice-Boltzmann method, which is discussed in chapter 2. The flow rate was constant. Their simulation results agreed qualitatively with published data from experiments and clinical trials in the following ways. First, the rate of growth relative to the number of cells reached a peak after approximately 20 days. Second, the rate of proliferation increases with the degree of injury, i.e. the depth to which the stent is pushed into the arterial wall, although the number of cells at the end of restenosis did not depend strongly on this deployment depth. Thinner stent struts were found to cause faster proliferation of cells, but the maximum number of cells was lower.

1.9 Other models of cerebral blood flow

Tateshima et al. [30] used a physical model to study the WSS in unruptured cerebral

aneurysms with blebs, or lobulations, which are small outpouchings of the aneurysm dome. Studies had shown that WSS contributes to the formation of aneurysms but little attention had been given to the effect of shear stress in aneurysms that were already present. The paper paid particular attention to the bleb, which is the point at which cerebral aneurysms commonly rupture. The walls were rigid in this study, which was reasonable for this type of model because previous work had found no remarkable difference in the flow between rigid and elastic physical models. The flow rates in each arterial branch were set in accordance with the cross-sectional area of the branch.

In this paper, the WSS in a basilar tip aneurysm and an MCA aneurysm in the COW was evaluated using geometrically realistic models. It was measured at ten points on each aneurysm; three in the inflow zone, four in the dome and three in the outflow zone. It was expressed as a percentage of the maximum WSS in the parent arteries. For both aneurysms, the inflow was at the distal side of the neck and the outflow was at the proximal side. The mean WSS was higher in the outflow than the inflow zone. The direction of the WSS was the same as the intra-aneurysmal flow. The bleb had the highest mean WSS and was the point at which the maximum WSS over time and space occurred. In the MCA aneurysm, the peak WSS was 93% and occurred in the early diastolic phase, whereas in the basilar tip aneurysm, the maximum WSS was 54.4% and occurred in the late systolic phase. The WSS varied at each point, unlike in idealised aneurysm models.

Wall shear stress impinges on endothelial functions, rather than having a direct mechanical influence. As the WSS increases, more endothelium-derived nitric oxide (a strong vasodilator) is produced. Increased WSS caused by increased velocity stimulates dilation, so velocity declines to the normal range. This is how the blood flow volume is regulated. Distribution of stress in a curved tube is not uniform, as it is in a straight tube. There may be local dilation of the wall. Experiments have shown that increased WSS causes aneurysms to form.

It remains unclear whether the endothelial cells on the aneurysmal wall are sensitive to modifications of WSS. From scanning electron microscope images, normally shaped arterial endothelial cells have been seen on the inner surface of an unruptured aneurysm sac. It is possible that endothelial cells in a cerebral aneurysm react to WSS in the same way as those in a normal artery. From the results obtained, there are two possible hypotheses. Regions of the aneurysm with high WSS could be more prone to bleb formation due to

increased production of nitric oxide. Alternatively, the bleb induced a higher WSS, which caused more nitric oxide to be produced, leading to degeneration of the vascular wall. This is because nitric oxide could cause degeneration of the walls and has been shown to decrease smooth muscle cell proliferation and migration. Studies have also shown that the walls of ruptured aneurysms contain fewer muscle cells and more irregular layers of collagen IV than unruptured ones. These hypothesis make use of biochemical factors, which the theories about WSS in [3, 25, 37] neglect.

Hillen et al. [1] wanted to study the flow in the PcomA. They only used half of the CoW. The PCA and ICA were the afferent arteries, the MCA and ACA were combined as one efferent artery and the PCA was the other. The CoW was assumed to be symmetric, so the flux through one side of it was half of the total flux. The idea of efferent resistances was applied by combining the resistances of the ACA and MCA in parallel, so the combined resistance was half that of the PCA. The combined resistance of all efferents was calculated and divided by two to take into account the two sides of the CoW. The PcomA connected the two sections, as shown in figure 1.17. Mass and momentum were conserved, as follows:

$$\frac{\partial A}{\partial t} + \frac{\partial}{\partial x}(Av) = 0 \quad (1.16)$$

$$\rho \left(\frac{\partial v}{\partial t} + v \frac{\partial v}{\partial x} \right) = -\frac{\partial p}{\partial x} - \frac{8\pi\eta v}{A}, \quad (1.17)$$

where A is the cross-sectional area.

The viscous friction is the Poiseuille resistance expression for the volume flow rate for steady laminar flow in a circular tube. This is because Womersley showed that for relatively small values of the Womersley number, $\alpha = \frac{D}{2} \sqrt{\frac{\omega}{\nu}}$, from equation (1.6), the additional inertial and frictional losses arising due to velocity profile distortion in pulsatile flow conditions do not differ greatly from steady flow conditions. The largest value of α is 3 in the study by Hillen et al. [1]. The pipes were modelled as distensible vessels here, as explained in section 1.10.

They found that when the resistance in the vertebral artery (section 45 of figure 1.17) is increased by reducing the cross-sectional area, the pressure at B, D and E decreases because of this change in resistance because $p = Z_R Q$. The velocity in 45 decreases, but the velocity in 56 decreases less and the velocity in 12 and 25 increases because of the reduced pressure at 5. More blood flows through the PcomA. Changing the peripheral

resistance at 6 shows that the afferent and efferent systems are not independent. In that case the ratio of volume flow rate $\frac{Q_{12}}{Q_{45}}$ would not change and $\frac{Q_{23}}{Q_{56}}$ would be linearly related to $\frac{Z_{R,6}}{Z_{R,3}}$. The peripheral resistance dominates since both ratios are close to the $\frac{Z_{R,6}}{Z_{R,3}}$. At $\frac{Z_{R,6}}{Z_{R,3}} = 3.1$, $\frac{Q_{12}}{Q_{45}}$ changes from being greater than $\frac{Q_{23}}{Q_{56}}$ to being less, so the flow in the PcomA changes direction.

If we increase the resistance in segment 45 while changing the diameter of the PcomA, there is a similar appearance of change of volume flow rate in segments 12 and 25. The changes in flow rate are greater if the PcomA is wider. The flow in segment 56 decreases, but by less than 10%, provided that the PcomA is not too narrow. Looking at the same results in a different way, Q_{45} decreases and Q_{25} increases as the diameter of the PcomA is increased. The effect is greater if section 45 is partially occluded. The total volume flux was independent of the diameter of the PcomA, but the afferent fluxes depend on it strongly. It was interesting that the normal range of variation of the diameter in the PcomA is in the region where the effect on the system is large.

They concluded that the PcomA is capable of performing the compensatory function by responding to physiological fluctuations in the blood flow in the afferent vessels, due to, for instance, movements of the spine, and the mechanism for this is clear, as in the paragraph above. It is what one would intuitively expect but it does confirm that increasing the resistance of 45 has both effects that we would expect; i.e. it both decreases the flow in 45 and the pressure at 5. The total flux is determined by the total peripheral resistance. The compensatory capacity of the vessel is limited only by very small diameters of the vessel. Previous work had concluded that opposing streams from carotid and PCAs meet to form a dead point. If this is valid for the PcomA, the study indicates that the diameters of the afferent vessels and the ratio of the peripheral resistances have to be finely tuned. The limitation of this model is the simple geometry.

The model was extended to include all the arterial segments of the CoW and the basilar artery in [5], with the positive flow directions as shown in figure 1.18. First the cross-sectional area of the basilar artery (16) was reduced. The results were similar to the earlier model. The other experiments in [1] were repeated and the results were identical. The pressure in the vertebral arteries, basilar arteries, PcomAs and both segments of the PCAs decreases, whereas it does not change in the ACAs, MCAs or AcomAs. The velocities in the vertebral arteries, basilar artery and P1 PCAs decrease, and the velocity

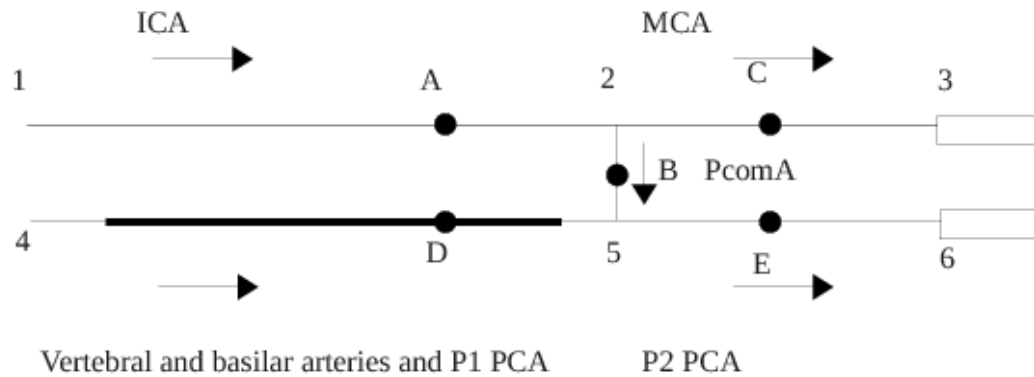


FIGURE 1.17: A model of half of the CoW, as studied by Hillen et al. [1]. The arrows show the normal directions of blood flow.

in the P2 PCA decreases slightly. The velocity in the ICA and PComA increases and it does not change in the MCA or ACAs, as in [1]. There is no flow in the AcomA, which is as expected due to the symmetry.

The study also assess the effects of asymmetry in the CoW. If the right PcomA is doubled in size, to 2mm, there are no differences in pressure between any points in the system and the corresponding points on the opposite sides and no difference in afferent or efferent flow rates. However, there is a clockwise reallocation of flow in the segments of the circle. Flow in the right PcomA is greater than the left PcomA due to its reduced resistance. This causes a flow to the right in the AcomA. Flow in the right P1 PCA is lower on the right than the left because flow is partially cancelled out by a greater flow from the anterior circulation. The flow in the right A1 ACA would be negative according to the arrow in figure 1.18 in the symmetric case. In the asymmetric case, the flow direction is reversed and this is why the flow is less than in the left A1 ACA.

The diameter of the right PcomA was then varied. The flux in the left and right PcomA and the AcomA (segments 13, 3 and 8 respectively in figure 1.18) were plotted against diameter of the right PcomA, producing an s-shaped graph, as shown in figure 1.19. The flow in the AcomA changes direction when the diameters of the PcomAs are equal. As the diameter of one PcomA increases, the flow in it increases, the flow in the contralateral PcomA decreases and the flow in the ipsilateral ICA increases. When the diameter of the ipsilateral PcomA is less than 1.85mm, the flow increases faster for smaller diameters

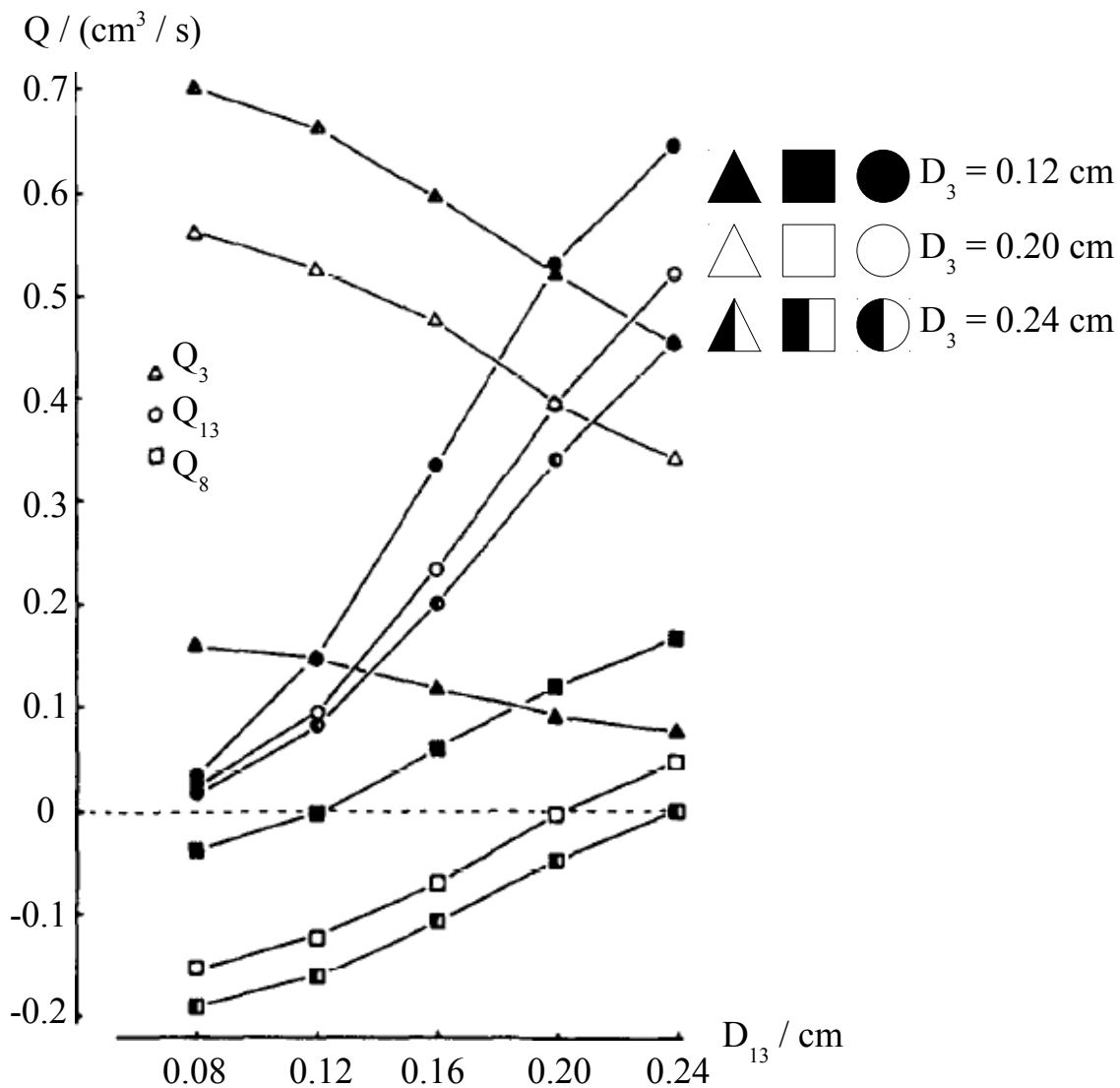


FIGURE 1.19: Flow rate through the left and right PcomA and AcomA (Q_{13} , Q_3 and Q_8 respectively) with respect to the diameter of the right PcomA). Graph taken from [5].

The maximum for a dead point to occur is below the minimum possible resistance for a diameter over 0.8mm, so a dead point cannot occur unless the diameter is less than 0.8mm.

They concluded that the conclusions drawn from the simplified model are valid for the CoW as a whole. The mechanism governing the efferent vessel fluxes is the ratio of the peripheral resistances. The flows in afferent segments and segments of the circle are strongly influenced by their own resistances. The change in the diameter of the PcomA affects the flux in all segments of the circle and afferent segments. The influence is strong in the range of anatomical variation, except that the influence of the diameter of one

PcomA on the flux in the opposite ICA reduces to zero in one case. This could be because the energy losses on both flow routes from the ICA to the PcomAs are equal, creating a balance. There is some doubt about the existence of a dead point in the PcomA and it should not be assumed that the flow is zero in the PcomA in models of the CoW. Models of the cerebral circulation should include the anatomical variations and the correlations within the variations, since these factors strongly influence the flow in the afferent vessels and the segments of the circle.

Hillen et al. [39] wanted to investigate the contribution of the refinements to the models in their previous studies and gain an insight into the governing mechanisms. They constructed an analytic relationship between the fluxes and vascular resistances, which are explained in section 1.5. They had to assume steady Poiseuille flow in each vessel to do this. Conservation of mass at each of the seven junctions of the CoW required the net flux to be zero, i.e.

$$Q_6 = Q_7 + Q_8. \quad (1.18)$$

The pressure is continuous for all branches of the junction, so we have equations such as

$$p_A - p_{II} = Z_{R,16}Q_{16}, \quad (1.19)$$

where p_A is the arterial pressure. Overall, a set of 23 linear equations for 23 unknowns was obtained. These were solved by matrix inversion to produce 23 equations for 23 unknowns (16 fluxes and 7 junction pressures). The fluxes did not differ by more than 10% compared to the ones from the previous study. They were lower, which was probably because the arterial diameters matched those in the previous study at diastole, so the time average was larger in the previous study.

To assess the dependence of the flux through a vessel on particular resistances, the flux through each artery from each junction was expressed as a function of its own resistance and the resistance of the other arteries from the same junction. For example, for junction Ia, segment 5, in figure 1.18:

$$Q_5 = \frac{a_1 Z_{R,3} + a_2 Z_{R,4} + a_3 + a_4}{d_1(Z_{R,3}Z_{R,4} + Z_{R,3}Z_{R,5} + Z_{R,4}Z_{R,5}) + d_2 Z_{R,3} + d_3 Z_{R,4} + d_4 Z_{R,5} + d_5}, \quad (1.20)$$

where the a_n and d_n are positive constants that depend on the other resistances. If we

then further simplify the expressions and look at the dependence of an arterial flow on its own radius, the flux through segment i is given by:

$$Q'_i = \frac{a}{dZ_{R,i} + e} = \frac{aR_i^4}{\eta'_i d + R_i^4} \quad (1.21)$$

where

$$\begin{aligned} \eta'_i &= \frac{8\eta L_i}{\pi}, \\ Q'_i &= \frac{Q_i}{p_A - p_V}, \end{aligned}$$

where p_A is the pressure at the entry points, p_V is the venous pressure, L_i is the length and a , d and e are positive or negative constants. Equation (1.8) has been used to express the flow rate through the vessel in terms of its radius. We obtain the same s-shaped graph of flux against radius as in the previous studies (figure 1.19), with a minimum flux of zero when the radius of the artery is zero and a maximum of $\frac{a}{d}$. The dependence of the flux in segment i on the radius of segment j from the same junction is also s-shaped, and is given by:

$$Q'_i = \frac{a\eta'_j + bR_j^4}{\eta'_j d + eR_j^4} \quad (1.22)$$

The minimum flux is $\frac{a}{d}$ at radius zero and the maximum is $\frac{b}{e}$ at large radii or vice versa if $\frac{a}{d} > \frac{b}{e}$ at large radii. The graphs are shown in figure 1.20.

A study was carried out on the posterior communicating artery and this was compared to [1] and [5]. If we calculate Q_3 and $Z_{R,1}, Z_{R,2}, Z_{R,3}, Z_{R,4}$ and $Z_{R,5}$ remain included with $Z_{R,16} = 0$ and all other resistances set to infinity, the model is identical to [1].

$$Q_3 = \frac{-\frac{Z_{R,1}}{Z_{R,1}+Z_{R,2}} + \frac{Z_{R,4}}{Z_{R,4}+Z_{R,5}}}{\frac{Z_{R,1}Z_{R,2}}{Z_{R,1}+Z_{R,2}} + \frac{Z_{R,4}Z_{R,5}}{Z_{R,4}+Z_{R,5}} + Z_{R,3}} (p_A - p_V) \quad (1.23)$$

Using data on the arterial resistances, we obtain

$$Z_{R,2} \gg Z_{R,1} \text{ and } Z_{R,5} \gg Z_{R,4} \Rightarrow Q_3 = \frac{-\frac{Z_{R,1}}{Z_{R,2}} + \frac{Z_{R,4}}{Z_{R,5}}}{Z_{R,1} + Z_{R,4} + Z_{R,3}} (p_A - p_V). \quad (1.24)$$

This shows the influence of the comparably small afferent resistances on the flux in the communicating segment. The flow changes direction when $\frac{Z_{R,1}}{Z_{R,2}} = \frac{Z_{R,4}}{Z_{R,5}}$, as in the previous

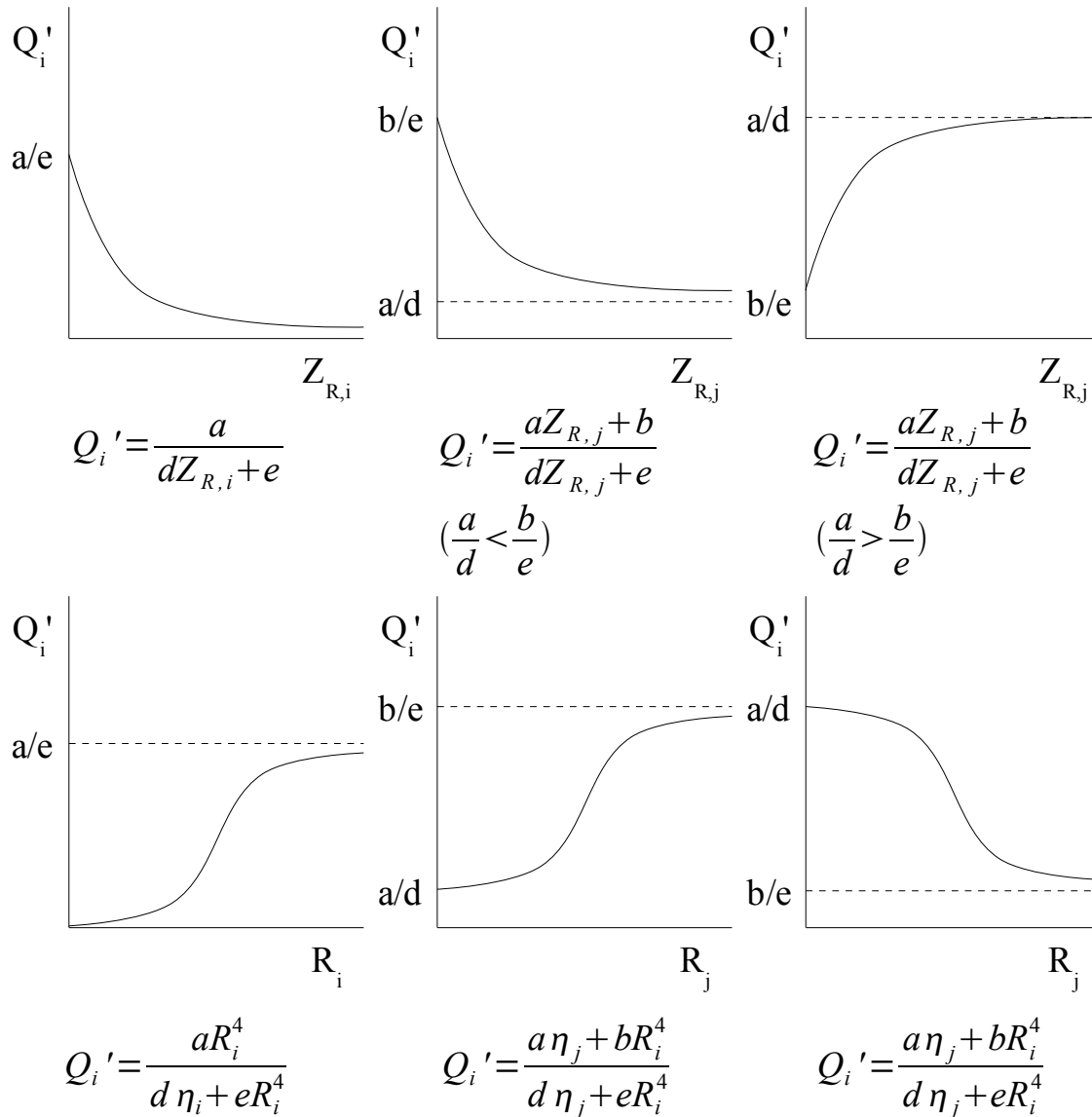


FIGURE 1.20: Relationships between flux through an artery vs resistance (top row) and flux vs radius.

studies. This mechanism is similar to the principle of the Wheatstone Bridge, in which the bridge current is zero when $\frac{Z_{R,1}}{Z_{R,2}} = \frac{Z_{R,3}}{Z_{R,x}}$ as shown in figure 1.21.

In [5], the influence of the contralateral PcomA on the flow in the ICA became very small for a certain value of the ipsilateral PcomA. It is difficult to determine whether the influence is truly zero or just close to zero. In this study, Q_1 was expressed as a function

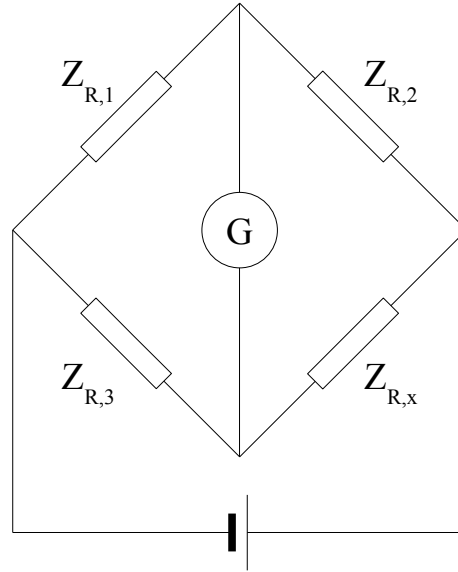


FIGURE 1.21: The Wheatstone bridge.

of R_1 , R_3 and R_{13} . The expression can be differentiated to give:

$$\frac{\partial Q_1}{\partial Z_{R,13}} = \frac{-a_1 Z_{R,3}^2 + a_2 Z_{R,3} + a_3}{(d_1 Z_{R,3} Z_{R,13} + d_2 Z_{R,3} + d_3 Z_{R,13} + d_4)^2} (p_A - p_V). \quad (1.25)$$

The denominator is always positive, but the numerator can be zero for a certain value of R_3 . This was consistent with the radius of 1.85mm. This simple model gave consistent conclusions with both previous models. Energy losses related to branching tubes and inlet phenomena are neglected and it may be expected that the energy losses will affect the outcomes of the models in a quantitative, but not a qualitative way. The model proves that the mechanisms that govern the flow in the CoW are simple and explainable by steady laminar flow relations or by electric current theory with capacitance and inductance neglected. An obvious shortcoming of all three models by Hillen et al. [1, 5, 39] is the lack of experimental confirmation.

Clark et al. [29] and Alastruey et al. [6] not only included vessel elasticity in the simulated vessels, but also included the elasticity of the distal vessels by using an RCR model at the outflow boundaries (see section 1.10). The first resistance was set to the impedance of the terminal vessel in both studies to minimise the total impedance of the lumped parameter model. Clark et al. [29] calculated the RCRs from the velocities at the outflows. They

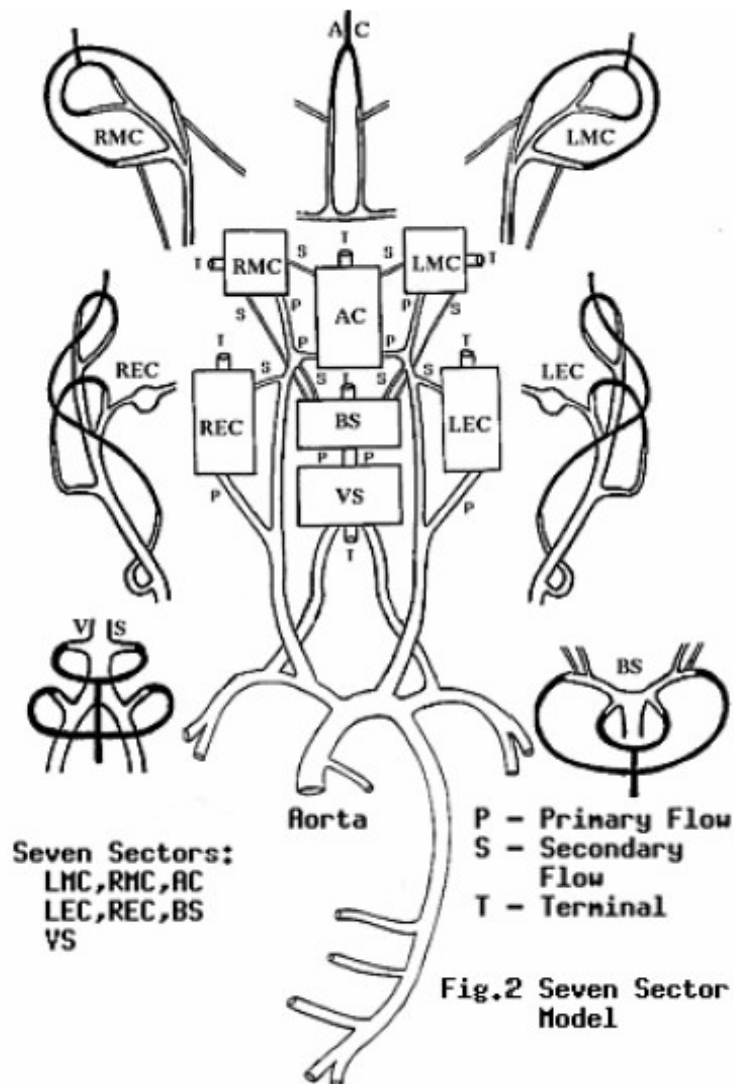


FIGURE 1.22: The sector model for blood vessels, by Alastruey et al. [6].

stated that the crucial unknowns were the second resistances in the model, but it is not clear how the capacitances were determined. To measure the velocities at all the outflows would take far too long, so the authors used a sector model. To determine the terminal resistance, it is necessary to be able to define the flow into and/or out of the sector. The primary input to each one comes from an artery in which the flow rate was measured using PCMRA. The secondary anastomoses are the arteries that join the sectors. The terminal efferents are the outflows that do not feed another sector. The terminal vessels of each sector are melded together into one. The configuration is shown in figure 1.22.

First a plausible set of resistances was estimated from a previous simulation or a steady flow simulation. At the start of the simulation, the velocity was zero and there was venous pressure everywhere. The aortic pressure waveform was used as the inlet boundary condition. The flow at the efferent, was assumed to be the same as the mean flow through the primary input to each sector, neglecting the secondary flows. This target flow rate is called a QGOAL. The simulation is done for a pulsatile period, then the RCRs are adjusted. The simplest way to do this is multiply the resistance by the ratio of mean flow rate achieved to the measured mean flow rate. This would correctly adjust one terminal flow, but the sectors are joined by the secondary flows, so many adjustments are needed. After a user-specified number of periods, the simulation was started again from zero flow and venous pressure at all nodes. When the terminal flows matched the QGOALS, the QGOALS were adjusted to take into account the secondary flows and the process was started again from zero flow and venous pressure. This iterative method tells us the output RCRs. They did not test whether the assumption that the resistance is inversely proportional to the brain mass irrigated is valid or not.

The method was carried out for three different patients who were about to undergo a BOT test and a simulation was carried out. Using the same RCRs, the same artery was occluded in the model as the one occluded in the BOT test. The generic model was also used in the same way. The mean volume flow rates were compared with measured flow rates from the PCMRA before and after the BOT test. The cerebral perfusion pressure (CPP)(difference between arterial and venous pressure) for both models was compared. The baseline flow results agreed closely with the PCMRA ones and were more consistent than the generic model. For the patient who passed the BOT test, the generic and sector models showed no drop in cerebral perfusion pressure, which is consistent with the result that the patient passed the test. For two patients who failed the BOT test, the model predicted drastically different flow patterns in several sectors. The reduction in flow in one sector in each patient was comparable with the BOT failure in which hemiparesis (paralysis of one side of the body) occurred. A similar result was found for the CPP values. The reduction in flow and pressure was not as pronounced in one patient than the other because the former patient failed the BOT only under hypotensive (low blood pressure) challenge. In the patient who failed the BOT test, there was an anomaly in the occluded AC sector, in which all possible paths to two sectors were blocked by occlusions, but the sector model found the one unblocked path, which was implausible because it found backward flow. To correct

the implausible solution, an eight-sector model was used. They concluded that patient specificity was achieved. However, studies in a large population of patients are needed.

Alastruey et al. [6] studied the effects of anatomical variations on the cerebral outflows of the CoW, both in healthy conditions and after a complete occlusion of an ICA or VA. Previous work had shown that the CoW can compensate for the omission of a single circulus vessel and that the worst configuration of the CoW when the ICA is partially occluded is that of a missing ipsilateral A1 ACA. They used equations (1.16) and (1.17), except that the viscous friction coefficient was $\frac{22\pi\eta v}{A}$. That might be due to the difference in friction between steady and pulsatile flow explained earlier in this section, but it is not clear why the difference between the coefficients should be so large. The resistance of the brain was calculated, but in contrast to other studies, the peripheral resistances were set to be inversely proportional to the areas of the arteries, giving them different resistances. They also used an RCR model.

The model captured wave propagation features observed in *in vivo* measurements along the aorta such as the increase in pulse pressure away from the heart, the notch at the end of systole and the diastolic decay due to the Windkessel effect. The peak flow decreases as we move down the aorta. This confirms that the flow boundary condition is realistic, perhaps more so than some other studies. However, Clark et al. [29] might give the more accurate estimate of the RCRs. The flow in the common carotid artery is always in the forward direction. The brachiocephalic and subclavian arteries have backward flow at the end of systole, which was in good qualitative agreement with *in vivo* measurements of velocity from Doppler ultrasound. A quantitative comparison cannot be achieved because there is little information about the inflow at the ascending aorta, the arterial geometry and elasticity and the terminal impedances of the subject. The pressure waves of the three arteries are almost identical, so the antegrade flow is a consequence of the length, diameter elasticity and mean flow (determined by the terminal resistances) of the common carotid and vertebral arteries and their adjacent arteries.

The volume outflows were compared under normal conditions. The MCAs receive the largest blood supply, followed by the ACAs. The values and distribution of the outflows agreed with *in vivo* measurements within acceptable limits. The flow in the AcomAs and PcomAs are small but sufficiently significant to maintain these vessels active, being 1 to 5% of the rates in the other CoW arteries. These flows arise from pressure phase

delays between both sides of the CoW caused by the asymmetry introduced by having the brachiocephalic artery on one side. This asymmetry does cause a difference in flow waveform shape and amplitude between the left and right sides of the CoW. The most common anatomies of the CoW described in section 1.3 were simulated. When one of the A1ACAs and P1PCAs is absent, the flow rates through the communicating arteries is higher. The direction of the flow shows which side it is. The flows in the efferent arteries changed by less than 15%. This suggests that flows through the communicating arteries are sufficient to supply all areas of the brain in subjects with a hypoplastic (small or underdeveloped) A1 ACA or P1 PCA. In the anatomies tested with missing communicating arteries, the flows in the other arteries changed by less than 1%. The results show that a significant flow in AcomA without significant stenosis of the ICAs or VAs implies that there is at least one missing or hypoplastic A1 ACA or P1 PCA.

The different anatomies of the CoW were then simulated with an occluded ICA or VA. The occlusion of the VA has relatively little effect compared to the occlusion of the ICA. If the right ICA is occluded, the highest decrease in flow in the efferent arteries occurs in the right MCA then the right A2 ACA. The decrease in flow is greater if the AcomA is absent than a PcomA because flow from the left ICA to the right ICA has less viscous dissipation through the AcomA than through the PcomAs. This shows that the AcomA is a more critical collateral pathway than both PcomAs if an ICA is occluded, in agreement with previous work. If the right VA is occluded, the P2 PCAs are the efferent arteries with the highest reduction in flow rates and the PcomAs become the more important collateral routes. The anatomy with a missing A1 ACA and complete occlusion of the contralateral ICA presents the highest reduction in outflow rates, and therefore the highest risk of ischaemia and stroke.

The effect of partial occlusions of the communicating arteries with occlusion of the right ICA were studied. The flows in the A2 ACA and MCA depend strongly on the calibre of the AcomA, whereas the P2 PCA flow remains almost constant. The diameter of the right PcomA affects the outflows at all three efferent arteries. The flow through the AcomA is higher for a given calibre than the flow through the PcomA if it has the same calibre. A reduction in the diameter of the AcomA produces a higher reduction in the mean flow rates of the A2 ACA and MCA than the same reduction in the PcomA, confirming that the AcomA is the more important collateral pathway. The flow in the PCA decreases as

the diameter of the PcomA increases because more blood flows to the anterior circulation. The minimum diameter of the PcomA for collateral flow is less than that for the AcomA because the PcomA is longer, so it has a higher resistance to flow.

Detailed information on elasticity and boundary conditions and geometry was not available. The data was for healthy young adults. This model has not analysed other mechanisms of autoregulation such as vasoconstriction and vasodilation and wall remodelling. The model can predict the effect of clinical interventions and can study the effects of changes in the cardiac output. It has the potential to simulate local flows in detail if coupled to a 3D simulation of a local area of the circulation, so flow patterns leading to aneurysms and atherosclerosis can be investigated.

Olufsen [24] studied the effects of different boundary conditions. For this model, the arteries were assumed to taper. Instead of using a completely one-dimensional model, a boundary layer was used, with a thickness of 1mm in all arteries. The velocity gradually decreases from the mean velocity to zero across the boundary layer. This is reasonable because measurements show that the velocity profile is almost flat in the aorta and more parabolic in the peripheral arteries. The RCR model (see section 1.10) was compared to a pure resistance model and a structured tree outflow condition. In this, the small arteries were modelled as a symmetric tree from each outlet, with 17 generations of bifurcations. The momentum equation (equation (1.2)) was linearised. Combining this with equation (1.28) below for the compliance gave a wave equation. The impedance of an arterial section was calculated, and the impedance of each tree was calculated by combining the impedances of each section. The impedance is assumed to be zero beyond the arterioles which is consistent with the fact that smaller arteries generate the peripheral resistance, and not the capillaries. The flow in the arterioles is assumed to be purely viscous and not pulsatile, but such assumptions are sensible, because velocity waves propagate and decay exponentially [75]. The structured tree condition maintains high frequency oscillations in the impedance and includes wave propagation effects for the entire tree, which is not possible with simpler models. The RCR and resistance models are likely to introduce artificial reflections at the outflow boundaries.

1.10 Inclusion of arterial elasticity

The displacement of the artery walls due to the elasticity might be as important as the pressure, velocity and stress flow fields in the development of cardiovascular disease, but most 3D CFD simulations assume that the walls are rigid, as explained in section 1.8. The elasticity is also likely to have important effects on the pressure, velocity and stress flow fields, since several of the studies reviewed in section 1.8 show that the flow fields are sensitive to small changes in the geometry. Hoi et al. [74] found that the wall shear stress across three planes differed by an average of 42%, 29% and 37% between a spheroidal CFD model of an aneurysm and a more realistic model with a volume that was 8% larger. This suggests that the flow fields are very sensitive to small changes in volume, which suggests that they would be significantly affected by the inclusion of elasticity. However, Jeays et al. [44] found an average difference of only 2% in the wall shear stresses obtained by a model of the superior mesenteric artery with moving boundaries agreed compared with those obtained by a model with rigid boundaries.

If the effects of arterial wall elasticity are to be included, an equation of motion for the vessel wall is needed. In models, the radius is usually assumed to change instantaneously with pressure [1, 5, 6, 24]. If we balance the circumferential tensile stress, σ and transmural pressure (the difference in pressure between the inside and outside of the artery) for a cylindrical vessel and use the fact that biological tissue is practically incompressible [6, 24, 76], we obtain:

$$p - p_0 = \frac{4}{3} \frac{Eh}{R_0} \left(1 - \frac{R_0}{R} \right), \quad (1.26)$$

where p is the pressure of the fluid inside, p_0 is the external pressure, E is the Young's modulus, h is the thickness of the wall and R_0 is the radius of the tube when $p = p_0$. Equation (1.26) is developed in more detail in section 3.2.1. One of the more important assumptions of the derivation is that the walls are thin, i.e. $h \ll R$.

In reality, the transmural pressure applies an outward force and the elasticity of the vessel applies an inward force, so the Newtonian equations of motion need to be integrated to find the radius of an artery or position of the wall at a particular time. As we would expect, there is a time delay in the response from a change in pressure to the corresponding change in cross-sectional area, which is as we would expect from integrating Newton's equations of motion, but Olufsen [24] commented that this is because the wall is viscoelastic.

The Young's modulus depends on the radius of the artery at zero transmural pressure. Olufsen [24] obtained an approximate functional fit for the Young's modulus as a function of R_0 . It decreases with vessel radius, which is consistent with [6], which used a Young's modulus of $4.0 \times 10^5 Pa$ for the systemic arteries, $8.0 \times 10^5 Pa$ for the carotid and vertebral arteries and $1.6 \times 10^6 Pa$ for the other arteries because intracranial arteries are stiffer than extracranial ones, in accordance with the reduced thickness of the elastic tissue described in section 1.1. Hassan et al. [54] used $E = 2.7 \times 10^6 Pa$, but they used a fluid structure interaction programmed into a software package called Fidap. It is difficult to model the Young's modulus accurately because the data vary widely between patients.

The compliance constant is defined as:

$$C = \frac{dV}{dp}, \quad (1.27)$$

where V is the volume. Using equation (1.26), the compliance in one artery is given by:

$$C = \frac{3\pi R^3 L}{Eh} \approx \frac{3\pi R_0^3 L}{Eh} \quad (1.28)$$

Alastruey et al. [6] used equation (1.26), but with the second term multiplied by $\frac{R}{R_0}$ to calculate the compliance constant (equation (1.29)), which gives a linear pressure-radius relationship. From experiments, the pressure-radius relationship of arteries is found to be linear, since the Young's modulus is not constant [76].

$$p = p_0 + \frac{\beta}{A_0} \left(\sqrt{A} - \sqrt{A_0} \right), \quad \beta = \frac{4\sqrt{\pi}hE}{3}. \quad (1.29)$$

Alastruey et al. [6] assumed a wall thickness of 25% of the internal radius, so the equation may not be valid because the derivation assumes $\frac{h}{r} \ll 1$.

In contrast to the other studies, Hillen et al. [1, 5] used a linear pressure-area relationship and estimated the compliance constant from the fact that the cross-sectional area of carotid and vertebral arteries at a systolic pressure of 120mmHg is 10% larger than that at a diastolic pressure of 80mmHg [77]. Therefore:

$$A = A_0(1 + \beta(p - p_d)), \quad (1.30)$$

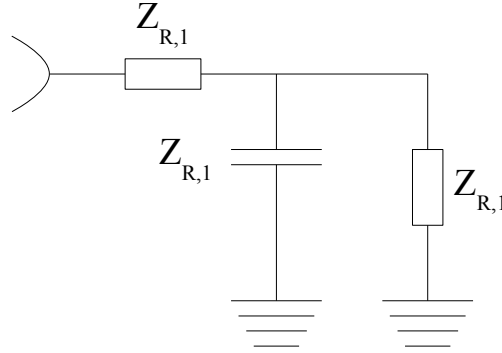


FIGURE 1.23: Resistance-capacitance-resistance model for the vessels beyond the outflow boundaries.

where p_d is the diastolic pressure and β is the compliance constant. Hillen et al. [5] used $\beta = 1.887 \times 10^{-5} \text{m}^2 \text{N}^{-1}$. This does not take into account the different elasticity of different arteries and could be quite inaccurate.

Using a constant peripheral resistance as an outflow boundary condition forces the pressure and velocity to be in phase at the outlet. This is not valid if the arteries lying beyond the simulation domain are large [24]. An alternative approach is to apply a Windkessel model at the outflow boundary. The most commonly used one is a three-element lumped parameter model which represents the resistance and elasticity of the vessels by an electrical model consisting of a resistance in series with a parallel combination of a resistor and a capacitor to simulate arterial compliance (figure 1.23).

The impedance is given by:

$$Z(\omega) = \frac{Z_{R,1} + Z_{R,2} + i\omega Z_C Z_{R,1} Z_{R,2}}{1 + i\omega Z_C Z_{R,2}} \quad (1.31)$$

Substituting

$$V = V_0 \exp i\omega t, I = I_0 \exp i\omega t, \quad (1.32)$$

where I is current and V is voltage, into this, gives the following differential equation [6]

$$V + R_2 Z_C \frac{dV}{dt} = I(Z_{R,1} + Z_{R,2}) + Z_{R,1} Z_{R,2} Z_C \frac{dI}{dt} \quad (1.33)$$

V is analogous to p and I is analogous to Q .

$$p + Z_{R,2}C \frac{dp}{dt} = Q(Z_{R,1} + Z_{R,2}) + Z_{R,1}Z_{R,2}C \frac{dQ}{dt}, \quad (1.34)$$

where Z_c is the peripheral compliance. If the Navier-Stokes equations are solved by methods explicit in time, the equation above cannot be solved directly because it requires knowledge of the flow fields at all times during the current pulsatile period. This has been overcome by using the flow fields from the previous pulsatile period to solve this equation alongside the Navier-Stokes equations and the solution converges within a few pulsatile periods [6, 24].

Alastruey et al. [6] state that the compliance for the whole arterial system is $9.45 \times 10^{-9} m^5 N^{-1}$. In this study, the compliance of the efferent arterial segments were calculated using equation (1.28). Compliances can be combined in the same way as capacitances in an electric circuit, so the peripheral compliances could be worked out from the total compliance. They were distributed in the same proportion as the flow distribution determined by the resistances, i.e. inversely proportional to the resistances, as explained in section 1.5.

A phase difference between the flows in the carotid arteries could be caused by a difference in wave propagation speeds, c_e .

$$c_e = \sqrt{\frac{aEh}{\rho R}}, \quad (1.35)$$

where a is a dimensionless constant, which is 2 [37] or $\frac{4}{3}$ [24]. Using a rough calculation for ideal fluids (fluids without viscosity), a phase difference of 2.25% could arise from differences in the compliance of the arteries, as calculated from a plausible set of parameters [37], for example $E_1 = 2.0 \times 10^6 \text{Pa}$, $E_2 = 1.5 \times 10^6 \text{Pa}$, $L_1 = 21 \text{cm}$, $L_2 = 20 \text{cm}$, $R_1 = R_2 = 0.3 \text{cm}$, $h_1 = 0.03 \text{cm}$, $h_2 = 0.02 \text{cm}$.

Vorp and Geest [78] discuss the mechanism of rupture of abdominal aortic aneurysms (AAA) and how the risk of rupture can be predicted. Rupture occurs when the stress within the arterial wall is greater than the stress that the tissue can withstand. Many experiments have shown that the wall strength decreases as an AAA forms, but the wall stress increases. In particular, *in vivo* measurements have shown that the elastic modulus increases in patients with the AAA. *Ex-vivo* experiments have shown that the mechanical

properties vary spatially. These variations must therefore be taken into account on a patient-specific basis. While equation (1.26) describes the pressure-radius relation for a cylinder, it is inadequate for a complex geometry and tissue constitutive relations must be used if the state of stress in the wall is to be determined accurately. Measurements of the wall thickness, the forces imparted by the fluid and boundary conditions at either side of the wall are required for this purpose.

Vorp and Geest [78] have recently developed a rupture potential index, which compares the stress acting on the wall of an aneurysm to the strength of the wall. In this model, the wall strength was calculated from a statistical model that had been derived by regression on data from many patients. The spatial variation of the wall strength depended on the ratio of the local transverse diameter to the maximum transverse diameter.

Watton et al. [79, 80] have developed models for the growth and stabilisation of aneurysms that take into account the following details of the structure of the arterial wall. The main load-bearing components of the arterial walls are elastin and collagen, but elastin bears most of the load at physiological strains. In unloaded tissue, most of the collagen fibrils are folded and a certain strain, called the recruitment stretch, is required before a fibre, consisting of a population of fibrils, can contribute to load bearing. The elastin fibres do not have this property. They are observed to degrade as an aneurysm grows. However, the collagen fibres are constantly being deposited and degrading and these processes act to change the configuration of the collagen fibres in response to changing physiological conditions. The models assume that new collagen fibres attach to the arterial wall at a constant strain and that the configuration of the fibres changes such that the recruitment strain relaxes towards this attachment strain. They also assume that the density of collagen fibres increases such that the rate of increase is proportional to the difference between the strain and the attachment strain. The constitutive relations for the collagen and elastin were nonlinear.

Watton et al. [80] analysed the deformation of pre-stretched cylindrical and spherical membranes subject to a constant internal pressure. They initially assumed that the stretch of the collagen fibres was equal to the attachment stretch. Equations were derived for the concentrations of collagen fibres when the membranes were in mechanical equilibrium. For the cylindrical and spherical membranes, the concentration must increase by the square and cube of the circumferential strain respectively. The equations were differentiated to find

the rate of change of concentration. It depended on the current fibre concentration, the difference between the collagen fibre stretch and the attachment stretch, the rate of change of fibre stretch, the rate of loss of elastin and the ratio of load borne by the elastinous and collagenous constituents. Upon substitution of an exponential degradation of elastin over time, the equations for the rate of change of collagen and elastin concentration had the same form. The rate of increase of fibre concentration necessary for stabilisation was larger for the spherical membrane.

The assumption about the stretch of the collagen fibres was relaxed and a more general fibre concentration evolution equation was proposed. Numerical analyses of the growth, collagen fibre stretch and collagen fibre concentration was carried out for cylindrical and spherical membranes using simplified fibre concentration equations, namely (1.36) and (1.37), along with a constitutive model for the membranes and a spatially uniform degradation of elastin.

$$\frac{dn_C}{dt} = a_0(\epsilon_{C,u} - \epsilon_{C,AT,u}), \quad (1.36)$$

$$\frac{dn_C}{dt} = \left(a_1 n_C + a_2 \left| \frac{dn_E}{dt} \right| \right) (\epsilon_{C,u} - \epsilon_{C,AT,u}), \quad (1.37)$$

where n is the number density of the fibres, $\epsilon_{C,u}$ and $\epsilon_{C,AT,u}$ are respectively the current and attachment stretches of the collagen fibres in the direction of the fibres, the subscripts C and E denote quantities for the elastin and collagen fibres respectively and a_1 and a_2 are positive constants. Modelling the concentration of the collagen fibres with equation (1.36) did not stabilise the growth of the the spherical or cylindrical vessels, but the growth was stabilised when equation (1.37) was used, provided that $a_1 > 0$. Incorporating sensitivity to the rate of elastin degradation, i.e. setting $a_2 > 0$, improved the stability of the growth.

Watton and Hill [79] simulated the development of an AAA due to an axisymmetric degradation of elastin in the arterial wall by applying the model described three paragraphs previously at each point in space. The pressure inside the artery was constant in time and space. The fractions of the load that were initially borne by the elastic and collagen fibres could be freely chosen. The artery was assumed to be cylindrical, but, in contrast to [80], the rate of degradation of elastin varied along its axis, causing an aneurysm to form in the centre instead of uniform growth of the artery. The rate of growth was approximately proportional to the diameter of the aneurysm for a range of values of the rate constants for the deposition of collagen and the relaxation of its recruitment strain. Increasing the rate

of turnover of collagen fibres increased the rate and nonlinearity of the dilation. Increasing the deposition rate reduced the rate of dilation. Increasing the proportion of load initially borne by the elastin rendered the artery more sensitive to the degradation of elastin and resulted in faster rates of dilation. Aneurysms of realistic dimensions could be developed from these parameters. It was tested slightly more rigorously by comparing the resulting mechanical properties of the wall with experimentally mechanical properties in aneurysms of the same radius.

Ventikos et al. [81, 82] extended the model of aneurysm evolution proposed in [79, 80] by simulating a blood flow through the vessel, and letting the rate of degeneration of the elastin fibres at each point on the wall depend on the wall shear stress (WSS) exerted by the blood. This rate of degeneration was a decreasing function of the wall shear stress (WSS) for WSSs between 0.5Pa and 2.0Pa, which is consistent with the fact that low WSS leads to the death of endothelial cells, as explained in section 1.8. The collagen fibres were assumed to bear 80% of the initial load at systole. Finite-volume and finite-element solvers were used to compute the fluid and wall dynamics respectively. The disparity in the timescales of the haemodynamic period and were tackled by either looking at systolic conditions or appropriate averaging. The aneurysm was represented by an initial outpouching.

At each point on the wall, The degeneration of the elastin due to the low WSS caused the aneurysm to grow in size, which further lowered the WSS. This mimicked the instability and subsequent rupture of aneurysms. There areas of lowest WSS corresponded to the areas where the greatest degeneration of elastin had occurred. The collagen content in the arterial wall increased to compensate for the loss of elastin, which enabled the aneurysm to stabilise. During the simulations in these studies, the elastin strains increased significantly, whereas the collagen strains increased negligibly. In one of these two studies [82], the simulation was started from a cylindrical geometry, but the elastin was originally degenerated in a small region of the outpouching. The elastin was allowed to degenerate in a larger region once this system had reached a steady state, i.e. an outpouching had formed.

Watton et al. [83] modelled the aneurysms in a similar way to [82], except that a second model was constructed for which the degradation of elastin at each point was linked to a high WSS gradient instead of a low WSS. When the degradation of elastin was linked to a low WSS, it degraded progressively until a peak in the WSS distribution developed

within the dome of the aneurysm due to the enlargement of the distal neck, which halted the growth of the aneurysm. When the degradation of elastin was linked to a high WSS gradient, it did not degrade progressively because the WSS was low and relatively uniform within the dome region of the aneurysm. The latter model led to aneurysms that propagated upstream and downstream. Neither model yielded aneurysms with a well defined neck.

The models described in [81-83] can mimic the growth and stabilisation or rupture of aneurysms, so they could be used to evaluate the risk of a haemorrhage. Measurements of aneurysm growth have been compared with the WSS results of haemodynamics simulations [21, 22] and they could be compared with the patient-specific models of this growth by Ventikos et al. [81] to develop their technique further.

Chapter 2

Lattice-Boltzmann methods

CFD simulations of cerebral blood flow have a high computational cost due to the intricate geometry of the vessels. Simulations with a high resolution or with many vessels must run efficiently in parallel if results are to be obtained within a reasonable timescale, which may be a few hours for a scientific study. CFD simulations could be used to help surgeons assess the risks of cerebrovascular disease in patients and the effects of surgical treatments on a patient before they are carried out [84, 85], as explained in section 1.4, in which case the results must be available within a few minutes. However, it is difficult to develop high-performance, scalable codes for continuum solvers [86]. The volumetric mesh required for the simulation is difficult to generate and involves significant human-computer interaction [87]. The lattice-Boltzmann method (LBM) provides an alternative. It is represented by a Boltzmann equation that is discretised in time, space and velocity.

The method is summarised in section 2.1. Its advantages over finite-element and finite-volume fluid solvers are described in section 2.2. Lattice-Boltzmann simulations of blood flow are reviewed in section 2.3 and their future utility for planning neurosurgery is discussed. Section 2.4 explains how the LBM was developed from Lattice Gas Automata. Section 2.5 explains the theory of the LBM in detail. An improvement to the method to simulate incompressible flow more accurately is discussed in section 2.6. Section 2.7 explains how simulation parameters are converted between physical and lattice units. The intrinsic accuracy of the LBM is discussed in section 2.8. Some methods for dealing with boundary conditions and their accuracy are reviewed in section 2.9. Further applications

of the LBM are discussed in section 2.10. Section 2.11 describes how the LBM can be used for simulations of non-Newtonian fluids.

2.1 Summary of the lattice-Boltzmann method

The LBM is represented by a Boltzmann equation that is discretised in time, space and velocity [16, 17]:

$$f_i(\mathbf{x} + \Delta t \mathbf{e}_i, t + \Delta t) - f_i(\mathbf{x}, t) = \chi_i(\mathbf{x}, t), i \in \{0, 1, 2, \dots, N - 1\}, \quad (2.1)$$

where $f_i(\mathbf{x}, t)$ describes the distribution function of the particle density at site \mathbf{x} at time t moving with microscopic velocity \mathbf{e}_i , $\chi_i(\mathbf{x}, t)$ is the collision operator and N is the number of discrete velocities. The density and macroscopic velocity are given by:

$$\sum_i f_i = \rho, \quad (2.2)$$

$$\sum_i f_i \mathbf{e}_i = \rho \mathbf{v}. \quad (2.3)$$

With an appropriate collision operator, the Navier-Stokes equations may be derived.

For all simulations of fluid flow in this thesis, I use the LBM with a Bhatnagar-Gross-Krook (BGK) operator, in which the distributions relax to equilibrium at a single timescale [16].

The lattice-Boltzmann equation (equation (2.1)) becomes [16, 17]:

$$f_i(\mathbf{x} + \Delta t \mathbf{e}_i, t + \Delta t) - f_i(\mathbf{x}, t) = -\frac{1}{\tau}(f_i(\mathbf{x}, t) - f_i^{(eq)}(\rho(\mathbf{x}, t), \mathbf{v}(\mathbf{x}, t))), \quad (2.4)$$

where τ is the dimensionless relaxation time and $f_i^{(eq)}(\rho, \mathbf{v})$ is the local equilibrium distribution function for density ρ and velocity \mathbf{v} . For practical implementation, this equation is divided into two steps: collision, in which the distributions functions are modified according to the right side of equation (2.4), i.e.

$$f_i^+(\mathbf{x}, t) = f_i(\mathbf{x}, t) - \frac{1}{\tau}(f_i(\mathbf{x}, t) - f_i^{(eq)}(\rho(\mathbf{x}, t), \mathbf{v}(\mathbf{x}, t))), \quad (2.5)$$

and streaming, in which the distribution functions are moved to the neighbouring sites, i.e.

$$f_i(\mathbf{x} + \Delta t \mathbf{e}_i, t + \Delta t) = f_i^+(\mathbf{x}, t). \quad (2.6)$$

At boundary sites, i.e. sites adjacent to the wall (edge sites), inlet or outlet, some of the neighbouring sites are solid, so some of the distributions are unknown after streaming. Many boundary condition methods have been devised to determine the distribution functions from the velocity or pressure and they are discussed in section 2.9.

I use the two-dimensional, 9-velocity model, D2Q9, or the three-dimensional 15-velocity model, D3Q15, [17] or their incompressible counterparts, D2Q9i and D3Q15i [88, 89], in all simulations in this thesis. The particle velocities, \mathbf{e}_i are given by Succi [17]. There is some freedom of choice in the equilibrium distribution functions [17]. For the compressible models, they can be chosen as:

$$f_i^{(eq)}(\rho, \mathbf{v}) = w_i \rho \left(1 + 3 \frac{\mathbf{e}_i \cdot \mathbf{v}}{c^2} + \frac{9}{2} \frac{(\mathbf{e}_i \cdot \mathbf{v})^2}{c^4} - \frac{3}{2} \frac{\mathbf{v} \cdot \mathbf{v}}{c^2} \right), \quad (2.7)$$

where the w_i used for the model in this study are given by Succi [17], Qian et al. [16] and Zou et al. [89], and $c = \Delta x / \Delta t$, where Δx is the lattice spacing.

Through a Chapman-Enskog expansion, it can be shown that the macroscopic equations are the incompressible Navier-Stokes equations with error terms as follows [89]:

$$\nabla \cdot \mathbf{v} = 0 + O(\Delta x^2) \quad (2.8)$$

$$\frac{\partial \mathbf{v}}{\partial t} + \mathbf{v} \cdot \nabla \mathbf{v} = -\frac{\nabla P}{\rho_0} + \nu \nabla^2 \mathbf{v} + O(\Delta x^2) + O(Ma^2) + O(Ma^3 \Delta t), \quad (2.9)$$

where $\Delta x = c \Delta t$, Ma is the Mach number and ρ_0 is the actual density of the fluid. The pressure is given by equation (2.10):

$$p = \rho c_s^2, \quad (2.10)$$

where the speed of sound is given by $c_s^2 = \frac{c^2}{3}$ for the D2Q9 and D3Q15 models. The kinematic viscosity is

$$\nu = \frac{c^2}{3} \left(\tau - \frac{1}{2} \right) \Delta t. \quad (2.11)$$

The stress tensor, $\sigma_{\alpha\beta}$, can be calculated directly from the distribution functions as follows [59, 90, 91]:

$$\sigma_{\alpha\beta} = \sum_i f_i^{(neq)} e_{i\alpha} e_{i\beta}, \quad (2.12)$$

The LBM is only valid for low Mach numbers, i.e. $|\mathbf{v}| \ll \Delta x/\Delta t$ due to the error terms in equation (2.9). The LBM also requires the time over which the fluid undergoes a macroscopic change, such as the period, T , in a range of distance L , to be much greater than the time taken by sound to travel that distance, i.e. $T \gg \frac{L}{c_s}$. This is explained in section 2.6.

Using an incompressible model eliminates the compressibility error of order Ma^2 [88, 89]. For this model, the density and macroscopic velocity are calculated by equation (2.13) instead of equations (2.2) and (2.3).

$$\sum_i f_i = \rho, \quad \sum_i f_i \mathbf{e}_i = \rho \mathbf{v}. \quad (2.13)$$

For the equilibrium distribution, the density appears inside the brackets, i.e. equation (2.7) becomes

$$f_i^{(eq)}(\rho, \mathbf{v}) = w_i \left(\rho + 3 \frac{\mathbf{e}_i \cdot \mathbf{v}}{c^2} + \frac{9}{2} \frac{(\mathbf{e}_i \cdot \mathbf{v})^2}{c^4} - \frac{3}{2} \frac{\mathbf{v} \cdot \mathbf{v}}{c^2} \right). \quad (2.14)$$

2.2 Advantages of the lattice-Boltzmann method

Finite-element or finite-volume fluid dynamics solvers have problems in 3D due to the computational costs of mesh generation, the need to solve the auxiliary Poisson equation for the pressure field, and approximations associated with the calculation of shear stress from the velocity field [86, 90]. It is difficult to develop high-performance, scalable parallel codes from continuum solvers. The intricate geometry of the vessels and calculation of boundary conditions at such walls are also very difficult for continuum-based solvers. Developing 3D models with the temporal resolution to address issues of pulsatile flow, phase differences and the effects of treatment is very powerful in understanding neurovascular patho-physiology and treatment [86].

LBM has a number of advantages over finite-element or finite-volume methods for computational fluid dynamics simulations. It is applied on a Cartesian grid of lattice points,

which is simple to generate [87]. It is ideally suited to computation on multicore machines because the distribution functions at each lattice site are calculated using only information from the nearest neighbours [16]. Consequently, numerical codes can be implemented efficiently in parallel [16, 90]. In a parallel implementation, a linear speed-up with number of processors can be achieved. Furthermore, the pressure, p , and the stress tensor, $\sigma_{\alpha\beta}$, can be calculated directly from the distribution functions using equations (2.10) and (2.12).

2.3 LBM simulations of blood flow

Recently, scientists have started to use the LBM to study blood flow through parts of patients' vasculatures [59, 85, 87]. In 2003, Artoli [59] simulated steady and pulsatile blood flow in the aortic bifurcation. Pressure boundary conditions were used at the inlets and outlets with the method by [9], which is described in section 2.9.2. However, this requires the inlets and outlets to be aligned with an axis. The distribution functions at walls that are unknown after streaming are determined by the bounce-back method, described in section 2.9.1. Artoli [59] found the flow was simple at the start of systole, but negative velocities were observed just proximal to the bifurcation later on. The flow then relaxed towards the end of systole. Complex flow occurred in the main aorta during diastole involving vortices and mixing. At all times during the pulsatile cycle, the flow at the outlets was in the forward direction, which demonstrates the function of the aorta as a reservoir. The von Mises stress, which is an invariant of the stress tensor, was calculated at the walls. High stress was found near the outlets, where the arteries are curved. While the accuracy of the steady and unsteady simulations were tested for a 3D cylinder, the flow fields obtained for the aortic bifurcation were not compared with those obtained in other studies.

More recently, both Axner [85] and He et al. [87] compared the flow fields that they obtained in a patient-specific system with a continuum solver and they mostly agreed well. He et al. [87] used vasculatures which included a saccular aneurysm. In one of the models, the jet flowing into the aneurysm impinged on a large area of the wall, so according to Cebal et al. [3], the risk of rupture was low. Axner [85] developed a tool for extracting the vasculature, editing it and computing the flow. An artery with severe

stenosis was simulated with and without a bypass to demonstrate the feasibility of the tool for simulating the effects of surgery.

In the GENIUS (Grid Enabled Neurosurgical Imaging Using Simulation) project [84], a tool called HemeLB has been developed [92, 93] to carry out interactive simulations of patient-specific cerebral blood flow, which is intended for use by clinicians for surgical planning. The configuration of lattice sites, including the identification the sites that are inside and outside of the fluid domain and those adjacent to inlets, outlets and walls, is constructed by using a fast and robust parallel ray-tracing technique with an efficient clustering algorithm [86]. While the simulation is running, images of the flow fields are sent to the user over a dedicated network while the simulation is running [84]. The user can change parameters on the fly to find out how a simulation responds to perturbations, without having to restart the simulation, which would be essential for surgical planning, as well as the ability to obtain the results within a clinically useful timescale.

In order to achieve this, HemeLB runs very efficiently on multicore machines. The fluid solver by itself scales linearly up to 256 and 1024 cores for geometries with 1.6 million and 4.7 million lattice sites respectively [92, 93]. The main reasons for this efficiency are as follows. First, each lattice site only requires information from neighbouring sites for the LBM. Second, buffers are set up for every processor to store information that is sent to or received from neighbouring processors and to store the indices of the send or receive buffers for the relevant lattice sites. Consequently, communication costs are minimised. Third, the domain is partitioned such that each processor deals with exactly the same number of fluid sites plus or minus one. Fourth, it uses a bi-level grid to store the configuration of lattice sites in the grid [86, 92]. This avoids the need to check every lattice site and reduces memory requirements. Axner [85]’s solver scales well up to 128 cores. In 2001, Gropp et al. [94] developed a non-LBM fluid solver that scales linearly up to 700 cores on a system with 2.8 million vertices.

The CrossGrid project aims to support pre-operative planning of vascular surgery in a similar way [95] to the GENIUS project, by allowing storage of the medical imaging data, generation of a computational mesh, simulation of the fluid flow and visualisation of the flow fields to take place in disparate geographical locations. The fluid dynamics are simulated in parallel on a computational grid involving multicore machines in different geographical locations. When this is complete, the results are transferred to a different computing

resource to allow the clinician to visualise the flow fields. The clinician can then assess the effects of surgery on the blood flow by editing the vasculature and running another simulation. For example, in a patient with atherosclerosis, a surgeon may consider placing a bypass to allow blood to flow past an occluded segment of an artery, as described in section 1.3.

Melchionna et al. [96] have also developed a tool for lattice-Boltzmann simulation of cerebral blood flow, including software to reconstruct patient-specific geometries from CT images. The lattice-Boltzmann software is capable of carrying out multi-scale simulations and is described by Bernaschi et al. [97], as discussed in section 2.10. Melchionna et al. [96] demonstrated its use for a simulation of the coronary artery and surrounding vessels, but only steady flow was considered, in contrast to the studies by Mazzeo and Coveney [92], Mazzeo et al. [93] and the majority of those described in section 1.8. The spatial resolution is $20\mu\text{m}$, which is much higher than that used in HemeLB. Therefore, 250×10^6 lattice points were required, which was higher than the numbers used in HemeLB. The resolution was chosen to be that beyond which the flow fields obtained in simulations of Poiseuille flow are no longer sensitive to the resolution. A rich structure was seen in the wall shear stress, particularly at the main bifurcations, although this was not compared with the WSS achieved from any other computational or experimental studies.

The distribution functions at lattice sites adjacent to the walls that are unknown after streaming are determined by the bounce-back method, described in section 2.9.1, due to its simplicity. An equilibrium scheme is used at the inlet and outlet, as described in section 2.9.4 to apply velocity boundary conditions, which contrasts with the majority of 3D CFD simulations of cerebral blood flow described in section 1.8, which use velocity and pressure boundary conditions at the inlets and outlets respectively. The flow rate at each outlet is set to be directly proportional to the area of the outlet such that the sum of the flow rates is equal to the flow rate at the inlet, as in the studies by Tatushima et al. [30] and Cebal et al. [3, 25]. A plug flow profile was used instead of the parabolic flow profile used in the other studies discussed in this thesis, because for the former flow profile, the flow rate is proportional to the area, while for the latter, it is proportional to the square of the area, as shown by equation (1.12). However, it would have been possible for them to use a parabolic profile with the flow rate directly proportional to the area, though it would have resulted in a different pressure distribution along the arteries. HemeLB uses pressure

boundary conditions at the inlets and outlets to the simulation. The method for applying the boundary conditions is described in [93] and section 2.9.6.

The techniques used by Melchionna et al. [96] to minimise the computational cost of simulations on multicore machines are similar to those in HemeLB: buffers are set up to store information that is sent to or received from neighbouring processors, the lattice sites are divided evenly between the processors and it uses an indirect addressing system in order to reduce memory requirements for sparse systems. Their simulations were carried out on graphical processing units. The scalability was only tested on a system with 4×10^6 lattice sites and up to eight processors, but a superlinear speedup was achieved, with 955 million site updates per second achieved with eight GT200 GPUs. HemeLB has achieved 576 million lattice site updates per second for a simulation with 1.6 million lattice sites running on 512 cores of the Ranger supercomputer at the Texas Advanced Computing Center.

2.4 Development from Lattice Gas Automata

In this section, I describe how the lattice-Boltzmann method was derived from lattice gas models. Lattice gas models consist of a regular lattice, with a set of variables $\{N_i\}, i \in \{1, \dots, b\}$ that describe the population of b given velocities, \mathbf{e}_i [16, 17, 98]. Each velocity on each lattice point has a population of either 0 or 1 particles. This had been designed to minimise the amount of memory that simulations needed. The dynamics consists of streaming from node to node according to the velocity \mathbf{e}_i and collision, in which the populations are redistributed as particles collide. This collision must be carried out in a way that conserves mass and momentum. The state of a Lattice point can be described by a vector with the same number of components as the number of velocities. For every possible state s , the probabilities of a transition to state s' are assigned, making sure that mass and momentum are conserved. At every collision, the system moves to state s' with probability $P(s')$. A collision matrix is needed to store the probabilities of each state s' from each state s . The equation for the evolution of the system using this method is [98]:

$$N_i(\mathbf{x} + \mathbf{e}_i, t + 1) = N_i(\mathbf{x}, t) + \chi_i, \quad (2.15)$$

where N_i is the occupation number of a lattice site for velocity i . χ is the collision term.

We have:

$$\chi_i = \sum_{s,s'} (s - s') P(s \rightarrow s') \prod_i N_i^{s_i} (1 - N_i^{s_i})^{1-s_i}, \quad (2.16)$$

where s is a vector describing the state and i is the index to the components. The entire product is 1 when the system is in state s , otherwise it is zero. A simpler way of writing this would be:

$$\chi_i = \sum_{s'} (s - s') P(s \rightarrow s'). \quad (2.17)$$

If f_i is the ensemble average of N_i , the density and momentum can be found by [16, 17, 98]:

$$\rho = \sum_i f_i(\mathbf{r}, t), \quad (2.18)$$

$$\rho \mathbf{v} = \sum_i f_i(\mathbf{r}, t) \mathbf{e}_i. \quad (2.19)$$

It has been shown that the Frisch-Hasslacher-Pomeau (FHP) model, and the face-centred hypercubic (FCHC) satisfy the incompressible Navier-Stokes equations in two and three dimensions respectively [16]. The FHP model is a hexagonal model in which the particles can have only six velocities, so they always propagate towards one of the nearest neighbours of the lattice point. There are no rest particles [17]. The FCHC model is a four-dimensional model with 24 directions. The model is projected onto a 3D geometry to simulate the flow [98]. These models are isotropic, whereas a square lattice with only four directions would not be isotropic, i.e. rotationally invariant, which means that angular momentum would not be conserved [17]. Equations (2.25) and (2.26) show this in more detail. Qian et al. [16] propose a 3-dimensional model with 14 moving directions and one rest particle, as explained in section 2.5. This satisfies isotropy with fewer directions, so it requires 42% less computer memory for simulations.

The main advantages of lattice gas techniques over conventional finite-difference methods for solving the Navier-Stokes equations were the intrinsic stability, easy introduction of boundary conditions and the simplicity of the numerical scheme. The populations of each velocity at each lattice site are calculated depending only on information from the nearest neighbours, so numerical codes can be implemented efficiently in parallel. However, there were several disadvantages. There was a lot of statistical noise, resulting in the need for spatial or time averaging. There was also some coupling of statistical fluctuations.

The Navier-Stokes equations are Galilean invariant. If one measures the acceleration of a point, one is looking at different fluid elements over time. The acceleration will be different in different frames of reference because one will be looking at a different set of fluid elements. The left hand side of equation (1.2), which is shown below, is the instantaneous acceleration of a fluid element when one is moving with the fluid, i.e. it is equal to the acceleration when \mathbf{v} is zero.

$$\rho \left(\frac{\partial \mathbf{v}}{\partial t} + \mathbf{v} \cdot \nabla \mathbf{v} \right) = \nabla \cdot \sigma.$$

This quantity is the same in all frames of reference, since the acceleration of a particular fluid element does not depend on its velocity. The lattice gas automata simulate Navier-Stokes equations, but there is a density dependent factor in the advection term (the second term), so it becomes [16, 98]:

$$\frac{g(\rho)}{\rho_0} \mathbf{v} \cdot \nabla \mathbf{v}. \quad (2.20)$$

It is Galilean variant, and by the equation, the pressure then depends on velocity.

This problem arises because only one particle is allowed in each velocity state on each lattice point. There is a semi-detailed balance of binary collisions, which means that:

$$\sum_s P(s \rightarrow s') = 1. \quad (2.21)$$

It can be shown that the collisions will force the system to approach a local equilibrium described by the Fermi-Dirac distribution [98]:

$$f_i = \frac{1}{1 + \exp(\alpha + \beta \mathbf{e}_i \cdot \mathbf{v})}, \quad (2.22)$$

where α and β are Lagrange multipliers determined by mass and momentum conservation. The particles should instead obey Maxwell-Boltzmann statistics.

Some attempts were made to improve on these disadvantages [16]. Using mean populations of particles instead of the Boolean variables of lattice gases, (i.e. using a population between 0 and 1 instead of 0 or 1 exclusively) reduced the statistical noise, but this required polynomials in the population functions for the collisions and was impractical for all but the simplest cases. An equation that uses mean populations of particles is called

the Lattice-Boltzmann Equation (LBE) (equation (2.1)):

$$f_i(\mathbf{r} + \mathbf{e}_i, t + 1) - f_i(\mathbf{r}, t) = \chi_i(\mathbf{r}, t), \quad (2.23)$$

where f_i is the probability distribution function for particles such that equations (2.2) and (2.3) hold [16, 17]:

$$\begin{aligned} \sum_i f_i &= \rho \\ \sum_i f_i \mathbf{e}_i &= \rho \mathbf{v}, \end{aligned}$$

and χ is the collision function

Another attempt to improve on these disadvantages involved using a simplified collision matrix, whose elements depend only on the angle of interacting particles. This suppressed statistical noise, but the lack of Galilean invariance remained. One more approach was tried, which uses Maxwellian particles, that violate the semi-detailed balance of binary collisions and introduce more populated rest particles. In this model, the collision rules were complicated.

In 1992, Qian et al [16] proposed the Lattice BGK model, which is a combination of the previous approaches, so that continuous distribution functions are used, rest particles were used and the collisions were simplified. The LBE is applied with a Bhatnagar-Gross-Krook (BGK) operator, as explained in section 2.1. With this term equation (2.23) becomes the LBGK equation (equation (2.4)) [16, 17].

$$f_i(\mathbf{r} + \mathbf{e}_i, t + 1) - f_i(\mathbf{r}, t) = -\frac{1}{\tau}(f_i(r, t) - f_i^{(eq)}(r, t)).$$

The equilibrium distribution functions are given by the Maxwellian equilibrium distribution functions. The approach was combined with a three-dimensional model with 14 moving directions, which were the axes and diagonals of a cube, which saved memory compared with the FCHC model. The exact Navier-Stokes equation was obtained, as shown in section 2.5. There was no density-dependent term in the Navier-Stokes equations, partly due to the choice of equilibrium distribution functions, which one is not free to choose with Lattice Gas methods [89]. The method was tested, as described in section 2.8. The only hypothesis necessary to derive the governing equations is that the dynamics of the

system can be decomposed into phenomena that evolve with different time scales, so that one can simulate a wide range of nonlinear partial differential equations by lattice BGK models with a suitable equilibrium distribution function [16].

2.5 Detailed Theory of the lattice-Boltzmann method

In this section, I derive the equilibrium distribution functions for the lattice-Boltzmann method (LBM) given in equation (2.7), then show how the Navier-Stokes equations are derived from the LBM. The LBM is also directly derived from the Boltzmann equation.

The equilibrium distribution functions depend on the lattice used. These functions must be intrinsically isotropic and Galilean invariant [16, 75, 98].

The equilibrium distribution may be found by expanding up to second order in the macroscopic velocity, \mathbf{v} [75]:

$$f_i^{(eq)}(\mathbf{v}) = f_i^{(eq)}(0)(1 + Av_\alpha e_{i\alpha} + Bv_\alpha v_\alpha + Cv_\alpha v_\beta e_{i\alpha} e_{i\beta}), \quad (2.24)$$

where \mathbf{e}_i is the microscopic velocity, which will usually be much greater than the macroscopic velocity.

The isotropy conditions required on the fourth order tensors may be explicitly introduced like this [75, 91]:

$$\sum_i f_i^{(eq)}(0) e_{i\alpha} e_{i\beta} = n_2 \delta_{\alpha\beta} \quad (2.25)$$

$$\text{and } \sum_i f_i^{(eq)}(0) e_{i\alpha} e_{i\beta} e_{i\gamma} e_{i\delta} = n_4 \Delta_{\alpha\beta\gamma\delta}, \quad (2.26)$$

$$\text{where } \Delta_{\alpha\beta\gamma\delta} = \delta_{\alpha\beta} \delta_{\gamma\delta} + \delta_{\alpha\gamma} \delta_{\beta\delta} + \delta_{\alpha\delta} \delta_{\beta\gamma}. \quad (2.27)$$

This cannot be achieved by a square or cubic lattice with only four velocities [17]. The following lattices are linear, square or cubic lattices that are satisfactory. They are denoted DdQb, where d is the number of dimensions and b is the number of lattice velocities [17].

D1Q3 has velocities $+c$, 0 and $-c$, for $i = 0, 1, 2$. D2Q9 has velocities:

$$\begin{aligned} c(0, 0), & & i = 0 \\ c(\pm 1, 0), c(0, \pm 1), & & i = 1, 2, 3, 4 \\ c(1, 1), c(-1, 1), c(-1, -1), c(1, -1), & & i = 5, 6, 7, 8. \end{aligned} \quad (2.28)$$

D3Q15 has velocities:

$$\begin{aligned} c(0, 0, 0) & & i = 0 \\ c(0, 0, \pm 1), c(0, \pm 1, 0), c(\pm 1, 0, 0) & & i = 1, 2, \dots, 6 \\ c(\pm 1, \pm 1, \pm 1) & & i = 7, 8, \dots, 14. \end{aligned} \quad (2.29)$$

D3Q19 has velocities:

$$\begin{aligned} c(0, 0, 0) & & i = 0 \\ c(0, 0, \pm 1), c(0, \pm 1, 0), c(\pm 1, 0, 0) & & i = 1, 2, \dots, 6 \\ c(\pm 1, \pm 1, 0), c(\pm 1, 0, \pm 1), c(0, \pm 1, \pm 1) & & i = 7, 8, \dots, 18. \end{aligned} \quad (2.30)$$

Figure 2.1 shows exactly how the directions are numbered for the D2Q9 and D3Q15 lattices. Qian et al. [16] proposed the D3Q15 model, but their model was unusual because the class I particles had a velocity of $2c$, i.e. they moved two lattice points at each timestep. The FHP model could be called the D2Q6 model.

For all these lattices, the equilibrium distribution functions may be derived by considering Galilean invariance of their 0th, 1st, 2nd and 3rd moments [75, 91], which are given by equations (2.31) to (2.34).

$$M_0(\mathbf{v}) = \sum_i f_i^{(eq)}(\mathbf{v}) \quad (2.31)$$

$$M_1(\mathbf{v}) = \sum_i (v_\gamma - e_{i\gamma}) f_i^{(eq)}(\mathbf{v}) \quad (2.32)$$

$$M_2(\mathbf{v}) = \sum_i (v_\gamma - e_{i\gamma})(v_\delta - e_{i\delta}) f_i^{(eq)}(\mathbf{v}) \quad (2.33)$$

$$M_3(\mathbf{v}) = \sum_i (v_\gamma - e_{i\gamma})(v_\delta - e_{i\delta})(v_\epsilon - e_{i\epsilon}) f_i^{(eq)}(\mathbf{v}) \quad (2.34)$$

If M_j is the j th moment, we require:

$$M_j(\mathbf{v}) = M_j(0), \quad j = 0, 1, 2, 3. \quad (2.35)$$

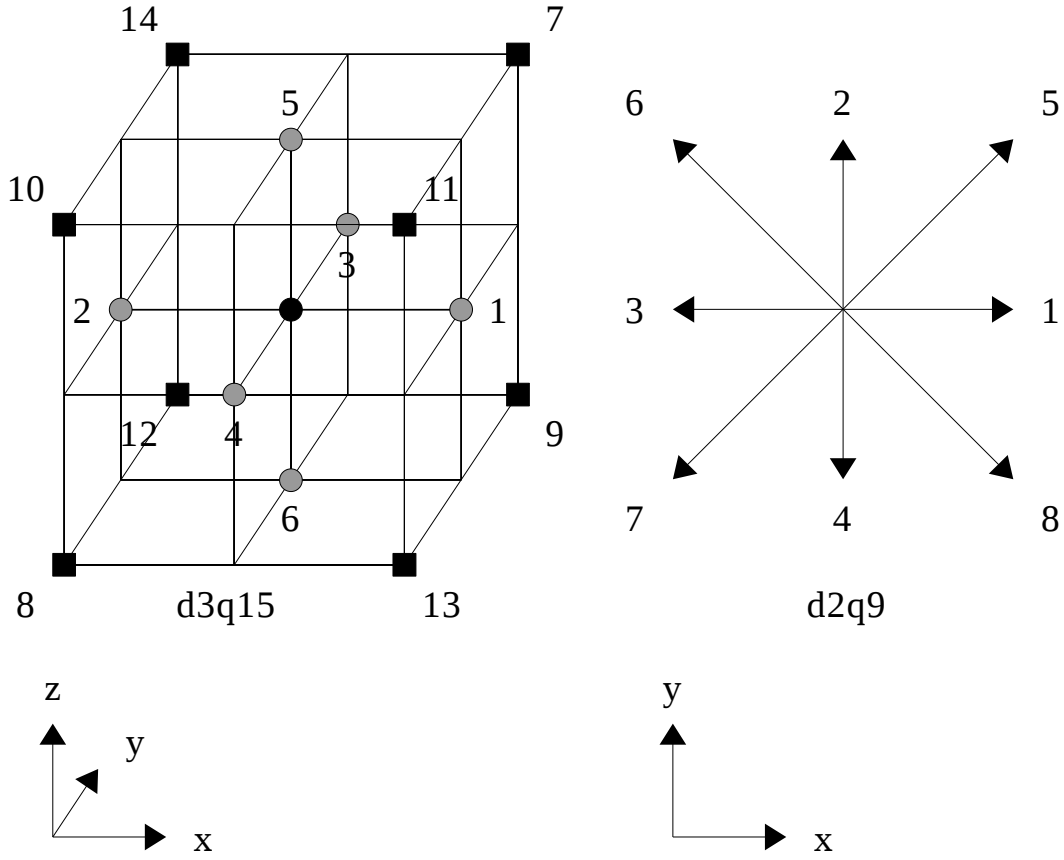


FIGURE 2.1: Lattice velocities for the D2Q9 and D3Q15 models.

This means that the moment is the same for all \mathbf{v} , so it is the same in all frames of reference. The invariance of the first moment implies that equation (2.2) holds in all frames of reference, i.e. mass is conserved and that of the second moment implies that equation (2.3) holds in all frames, i.e. momentum is conserved.

This derivation is given below for the D3Q15 model. Let class j represent particles with j equal to the square modulus of the particle velocities, divided by c^2 . The values of $f_i^{(eq)}(0)$ in equation (2.24) are defined as:

$$\begin{aligned}
 f_i^{(eq)}(0) &= f^0 & i = 0 & & \text{(class 0)} \\
 f_i^{(eq)}(0) &= f^I & i = 1, 2, \dots, 6 & & \text{(class I)} \\
 f_i^{(eq)}(0) &= f^{II} & i = 7, 8, \dots, 14 & & \text{(class II)}.
 \end{aligned}
 \tag{2.36}$$

From the lattice velocities and the isotropy conditions (2.25) and (2.26), we obtain:

$$n_4 = 8w^{II} = w^I c^4, \quad (2.37)$$

$$n_2 = 3w^I c^2. \quad (2.38)$$

$$\sum_{i=0}^{14} f_i^{(eq)}(0) = \rho \text{ (from (2.2))}, \quad (2.39)$$

$$\sum_{i=0}^{14} f_i^{(eq)}(0) e_{i\alpha} = 0, \quad (2.40)$$

$$\sum_{i=0}^{14} f_i^{(eq)}(0) e_{i\alpha} e_{i\beta} = n_2 \delta_{\alpha\beta}, \quad (2.41)$$

$$\sum_{i=0}^{14} f_i^{(eq)}(0) e_{i\alpha} e_{i\beta} e_{i\gamma} = 0, \quad (2.42)$$

$$\sum_{i=0}^{14} f_i^{(eq)}(0) e_{i\alpha} e_{i\beta} e_{i\gamma} e_{i\delta} = n_4 \Delta_{\alpha\beta\gamma\delta}, \quad (2.43)$$

$$\sum_{i=0}^{14} f_i^{(eq)}(0) e_{i\alpha} e_{i\beta} e_{i\gamma} e_{i\delta} e_{i\epsilon} = 0. \quad (2.44)$$

Applying Galilean invariance to the moments of the equilibrium distributions, i.e. applying equations (2.31) to (2.34), then using equations (2.24), (2.27) and (2.39) to (2.44), then equating terms in v , $v^2 \delta_{\gamma\delta}$, $v_\gamma v_\delta$ and terms of order 1, gives equations (2.45) to (2.49):

$$\rho B + n_2 C = 0, \quad (2.45)$$

$$\rho - n_2 A = 0, \quad (2.46)$$

$$\rho - 2n_2 A + 2n_4 C = 0, \quad (2.47)$$

$$B n_2 + C n_4 = 0, \quad (2.48)$$

$$n_2 - A n_4 = 0. \quad (2.49)$$

Solving equations (2.37) to (2.39) and (2.45) to (2.49) gives $A = \frac{3}{c^2}$, $f^I = \frac{\rho}{9}$, $f^{II} = \frac{\rho}{72}$, $f^0 = \frac{2\rho}{9}$, $C = \frac{9}{2c^4}$ and $B = -\frac{3}{2c^2}$. We also have:

$$n_2 = \frac{\rho c^2}{3}, \quad (2.50)$$

$$n_4 = \frac{\rho c^4}{9}. \quad (2.51)$$

We therefore have the following equilibrium distribution [16, 17, 75]:

$$f_i^{(eq)}(v) = w_i \rho \left(1 + 3 \frac{v_\alpha e_{i\alpha}}{c^2} - \frac{3v_\alpha v_\alpha}{2c^2} + \frac{9v_\alpha v_\beta e_{i\alpha} e_{i\beta}}{2c^4} \right), \quad (2.52)$$

where w^0, w^I, w^{II} and w^{III} represent the weights w_i for classes 0, 1, 2 and 3 respectively, where the class is the square modulus of the particle velocity. The weights for this model and the D1Q3, D2Q9 and D3Q19 models are given in table 2.1.

Model	w^0	w^I	w^{II}	w^{III}
D1Q3	2/3	1/6	0	0
D2Q9	4/9	1/9	1/36	0
D3Q15	2/9	1/9	0	1/72
D3Q19	1/3	1/18	1/36	0

TABLE 2.1: Coefficients for the equilibrium distribution functions of various lattice-Boltzmann models [16–18].

On the other hand, Kandhai et al. [18] say that the equilibrium distribution can be chosen in many ways, which seems to contradict the requirements discussed earlier in the section. The distribution stated in equation (2.52) is a common choice. Zou and He use the following distribution [9]:

$$\begin{aligned} f_i^{(eq)}(\mathbf{v}) &= w_i \rho \left(1 - \frac{8}{3} \frac{v^2}{c^2} \right), & i = 0 \\ f_i^{(eq)}(\mathbf{v}) &= w_i \rho \left(1 + \frac{8}{3} \frac{e_{i\alpha} v_\alpha}{c^2} + 4 \frac{e_{i\alpha} e_{i\beta} v_\alpha v_\beta}{c^4} - \frac{4}{3} \frac{v^2}{c^2} \right), & i \neq 0 \end{aligned} \quad (2.53)$$

with $w^0 = \frac{\rho}{8}, w^I = \frac{\rho}{8}, w^{II} = \frac{\rho}{64}$. The isotropy conditions (2.25) and (2.26) hold for this distribution and the zeroth, first and second moments are Galilean invariant, but the third moment is not, as shown here. From the lattice velocities, we obtain equations (2.39) to (2.43) again, but we have $n_2 = \frac{3}{8} \rho c^2$ and $n_4 = \frac{1}{8} \rho c^4$, instead of equations (2.50) and (2.51).

The third moment of the equilibrium distribution is:

$$\begin{aligned} M_3(\mathbf{v}) &= \sum_{i=0}^{14} f_i^{(eq)}(0) \left(1 + \frac{8}{3} \frac{e_{i\alpha} v_\alpha}{c^2} + 4 \frac{e_{i\alpha} e_{i\beta} v_\alpha v_\beta}{c^4} - \frac{4}{3} \frac{v_\alpha v_\alpha}{c^2} \right) (v_\gamma - e_{i\gamma})(v_\delta - e_{i\delta})(v_\epsilon - e_{i\epsilon}) \\ &\quad - \frac{4}{3} f^0 \left(\frac{v^2}{c^2} \right) \end{aligned} \quad (2.54)$$

$$\begin{aligned}
&= \rho v_\gamma v_\delta v_\epsilon + \frac{3}{8} \rho c^2 (v_\gamma \delta_{\delta\epsilon} + v_\delta \delta_{\gamma\epsilon} + v_\epsilon \delta_{\gamma\delta}) \\
&\quad - \frac{1}{3} \rho c^2 v_\alpha (\delta_{\alpha\gamma} \delta_{\delta\epsilon} + \delta_{\alpha\delta} \delta_{\gamma\epsilon} + \delta_{\alpha\epsilon} \delta_{\gamma\delta}) - \rho v_\alpha (v_\gamma v_\delta \delta_{\alpha\epsilon} + v_\gamma v_\epsilon \delta_{\alpha\delta} + v_\delta v_\epsilon \delta_{\alpha\gamma}) \\
&\quad + \frac{1}{2} \rho v_\alpha v_\beta (v_\gamma (\delta_{\alpha\beta} \delta_{\delta\epsilon} + \delta_{\alpha\delta} \delta_{\beta\epsilon} + \delta_{\alpha\epsilon} \delta_{\beta\delta}) + v_\delta (\delta_{\alpha\beta} \delta_{\gamma\epsilon} + \delta_{\alpha\gamma} \delta_{\beta\epsilon} + \delta_{\alpha\epsilon} \delta_{\beta\gamma}) \\
&\quad + v_\epsilon (\delta_{\alpha\beta} \delta_{\gamma\delta} + \delta_{\alpha\gamma} \delta_{\beta\delta} + \delta_{\alpha\delta} \delta_{\beta\gamma})) \\
&\quad + \frac{3}{2} \frac{\rho}{c^2} v_\alpha v_\beta v_\gamma v_\delta v_\epsilon \delta_{\alpha\beta} - \frac{1}{2} v^2 \rho (v_\gamma \delta_{\delta\epsilon} + v_\delta \delta_{\gamma\epsilon} + v_\epsilon \delta_{\gamma\delta}) - \frac{3}{2} \left(\frac{\rho}{c^2}\right) v^2 v_\gamma v_\delta v_\epsilon, \\
&\quad \Rightarrow M_3(0) = 0.
\end{aligned} \tag{2.55}$$

Therefore, it may not be sensible to use the distribution given in equation (2.53), even though the LBM still gives rise to the Navier Stokes equations when this distribution is used.

I now show how the Navier-Stokes equations are derived from the LBM using the D3Q15 model. From equations (2.2) and (2.3) and from the fact that the zeroth and first moments are Galilean invariant, we have:

$$\sum_i f_i^{(eq)}(\mathbf{v}) = \rho, \tag{2.57}$$

$$\sum_i f_i^{(eq)}(\mathbf{v}) e_{i\alpha} = \rho v_\alpha. \tag{2.58}$$

Using equations (2.39) to (2.44), (2.50) and (2.51) and replacing α and β in equation (2.52) with δ and ϵ respectively, we have:

$$\sum_{i=0}^{i=15} f_i^{(eq)}(\mathbf{v}) e_{i\alpha} e_{i\beta} = \frac{\rho c^2}{3} \delta_{\alpha\beta} + \rho v_\alpha v_\beta. \tag{2.59}$$

$$\sum_{i=0}^{i=15} f_i^{(eq)}(\mathbf{v}) e_{i\alpha} e_{i\beta} e_{i\gamma} = \frac{3}{c^2} n^4 v_\delta (\delta_{\delta\alpha} \delta_{\beta\gamma} + \delta_{\delta\beta} \delta_{\alpha\gamma} + \delta_{\delta\gamma} \delta_{\alpha\beta}). \tag{2.60}$$

$$\Rightarrow \sum_{i=0}^{i=15} f_i^{(eq)}(\mathbf{v}) e_{i\alpha} e_{i\beta} e_{i\gamma} = \frac{\rho c^2}{3} (v_\alpha \delta_{\beta\gamma} + v_\beta \delta_{\alpha\gamma} + v_\gamma \delta_{\alpha\beta}). \tag{2.61}$$

The LBGK equation (2.4) is:

$$f_i(\mathbf{r} + \Delta t \mathbf{e}_i, t + \Delta t) - f_i(\mathbf{r}, t) = -\frac{1}{\tau} (f_i(r, t) - f_i^{(eq)}(r, t)),$$

where τ is the relaxation time divided by Δt . We must Taylor expand it:

$$\begin{aligned} & f_i(\mathbf{r} + \mathbf{e}_i \Delta t, t + \Delta t) - f_i(\mathbf{r}, t) \\ & \approx \left[\Delta t \partial_t + \Delta t e_{i\alpha} \partial_\alpha + \frac{(\Delta t)^2}{2} e_{i\alpha} \partial_\alpha (e_{i\beta} \partial_\beta + \partial_t) + \frac{(\Delta t)^2}{2} \partial_t (e_{i\alpha} \partial_\alpha + \partial_t) \right] f_i(\mathbf{r}, t). \end{aligned} \quad (2.62)$$

Fluid dynamics emerges from a perturbative treatment of the kinetic equations. The perturbation parameter is the Knudsen number, namely the ratio between the molecular mean free path and the shortest scale at which macroscopic variations can be appreciated:

$$\epsilon = \frac{L_{mfp}}{L_M}. \quad (2.63)$$

The Chapman-Enskog procedure is an expansion in the smallness parameter, ϵ of both dependent variables, such as $f(\mathbf{r}, \mathbf{v}, t)$ and independent variables, such as \mathbf{r} and t . The idea is to represent space time variables on a hierarchy of slow or fast scales such that each variable is $O(1)$ at its own scale [17]. In fluid flow, we have the processes of advection and diffusion. Advection along length L_M takes time:

$$t = \frac{L_M}{L_{mfp}} t_{coll}, \quad (2.64)$$

where t_{coll} is the time between collisions. Diffusion along the same length takes much longer:

$$t = \left(\frac{L_M}{L_{mfp}} \right)^2 t_{coll} = \epsilon^{-2} t_{coll}. \quad (2.65)$$

Both these processes happen over a distance:

$$x = \epsilon^{-1} L_{mfp}. \quad (2.66)$$

If x_1 is the ratio of a spatial coordinate to L_M , and t_1 and t_2 are the ratios of a temporal coordinate to the times required for advection and diffusion respectively over a distance L_M , the spatial and temporal derivatives of a function describing a process involving advection and diffusion are as follows:

$$\partial_t = \epsilon \partial_{1t} + \epsilon^2 \partial_{2t}, \quad (2.67)$$

$$\partial_{\mathbf{r}} = \epsilon \partial_{1\mathbf{r}}. \quad (2.68)$$

We can expand the distribution functions like this, where superscript *eq* denotes local equilibrium and superscripts 1 and 2 are departures from local equilibrium:

$$f_i = f_i^{(eq)} + \epsilon f_i^{(1)} + \epsilon^2 f_i^{(2)}. \quad (2.69)$$

Therefore, equations (2.57) and (2.58) imply:

$$\sum_{i=0}^{15} f_i^{(a)} = \sum_{i=0}^{15} f_i^{(a)} e_{i\alpha} = 0 \text{ for } a = 1, 2. \quad (2.70)$$

Substituting equations (2.67), (2.68) and (2.69) into (2.62) gives:

$$\begin{aligned} & \left\{ \Delta t (\epsilon \partial_{1t} + \epsilon^2 \partial_{2t}) + \Delta t e_{i\alpha} \epsilon \partial_{1\alpha} + \frac{(\Delta t)^2}{2} e_{i\alpha} \epsilon \partial_{1\alpha} [e_{i\beta} \epsilon \partial_{1\beta} + (\epsilon \partial_{1t} + \epsilon^2 \partial_{2t})] \right. \\ & \left. + \frac{(\Delta t)^2}{2} (\epsilon \partial_{1t} + \epsilon^2 \partial_{2t}) [e_{i\alpha} \epsilon \partial_{1\alpha} + (\epsilon \partial_{1t} + \epsilon^2 \partial_{2t})] \right\} \\ & \times \left(f_i^{(eq)} + \epsilon f_i^{(1)} + \epsilon^2 f_i^{(2)} \right) = -\frac{1}{\tau} (f_i^{(eq)} + \epsilon f_i^{(1)} + \epsilon^2 f_i^{(2)} - f_i^{(eq)}). \end{aligned} \quad (2.71)$$

The notation $\partial_{1\mathbf{r}} = \partial_{1\alpha}$ has been used. To first order in ϵ , equation (2.71) is:

$$\Delta t \partial_{1t} f_i^{(eq)} + \Delta t \partial_{1\alpha} e_{i\alpha} f_i^{(eq)} = -\frac{1}{\tau} f_i^{(1)}. \quad (2.72)$$

Summing equation (2.72) over all *i*, using equations (2.58) and (2.59) gives:

$$\Delta t \partial_{1t} \sum_{i=0}^{15} f_i^{(eq)} + \Delta t \partial_{1\alpha} \sum_{i=0}^{15} e_{i\alpha} f_i^{(eq)} e_{i\alpha} = -\frac{1}{\tau} \sum_{i=0}^{15} f_i^{(1)}. \quad (2.73)$$

$$\Rightarrow \partial_{1t} \rho + \partial_{1\alpha} \rho v_\alpha = 0. \quad (2.74)$$

Multiplying equation (2.72) by $e_{i\beta}$ we get:

$$\Delta t \partial_{1t} e_{i\beta} f_i^{(eq)} + \Delta t \partial_{1\alpha} e_{i\alpha} e_{i\beta} f_i^{(eq)} = -\frac{1}{\tau} f_i^{(1)} e_{i\beta}. \quad (2.75)$$

Summing this in the same way as 2.72, using equations (2.58), (2.59) and (2.70), then dividing by Δt gives:

$$\partial_{1t} \rho v_\beta + \partial_{1\alpha} \rho v_\alpha v_\beta + \partial_{1\alpha} \left(\frac{\rho c^2}{3} \delta_{\alpha\beta} \right) = 0. \quad (2.76)$$

To second order in ϵ we get:

$$\begin{aligned} & \Delta t \partial_{2t} f_i^{(eq)} + \Delta t \partial_{1t} f_i^{(1)} + \Delta t \partial_{1\alpha} e_{i\alpha} f_i^{(1)} + \frac{(\Delta t)^2}{2} \partial_{1t} (\partial_{1t} f_i^{(eq)} + \partial_{1\alpha} e_{i\alpha} f_i^{(eq)}) \\ & + \frac{(\Delta t)^2}{2} \partial_{1\alpha} (\partial_{1t} e_{i\alpha} f_i^{(eq)} + \partial_{1\beta} e_{i\beta} e_{i\alpha} f_i^{(eq)}) = -\frac{1}{\tau} f_i^{(2)}. \end{aligned} \quad (2.77)$$

Summing equation (2.77) over i , terms two and three on the left side and the term on the right side are zero from equation (2.70). Terms four and five sum to give the left hand sides of equations (2.74) and (2.76). The right hand sides of the equations are zero, so these terms sum to zero. This leaves:

$$\partial_{2t} \rho = 0. \quad (2.78)$$

Multiplying equation (2.77) by $e_{i\gamma}$ and summing over i gives:

$$\begin{aligned} & \sum_{i=0}^{15} \left[\Delta t \partial_{2t} e_{i\gamma} f_i^{(eq)} + \Delta t \partial_{1t} e_{i\gamma} f_i^{(1)} + \Delta t \partial_{1\alpha} e_{i\gamma} e_{i\alpha} f_i^{(1)} \right. \\ & \left. + \frac{(\Delta t)^2}{2} \partial_{1t} (\partial_{1t} e_{i\gamma} f_i^{(eq)} + \partial_{1\alpha} e_{i\gamma} e_{i\alpha} f_i^{(eq)}) + \frac{(\Delta t)^2}{2} \partial_{1\alpha} (\partial_{1t} e_{i\alpha} e_{i\gamma} f_i^{(eq)} + \partial_{1\beta} e_{i\gamma} e_{i\beta} e_{i\alpha} f_i^{(eq)}) \right] \\ & = -\frac{1}{\tau} f_i^{(2)} e_{i\gamma}. \end{aligned} \quad (2.79)$$

The second term and right hand side are zero by equation (2.70). The fourth term is zero by equation (2.76). Using equations (2.59) and (2.60), the fifth term is:

$$\begin{aligned} & \frac{(\Delta t)^2}{2} \partial_{1\alpha} \partial_{1t} \left(\frac{\rho c^2}{3} \delta_{\alpha\gamma} + \rho v_\alpha v_\gamma \right) + \\ & \frac{(\Delta t)^2}{2} \partial_{1\alpha} \partial_{1\beta} \left(\frac{\rho c^2}{3} (v_\gamma \delta_{\beta\alpha} + v_\beta \delta_{\gamma\alpha} + v_\alpha \delta_{\gamma\beta}) \right). \end{aligned} \quad (2.80)$$

Considering equation (2.72) multiplied by $\Delta t \partial_{1\beta} e_{i\beta} e_{i\gamma}$ and summed over i , then swapping α and β :

$$\begin{aligned} & \Delta t \partial_{1\alpha} \sum_{i=0}^{15} f_i^{(1)} e_{i\alpha} e_{i\gamma} = -\tau (\Delta t)^2 \times \\ & \left\{ \partial_{1t} \partial_{1\alpha} \left(\frac{\rho c^2}{3} \delta_{\alpha\gamma} + \rho v_\alpha v_\gamma \right) + \partial_{1\alpha} \partial_{1\beta} \left(\frac{\rho c^2}{3} (v_\alpha \delta_{\beta\gamma} + v_\beta \delta_{\alpha\gamma} + v_\gamma \delta_{\alpha\beta}) \right) \right\}. \end{aligned} \quad (2.81)$$

Adding equations (2.80) and (2.81) gives the following to order v :

$$\left\{ \frac{1}{2} - \tau \right\} \times (\Delta t)^2 \left\{ \frac{c^2}{3} \partial_{1t} \partial_{1\alpha} \rho \delta_{\alpha\gamma} + \frac{c^2}{3} \partial_{1\alpha} \partial_{1\beta} \rho (v_\alpha \delta_{\beta\gamma} + v_\beta \delta_{\alpha\gamma} + v_\gamma \delta_{\alpha\beta}) \right\}. \quad (2.82)$$

Using equation (2.74) to convert time derivatives into spatial derivatives:

$$\left\{ \frac{1}{2} - \tau \right\} \times \left\{ -\frac{c^2}{3} \partial_{1\gamma} \partial_{1\alpha} \rho v_\alpha + \frac{c^2}{3} \partial_{1\alpha} \partial_{1\gamma} \rho v_\alpha + \frac{c^2}{3} \partial_{1\beta} \partial_{1\gamma} \rho v_\beta + \frac{c^2}{3} \partial_{1\alpha} \partial_{1\alpha} \rho v_\gamma \right\}. \quad (2.83)$$

Substituting this expression for the third minus the fifth term into equation (2.79) and using equation (2.58) for the first, then dividing by Δt gives:

$$\partial_{2t} \rho v_\gamma = \nu \partial_{1\alpha} \partial_{1\alpha} \rho v_\gamma + \zeta \partial_{1\gamma} \partial_{1\alpha} \rho v_\alpha, \quad (2.84)$$

where ν is the kinematic shear viscosity and ζ is the kinematic bulk viscosity, which are both the same in this case. We have [16, 91]:

$$\nu = \zeta = \frac{c^2}{3} \left(\tau - \frac{1}{2} \right) \Delta t. \quad (2.85)$$

Adding $\epsilon(2.74)$ to $\epsilon^2(2.78)$, then recombining the derivatives gives us the continuity equation:

$$\partial_t \rho + \partial_\alpha \rho v_\alpha = 0. \quad (2.86)$$

Adding $\epsilon(2.76)$ to $\epsilon^2(2.84)$, swapping some suffixes, then recombining the derivatives gives us the other Navier-Stokes equation:

$$\partial_t \rho v_\alpha + \partial_\beta \rho v_\beta v_\alpha = -\partial_\alpha \left(\frac{\rho c^2}{3} \right) + \nu \partial_\beta \partial_\beta \rho v_\alpha + \zeta \partial_\alpha \partial_\beta \rho v_\beta. \quad (2.87)$$

The neglected term resulting from only finding equation (2.82) to order v was $-\epsilon^2 \nu \partial_{1t} \partial_{1\alpha} \rho v_\beta v_\gamma$.

This term can be converted to the following spatial derivative:

$$-\epsilon^2 \nu \partial_{1\alpha} \partial_{1\beta} \rho v_\alpha v_\beta v_\gamma. \quad (2.88)$$

The equations have been derived up to second order in the Knudsen number, so in both of them, there will be an error of order ϵ^3 .

The lattice-Boltzmann method gives the compressible Navier-Stokes equations with an ideal gas equation of state, i.e.

$$p = \rho c_s^2, \quad (2.89)$$

where p is the pressure and c_s is the speed of sound. For an ideal gas, this only holds if c_s is the isothermal sound speed. Here, we had:

$$c_s^2 = \frac{c^2}{3}, \quad (2.90)$$

where c is the speed of lattice particles moving horizontally or vertically. Only the gradient of pressure features in the Navier-Stokes equations, so the lattice-Boltzmann method will model a fluid with an equation of state given by:

$$p = p_0 + c_s^2(\rho - \rho_0). \quad (2.91)$$

The same results would be achieved for the equilibrium distribution functions, sound speed and Navier-Stokes equations for the D1Q3, D2Q9 and D3Q19 models [17, 75].

From equation (2.85), the relaxation parameter, τ , must be greater than 0.5 for the viscosity to be positive. If it is not, the LBGK equation will be unstable. The requirement is the same as that of the relaxation method. If the parameter is too low, the RHS of equation (2.4) may become large, so the distribution functions, which represent particle densities could become negative [16] at the next timestep. Applying the equation repeatedly would cause them to become more and more negative, i.e. unstable. Instability can also occur in the same way if the Mach number is high and τ is greater than, but close to 0.5. The region of parameter space for which LBM simulations are stable is strongly dependent on the choice of boundary conditions [59]. The equilibrium distribution functions were expanded up to second order in velocity, so it can be shown that the maximum Mach number for stable simulations is $\sqrt{2}$ for one dimension and $\sqrt{5/2}$ for two or three dimensions.

2.5.1 Derivation of the lattice-Boltzmann equation from the Boltzmann equation

He and Luo [99] derive the lattice-Boltzmann equation, including the equilibrium distribution functions, directly from the Boltzmann equation. They begin by using the Bhatnagar-Gross-Krook approximation with the Boltzmann equation, so that it reads

$$\frac{Df}{Dt} = \frac{1}{\tau'}(f(\mathbf{r}, \mathbf{e}, t) - g(\rho, \mathbf{e}, \mathbf{v})), \quad (2.92)$$

where $\frac{D}{Dt} = \frac{\partial}{\partial t} + \mathbf{v} \cdot \nabla$ is the convective derivative, \mathbf{e} is the velocity of a particle, \mathbf{v} is the macroscopic velocity, f is the single-particle distribution function, τ' is the relaxation time and g is the Maxwell-Boltzmann distribution function given by

$$g = \frac{\rho}{(2\pi R\theta)^{N_D/2}} \exp\left[-\frac{(\mathbf{e} - \mathbf{v})^2}{2R\theta}\right], \quad (2.93)$$

where N_D is the number of dimensions, R is the ideal gas constant and θ is the temperature. Equation (2.92) can be formally integrated over a time interval Δt :

$$f(\mathbf{x} + \mathbf{e}\Delta t, \mathbf{e}, t + \Delta t) - f(\mathbf{x}, \mathbf{e}, t) = \frac{1}{\tau'} e^{-\Delta t/\tau'} \times \int_0^{\Delta t} e^{t'/\tau'} (f - g)(\mathbf{r} + \mathbf{e}t', \mathbf{e}, t + t') dt'. \quad (2.94)$$

Taylor expanding the right hand side and neglecting terms of order Δt^2 or smaller, we obtain:

$$f(\mathbf{r} + \mathbf{e}\Delta t, \mathbf{e}, t + \Delta t) - f(\mathbf{r}, \mathbf{e}, t) = -\frac{1}{\tau} [f(\mathbf{r}, \mathbf{e}, t) - g(\mathbf{r}, \mathbf{e}, t)], \quad (2.95)$$

where $\tau = \frac{\tau'}{\Delta t}$ is the dimensionless relaxation time.

The equilibrium distributions for the lattice-Boltzmann method (LBM) can be derived as follows. The distribution function g is first expanded as a Taylor series in \mathbf{v} up to the \mathbf{v}^2 term:

$$g = \frac{\rho}{(2\pi R\theta)^{N_D/2}} \exp\left(-\frac{\mathbf{e}^2}{2R\theta}\right) \left[1 + \frac{\mathbf{e} \cdot \mathbf{v}}{R\theta} + \frac{(\mathbf{e} \cdot \mathbf{v})^2}{2(R\theta)^2} - \frac{\mathbf{v}^2}{2R\theta}\right]. \quad (2.96)$$

The moment integral, $\mathbf{e}^m f^{(eq)} d\mathbf{e}$, is required to derive the Navier-Stokes equation, where m is an integer such that $0 \leq m \leq 3$ for isothermal models and $0 \leq m \leq 4$ otherwise. This integral contains the following:

$$I = \int \exp\left(-\frac{\mathbf{e}^2}{2R\theta}\right) h(\mathbf{e}) d\mathbf{e}. \quad (2.97)$$

The integral I can be evaluated by Gaussian quadrature in two or three dimensions. Gaussian quadrature is the approximation of the definite integral of a function $f(x)$ as a weighted sum of the values of f at a number of different points x_i in the integration domain, which are called abscissas. That is, $\int_a^b f(x) dx = \sum_{i=1}^n w_i f(x_i)$. The approximation is exact if $f(x)$ is a polynomial of order $2n - 1$ or less. It is accurate provided that $f(x)$ is well approximate by such a polynomial between $x = a$ and $x = b$. Therefore, the integral I

can be expressed as

$$\sum_i W_i \exp\left(-\frac{\mathbf{e}_i}{2R\theta}\right) h(\mathbf{e}_i), \quad (2.98)$$

where $h(\mathbf{e})$ is a polynomial and W_i and \mathbf{e}_i are the weights and abscissas (or discrete velocities) of the quadrature.

The equilibrium distributions for the D2Q9 model are derived here as an example of this quadrature. Splitting the exponential in the integral I in equation (2.97) gives

$$I = 2R\theta \int \int \exp(-e_x'^2) \exp(-e_y'^2) h(\mathbf{e}'\sqrt{2R\theta}) de'_x de'_y, \quad (2.99)$$

where the substitution

$$e'_x = \frac{e_x}{\sqrt{2R\theta}}, \quad e'_y = \frac{e_y}{\sqrt{2R\theta}}, \quad (2.100)$$

has been used. The integral of $h(x) \exp(x^2)$ is evaluated as follows:

$$\begin{aligned} \int_{-\infty}^{\infty} h(x) \exp(x^2) dx &= \sum_{i=1}^n w_i h(x_i), \\ w_i &= \frac{2^{n-1} n! \sqrt{\pi}}{n^2 |H_{n-1}(x_i)|^2}, \end{aligned} \quad (2.101)$$

where H_n is the n th Hermite polynomial. For the D2Q9 model, $n = 3$ is a suitable choice. Therefore the polynomial $H_2(x) = 4x^2 - 2$ is required to calculate the weights, w_i , from the abscissas x_i in equation (2.101). The three weights and abscissas for the integral (2.101) are:

$$\begin{aligned} x_1 = -\frac{\sqrt{3}}{2}, \quad x_2 = 0, \quad x_3 = \frac{\sqrt{3}}{2}, \\ w_1 = \frac{\sqrt{\pi}}{6}, \quad w_2 = \frac{2\sqrt{\pi}}{3}, \quad w_3 = \frac{\sqrt{\pi}}{6} \end{aligned} \quad (2.102)$$

Substituting this into equation (2.101) for the nine possible combinations of e'_x and e'_y gives

$$I = 2R\theta \left[w_2^2 h(\mathbf{0}) + \sum_{i=1}^4 w_1 w_2 h(\mathbf{e}_i) + \sum_{i=5}^8 w_2^2 h(\mathbf{e}_i) \right], \quad (2.103)$$

where $e_i = \mathbf{0}$ for $i = 0$, $\sqrt{3R\theta}(\pm 1, 0)$ and $\sqrt{3R\theta}(0, \pm 1)$ for $i = 1, 2, 3, 4$ and $\sqrt{3R\theta}(\pm 1, \pm 1)$ for $i = 5, 6, 7, 8$ and we have used $\mathbf{e}_i = \sqrt{2R\theta} \mathbf{e}'_i$ from equation (2.100) to calculate the values of \mathbf{e}_i from the abscissas e'_i given in equation (2.102). The polynomial $h(\mathbf{e}_i)$ contains the terms $e_{ix}^m e_{iy}^n$, where m and n are integers. The quadrature above is exact for $m + n \leq 5$.

The weights W_i in equation (2.98) are identified by comparing it with equation (2.103):

$$W_i = 2\pi R\theta \exp\left(\frac{e_i^2}{2R\theta}\right) w_i \quad (2.104)$$

with

$$w_i = \begin{cases} 4/9, & i = 0 \\ 1/9, & i = 1, 2, 3, 4 \\ 1/36, & i = 5, 6, 7, 8 \end{cases} \quad (2.105)$$

The equilibrium distribution for the D2Q9 model is $f_i^{(eq)} = W_i f^{(eq)}(\mathbf{r}, e_i, t)$. Therefore, from equation (2.96), we obtain equation (2.52) with the weights given in table 2.1.

To obtain the nine-direction model, configuration space is discretised into a square lattice with spacing $\Delta x = \sqrt{3R\theta}\Delta t = c\Delta t$. The isothermal speed of sound is $c_s = \sqrt{R\theta}$, therefore $c_s^2 = \frac{c^2}{3}$.

In this derivation, the discretisation of momentum is determined by the spatial discretisation. However, it is possible to choose the discretisations independently, which allows an arbitrary mesh to be used. In this case, a local LBE is built at each point and collision is carried out as usual. However, each distribution function at a mesh grid point no longer goes to another grid point through the streaming process, so interpolation is used to construct the distribution functions after streaming. They demonstrate the accuracy of this simulation method by comparing its results for a backward facing step with those from a normal lattice-Boltzmann (LB) simulation. One can also raise the Reynolds number without adjusting τ or the maximum velocity by using a finer mesh than the one normally used for the usual LBM.

2.6 Incompressible models

In this section, I explain how compressibility errors arise in LB simulations and how the accuracy can be improved by using the incompressible model developed by Zou et al. [89]. The LBM as it stands never solves the continuity equation exactly because one must determine the pressure through an equation of state. The density has to vary in space for the pressure to vary [90].

Substituting equation (2.86) into (2.87) and using the fact that the shear and bulk viscosities are equal for the LBM with a BGK collision operator, i.e. $\nu = \zeta$, as described in section 2.5, we obtain the following equation:

$$\begin{aligned} & \rho(\partial_t v_\alpha + v_\beta \partial_\beta v_\alpha) + v_\alpha(\partial_t \rho + \partial_\beta(\rho v_\beta)) \\ &= -\partial_\alpha \left(\frac{\rho c_s^2}{3} \right) + \nu \partial_\beta (\partial_\beta \rho v_\alpha + \partial_\alpha \rho v_\beta). \end{aligned} \quad (2.106)$$

Since the second term on the left hand side of this equation is 0 from equation (2.86), and $p = \rho c_s^2$ from equation (2.10), we have the following, where we include equation (2.86):

$$\partial_t \rho + \nabla \cdot (\rho \mathbf{v}) = 0, \quad (2.107)$$

$$\rho(\partial_t v_\alpha + v_\beta \partial_\beta v_\alpha) = -\partial_\alpha p + \nu \partial_\beta (\partial_\beta \rho v_\alpha + \partial_\alpha \rho v_\beta). \quad (2.108)$$

In the case of steady flow, the equations are as follows:

$$\nabla \cdot (\rho \mathbf{v}) = 0 \quad (2.109)$$

$$\rho v_\beta \partial_\beta v_\alpha = -\partial_\alpha p + \nu \partial_\beta (\partial_\beta \rho v_\alpha + \partial_\alpha \rho v_\beta) \quad (2.110)$$

Comparing to the exact steady incompressible Navier-Stokes equations at constant density ρ_0 (derived from equations (1.1) and (1.2) considering steadiness):

$$\nabla \cdot \mathbf{v} = 0 \quad (2.111)$$

$$v_\beta \partial_\beta v_\alpha = -\partial_\alpha \left(\frac{p}{\rho_0} \right) + \nu \partial_\beta (\partial_\beta v_\alpha + \partial_\alpha v_\beta) \quad (2.112)$$

we see that terms containing the spatial derivative of ρ are neglected. For example, the continuity equation (2.109), $\nabla \cdot (\rho \mathbf{v}) = 0$ gives $\rho \nabla \cdot \mathbf{v} + (\nabla \rho) \cdot \mathbf{v} = 0$. When this is used to approximate equation (2.111), the term $(\nabla \rho) \cdot \mathbf{v}$ is neglected and a compressibility error arises.

$$\frac{\nabla \rho}{\rho} \sim O(Ma^2), \quad (2.113)$$

from the left side of equation (2.112), so this will be the compressibility error for any finite Mach number.

To improve the accuracy of lattice-Boltzmann simulations, Zou et al [89] proposed an incompressible model. This was based on the idea of using $\mathbf{v} = \rho \mathbf{v}$ to represent the

velocity, which had been applied to the Lattice Gas method. Theoretically, it simulates the incompressible continuity equation (equation (2.111)) for \mathbf{v} , but the Navier-Stokes equation still has the factor $\frac{g(\rho)}{\rho_0}$ in the advection term (see equation (2.20)). The compressibility error comes from ignoring the change of ρ in this term. In the LBM, the nonlinear term can be made exact by choosing an appropriate equilibrium distribution function, which is a choice we do not have in Lattice Gas Automata. Using:

$$\sum_i f_i = \rho \quad (2.114)$$

$$\sum_i f_i \mathbf{e}_i = \mathbf{v}, \quad (2.115)$$

and changing the equilibrium functions such that ρ is inside the bracket, we have for the D3Q15 model for example:

$$f_i^{(eq)}(\mathbf{v}) = w_i \left(\rho + 3 \frac{v_\delta e_{i\delta}}{c^2} - \frac{3v_\delta v_\delta}{2c^2} + \frac{9v_\delta v_\epsilon e_{i\delta} e_{i\epsilon}}{2c^4} \right), \quad (2.116)$$

with the weights given in table 2.1. We obtain the exact incompressible steady NS equations from this, though the errors due to the lattice size remain. All incompressible models are given i as a suffix, so D3Q15 becomes D3Q15 i . [89] state that the model is only valid for steady flows because the temporal derivative of ρ in the continuity equation is nonzero in time-dependent flows. It is related to the temporal derivative of pressure and cannot easily be handled.

Equation (2.116) can be derived by substituting $\rho = \rho_0 + \delta\rho$ into the equilibrium distribution functions and neglecting the terms proportional to $\delta\rho \left(\frac{\mathbf{v}}{c}\right)$ and $\delta\rho \left(\frac{\mathbf{v}}{c}\right)^2$, which are of order Ma^3 or higher [88]. The reference density of the fluid, ρ_0 , can be set to one. Through the Chapman-Enskog procedure, it can be shown that the incompressible model gives rise to the following equations when time-dependent terms are kept:

$$\frac{1}{c_s^2} \frac{\partial p}{\partial t} + \nabla \cdot \mathbf{v} = 0, \quad (2.117)$$

$$\frac{\partial \mathbf{v}}{\partial t} + \mathbf{v} \cdot \nabla \mathbf{v} = -\nabla p + \nu \nabla^2 \mathbf{v}, \quad (2.118)$$

$$\nu = \left(\frac{\tau - 0.5}{3} \right) c^2 \Delta t. \quad (2.119)$$

A dimensionless form of equation (2.117) is:

$$\frac{1}{T} \frac{\partial p'}{\partial t'} + \frac{c_s}{L} \nabla' \cdot \mathbf{v}' = 0, \quad (2.120)$$

where $p' = \frac{p}{c_s^2}$, $t' = \frac{t}{T}$, $\nabla' = L\nabla$, $\mathbf{v}' = \frac{\mathbf{v}}{c_s}$ and L and T are characteristic length and time respectively. Therefore, the incompressible model can accurately simulate fluid flow provided that the slow flow condition is satisfied, so the time over which the fluid undergoes a macroscopic change, such as the period, in a range of distance L , must be much greater than the time taken by sound to travel that distance, i.e.

$$T \gg \frac{L}{c_s}. \quad (2.121)$$

The incompressible models eliminate terms of $O(Ma^2)$ but error terms of higher order in the Mach number still remain in the case of unsteady flow, as discussed in section 2.8, so it is still necessary to have $Ma \ll 1$. Most simulations have $Ma < 0.15$. Even for steady flow, it is necessary to have $Ma < 1$ to avoid instability, as discussed at the end of section 2.5.

Despite the accuracy of incompressible models, the second and third moments of the distribution functions may not be Galilean invariant. If the j th moment is taken to be:

$$M_j(\mathbf{v}) = \sum_i (\mathbf{v} - \mathbf{e}_i)^j f_i^{(eq)}(\mathbf{v}), \quad (2.122)$$

one obtains $\sum_i f_i = \rho$ and $\sum_i f_i \mathbf{e}_i = \mathbf{v}$ with $j = 0$ and $j = 1$, as expected but it can be shown that the second and third moments are not Galilean invariant.

2.7 Conversion of parameters into lattice units

During a lattice-Boltzmann simulation, it is often convenient to set $\Delta x = \Delta t = 1$, so we have $c = 1$, and also set ρ_0 to 1 or a nominal value [89]. It can be shown, for both compressible and incompressible models (section 2.6) that ρ_0 is an irrelevant variable and changing it will not change the simulation results. Setting the parameters to one ensures that the numbers calculated during the simulation are as close to order 1 as possible. When applying the Lattice Boltzmann method to a simulation of blood flow, we must

have a way of converting parameters from physical units to Lattice units. In this section, Q represents a quantity in physical units and Q^* is the Quantity in lattice units.

In this section, we will need equations (2.91), (2.90), (2.85), (1.5), (1.6):

$$\begin{aligned} p &\approx p_0 + c_s^2(\rho - \rho_0), \\ c_s^2 &= \frac{c^2}{3}, \\ \nu &= \frac{c^2}{3} \left(\tau - \frac{1}{2} \right) \Delta t, \\ Re &= \frac{v_{max} D}{\nu}, \nu = \frac{\eta}{\rho}, \\ \alpha &= \frac{D}{2} \sqrt{\frac{\omega}{\nu}}. \end{aligned}$$

Any length or time can be converted easily, as follows:

$$L^* = \frac{L}{\Delta x}, \quad (2.123)$$

$$t^* = \frac{t}{\Delta t}. \quad (2.124)$$

Since we set the density of the fluid $\rho_0^* = 1$ in lattice units, we can define the lattice unit of mass as follows:

$$\Delta m = \rho_0 \Delta x^{N_D}, \quad (2.125)$$

where N_D is the number of dimensions and in 2D, we define the density as the mass per unit area. Any quantity can be converted by considering its dimensions. For velocity and kinematic viscosity, we have

$$v^* = v \frac{\Delta t}{\Delta x}, \quad (2.126)$$

$$\nu^* = \frac{\nu \Delta t}{\Delta x^2}. \quad (2.127)$$

The value of τ is given by rearranging equation (2.85), so

$$\tau = \frac{1}{2} + \frac{3}{\Delta t \nu} \Delta x^2. \quad (2.128)$$

For the pressure, let $\Delta p = p - p_0$, $\Delta \rho = \rho - \rho_0$. Therefore,

$$\Delta p^* = \frac{\Delta p \Delta t^2 \Delta x^{N_D-2}}{\Delta m}, \quad (2.129)$$

where the 2D pressure is the force per unit length. The same equation can be used for any quantity that has dimensions of pressure, for example the Young's modulus of the wall if elasticity is included in the simulation. Substituting equation (2.125) into equation (2.129) gives

$$\Delta p^* = \frac{\Delta p}{\rho_0} \Delta t^2 \Delta x^2. \quad (2.130)$$

It is more convenient to express this in terms of ρ for LBM by substituting equation (2.91) into this:

$$\Delta \rho^* = \frac{\Delta p}{\rho_0 c_s^*{}^2} \Delta t^2 \Delta x^2. \quad (2.131)$$

If we convert the speed of sound, c_s , using equation (2.127), it will not generally match the actual speed of sound in the fluid we are simulating due to the restriction on c_s^* (equation (2.90)). Therefore, from equation (2.91), the fractional change in density due to differences in pressure in the fluid will not match, resulting in a compressibility error. From section 1.6, some typical parameters for blood flow are: $D = 5 \times 10^{-3} \text{m}$, $c_s = 1580 \text{m s}^{-1}$ where D is the diameter of an artery. If we choose the spatial resolution $\Delta x = 2.5 \times 10^{-4} \text{m}$ and match the speed of sound in the simulation to that of blood, we would have $\Delta t = 1.06 \times 10^{-7} \text{s}$. Using such a small timestep would be very computationally costly. Using equation (2.91), the change in density of the blood is given by $\frac{\Delta \rho}{\rho_0} = 7.6 \times 10^{-7}$, which is tiny, so blood flow can be taken as incompressible. The compressibility error from the LBM is of order Ma^2 , as explained in section 2.8. Therefore, the Mach number should be kept much smaller than one.

2.7.1 The law of similarity

For a steady incompressible flow, then for the parameters that characterise the fluid itself, only the kinematic viscosity, ν , appears in the Navier-Stokes equations [36]. Therefore the unknown functions that have to be determined by solving them are the velocity and the ratio $\frac{\mathbf{p}}{\rho_0}$, which depends on the velocity of the fluid through ν . If the shape of the body is given, the geometrical properties are specified by a characteristic length, D . Then

any flow is specified by three parameters, ν , D and the speed of the main fluid stream, v . Only one dimensionless quantity can be formed from the above three, which is called the Reynolds number. Any other dimensionless quantity can be written as a function of the Reynolds number.

If the lengths are measured in terms of D and the velocities are measured in terms of v , the velocity distribution obtained by solving the equations of incompressible flow is given by a function of the form

$$\mathbf{v} = vf\left(\frac{\mathbf{r}}{D}, Re\right). \quad (2.132)$$

From this expression, we can see that in flow of the same type, the velocities $\frac{\mathbf{v}}{v}$ are the same functions of the ratio $\frac{\mathbf{r}}{D}$ if the Reynolds number is the same for each flow [36]. Such flows are said to be similar. Therefore, when carrying out a lattice-Boltzmann simulation of these flows, it is only necessary to match the Reynolds number in physical and lattice units. Therefore, two of the three parameters mentioned in the last but one paragraph may be chosen freely, for example, the system size and velocity. Setting these parameters is equivalent to choosing the spatial and temporal resolution, Δx and Δt . The value of τ must then be calculated from the viscosity using equation (2.128). An equation similar to (2.132) can be developed for the pressure distribution by constructing a dimensionless parameter involving pressure:

$$p = \rho_0 v^2 f\left(\frac{\mathbf{r}}{D}, Re\right). \quad (2.133)$$

Unsteady flows are characterised by four parameters: v , ν , D and a time interval T [36]. From these parameters, we can construct two independent dimensionless quantities which match between flows that are similar. When simulating a flow, we therefore have two degrees of freedom. A possible choice of independent dimensionless parameters are the Reynolds number and the Womersley number, given by equation (1.6). The Strouhal number, expressed by equation (2.134) [36], is an alternative dimensionless parameter.

$$St = \frac{vT}{D}. \quad (2.134)$$

2.8 Simulation accuracy of lattice-Boltzmann method

When Qian et al proposed the Lattice BGK model [16], a simulation was performed with a D3Q15 model on a $128 \times 1 \times 1$ lattice, with a small amplitude sinusoidal wave. The speed of sound agreed with equation (2.85) within 0.4%. Chen et al. [98] also tested the method for Beltrami flow. This involves rewriting the incompressible Navier-Stokes equation (1.2) in the form:

$$\frac{\partial \mathbf{v}}{\partial t} + \boldsymbol{\omega} \times \mathbf{v} = -\nabla \left(\frac{p}{\rho} + \frac{v^2}{2} \right) - \nu(\nabla \times \boldsymbol{\omega}), \quad (2.135)$$

where

$$\boldsymbol{\omega} = \nabla \times \mathbf{v} \quad (2.136)$$

is the vorticity. For Beltrami flows,

$$\mathbf{v} \times \boldsymbol{\omega} = 0. \quad (2.137)$$

Periodic boundaries were used, so the first term on the right hand side of equation (2.135) is zero, and we obtain:

$$\frac{\partial \mathbf{v}}{\partial t} = -\nu(\nabla \times \boldsymbol{\omega}) \quad (2.138)$$

Taking the curl of both sides of this equation, using equation (2.136), and applying some vector calculus identities as follows gives a diffusion equation for vorticity:

$$\frac{\partial \boldsymbol{\omega}}{\partial t} = -\nu(\nabla \times \nabla \times \boldsymbol{\omega}) \quad (2.139)$$

$$= -\nu(\nabla(\nabla \cdot \boldsymbol{\omega}) - \nabla^2 \boldsymbol{\omega}) \quad (2.140)$$

$$= -\nu(\nabla(\nabla \cdot (\nabla \times \mathbf{v})) - \nabla^2 \boldsymbol{\omega}) \quad (2.141)$$

$$= \nu \nabla^2 \boldsymbol{\omega} \quad (2.142)$$

The flow therefore has a solution that exponentially decays with time. Simulations were carried out on a $64 \times 64 \times 64$ D3Q15 lattice for 100 timesteps between $\tau = 0.55$ and $\tau = 3$.

$$\langle (\mathbf{v} \times \boldsymbol{\omega})^2 \rangle = 0, \quad (2.143)$$

where $\langle \rangle$ denotes spatial averaging, is the basic Beltrami property and was obtained throughout the simulation. Equation (2.138) was satisfied. The viscosity was calculated

from the rate of decay and it satisfied the theoretical relation (equation (2.85)):

$$\nu = \frac{c^2}{3} \left(\tau - \frac{1}{2} \right).$$

A $128 \times 128 \times 128$ lattice was used to test a decaying Taylor-Green Vortex, which has a turbulent decay mechanism. The lattice Boltzmann method was compared to a spectral method. The quantity $\langle \omega^2 \rangle$ was measured over time, and the results agreed well at most times, but not at the peak of the vorticity. This is probably because the spectral methods solves the incompressible Navier-Stokes equations, whereas the lattice Boltzmann method solves the compressible ones and the scheme is first order accurate in time and second-order accurate in space. The quantities $\frac{\langle v_y^2 \rangle}{\langle v_x^2 \rangle}$, $\frac{\langle v_z^2 \rangle}{\langle v_x^2 \rangle}$, $\frac{\langle \omega_y^2 \rangle}{\langle \omega_x^2 \rangle}$, and $\frac{\langle \omega_z^2 \rangle}{\langle \omega_x^2 \rangle}$ agreed very well. The velocity contour lines are also in good agreement. Finally, there was good agreement between the energy spectra in three-dimensional isotropic turbulence. The system energy oscillated below a viscosity of about 0.001. This allows for a maximum Reynolds number of about 1000.

All of these early tests were designed to study the intrinsic accuracy of the Lattice-Boltzmann method, without boundary condition methods, which can introduce further inaccuracies, as shown in section 2.9. Therefore, periodic boundary conditions were used, in which all particles leaving the system on one side are injected into the other side with the same velocity.

There will be some small simulation errors, and one can quantify these. In the Lattice-Boltzmann method, the distance between the lattice points is much greater than the molecular mean free path, because we are interested in the macroscopic behaviour of the fluid, not the motions of individual molecules. We still have diffusion and advection of the lattice particles, but their mean free path is directly proportional to the lattice spacing. It also depends on the relaxation parameter, τ . Therefore, the Knudsen number is directly proportional to lattice spacing divided by system size.

$$\epsilon \propto O\left(\frac{\Delta x}{L}\right). \quad (2.144)$$

As shown in section 2.5, there is an error of $O(\epsilon^3)$. The lowest order terms in the Navier-Stokes equations are $O(\epsilon)$, so the relative error is of the order of the square of the lattice

spacing. A similar argument applies to the neglected term in equation (2.88). The lattice spacing $\Delta x = c\Delta t$, so the derived Navier Stokes equations (using equations (2.86) and (2.87)) are [89, 90]:

$$\partial_t \rho + \partial_\alpha \rho v_\alpha = 0 + O(\Delta x)^2, \quad (2.145)$$

$$\begin{aligned} \partial_t \rho v_\alpha + \partial_\beta \rho v_\beta v_\alpha &= \partial_\alpha \left(\frac{\rho c^2}{3} \right) + \nu \partial_\beta (\partial_\beta \rho v_\alpha + \partial_\alpha \rho v_\beta) + O(\Delta x)^2 \\ &+ O(\Delta x v^3). \end{aligned} \quad (2.146)$$

Substituting (2.145) into (2.146), and following the short procedure used in section 2.6 to derive equations (2.107) and (2.108), we obtain the compressible Navier-Stokes equations with error terms:

$$\partial_t \rho + \nabla \cdot (\rho \mathbf{v}) = 0 + O(\Delta x)^2 \quad (2.147)$$

$$\begin{aligned} \rho (\partial_t v_\alpha + v_\beta \partial_\beta v_\alpha) &= -\partial_\alpha p + \nu \partial_\beta (\partial_\beta \rho v_\alpha + \partial_\alpha \rho v_\beta) \\ &+ O(\Delta x)^2 + O(\Delta x v^3) \end{aligned} \quad (2.148)$$

The equation looks first order in time and space, but it is in fact first order in time and second order in space. The last term in equation (2.148) represents an error of order $\Delta x Ma^3$, where Ma is the Mach number. Since this term came from a time derivative, it is not present in the case of steady flow.

In section 2.6, it was shown that the lattice-Boltzmann method gives rise to compressibility errors given by equation (2.113):

$$\frac{\nabla \rho}{\rho} \sim O(Ma^2),$$

where Ma is the Mach number. One can try to minimise the Mach number, but this can be impractical as shown in section 2.7. Most flows of interest occur at moderately high Reynolds numbers in nominally incompressible regimes [90]. Incompressible models, described in section 2.6, have been developed to address this problem.

As well as testing the sound speed and viscosity, as written about earlier in this section, studies have also tested that the errors in velocity are as we would expect from the theory. Errors in velocity relative to an analytical solution are normally calculated using the L^2

norm [88, 89]:

$$E_{analytic} = \sqrt{\frac{\sum_{\mathbf{r}} |\mathbf{v}(\mathbf{r}, t) - \mathbf{v}_{analytic}(\mathbf{r}, t)|^2}{\sum_{\mathbf{r}} |\mathbf{v}(\mathbf{r}, t)|^2}}. \quad (2.149)$$

Zou et al [89] tested the compressibility error for flow in a square cavity with a moving top which had 256×256 lattice points. There is no analytic solution for this, so the errors were calculated using the stream function, as follows:

$$\psi(x_1, y) = \int_0^{x_1} v_y dx. \quad (2.150)$$

We would expect this to be zero at the walls, i.e. at $x_1 = L$ because the flow in the positive y direction should be balanced by flow in the negative y direction at all places. If it is not, there is a compressibility error. The simulation confirmed that this was proportional to Ma^2 . The flow behaviour was the same in all simulations, because Re was constant. It was tested for velocities between 0.1 and 0.01 in lattice units. Other simulations of flow in a cavity have been compared with solutions from finite-difference methods [90].

Comparisons of compressible and incompressible models on the vortex centres in the cavity and velocity of flow in a square region with a constant body force were also carried out [89]. This was used instead of a pressure boundary condition, in order to avoid errors from the boundary conditions. An extra term is introduced into the LBGK equation, so we have

$$f_i(\mathbf{r} + \mathbf{e}_i, t + \Delta t) - f_i(\mathbf{r}, t) = \frac{-1}{\tau}(f_i(r, t) - f_i^{(eq)}(r, t)) + \frac{(\Delta t)^2}{\Delta x} g_i, \quad (2.151)$$

where g_i is adjusted in proportion to the weight of the equilibrium distribution for direction i . For example we have the following for the D2Q9 model [100]:

$$g_i = \begin{cases} 0, & i = 0 \\ \frac{1}{3c} \mathbf{e}_i \cdot \mathbf{F}, & i = 1, 2, 3, 4 \\ \frac{1}{12c} \mathbf{e}_i \cdot \mathbf{F}, & i = 5, 6, 7, 8, \end{cases} \quad (2.152)$$

where \mathbf{F} is the force per unit volume, which appears on the right hand side of the Navier-Stokes momentum equation (equation (2.108)), as shown here:

$$\rho(\partial_t v_\alpha + v_\beta \partial_\beta v_\alpha) = -\partial_\alpha p + \nu \partial_\beta (\partial_\beta \rho v_\alpha + \partial_\alpha \rho v_\beta) + F_\alpha \quad (2.153)$$

Keeping $v = 0.1$, $Re = 100$, the errors for the compressible model levelled off to 0.004 as the lattice resolution was increased due to the constant compressibility error, but the errors for the incompressible model kept decreasing as Δx^2 . The stability behaviour of the incompressible model was also better than the compressible one.

The accuracy of the incompressible model was also thoroughly tested by [90] for the flow over a step, i.e. into the narrow end of a stepped cavity. They used velocity boundary conditions, assuming a Poiseuille flow at the inlet, and pressure boundary conditions at the outlet using bounceback of the nonequilibrium distribution as proposed by Zou and He (see section 2.9). The lattice resolution, system shape and Reynolds number were varied. The error was measured using the normalised divergence,

$$\frac{\nabla \cdot \mathbf{v}}{\mathbf{v}} < tol \quad (2.154)$$

This error was always less than 3×10^{-6} . The stream functions also agreed with theory correct to 0.1%. The pressure contours were also the same as those found from Navier-Stokes methods. The stress is calculated directly from the distribution functions using equation (2.246), in contrast to finite-difference methods which need to calculate it from the velocity flow field. The improvement in accuracy has been confirmed.

He and Luo [88] used the incompressible model to study Poiseuille flow in two dimensions. The system had only 17×5 lattice points. A pressure boundary condition was applied at the outlet. Both a pressure and a velocity boundary condition were tried at the inlet. The boundary condition method was not stated. The simulation achieved machine accuracy for $\tau = 0.75, 1.0$ and 2.0 for the incompressible models. This is because the Lattice Boltzmann method is second order accurate in space, and in Poiseuille flow, the last term is second order in space. Noble et al [101] and Zou and He [9] also achieved machine accuracy using consistent methods at all boundaries and [9] achieved second-order accuracy for other boundary conditions (see section 2.9). They constructed a table showing the mean relative error in velocity against the lattice size and type of boundary condition for three pair of Re and τ . The order of convergence was calculated using least-squares fitting. A relative error in velocity of less than 1.0×10^{-3} was achieved for $Re = 10, \tau = 0.6$; $Re = 10, \tau = 0.8$ and $Re = 1, \tau = 1.1$, with a 64×32 lattice. The consistent method. The Lattice-Boltzmann method is also second order in the case of flow between two porous parallel plates, in

which the top plate is moving, which drives the flow. Even if there is, in addition, a flow normal to the boundaries, the method achieves second order accuracy provided that accurate boundary conditions are used (i.e. the consistent method) [101, 102]. The same accuracy can also be achieved for cavity flow with an analytical solution and the oscillating plate problem [102].

Zou and He [9] also carried out simulations of steady flow in a 3D square duct under different boundary conditions. The errors were larger in this case, but still second order convergent for most boundary conditions, falling below 10^{-2} for a $64 \times 32 \times 32$ lattice, except for the simple bounce-back without collision (section 2.9). Mazzeo and Coveney [92], Mazzeo et al. [93] carried out simulations under the same parameters with the consistent method for pressure by Zou and He with bounce-back, nonequilibrium extrapolation and a new extrapolation method (see section 2.9). These boundary conditions are first order and the order of convergence was approximately first order in the simulations. The errors were higher, but fell below 1.0×10^{-1} for a $64 \times 32 \times 32$ system for two of the boundary condition methods.

In simulations of two-dimensional Womersley flow with $T=1000$ and $T=2000$ and a system of 21×21 lattice points, compressible and incompressible models have been compared, while the pressure difference between the inlet and outlet was varied [88]. The results are in excellent agreement with the analytic solution. With a small pressure difference, the models have comparable errors, but the error in the compressible model grows faster. The term $\frac{\delta p}{\rho} \propto Ma^2$, but this does not mean the velocity is proportional to Ma^2 . The errors were found to be of order 0.96 and 1.24 for the incompressible and compressible models. The compressibility error was reduced. In contrast to the other literature, it is found that the error in velocity is second order in the temporal resolution. The second-order error in Mach number was obtained under a constant system size, period of oscillation and viscosity. Therefore, the Reynolds number was changed between the simulations. This shows that it is not necessary to ensure that the Reynolds is the same to test the error with respect to T , system size or Ma .

Sometimes strange effects can occur, such as the Lattice Boltzmann solution approaching the steady state solution, then diverging from it if the tolerance (permitted difference between current and previous timestep for us to say the method has converged on a

solution) is too low. The solution may even reach a nearly periodic state [89]. One must watch out for this in simulations.

If rest particles were not included in the D3Q15 and D3Q19 models, we would have the D3Q14 and D3Q18 models respectively. Likewise, the FHP or D2Q6 model would become D2Q7 if rest particles were included. The presence of rest particles often improves the accuracy of the model. Furthermore, for a small relaxation time τ , the rest particles may be needed to stabilise the system [18]. Ladd [91] did not use rest particles in his lattice-Boltzmann simulations, but set the speed of sound $c_s = \sqrt{\frac{1}{2}}$ instead of $c_s = \sqrt{\frac{1}{3}}$, which causes the viscous stresses to be incorrect if the flow is significantly compressible.

Using 14 moving directions instead of 18 can result in a checkerboard effect. If we colour the lattice points at the beginning of the simulation so they are black if $x + y + z$ is odd and white if $x + y + z$ is even, as shown in figure 2.2, then, if there are no obstacles in the system, it is clear to see that, in the D3Q14 model, the colour of the lattice point at which a given particle resides changes at every time step. Therefore, the black and white populations are entirely independent of each other, so the mass and momentum are conserved separately for the black and white particles, which is unphysical. In the D3Q18 model, the black and white populations mix immediately with each other. In the D3Q15 models, the populations of black and white particles are not entirely independent because they are coupled by the rest particles, but checkerboard effects may also lead to unphysical behaviour here [18].

In summary, the error is composed of the following terms (see also section 2.9):

- An error of order $(\Delta x)^2$ due to the intrinsic accuracy of the Lattice Boltzmann Method.
- $O(\Delta x)^2$ or $O(\Delta x)$ due to the boundary condition method. The lower order term dominates.
- $O(\Delta t Ma^3)$ in a time-dependent flow due to the intrinsic accuracy.
- $O(\Delta t)$ from boundary conditions in the new extrapolation method (section 2.9.6)
- $O(Ma^2)$ for compressible models.

The following conditions must be satisfied:

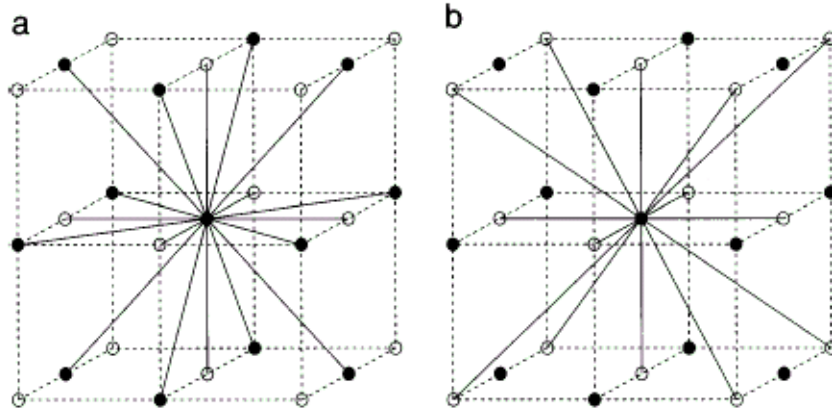


FIGURE 2.2: Checkerboard colouring of the lattice structures of D3Q19 (left) and D3Q15 (right) models. Image taken from [18].

- The lattice spacing must be much less than the region over which there is a macroscopic change in the fluid velocity (see section 2.5).
- The Mach number must be significantly less than 1, so that the error terms listed above are not too large.
- For time-dependent flows, the slow flow condition must be satisfied, so the period of oscillation must be much greater than the advection time for information to pass along the length of the system, i.e. $T \gg \frac{L}{c}$ (section 2.6).

2.9 Boundary condition methods

In most research and engineering problems in hydrodynamics, it is essential to specify pressure and velocity boundary conditions, so that a unique solution to the particular flow problem can be found. They affect the flow either near the boundaries or in the bulk of the system. The Lattice-Boltzmann method presents a particular challenge in boundary conditions, because at the wall or the inlet or outlet of a system, collision and streaming alone cannot determine the distribution functions in the inward-pointing directions because there are no fluid sites that stream to the boundary sites in those directions. New methods are needed to deal with these functions.

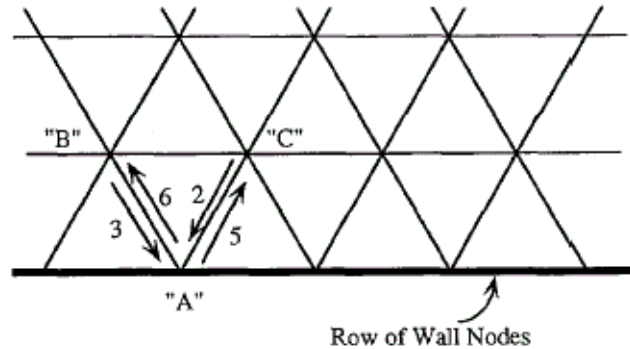


FIGURE 2.3: Illustration of the bounce-back method on a hexagonal lattice. Image from [103].

In viscous flow situations, a non-slip boundary condition usually applies, which means that the velocity parallel to the wall is zero in addition to the velocity perpendicular to the wall.

2.9.1 Bounce back

The simplest boundary condition method is the bounce-back rule. Here, particles that meet a wall node are bounced back with a reversed velocity. The bounce back condition was originally used in the Lattice Gas method [103]. It is illustrated in figure 2.3. Whenever a direction-3 particle arrives from node B, a direction-6 particle is sent back to B at the following time step, and similarly for direction-2 particles from node C. The time average of the population has an equal number of direction-3 and direction-6 particles and direction-2 and direction-5 particles, so the average velocity is zero. This technique has been used in lattice-Boltzmann simulations. If the value of the distribution function of 3-direction particles, f_3 , arriving at A from B is 0.19 while f_2 from C is 0.17. Using the bounce-back algorithm, f_6 from A is 0.19 and f_5 from A is 0.17. Nodes B and C receive particles from a population identical to their own, but travelling in the opposite direction. This is different from the intended result of having a no-slip wall at A. For simple analytical flow, it can be shown both theoretically and computationally that this gives a first-order slip velocity [100, 101] and first-order errors throughout the fluid domain [9, 18, 90]. This has also been shown computationally for 2D cavity flows [9].

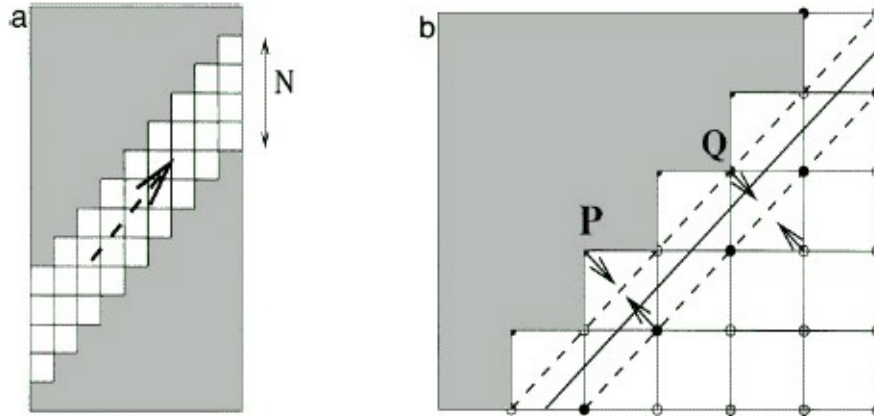


FIGURE 2.4: The inclined tube flow computation for an inclination of 45 degrees. On the left the computational grid is shown and on the right the location of the wall. Image taken from [18].

An alternate interpretation of the bounce-back condition corresponds to a no-slip wall halfway between the nodes A and B-C. This is because the velocity at A in the opposite direction is the symmetric reflection of the state at BC through the no-slip wall in between. Using half-way wall bounceback gives much improved accuracy in simulations [103]. The slip velocity is then second order [100] and it has been shown computationally to give second-order errors throughout the fluid domain for Poiseuille flow in two and three dimensions [9].

The bounce-back rule leads to a non-slip boundary somewhere between the wall nodes and the adjacent fluid sites. It may be different from exactly half way in between in the case of an inclined wall [18], but the simulation error in a 2D inclined tube is still second-order in the velocity. It is first-order for the simple bounce-back scheme. In both cases, the errors are about 50% higher with such a staircased geometry, as shown in figure 2.4. The geometry is staggered between lines through P-type and Q-type points in this figure. Therefore the half-way shifted boundary is also staggered, between the two dotted lines. The location of the boundary can be taken as the average of these two lines, i.e. the thick solid line.

The equilibrium and nonequilibrium parts of the distribution function, in terms of the flow physics, refer to the contribution of velocity gradients. For steady uniform flow, the distribution functions are the equilibrium ones. When there are velocity gradients,

the distribution functions are no longer at equilibrium. In this situation, the particle population arriving at a node will have contributions from neighbourhoods having higher and lower velocities than the nodal velocity. The collision operator, representing viscosity, operates on the deviations of the populations from their zero-gradient values and moves them toward the equilibrium values. For high viscosity, the nonequilibrium values are adjusted very little so the momentum excess or deficit can propagate through a given node to the next neighbours, so that their velocities are more likely to match. For a low viscosity, the operator moves the nonequilibrium contribution strongly towards zero, so the velocity gradients have little effect on the velocity in neighbouring nodes.

With half-way wall bounceback, the populations coming from nodes A and going to nodes B-C will correspond to zero velocity halfway between, but will carry inaccurate velocity gradient information. There will therefore be errors of order $\nabla^2 \mathbf{v}$ in the velocity, i.e. second-order errors.

Ziegler [103] proposed a more accurate alternative, in which the boundary is kept coincident with the first line of nodes. During the streaming phase, the precollision distributions pointing into the fluid (which are unknown) are set to the ones pointing outwards that arrive from within the fluid. For example, in a d2q9 model with the boundary at the bottom, we would have $f_2 = f_4$, $f_5 = f_7$ and $f_6 = f_8$. The other distribution functions (in this case those pointing along the boundary) are then set equal to the average of the incoming ones. During the collision phase, collision is done at the boundary nodes as well as in the bulk. This should be more accurate because the effects of viscosity are taken into account at the boundary nodes. From a simulation of Poiseuille flow, the velocities given by the half-way wall bounceback and the improved method were found to be exactly the same except for the first two lattice points away from the wall. The wall shear stress was calculated by working out the momentum difference between particles arriving and leaving the wall and by the velocity gradient. The strain rate was then multiplied by the viscosity. The results should be the same and consistent with the total force applied to the system by the pressure gradient. The two methods of calculation gave more consistent answers with the new method than the half-way bounceback.

The bounceback methods can be used in any geometry and are easy to implement. However, it cannot be used for boundaries that have a non-zero velocity [100, 101], such as the problem with flow between two porous plates described in section 2.8. The different types

of bounceback condition as well as the equilibrium method were analysed by He et al [100] by solving the LBGK equation and confirming the results with numerical simulation, but this was only done for Poiseuille and Couette flow.

Instead of the distribution functions being bounced back on the nodes, they may be bounced back on the links instead. That is, particles that leave a fluid node at time t and propagate towards a solid node with velocity \mathbf{e}_k arrive back at the fluid node at time $t + \Delta t$ with velocity $\mathbf{e}_i = -\mathbf{e}_k$. Since the velocity is constant before and after reflection, the particles travel a distance $\frac{\Delta x}{2}$ before being reflected. Therefore, a no-slip and no-penetration condition should be applied at that point. If the wall is not located half way between the fluid and solid sites, the simulation errors are of order Δx . However, Noble et al. [101] and Inamuro et al. [104] have shown that a slip velocity remains if τ is significantly greater than one, and that it increases with τ , eventually becoming equal to the velocity in the centre of the channel. Noble et al. [101] state that this is because the mean free path increases with τ , so at very high values of τ , it is large compared to the size of the system.

Ladd [91] adjusted the bounce back condition so that a non-zero velocity can be imposed at the wall. The distribution function that is unknown after streaming is determined by

$$f_i(\mathbf{r}, t + \Delta t) = f_k^+(\mathbf{r}, t) + f_i^{(eq)}(\rho(\mathbf{r}, t), \mathbf{v}_b) - f_i^{(eq)}(\rho(\mathbf{r}, t), \mathbf{v}_b), \quad (2.155)$$

where $\mathbf{e}_k = -\mathbf{e}_i$ is the lattice direction pointing towards a solid site and $f_k^+(\mathbf{r}, t)$ is the postcollision distribution function in direction k at time t . Substituting equation (2.52) into this gives

$$f_i(\mathbf{r}, t + \Delta t) = f_k^+(\mathbf{r}, t) + w_i \rho \left(\frac{6\mathbf{e}_i \cdot \mathbf{v}}{c^2} \right), \quad (2.156)$$

where w_i is the weight of the distribution function $f_i^{(eq)}$ given in table 2.1. While the equilibrium distribution functions are adjusted, bounce-back is still being carried out for the nonequilibrium distribution functions. Therefore, the behaviour of the stress tensor at the boundaries will be the same as it is for the usual bounce-back condition.

Bouzidi et al. [7] combined the bounce back scheme with a spatial interpolation of the distribution functions in order to improve its accuracy by ensuring that each particle distribution function that propagates towards a solid site is reflected at the wall, which is

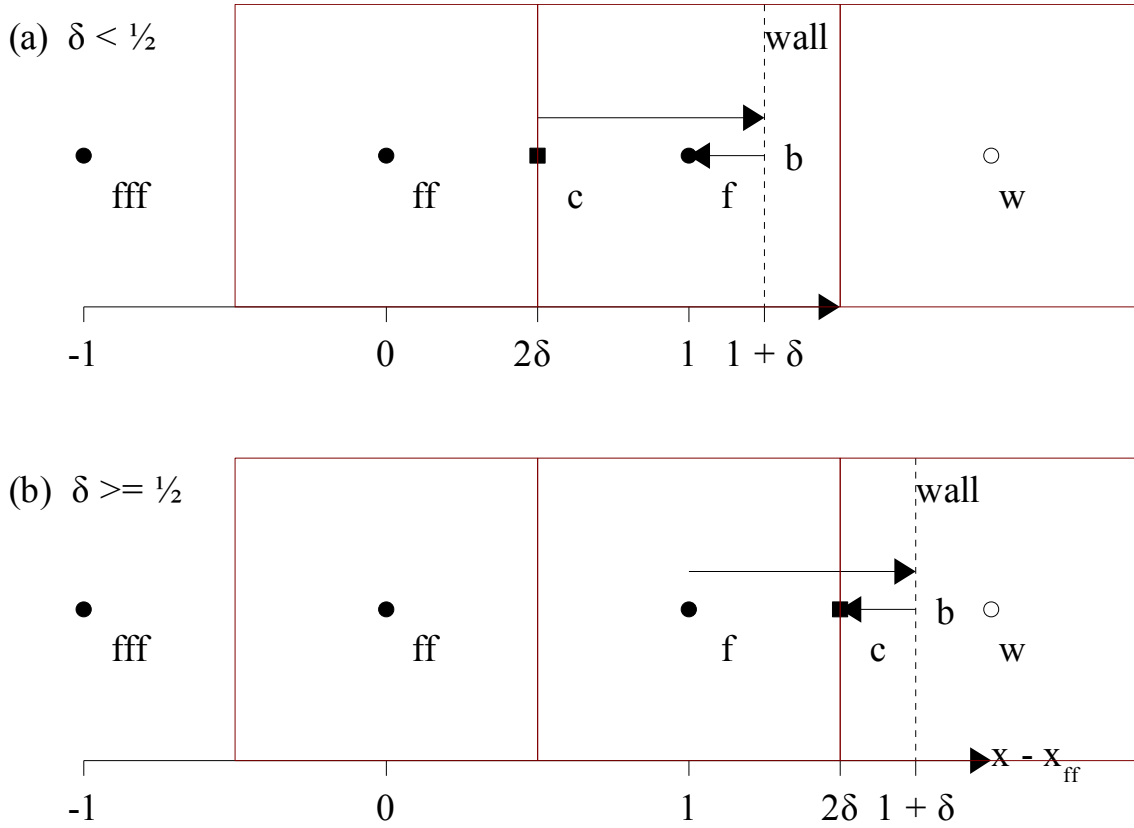


FIGURE 2.5: Details of the bounceback of the distribution functions used in the method by Bouzidi et al. [7] and the cells surrounding the lattice sites for the method by Verberg and Ladd [8].

not generally half way between the fluid and solid sites. Therefore, a particle leaving node f at time t with velocity \mathbf{e}_k does not arrive back at node ff after moving a distance Δx , so the distribution function of particles at node ff at time $t + \Delta t$ in direction $\mathbf{e}_i = -\mathbf{e}_k$ is not known, as shown in figure 2.5.

For this method, we need to consider the link from the edge site f to a neighbouring solid site w . The link intersects the wall at point b and the fraction of the intersected link in the fluid region is

$$\delta = \frac{|\mathbf{x}_f - \mathbf{x}_b|}{|\mathbf{x}_f - \mathbf{x}_w|}, \quad (2.157)$$

where \mathbf{x}_f , \mathbf{x}_w and \mathbf{x}_b denote the position vectors of site f , site w and point b respectively. This definition is also used for other boundary condition methods [10, 14]. At this point, I generalise the definition of δ such that it would be negative if the wall has crossed the site

f , i.e. if point b lies between sites f and ff , but it would have the same value otherwise:

$$\delta = \frac{(\mathbf{x}_b - \mathbf{x}_f) \cdot (\mathbf{x}_w - \mathbf{x}_f)}{|\mathbf{x}_w - \mathbf{x}_f|^2}. \quad (2.158)$$

I define the normalised cut distance at an edge site as the value of δ . This generalized definition will be useful in section 5.5.

To apply the velocity boundary condition for $\delta < \frac{1}{2}$, Bouzidi et al. [7] constructed a fictitious distribution function for particles at point c at time t for particles that would arrive at site f after bouncing back on the wall at point b , having travelled a total distance of Δx . This distribution function was calculated by linear interpolation of the postcollisional distribution functions between sites f and ff :

$$f_i(\mathbf{x}_f, t + \Delta t) = f_k^+(\mathbf{x}_c, t) \quad (2.159)$$

$$= 2\delta f_k^+(\mathbf{x}_{ff}, t) + (1 - 2\delta)f_k^+(\mathbf{x}_f, t), \quad (2.160)$$

where f_k^+ is a post-postcollisional distribution function. For $\delta \geq \frac{1}{2}$, $f_i(\mathbf{x}_f, t + \Delta t)$ was calculated by linear interpolation between the distribution functions arriving at point c and site ff respectively at time $t + \Delta t$:

$$f_i(\mathbf{x}_f, t + \Delta t) = \left(1 - \frac{1}{2\delta}\right) f_i(\mathbf{x}_{ff}, t + \Delta t) + \left(\frac{1}{2\delta}\right) f_i(\mathbf{x}_c, t + \Delta t) \quad (2.161)$$

$$= \left(\frac{2\delta - 1}{2\delta}\right) f_i^+(\mathbf{x}_f, t) + \left(\frac{1}{2\delta}\right) f_k^+(\mathbf{x}_f, t). \quad (2.162)$$

For moving boundaries, Bouzidi et al. [7] adjusted the distributions in the same way as Ladd [91]. The second term on the right hand side of equation (2.156) was multiplied by the coefficient of the distribution that was bounced back, i.e. the coefficient of $f_k^+(\mathbf{x}_c, t)$ in equation (2.159) and that of $f_k^+(\mathbf{x}_f, t)$ in equation (2.161). That is, expressions (2.163) and (2.164) were added to the RHSs of equations (2.160) and (2.162):

$$w_i \rho \left(\frac{6e_i \cdot \mathbf{v}}{c^2} \right). \quad (2.163)$$

$$\left(\frac{1}{2\delta} \right) w_i \rho \left(\frac{6e_i \cdot \mathbf{v}}{c^2} \right). \quad (2.164)$$

Bouzidi et al. [7] also gave equations for quadratic interpolation involving site fff in

figure 2.5, but the distribution functions at site f would no longer be determined by those from the nearest neighbours alone. Simulations of Poiseuille flow in a channel using their method were much more accurate than those using conventional bounce-back and the velocity at the walls of the channel were zero. Good agreement between the velocity field and the analytical solutions was also achieved with Bouzidi et al. [7]’s method for plane Couette flow, time-dependent flow inside both a static and an impulsively started circle, and flow past a periodic array of cylinders. For the flows in channels, body forcing was used to drive the flow. The transfer of momentum for the fluid to the boundary was also calculated for circular flows and this also agreed closely with the analytical solution.

Verberg and Ladd [8] only allowed particles to move a total distance of Δx during the timestep in which they bounce back on the wall, in common with [7], by considering the unit square centred on site w in figure 2.5, which I will call cell w , to be partially filled with fluid. If the wall is vertical, the volume fraction of fluid in cell w is $\phi_w = \delta - 0.5$. The distribution function $f_k^+(\mathbf{x}_f, t)$, which represents the population density of fluid moving with velocity e_k after collision, is split into three fractions, such that the population densities in cells f and w are given by

$$f_k(\mathbf{x}_w, t + 1) = f_k^+(\mathbf{x}_f, t), \quad (2.165)$$

$$f_i(\mathbf{x}_w, t + 1) = f_k^+(\mathbf{x}_f, t), \quad (2.166)$$

$$f_i(\mathbf{x}_f, t + 1) = (1 - 2\phi_w)f_k^+(\mathbf{x}_f, t) + \phi_w[f_k^+(\mathbf{x}_w, t) + f_i^+(\mathbf{x}_w, t)], \quad (2.167)$$

$$f_k(\mathbf{x}_f, t + 1) = \phi_w f_k^+(\mathbf{x}_f, t) + f_k^+(\mathbf{x}_{ff}, t). \quad (2.168)$$

All the fluid particles within the population represented by $f_i^+(\mathbf{x}_w, t)$ reach cell f . Since the fluid occupies fraction ϕ_w of cell w , this gives rise to the third term on the right of equation (2.167). Similarly, all the fluid particles represented by distribution function $f_k^+(\mathbf{x}_w, t)$ bounce back on the wall and reach cell f , giving rise to the second term on the right of equation (2.167). A fraction ϕ_w of the fluid represented by $f_k^+(\mathbf{x}_f, t)$ does not reach the wall because it lies further away than Δx , the distance that the fluid particles travel during one timestep. It therefore remains in cell f , which gives rise to the first term on the right of equation (2.168). A further fraction ϕ_w of the fluid represented by $f_k^+(\mathbf{x}_f, t)$ reaches the wall but does not return to cell f because the distance to the wall and back is greater than Δx , which gives rise to the first term on the right of equation

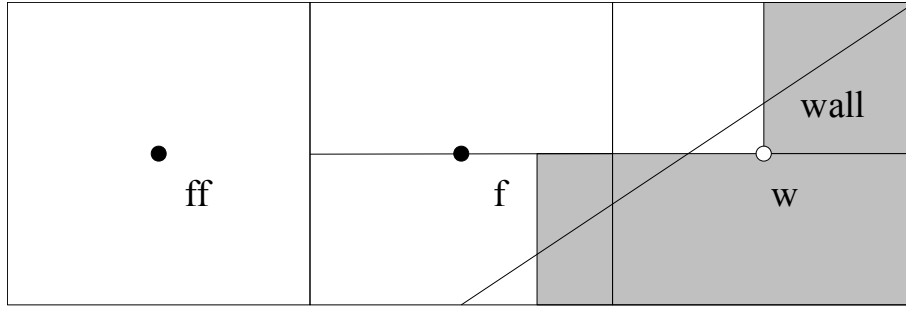


FIGURE 2.6: Representation of an inclined wall (the diagonal line) for the method proposed by Verberg and Ladd [8]. The shaded portions of the diagram represent the areas that are considered to be solid.

(2.167). Equations (2.165) to (2.168) are only valid if $\phi_w < 0.5$, otherwise none of the reflected population density is returned to cell f .

The authors note that the fluid velocity in the partially filled cells is only first order accurate. They subsequently make a better approximation by assuming that the population density $f_i^+(t)$ varies linearly along the line connecting point f to point w , i.e.

$$f_i(\mathbf{x}, t) = \frac{2(\mathbf{x} - \mathbf{x}_f)}{(1 + \phi_w)|\mathbf{x}_w - \mathbf{x}_f|} [f_i^+(\mathbf{x}_w, t) - f_i^+(\mathbf{x}_f, t)] + f_i^+(\mathbf{x}_f, t) \quad (2.169)$$

The propagation and bounceback of particles represented by $f_i^+(\mathbf{x}, t)$ is considered for every location in the relevant cells by integrating $f_i(\mathbf{x}, t)$ along the line between sites f and w , e.g.

$$f_k(x, t + 1) = \frac{1}{\phi_w} \int_{-1/2}^{\phi_w - 1/2} f_i(x, t) dx, \quad (2.170)$$

if this line is in the x -direction. For inclined boundaries, the method is adapted by splitting cells f and w such that a fraction of the population density is reflected in cell f , while the remainder bounces back in cell w and the boundary is represented as shown in figure 2.6. If the boundary is almost parallel to the horizontal direction, the population density would be bounced back over many cells.

Their method was much more accurate than the simple bounce back method for simulations of Poiseuille flow in inclined channels, and, in contrast to that method, the accuracy was not sensitive to the position of the lattice sites relative to the wall. For their simulations of flow past periodic arrays of disks and spheres, the drag coefficients were independent of the positions of the boundary nodes and agreed closely with the theoretical values.

2.9.2 Consistent methods

One can eradicate the slip velocity that arises from the bounce-back condition by forcing the unknown distribution functions to satisfy equations (2.2) and (2.3). Methods that use this are called consistent methods [101, 104, 105].

$$\begin{aligned}\sum_i f_i &= \rho \\ \sum_i f_i \mathbf{e}_i &= \rho \mathbf{v}\end{aligned}$$

Consistent methods can be used for walls with any velocity, as well as inlet or outlet boundary conditions [9, 101, 105]. At the wall, we know all components of the velocity, but not the density. The velocity in the plane of the inlet or outlet is generally taken to be zero, so if we use velocity boundary conditions, we also know the velocity but not the density. If we use pressure boundary conditions, we know the density and all but one components of the velocity. Equations (2.2) and (2.3) can be used to find a consistency condition to determine the unknown velocity or density. Some of the distribution functions will be unknown after streaming.

Noble et al. [101] used a FHP model with rest particles, i.e. D2Q7. In this model, the above equations give rise to three equations. There are two unknown distribution functions and either an unknown density or component of the velocity, so there are three unknowns in total.

The works in [100] and [105] provide a better theoretical understanding of the various boundary condition methods by analysing the slip velocity in terms of momentum exchange between the layer of boundary nodes and the adjacent fluid layer. If there is no slip velocity, the momentum exchange calculated from the distribution functions should be equal to the exchange carried by the vertical velocity plus the viscous force.

There are usually more unknowns than equations to determine them at the boundaries for the D2Q9 and D3Q15 models, so to close the system of equations, we assume that the bounceback condition is still correct for the nonequilibrium part of the particle distribution

for some of the directions, as proposed by Zou and He [9]. We have:

$$f_i - f_i^{(eq)} = f_{i+2} - f_{i+2}^{(eq)} \quad (2.171)$$

for the 2D case and

$$f_i - f_i^{(eq)} = f_{i+1} - f_{i+1}^{(eq)} \quad (2.172)$$

for the 3D case (see figure 2.1).

For the 2D case at the inlet or wall we know all but three distribution functions after streaming, so there are four unknowns but only three equations from (2.2) and (2.3). Bounceback of the nonequilibrium part normal to the boundary is used. For example, in the 2D case, for a node at the bottom wall in a tube with its axis in the x-direction, we know v_x and v_y , but need to determine f_2 , f_5 , f_6 and ρ . We have:

$$f_2 + f_5 + f_6 = \rho - (f_0 + f_1 + f_3 + f_4 + f_7 + f_8) \quad (2.173)$$

$$f_5 - f_6 = \rho v_x - (f_1 - f_3 - f_7 + f_8) \quad (2.174)$$

$$f_2 + f_5 + f_6 = \rho v_y + (f_4 + f_7 + f_8) \quad (2.175)$$

Equations (2.173) and (2.175) give the consistency condition:

$$\rho = \frac{1}{1 - v_y} [f_0 + f_1 + f_3 + 2(f_4 + f_7 + f_8)]. \quad (2.176)$$

Bounceback of the nonequilibrium part gives:

$$f_2 - f_2^{(eq)} = f_4 - f_4^{(eq)}. \quad (2.177)$$

The distribution functions f_5 and f_6 can then be determined from the equilibrium distributions for the D2Q9 model (equation (2.52) and table 2.1). We obtain:

$$f_2 = f_4 + \frac{2}{3}\rho v_y, \quad (2.178)$$

$$f_5 = f_7 - \frac{1}{2}(f_1 - f_3) + \frac{1}{2}\rho v_x + \frac{1}{6}\rho v_y, \quad (2.179)$$

$$f_6 = f_8 + \frac{1}{2}(f_1 - f_3) - \frac{1}{2}\rho v_x + \frac{1}{6}\rho v_y. \quad (2.180)$$

For a pressure boundary condition at the inlet, we have $\rho = \rho_{in}$, $v_y = 0$ and after streaming f_2 , f_3 , f_4 , f_6 and f_7 are known. v_x and f_1 , f_5 and f_8 are unknown. We have:

$$f_1 + f_5 + f_8 = \rho_{in} - (f_0 + f_2 + f_3 + f_4 + f_6 + f_7), \quad (2.181)$$

$$f_1 + f_5 + f_8 = \rho_{in} v_x + (f_3 + f_6 + f_7), \quad (2.182)$$

$$f_5 - f_8 = -f_2 + f_4 - f_6 + f_7. \quad (2.183)$$

Equations (2.181) and (2.182) give the consistency condition:

$$v_x = \frac{f_0 + f_2 + f_4 + 2(f_3 + f_6 + f_7)}{\rho_{in}}. \quad (2.184)$$

One then proceeds in the same way as for a wall node, using the bounceback for the non-equilibrium part of the particle distribution normal to the inlet, i.e.

$$f_2 - f_2^{(eq)} = f_4 - f_4^{(eq)}. \quad (2.185)$$

The corner nodes at the inlet and outlet need special treatment if we use pressure boundary conditions. Both the velocity and density are specified and there are five unknown distribution functions after streaming. There are five unknowns and three equations, so bounceback of the nonequilibrium part is used normal to both the wall and inlet or outlet. For example, for the bottom node at the inlet, we would use:

$$f_1 - f_3 = f_1^{(eq)} - f_3^{(eq)}, \quad (2.186)$$

$$f_2 - f_4 = f_2^{(eq)} - f_4^{(eq)}. \quad (2.187)$$

Using $U - x = v_y = 0$ and the equilibrium distribution functions, we obtain:

$$f_1 = f_3, \quad (2.188)$$

$$f_2 = f_4. \quad (2.189)$$

For complex geometries, we may have a boundary node that is on two walls, as shown in figure 2.7. In the case of a node such as A, f_1 , f_3 , f_5 , f_6 and f_8 need to be specified. Using no-slip conditions we have $v_x = v_y = 0$. Using bounceback for the normal distribution

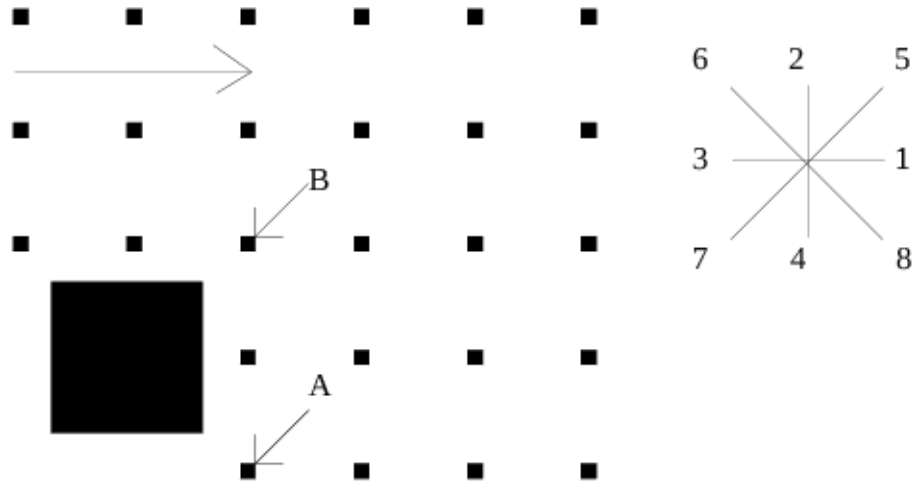


FIGURE 2.7: 2D lattice geometry for the flow over a backward facing step. The arrow shows the direction of flow.

gives $f_1 = f_3$, $f_2 = f_4$. Expressions of x and y momenta give:

$$f_5 - f_6 + f_8 = -(f_1 - f_3 - f_7) = f_7, \quad (2.190)$$

$$f_5 + f_6 - f_8 = -(f_2 - f_4 - f_7) = f_7. \quad (2.191)$$

From these two equations:

$$f_5 = f_7, \quad (2.192)$$

$$f_6 = f_8 = \frac{1}{2}[\rho - (f_0 + f_1 + f_2 + f_3 + f_4 + f_5 + f_7)], \quad (2.193)$$

but there are no more equations available to determine ρ , so it is assumed to be equal to that of its neighbouring node [9, 90].

For node B, there is a lack of freedom, so only f_5 can be specified [90]. One can choose:

$$f_5 = f_7. \quad (2.194)$$

This avoids the slip velocity in the diagonal direction.

For an inlet, outlet or wall node in the 3D case there are five unknown distribution functions, so there are six unknowns in total. Bounceback of the nonequilibrium part can be

used for all five of the distribution functions (equation (2.172)), so there are more equations than unknowns. In order to obtain the correct velocity parallel to the boundary, the unknowns are modified in the following way with a suitable choice of δ_α and $\delta_{\alpha+1}$, except the one normal to the boundary, which leaves the momentum normal to the boundary unchanged:

$$f_i \leftarrow f_i + \frac{1}{4}e_{i\alpha}\delta_\alpha + \frac{1}{4}e_{i(\alpha+1)}\delta_{\alpha+1}, \quad (2.195)$$

where α and $\alpha + 1$ are directions parallel to the boundary and For example, for the inlet boundary condition ρ is given by equation (2.2) and (2.3) gives:

$$\rho_{in}v_x = f_1 + f_7 + f_9 + f_{11} + f_{13} - (f_2 + f_8 + f_{10} + f_{12} + f_{14}). \quad (2.196)$$

Consistency of these determines v_x when pressure boundary conditions are used or ρ when velocity boundary conditions are used:

$$\rho_{in}v_x = \rho_{in} - [f_0 + f_3 + f_4 + f_5 + f_6 + 2(f_2 + f_8 + f_{10} + f_{12} + f_{14})]. \quad (2.197)$$

We use bounceback of the nonequilibrium parts for f_1, f_7, f_9, f_{11} , and f_{13} . f_7, f_9, f_{11} and f_{13} are modified:

$$f_i \leftarrow f_i + \frac{1}{4}e_{iy}\delta_y + \frac{1}{4}e_{iz}\delta_z. \quad (2.198)$$

We find:

$$f_1 = f_2 + \frac{2}{3}\rho_{in}v_x \quad (2.199)$$

$$f_i = f_{i+1} + \frac{1}{12}\rho_{in}v_x - \frac{1}{4}[e_{iy}(f_3 - f_4) + e_{iz}(f_5 - f_6)], i = 7, 9, 11, 13. \quad (2.200)$$

For incompressible models, $\rho\mathbf{v}$ must be replaced with \mathbf{v} .

The consistent methods by Noble et al. [101], Zou and He [9] and Inamuro et al. [104] give machine accuracy for Poiseuille flow in a 2D square duct, even for high values of τ , unlike the bounce-back method, because the slip velocity has been eradicated and the Lattice-Boltzmann method is of second order in space (i.e. it includes terms up to ϵ^2 and terms of order ϵ^3 arise only from third derivatives in space or higher; Poiseuille flow has no terms beyond second order). It is second order for other types of flow, such as flow through a pair of porous parallel plates. For steady flow in a 3D square duct, it is second

order [9, 90] but does not achieve machine accuracy. This may be because problems in resolving the four edges pose additional difficulties in resolving the flow. The density is also not uniform in cross section as it should be.

The disadvantage of this method is that two of the directions need to be perpendicular to the wall and some need to be parallel, so it can only be used for boundaries aligned with certain planes.

One possible approach to the boundary condition at the wall is to set the unknown distribution functions to the equilibrium distribution for the velocity of the wall. The velocity along the wall obtained with this assumption is not equal to the wall velocity, although the normal velocity is equal to that of the wall [104]. Inamuro et al. [104] compensate for this by setting the unknown distribution functions to the equilibrium ones given by equation (2.7), with the density replaced by ρ' and the velocity replaced by $\mathbf{v}_{wall} + \mathbf{v}'$, where \mathbf{v}' is a counter-slip velocity tangential to the wall. Since the density of the fluid, ρ , is unknown as well as ρ' , and, in N_D dimensions, the slip velocity has $N_D - 1$ components, there are $N_D + 1$ unknowns. Equations (2.2) and (2.3) provide $N_D + 1$ constraints on these unknowns, in a similar way to the methods described by Zou et al. [89] and Noble et al. [101]. It may not be possible to use the method for all non-axis aligned boundaries because the equations for ρ' and \mathbf{v}' require certain distribution functions.

To apply pressure boundary conditions at the inlet and outlet, Inamuro et al. [104] calculated the unknown distribution functions as follows:

$$f_{i,inlet} = f_{i,outlet} + w_i k, \quad (2.201)$$

where w_i is the weight for the equilibrium distribution function $f_i^{(eq)}$ given in table 2.1 and the constant k is chosen such that $\sum_i f_i = \rho_{in}$. The same method is applied at the outlet. This method requires the distribution function f_i to be determined by streaming at the outlet. At sites adjacent to both the wall and the inlet or outlet, this method is applied to the distribution functions for particles entering the wall or moving along its tangent, then the no-slip condition is applied to determine the unknown distribution functions for particles entering the fluid domain.

Hecht and Harting [106] showed how to extend Zou and He [9]’s method to nonflat boundaries, but one has to derive a separate scheme for every possible combination of neighbouring lattice sites to a boundary.

2.9.3 Comparison of body force with pressure boundary conditions

Kandhai et al. [18] compared body force to a pressure boundary condition method by considering fluid flow through an infinite vertical array of cylinders. The errors in the velocity, pressure and drag forces acting on each cylinder were calculated. Flow in a disordered porous medium was also simulated. They found that the body force approach is quite an accurate substitute for pressure boundaries, but for low Reynolds number flows and complicated geometries, pressure boundary conditions may be needed.

2.9.4 Equilibrium schemes

An alternative to the bounceback method is the equilibrium scheme [100]. One can assign the unknown equilibrium distribution functions to the equilibrium ones for the velocity and pressure of the boundary. However, the velocity calculated from the resulting equilibrium distribution functions will in general be different from the intended velocity of the boundary. A slip velocity is the special case of this when the velocity should be zero at the boundary. Melchionna et al. [96] used an equilibrium scheme for the pressure boundary conditions at the inlet and outlet.

2.9.5 Extrapolation methods

Extrapolation methods find the unknown distribution functions at the boundary sites by extrapolating from nearby fluid sites. Zhao-Li et al. [10, 102] proposed a nonequilibrium extrapolation method to calculate the distribution functions at the edge sites, f . Equations (2.5) and (2.6) represent the collision and streaming steps of the lattice-Boltzmann equation. We require $f_i^+(\mathbf{x}_w, t)$ to finish the streaming step at site f , as shown in figure 2.5. One can decompose $f_i(\mathbf{x}_w, t)$ into local equilibrium and nonequilibrium parts:

$$f_i(\mathbf{x}, t) = f_i^{(eq)}(\rho(\mathbf{x}_w, t), \mathbf{v}(\mathbf{x}_w, t)) + f_i^{(neq)}(\mathbf{x}, t), \quad (2.202)$$

where $f_i^{(eq)}$ and $f_i^{(neq)}$ are the equilibrium and nonequilibrium parts of f_i respectively. The density, velocity and nonequilibrium distributions are approximated by the following extrapolations involving sites f and ff :

$$\rho_w = \rho_f, \quad (2.203)$$

$$\mathbf{v}_w = \begin{cases} (\mathbf{v}_b + (\delta - 1)\mathbf{v}_f)/\delta, & \delta \geq 0.75 \\ \mathbf{v}_b + (\delta - 1)\mathbf{v}_f + \left(\frac{1-\delta}{1+\delta}\right)(2\mathbf{v}_b(t) + (\delta - 1)\mathbf{v}_{ff}), & \delta < 0.75 \end{cases}, \quad (2.204)$$

$$f_i^{(neq)}(\mathbf{x}_w, t) = \begin{cases} f_i^{(neq)}(\mathbf{x}_f, t), & \delta \geq 0.75 \\ \delta f_i^{(neq)}(\mathbf{x}_f, t) + (1 - \delta)f_i^{(neq)}(\mathbf{x}_{ff}, t), & \delta < 0.75 \end{cases}, \quad (2.205)$$

where $\rho_w = \rho(\mathbf{x}_w, t)$, $\rho_f = \rho(\mathbf{x}_f, t)$, $\mathbf{v}_w = \mathbf{v}(\mathbf{x}_w, t)$, etc., and δ is the normalised cut distance, given by equation (2.158). The post-collision distribution function at site w is given by

$$f_i^+(\mathbf{x}_w, t) = f_i^{(eq)}(\rho_w, \mathbf{v}_w) + (1 - \tau^{-1})f_i^{(neq)}(\mathbf{x}_w, t), \quad (2.206)$$

where τ is the dimensionless relaxation parameter.

The extrapolation in velocity is of order $(\Delta x)^2$. From the Chapman-Enskog expansion (equation (2.69)), it can be shown that the extrapolation of the nonequilibrium distribution is also of second order [102]. We have

$$f_i^{(neq)} = \epsilon f_i^{(1)} + O(\epsilon^2) \quad (2.207)$$

Node w is a neighbour of node f at a distance $\Delta x = O(L\epsilon)$ (equation (2.144)), and using equation (2.68), i.e. $\partial_{\mathbf{r}} = \epsilon \partial_{1\mathbf{r}}$, we have:

$$f_i^{(1)}(\mathbf{x}_w, t) = f_i^{(1)}(\mathbf{x}_f, t) + O(\epsilon) \quad (2.208)$$

Therefore, at node w , we have

$$f_i^{(neq)}(\mathbf{x}_w, t) = f_i^{(neq)}(\mathbf{x}_f, t) + O(\epsilon^2). \quad (2.209)$$

Setting the nonequilibrium distribution function equal to that at node f gives an error of order Δx^2 , since $\Delta x = O(L\epsilon)$. For the velocity boundary condition, we do not know the

pressure at site w , so this is also extrapolated from site f

$$p(\mathbf{x}_w, t) - p(\mathbf{x}_f, t) = (\mathbf{e}_2 \cdot \nabla p) \Delta x = O(\epsilon Ma^2), \quad (2.210)$$

using equations (2.68) and (2.113). We have:

$$f_i^{(eq)}(\mathbf{x}_w, t) = f_i^{(eq)}(p(\mathbf{x}_f, t), \mathbf{v}(O, t)) + O(\Delta x Ma^2). \quad (2.211)$$

If the Reynolds number, $Re = \frac{vD}{\nu}$ is kept constant as Δx is reduced, i.e. the width of the channel in lattice units is increased, and the viscosity is kept the same, i.e. τ is constant, then $v \propto \frac{1}{D}$. The speed of sound is $\frac{1}{\sqrt{3}}$ in lattice units, so the Mach number, $Ma \propto \frac{1}{D}$. Therefore, the error from the extrapolation of pressure is of order Δx^3 . [102] achieved second order accuracy in space with Poiseuille flow, porous plate flow and cavity flow when comparing their results with an analytical solution and keeping the Reynolds number constant.

The wall may be curved in such a way that site ff is solid, as well as site w , and therefore the information that may be required from that site is not available. Zhao-Li et al. [102] do not explain how to deal with this case.

Zhao-Li et al. [102] explain how this method can also be used for pressure boundary conditions and show that it is expected to have the same accuracy.

Fang et al. [14] use a similar method that also extrapolates the information from sites f and ff to find the distribution function at site w . For the density and nonequilibrium distribution, equations (2.212) and (2.214) are used instead of equations (2.203) and (2.205) respectively, and the velocity is extrapolated using equation (2.213) for all δ , not $\delta \geq 0.75$.

$$\rho_w = \rho_f, \quad (2.212)$$

$$\mathbf{v}_w = (\mathbf{v}_b + (\delta - 1)\mathbf{v}_f)/\delta, \quad (2.213)$$

$$f_i^{(neq)}(\mathbf{x}_w, t) = 2f_i^{(neq)}(\mathbf{x}_f, t) - f_i^{(neq)}(\mathbf{x}_{ff}, t). \quad (2.214)$$

The relative errors arising from the application of the method are second order in space, by similar arguments to those earlier in the section. Fang et al. [14] only consider a lattice site to be a fluid site if it is inside the wall and the wall does not cross the unit square

centred on the lattice site. Therefore, the normalised cut distances lie within the range $0.5 \leq \delta < 1.5$.

Filippova and Hanel [107, 108] have also developed an extrapolation method to find the distribution functions at site f that cannot be determined by streaming. For the clarity of the following discussion, we state the lattice BGK equation (equation (2.4)) at site f for the distribution function f_i , such that the lattice vector \mathbf{e}_i points away from the solid site w :

$$f_i(\mathbf{x}_f, t + \Delta t) = (1 - \tau^{-1})f_i(\mathbf{x}_w, t) + \tau^{-1}f_i^{(eq)}(\rho(\mathbf{x}_w, t), \mathbf{v}(\mathbf{x}_w, t)). \quad (2.215)$$

Since the distribution functions coming from site w are unknown, this is replaced with

$$f_i(\mathbf{x}_f, t + \Delta t) = (1 - \tau^{-1})f_k(\mathbf{x}_f, t) + a_1\tau_i^{-1}f_k^{(eq)}(\mathbf{x}_w, t) + a_2\tau_i^{-1}f_k^{(eq)}(\mathbf{x}_f, t), \quad (2.216)$$

where $\mathbf{e}_k = -\mathbf{e}_i$ is the lattice direction pointing towards site w , the relaxation parameter τ_i^{-1} can be varied, and $a_1a_2 = 0$, $a_1^2 + a_2^2 = 1$. The equilibrium distribution at site w is calculated in the similar way as in [10] with the following exceptions. First, the 2nd and 3rd terms use the velocity at site f , not site w , i.e. we have

$$f_i^{(eq)}(\mathbf{x}_w, t) = w_i\rho_f \left(1 + 3\frac{\mathbf{e}_i \cdot \mathbf{v}_w}{c^2} + \frac{9}{2}\frac{(\mathbf{e}_i \cdot \mathbf{v}_f)^2}{c^4} - \frac{3}{2}\frac{\mathbf{v}_f \cdot \mathbf{v}_f}{c^2} \right) \quad (2.217)$$

instead of equation (2.7). Second, the velocity \mathbf{v}_b is calculated by equation (2.204), as if $\delta \geq 0.75$, regardless of its actual value. This causes instability as $\delta \rightarrow 0$. Equation (2.216) reduces to the simple bounce-back condition if $\tau_i^{-1} = 0$. If $\tau_i = \tau$ and $a_2 = 0$, the equation reduces to the lattice-BGK equation for $f_i(\mathbf{x}_f, t + \Delta t)$ with $f_i(\mathbf{x}_w, t)$ replaced with $f_k(\mathbf{x}_f, t)$. Filippova and Hanel [107, 108] use the following values for τ_i^{-1} , a_1 and a_2 .

$$\begin{aligned} \tau_i^{-1} &= \tau^{-1}(2\delta - 1), & a_1 &= 1, & a_2 &= 0, & \delta &\geq 0.5; \\ \tau_i^{-1} &= \tau^{-1}\left(\frac{2\delta-1}{1-\tau^{-1}}\right), & a_1 &= 0, & a_2 &= 1, & \delta &< 0.5. \end{aligned} \quad (2.218)$$

Equation (2.216) is only valid for stationary boundaries, i.e. $\mathbf{v}_b = 0$. For moving boundaries, the term $-6w_i\mathbf{v}_b \cdot \mathbf{e}_k$ is added to the RHS [108].

2.9.6 Methods involving extrapolation in time

Mazzeo et al. [93, section 3.1] developed a new extrapolation method. This method is used in HemeLB for patient-specific simulations of cerebral blood flow, as described in section 2.3. Results for simulations of a 2D channel and a 3D square duct using this method are presented in Mazzeo et al. [93, section 3.1] and [92]. It is applied as follows. Instead of carrying out collision at the sites adjacent to the wall, labelled f in figure 2.5, the post-collisional distribution functions are set to the equilibrium ones with density $\rho(\mathbf{x}, t)$ and the velocity to be prescribed at site f , which is assumed to be the same as the velocity of the wall, i.e.

$$f_i^+(\mathbf{x}_f, t) = f_i^{(eq)}(\rho(\mathbf{x}_f, t), \mathbf{v}_b). \quad (2.219)$$

At all other fluid sites, collision is carried out as usual, followed by streaming. However, at a site of type f , the distribution functions that cannot be determined by streaming, which we call the unknown distribution functions, are set to the postcollisional ones, i.e.

$$f_i(\mathbf{x}_f, t + \Delta t) = f_i^+(\mathbf{x}_f, t). \quad (2.220)$$

This is almost equivalent to an extrapolation of the unknown distribution functions in time, $f_i(\mathbf{x}_f, t + \Delta t) = f_i(\mathbf{x}_f, t + \Delta t)$. Such an extrapolation is reasonable provided that the slow flow condition, $T \gg \frac{L}{c}$, described in section 2.8, is satisfied. One can see this from the Taylor expansion of the distribution functions in terms of time: $f_i(\mathbf{r}, t + \Delta t) = f_i(\mathbf{r}, t) + \Delta t \frac{\partial f_i}{\partial t}$ [109]. $\Delta x = c\Delta t$, so the method is first order accurate in time and space. The explanations of this method in [92, 93] is slightly different, but the method is exactly equivalent.

The method can also be used for pressure boundary conditions; the post-collisional distributions are set to the equilibrium distributions with a prescribed density ρ_{set} and the velocity at the end of the previous time step, i.e. equation (2.219) is replaced with:

$$f_i^+(\mathbf{x}_f, t) = f_i^{(eq)}(\rho_{set}, \mathbf{v}(\mathbf{x}_f, t)). \quad (2.221)$$

At a fluid site adjacent to a wall and an inlet or outlet, the density and velocity can be prescribed, i.e.

$$f_i^+(\mathbf{x}_f, t) = f_i^{(eq)}(\rho_{set}, \mathbf{v}_b). \quad (2.222)$$

In contrast to the extrapolation method by Zhao-Li et al. [10], this method assumes that the pressure and/or velocity is equal to that at the boundary, i.e. it does not take into account the distance from the boundary. Interpolation could be carried out to do this.

Since this method sets the nonequilibrium parts of the post-collisional distribution functions to zero, the deviatoric stress tensor at the boundary site is zero immediately after this stage. This may cause inaccuracy, particularly when it is applied at sites adjacent to the wall, because the shear stress is expected to reach a maximum there if the flow is parabolic. For example, for Poiseuille flow in a 3D cylinder in the x -direction, the velocity is given by equation (1.12). The y and z -components of the velocity are zero. The component of the stress $\tau_{xr} = \eta \frac{\partial v_x}{\partial r}$, from equation (1.3). Therefore, $\tau_{xr} = -\frac{r \nabla p}{2\nu\rho}$, where ν is the kinematic viscosity and ρ is the density. The maximum is clearly at $r = R$. When the flow fields are calculated at the end of the time step, after streaming, the distributions at the boundary sites are no longer given one of the equations (2.219) to (2.222), so the nonequilibrium parts of the distribution functions are nonzero and the stress is nonzero, but it may still be inaccurate.

2.9.7 Grid refinement

Boundary condition methods that do not take into account the distance from the lattice sites at the edge of the fluid domain to the boundary, such as the bounce-back condition, impose velocity boundary conditions on a staircased boundary, leading to large simulation errors for nonflat boundaries, as described in section 2.9.1. This can be improved by using a more sophisticated boundary condition method. Alternatively, local grid refinement can be applied to regions where large changes of solution are expected. Filippova and Hanel [108] proposed a scheme to apply this to the LBM. The grid is refined by a factor n , and the timestep is reduced to $\frac{\Delta t}{n}$. In order to ensure that the viscosity, which is given by equation (2.11), is the same for the coarse and fine grids, the values of τ for these grids are related by

$$\tau_{fine} = \frac{1 + n(2\tau_{coarse} - 1)}{2}. \quad (2.223)$$

Since the velocity and density and their derivatives must be continuous over the interface between the two grids, we have the following relationships between the post-collisional

distribution functions:

$$f_i^{+,coarse} = f_i^{(eq),fine} + (f_i^{+,fine} - f_i^{(eq),fine}) \left(\frac{n(1 - \tau_{coarse}^{-1})\tau_{fine}^{-1}}{(1 - \tau_{fine}^{-1})\tau_{coarse}^{-1}} \right), \quad (2.224)$$

$$f_i^{+,fine} = f_i^{(eq),coarse} + (f_i^{+,coarse} - f_i^{(eq),coarse}) \left(\frac{(1 - \tau_{fine}^{-1})\tau_{coarse}^{-1}}{n(1 - \tau_{coarse}^{-1})\tau_{fine}^{-1}} \right). \quad (2.225)$$

2.10 Further applications of the lattice-Boltzmann method

Kandhai et al. [18] simulated the flow through a porous medium. Dimensional analysis suggests that, for a constant body force, the saturation time t_{sat} needed to reach the steady state is of the form:

$$t_{sat} \propto \frac{R_{pore}^2}{\nu}, \quad (2.226)$$

where R_{pore} is the characteristic length of pore in the system. Saturation times can be very long for high porosities. Tens of thousands of time steps may be needed, so a constant body force may be computationally inefficient, especially when one is only interested in the steady-state solution. The iterative momentum relaxation method proposed by Kandhai et al. [18] reduces computing time by adjusting the force at certain intervals of time to the total momentum loss in the fluid due to viscous forces. Since the LBM is very useful for simulating fluid flow through complex geometries, Filippova and Hanel [107] used it to simulate gas particle flow in filters in 2D. The drag force on each particle was calculated using Stokes' law for spherical particles. A particle was deposited when it touched part of the filter or another particle that had been deposited. At that point, the lattice sites inside the region of the particles became solid. The collection efficiency of the filter matched experimental results closely.

Ladd [91] proposed a method for simulating a colloidal system using the LBM. The bounce-back method was suitable for dealing with the nonflat boundaries between the solid particles and the fluid domain and it was adjusted to take into account the non-zero velocities of the particles, as described in section 2.9.1.

Bernaschi et al. [97] developed a lattice-Boltzmann code called MUPHY for carrying out multi-scale simulations. They have coupled lattice-Boltzmann and molecular dynamics methods and hence simulated the translocation of DNA across a multi-hole membrane, which was driven by a force from an electric field. The lattice spacing was 50nm, therefore

thermal effects were important and were taken into account by a stochastic forcing term applied to each lattice site. The timesteps used to integrate the equation of motion of each polymer bead were much smaller than the lattice-Boltzmann timesteps. The translocation of DNA is an important processes occuring during a viral infection by phages, inter-bacterial DNA transduction and gene therapy. In addition, understanding this process may open a way to fast gene-sequencing by sensing the base-sensitive electronic signal as the biopolymer passes through a nanopore.

2.11 Application to non-Newtonian fluids

Blood is not a Newtonian fluid, as shown in section 1.6. To make the simulation of blood flow using Lattice-Boltzmann methods more realistic, non-Newtonian effects should be included. In this section, the attempts to incorporate non-Newtonian behaviour into Lattice-Boltzmann simulations and the characterisation of non-Newtonian fluids are discussed.

In a non-Newtonian fluid, the stress is not directly proportional to the strain rate, but a function of it. Non-Newtonian fluids are often categorised into idealised types of fluids. Power-law fluids have the following stress-strain relationship.

$$\sigma = k \left(\frac{\partial v_x}{\partial y} \right)^n \quad (2.227)$$

They can be divided into shear thickening fluids, where, in which the additional stress needed to increase the velocity of the fluid increases with strain rate. In a shear thinning fluid, less and less additional stress is required to increase the velocity as the strain rate increases, so it flows more easily. A third type is a Bingham fluid, which can bear some shear stress before it starts flowing, but once it starts flowing, the stress increases linearly with strain rate.

$$\begin{aligned} \frac{\partial v_x}{\partial y} &= 0, & \sigma &< \sigma_0 \\ \frac{\partial v_x}{\partial y} &= \frac{\sigma - \sigma_0}{k}, & \tau &\geq 0 \end{aligned} \quad (2.228)$$

It is sometimes difficult to characterise the behaviour of a fluid, but one can define an apparent viscosity [25, 110–112], so that equation (1.4) for Newtonian flow can still be

used. For a power-law fluid, the viscosity is given by:

$$\eta = k \left(\frac{\partial v_x}{\partial y} \right)^{n-1} \quad (2.229)$$

The apparent viscosity increases with strain rate for a shear thickening fluid and decreases for a shear thinning fluid.

Fluids may be time-independent (purely viscous) [110], so the shear stress depends only on the shear rate, as in the models described above. In time-dependent fluids, the shear stress is a function of both the magnitude and the duration of the shear rate and possibly of the time lapse between consecutive applications of the shear stress. The flow curve can involve a hysteresis loop whose shape depends on the rate at which the shear stress is applied. One example of this is viscoelastic fluids, which show partial elastic recovery upon the removal of a deforming shear stress. The viscosity may then be expressed as a complex number. The elastic modulus of blood is usually very small, as shown in section 1.6, so in this study, it will be modelled as a purely viscous fluid.

The equations quoted so far have assumed that the flow is a simple shear flow, so the velocity is always in the same direction and does not vary with z . A more difficult problem is how to generalise the stress-strain-rate relationship to three dimensions. For a Newtonian fluid, the stress tensor in the Navier-Stokes equations is (see equation (1.3)):

$$\sigma_{ij} = 2\eta\epsilon_{ij}, \quad (2.230)$$

where the tensor on the right is the strain-rate tensor:

$$\epsilon_{ij} = \frac{1}{2} \left(\frac{\partial v_i}{\partial x_j} + \frac{\partial v_j}{\partial x_i} \right) \quad (2.231)$$

Writing this out explicitly:

$$\sigma = \eta \begin{pmatrix} 2\frac{\partial v_x}{\partial x} & \frac{\partial v_x}{\partial y} + \frac{\partial v_y}{\partial x} & \frac{\partial v_x}{\partial z} + \frac{\partial v_z}{\partial x} \\ \frac{\partial v_y}{\partial x} + \frac{\partial v_x}{\partial y} & 2\frac{\partial v_y}{\partial y} & \frac{\partial v_y}{\partial z} + \frac{\partial v_z}{\partial y} \\ \frac{\partial v_z}{\partial x} + \frac{\partial v_x}{\partial z} & \frac{\partial v_z}{\partial y} + \frac{\partial v_y}{\partial z} & 2\frac{\partial v_z}{\partial z} \end{pmatrix}. \quad (2.232)$$

For a power-law fluid, one might expect:

$$\sigma = \eta \begin{pmatrix} 2 \left(\frac{\partial v_x}{\partial x}\right)^n & \left(\frac{\partial v_x}{\partial y}\right)^n + \left(\frac{\partial v_y}{\partial x}\right)^n & \left(\frac{\partial v_x}{\partial z}\right)^n + \left(\frac{\partial v_z}{\partial x}\right)^n \\ \left(\frac{\partial v_y}{\partial x}\right)^n + \left(\frac{\partial v_x}{\partial y}\right)^n & 2 \left(\frac{\partial v_y}{\partial y}\right)^n & \left(\frac{\partial v_y}{\partial z}\right)^n + \left(\frac{\partial v_z}{\partial y}\right)^n \\ \left(\frac{\partial v_z}{\partial x}\right)^n + \left(\frac{\partial v_x}{\partial z}\right)^n & \left(\frac{\partial v_z}{\partial y}\right)^n + \left(\frac{\partial v_y}{\partial z}\right)^n & 2 \left(\frac{\partial v_z}{\partial z}\right)^n \end{pmatrix}. \quad (2.233)$$

In this case, the apparent viscosity would be a fourth-order tensor and would be very difficult to define. In the lattice-Boltzmann equation with the Bhatnagar-Gross-Krook collision operator (equation (2.4)), the viscosity is a scalar, so the method would have to be modified to accommodate a fluid that behaves like this, which could ruin the excellent parallel performance of the Lattice-Boltzmann.

However, a fluid cannot obey equation (2.233) because the shear stress and shear rate are measurable quantities and the law that relates them must be rotationally invariant, because with any phenomenon, viewing it from a different angle should make no difference to the physical laws. Define:

$$\mu_{ij} = \frac{\partial v_i}{\partial x_j} \quad (2.234)$$

For any purely viscous fluid, we have:

$$\sigma_{ij} = f(\mu_{ij}) + f(\mu_{ji}) \quad (2.235)$$

In a different frame of reference, we should obtain.

$$\sigma_{i'j'} = f(\mu_{i'j'}) + f(\mu_{j'i'}) \quad (2.236)$$

A rotation matrix relates the tensors in the old and new frames of reference:

$$\sigma_{i'j'} = \mathbf{R}\sigma_{ij}, \mu_{i'j'} = \mathbf{R}\mu_{ij} \quad (2.237)$$

Therefore:

$$f(\mathbf{R}\mu_{ij}) + f(\mathbf{R}\mu_{ji}) = \mathbf{R}\sigma_{ij} = \mathbf{R}f(\mu_{ij}) + \mathbf{R}f(\mu_{ji}), \quad (2.238)$$

using (2.235) This can only be satisfied if:

$$f(\mu_{ij}) = k\mu_{ij}, \quad (2.239)$$

where k is a scalar. Then:

$$\mathbf{R}f(\mu_{ij}) = \mathbf{R}(k\mu_{ij}) = k\mathbf{R}\mu_{ij} = f(\mathbf{R}\mu_{ij}) \quad (2.240)$$

as required for equation (2.238).

The scalar k is the apparent viscosity, which is a function of the different components of the strain rate. The value of k must be independent of the basis in which the strain rate is measured. Therefore, k is a function of three invariants of the strain rate tensor [110, 111], i.e.

$$\sigma_{ij} = \eta(I, II, III) \left(\frac{\partial v_i}{\partial x_j} + \frac{\partial v_j}{\partial x_i} \right). \quad (2.241)$$

The studies state that this simple relation has been used, but not that it has been proven to hold, suggesting that some validation of this is still required. For an incompressible fluid, the first invariant vanishes, and for a simple shear flow even the third invariant vanishes, so we have:

$$\eta = \eta \left(\sqrt{\frac{II}{2}} \right), \quad (2.242)$$

e.g.

$$\eta = \eta_0 \left(\sqrt{\frac{II}{2}} \right)^{n-1} \quad (2.243)$$

for a power law fluid. Equation (2.242) is dimensionally correct because II has dimensions of the square of strain rate. It is given by [110]:

$$II = 2 \left[\left(\frac{\partial v_x}{\partial x} \right)^2 + \left(\frac{\partial v_y}{\partial y} \right)^2 + \left(\frac{\partial v_z}{\partial z} \right)^2 \right] + \left(\frac{\partial v_x}{\partial y} + \frac{\partial v_y}{\partial x} \right)^2 + \left(\frac{\partial v_x}{\partial z} + \frac{\partial v_z}{\partial x} \right)^2 + \left(\frac{\partial v_y}{\partial z} + \frac{\partial v_z}{\partial y} \right)^2, \quad (2.244)$$

or equivalently [112]:

$$II/2 = \sqrt{\epsilon_{ij} \dot{\epsilon}_{ij}}. \quad (2.245)$$

This apparent viscosity is a scalar quantity, so one can use it directly in the Lattice-Boltzmann method, which was done for a power law fluid with $n < 1$ in [112]. It may be

calculated at the beginning of each time step for every lattice point based on the velocities that were calculated at the end of the previous time step. As explained in section 2.2, the stress can be calculated directly from the distribution functions instead of using a finite difference method to find the velocity gradients [59, 90, 91], which will make the calculation faster and more accurate, as shown in equation (2.246).

$$\sigma_{\alpha\beta} = - \left(1 - \frac{1}{2\tau}\right) \sum_i f_i^{neq} e_{i\alpha} e_{i\beta} \quad (2.246)$$

For a non-Newtonian flow, the strain rate is related to the stress by equation (2.241), i.e.

$$2\eta(t)\epsilon_{\alpha\beta} = - \left(1 - \frac{1}{2\tau}\right) \sum_i f_i^{neq}(t) e_{i\alpha} e_{i\beta}. \quad (2.247)$$

Substituting equation (2.242) into this gives

$$2\eta(II/2)\epsilon_{\alpha\beta} = - \left(1 - \frac{1}{2\tau}\right) \sum_i f_i^{neq}(t) e_{i\alpha} e_{i\beta}, \quad (2.248)$$

which can be used to update the viscosity, η , at every time step. Each component of the stress tensor depends on all the components of the strain tensor. Therefore, the set of equations we obtain is not straightforward to invert to find the apparent viscosity.

Replacing $\eta(t)$ with $\eta(t - \Delta t)$ in equation (2.247) gives

$$\epsilon_{\alpha\beta} = - \left(\frac{1}{2\eta(t - \Delta t)} - \frac{1}{4\tau\eta(t - \Delta t)} \right) \sum_i f_i^{neq}(t) e_{i\alpha} e_{i\beta}, \quad (2.249)$$

from which it is very straightforward to estimate the strain rate. Equation (2.245) can then be used to find the second invariant of the strain rate, from which the viscosity $\eta(t)$ can be estimated with equation (2.242). With this approach, the lattice-Boltzmann method should remain fast and accurate if the time step is short compared to the time over which the viscosity undergoes a major change, but instabilities may arise due to the replacement of $\eta(t)$ with $\eta(t - \Delta t)$ and the calculation of the viscosity will be less accurate than using equation (2.248).

No fluids obey the power law perfectly. For example, pseudoplastic fluids are Newtonian at low shear rates, shear thinning fluids that obey a power law at high shear rates and they require a transition region in between. A modified power law can describe the apparent

viscosity more accurately. [110, 111].

$$\eta = \frac{\eta_0}{1 + \frac{\eta_0}{k}(2\dot{\epsilon})^{1-n}}. \quad (2.250)$$

Park and Lee [110] investigated the pressure drop in a rectangular duct for steady flow. The friction factor, or resistance of the duct was calculated, as explained in section 1.5, as a function of the Reynolds number. An iterative method was used, in which the velocity profile was initially set to the analytic one for a rectangular duct, the viscosities were calculated based on the strain rates, then the new velocities were calculated. There was good agreement between theory and experiment. Similar work was carried out by the same authors to model heat transfer [111]. The data was compared with experimental data and was much more accurate than using a simple power law, which leads to large errors in the Newtonian region because the apparent viscosity becomes infinite at zero shear rate which occurs at maxima or minima in velocity. The studies also demonstrate the validity of equation (2.242).

Casson's model is one of the most common models for blood viscosity. It requires a shear stress before it starts flowing, like a Bingham fluid, but with an equation in the form of a modified power law [25].

$$\sqrt{\sigma} = \sqrt{\sigma_0} + \sqrt{\eta\dot{\epsilon}}. \quad (2.251)$$

The apparent viscosity is:

$$\eta = \left(\sqrt{\frac{\sigma_0}{II}} + \sqrt{\eta_0} \right)^2. \quad (2.252)$$

In this study, the Navier-Stokes equations were solved with a finite-element approach. Both finite-element and lattice-Boltzmann methods cannot cope with very high viscosities. In [25], the expression was modified as follows to prevent the viscosity from becoming infinite at zero shear rate:

$$\eta = \left[\sqrt{\sigma_0 \left(\frac{1 - \exp(-mII)}{II} \right)} + \sqrt{\eta_0} \right]^2. \quad (2.253)$$

In [112], the authors state that lattice-Boltzmann simulations are less accurate and take more time to converge for very high values of τ , so τ was limited to 10. However, [101] achieved machine accuracy for 2D Poiseuille flow for values of τ up to 50.0, because accurate boundary conditions were used (sections 2.8 and 2.9).

Sullivan et al. [112] studied the flow of a power-law fluid through porous media. In the past, numerical models had used idealised porous media by assuming that each pore was a parallel pipe. Analytical solutions relating the flow rate to the pressure drop and density of pores had been derived from this. The models required correction factors in order to agree with experiment. Numerical models with various arrangements of spheres to represent the pores better describe the nature of porous media. The analytical solutions could be corrected by changing the constants of proportionality. The analytical solution was extended to power law fluids. The Lattice-Boltzmann method was used in this study to simulate the flow and good agreement with the established theory was obtained.

Chapter 3

A new method for lattice-Boltzmann simulations of fluid flow through axially symmetric elastic systems

The simulation of viscous fluid flow in elastic pipes is an area of considerable practical interest. For instance, three-dimensional (3D) computational fluid dynamics (CFD) simulations of cerebral blood flow have enhanced our understanding of cerebrovascular diseases, as explained in section 1.8. These studies usually assume that the arterial walls are rigid, but the displacement of the wall could influence or be influenced by cardiovascular disease and is likely to have important effects on the pressure, velocity and stress fields, as explained in section 1.10.

The effect of elasticity on fluid flow is also paramount in models of the bladder and urinary tract [113]. It is necessary to understand the dynamics of elastic pipes carrying fluids in many engineering projects, including nuclear reactor components, marine drilling and oil pipelines because, in practice, the pipes are not completely rigid [114, 115]. Studies of the response of elastic pipes to various flow conditions include a theoretical analysis of the deflection of oil pipelines [114, 115], and a demonstration of a finite-element method for some simple types of piping systems [115].

Many of the systems of interest require three-dimensional simulations in complex geometries. These simulations must run efficiently on multicore computers if the results are to be obtained within a reasonable timescale, especially in the case of interactive simulations. This is particularly important in simulations of cerebral blood flow, especially if these simulations are to be used to plan neurosurgery, as discussed in section 2.3. The lattice-Boltzmann method (LBM) [16, 17, 75, 88, 89] is ideally suited to computation on multicore machines because the algorithm for calculating the flow fields at each lattice site depends only on information from its nearest neighbours [16], as explained in section 2.2. The efficiency can be improved further if buffers are set up for every processor to store information that is sent to or received from neighbouring processors, as described in section 2.3. If the effects of vessel elasticity are to be included in a large lattice-Boltzmann simulation of fluid flow in complex geometries, it is essential that the method retains the aforementioned characteristics.

For the method developed in this chapter, no fluid nodes are created or destroyed as the wall moves over the lattice sites, as explained in section 3.5.1, in contrast to the lattice-Boltzmann schemes involving moving boundaries in the literature, which are reviewed in section 3.1. Keeping the number of lattice sites constant would make it easy to set up buffers for the information exchanged between processors. It would also not have a dramatic effect on the accuracy of the simulation, as explained in section 3.5.1.

It is also important that methods for simulating fluid flow in elastic pipes are sensitive to small displacements. For example, experimental data shows that the cross-sectional areas of the vertebral and internal carotid arteries, the largest arteries in the brain, are approximately 10% larger at a static pressure of 120 mmHg than they are at 80 mmHg [77], as explained in section 1.10. Cerebral arteries branch out and become smaller and smaller so, if the lattice-Boltzmann method is used, the smallest arteries may be only a few lattice points across and if the cross-sectional area of these only changes by 10%, displacements of a fraction of the lattice spacing must be considered. Furthermore, methods for simulating cerebral blood flow must be stable and accurate for realistic values of the dimensionless parameters, such as the Reynolds number, which is given by $Re = \rho v_{\max} D / \eta$, where ρ is the density of the fluid, v_{\max} is its maximum speed, η is the dynamic viscosity, and D is the diameter of the vessel, from equation (1.5). These parameters vary widely between human subjects, but $Re > 100$ is typical in the larger cerebral arteries and typical parameters are

given in section 1.6. For example, in the internal carotid artery, we have $\rho \approx 1000 \text{kg m}^{-3}$, $\eta \approx 3.5 \times 10^{-3} \text{Pa s}$, $D \approx 3 \times 10^{-3} \text{m}$, $v_{max} \approx 0.7 \text{m s}^{-1}$, which gives $Re = 600$.

The work in this chapter is largely taken from Doctors et al. [116]. In this chapter, a new method for carrying out lattice-Boltzmann simulations of fluid flow in 3D elastic pipes is proposed whilst all the issues described above are addressed. It is organised as follows. In section 3.1, some existing methods for including wall elasticity in lattice-Boltzmann models are described. In section 3.2, I describe the equations of motion for the elastic walls and summarise lattice-Boltzmann scheme used in this study. The accuracy of several different combinations of lattice-Boltzmann boundary condition methods and their suitability for 3D computations of fluid flow through elastic vessels is tested in section 3.3. This is also done for 2D computations in section 3.4 because some of the simulations in chapter 5 require such simulations at higher Reynolds numbers than those achieved in the tests of the boundary condition methods in section 3.3. Section 3.5 contains a description of our method for simulating fluid flow through elastic vessels and details of the analytical solution with which the numerical results are compared. Section 3.6 contains results concerning the accuracy of the simulation method and its computational cost. Section 3.7 discusses the implications of the results. The conclusions are presented in section 3.8.

3.1 Summary of lattice-Boltzmann fluid flow simulations in elastic pipes

A few modifications to lattice-Boltzmann methods have already been proposed to simulate fluid flow in distensible vessels.

Fang et al. [14, 117] simulated fluid flow through a channel oriented in the x -direction. The wall was allowed to move in the direction of the normal. The wall was divided into segments of length one lattice spacing, which were allowed to move in the y -direction. The force on each wall segment was linear in the displacement and the equation of motion of the wall was integrated at each time step to find its new position and velocity. The velocity of the fluid next to the wall was equal to the velocity of the wall because no-slip and no-penetration conditions were applied there. Steady and pulsatile flow was simulated in both studies. The position of the wall agreed very closely with the analytical solution

when the simulations had reached a steady state. Pulsatile flow was also simulated and compared with experimental results from the aorta. The agreement in [117] appears to be better than in [14].

The dimensionless relaxation parameter, $\tau = 1$ and 2 in [117] and [14] respectively. The ratio of the mass of a wall of length Δx , the lattice spacing, to the mass of the fluid at a lattice site was 500 in both studies, which is unrealistically high for a simulation of blood flow. For blood flow, The density of the arterial walls, ρ_w is approximately equal to the density of the blood ρ_f . For large arteries, the thickness, h , is approximately one-fifth of the radius, R , as described in section 1.10. Therefore, for a realistic 2D simulation, the ratio of the mass of a segment of the wall of length Δx , the lattice spacing, to the mass of the fluid at a lattice site is expected to be $\frac{R}{5\Delta x}$, where R is the half-width. In [14], $R \approx 5$, so this ratio would be of $O(1)$.

In both of these studies, three types of lattice sites were defined: if the wall crossed the unit square centred on a lattice site, the site was defined to be a boundary site, otherwise, it was a fluid site if it lay inside the channel and a solid site if it lay outside. However, the simulation methods differed slightly. In their 1998 study [117], the velocity of the fluid at the boundary nodes was calculated by a quadratic interpolation or extrapolation, which seems to assume that a Poiseuille flow will occur, since the velocity is quadratic in the distance from the centreline. The density was given by a second-order extrapolation, then the distribution functions that were unknown after streaming were calculated from the method by Zou et al. [89]. When a boundary node became a fluid node, the distribution functions were not changed. The force on each segment of the wall was given by considering the change in momentum at the boundary nodes due to the distribution functions. While the method is accurate, it is unsuitable for large simulations that run in parallel and the difficulties arising with buffers when fluid nodes are created or destroyed.

In [14], the distances from the wall to the fluid sites adjacent to boundary sites in the horizontal, vertical and diagonal directions were calculated. An extrapolation method similar to that by Zhao-Li et al. [102], is applied at the wall. It is described in section 2.9.5. When a boundary site became a fluid site, the distribution functions were set to the average of values given by second-order extrapolation in the directions pointing towards solid sites, which conserves mass, as explained in section 5.6.4. While the distributions at each boundary site still required information from the first and second neighbouring fluid

sites in particular directions, only distributions pointing towards fluid sites were required, for which streaming between the boundary sites was not needed, in contrast to [117]. Therefore, each site only required information from its nearest neighbours for this part of the method.

Hoekstra *et al* [118] compared the accuracy of simulations that use the velocity boundary condition method of Fang *et al* [14] to those of Zou and He [9] and Bouzidi [7], while Fang *et al*'s method was used for creation and destruction of fluid nodes. In contrast to that study, the wall was massless. The simulation error in the displacement of the wall relative to the analytical solution was approximately equal when the Fang or Zou and He velocity boundary condition method was used, but it was ten times larger for the Bouzidi boundary condition. This error was also first order in the grid spacing. Fang *et al*'s method was validated for pulsatile flows by comparing the wavelength and attenuation constant of the waves in the wall displacement to theoretical solutions derived by Womersley. The wavelengths agreed within the error in estimating them from the simulation, while the attenuation constants agreed well for Womersley numbers greater than 6. The Womersley number is given by $\alpha = R\sqrt{\omega/\nu}$, where R is the radius of the tube, ω is the angular frequency and ν is the dynamic viscosity. For Womersley numbers less than 6, Hoekstra *et al* showed that the inaccuracy is partly due to the large grid spacing used.

Buxton *et al.* [119] coupled the lattice-Boltzmann method with a lattice-spring model, which consisted of a cubic lattice of linear springs with point masses at the corners. A Verlet algorithm was used to integrate the equations of motion. At the fluid sites that were adjacent to solid sites, they used a bounce-back method that was modified to apply a given velocity half way along the link between the fluid and solid sites, as described in section 2.9.1, in order to apply no-slip and no-penetration conditions at the wall. This velocity was given by a weighted average of the velocities at nearby points on the wall. On the other hand, the force at a point on the wall was calculated as a weighted average of the forces half way along the aforementioned links, which in turn are calculated from the bounce-back condition. However, the linear compliance force does not take into account the stress at the boundaries. The method is valid for any general geometry because it takes into account the interaction between different points on the elastic wall. However, the Poisson's ratio, which is the ratio of transverse to axial strain, is restricted to 0.25. The method, including the creation and destruction of fluid nodes, only requires information

from the nearest neighbouring sites, in contrast to that described in [14]. However, for the weighted averaging, lattice sites and wall points within several lattice lengths of the desired point had to be taken into account. They use a multiple-time relaxation LBM, which allowed the shear and bulk viscosities to be varied independently. For most of their simulations, the shear viscosity is chosen such that the distribution functions relax to equilibrium in one timestep, which is equivalent to setting $\tau = 1$. This optimised the accuracy when new fluid sites are created, since the distribution functions at these sites were set to equilibrium. The ratio of the density of the wall to that of the fluid was 11, significantly less than the ratio used by [14].

Buxton et al. [119] use their method to simulate an elastic spherical shell filled with a compressible fluid, in contrast to most other studies described in this thesis, which attempt to simulate incompressible fluids. They studied breathing mode oscillations for elastic shells of different thicknesses *in vacuo*, then in fluid-filled spherical shells with different Young's moduli. The frequencies of oscillations agreed closely with the analytical predictions. For the fluid-filled shell, the damping of the oscillations increased as the bulk viscosity increased, but was unaffected by the shear viscosity. The collision of the shell with a hard wall and an adhesive wall was studied under a variety of different parameters by introducing a force on the elastic wall nodes that depended on their position. The authors discuss the application of these simulations to the design of effective microcapsules for the pharmaceutical industry.

The method proposed by Leitner *et al* [120] involved a threshold pressure equal to the pressure required to balance the restoring forces from the wall elasticity and to maintain the wall in equilibrium. The pressure was calculated at each fluid and solid node, the pressure of a solid node being determined by the pressure exerted by the surrounding fluid nodes. If the pressure was below a threshold, the node would become solid, otherwise it would become a fluid node. Certain update rules were then applied to eliminate artefacts and holes in the wall [120]. While the method is simple and accurate, it requires constant creation and destruction of fluid nodes and is not sensitive to wall displacements of less than the size of one fluid node, so it is not sufficiently sensitive for fluid flow through complex, branching geometries.

In this chapter, a new method is proposed for simulating fluid flow in three-dimensional elastic vessels with curved boundaries, in which the distances from sites at the edge of the

simulation box to the wall in the lattice directions are estimated from the displacement of the closest point on the wall and the curvature there. A nonequilibrium extrapolation method is then applied to the sites at the edge. No fluid nodes are created or destroyed, which is advantageous for running on parallel architectures. The accuracy and computational cost of the method are tested for pressure-driven flow in an elastic cylinder.

3.2 Theoretical background

The equations of motion for elastic walls in a system through which a fluid flows are developed in this section. This is followed by a summary of the lattice-Boltzmann model employed in this chapter.

3.2.1 Equations of motion for the elastic walls

In a simulation of fluid flow in an elastic vessel, an equation of motion for the wall is required. If the wall is in equilibrium, the circumferential tensile stress, $\sigma_{\theta\theta}$, balances the transmural pressure (the difference between the pressure of the fluid inside, p , and the pressure outside, p_0), provided that loading and deformation are axisymmetric, i.e. we have $\sigma_{r\theta} = \sigma_{z\theta} = 0$ and the radius of the vessel varies slowly along its length, i.e. σ_{zr} is negligible. Resolving the forces for an infinitesimal element of the wall of a cylindrical vessel (see figure 3.1), we have [24]:

$$T d\theta = (p - p_0) R dl d\theta; \quad (3.1)$$

therefore:

$$\sigma_{\theta\theta} h dl d\theta = (p - p_0) R dl d\theta, \quad (3.2)$$

which implies

$$\frac{\sigma_{\theta\theta} h}{R} = p - p_0, \quad (3.3)$$

where T is the tensile force, dl is a small element of length, h is the wall thickness, R is the radius of the vessel and $d\theta$ is a small angle. The walls are assumed to be thin, i.e. $\frac{h}{R} \ll 1$, so that the area of an element of the wall on the inside is equal to that on the outside and the forces are balanced correctly in equation (3.3).

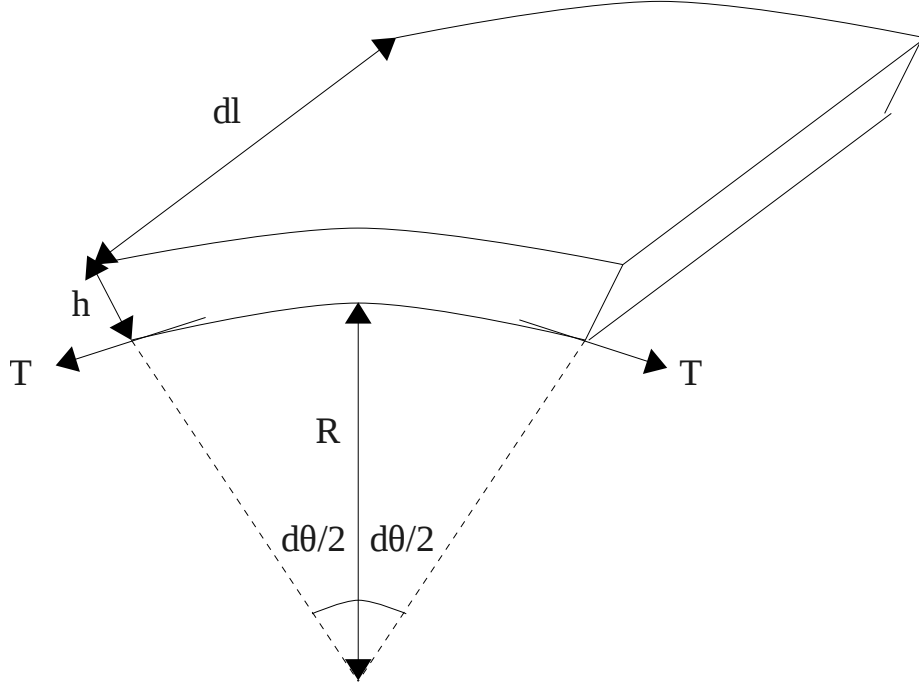


FIGURE 3.1: Balance of transmurial pressure and tensile stress in the arterial wall.

To express the pressure in terms of the radius, we require Hooke's law for the diagonal components of the strain tensor in cylindrical polar coordinates [121]:

$$\epsilon_{rr} = \frac{1}{E} [\sigma_{rr} - \Omega(\sigma_{\theta\theta} + \sigma_{zz})], \quad (3.4)$$

$$\epsilon_{\theta\theta} = \frac{1}{E} [\sigma_{\theta\theta} - \Omega(\sigma_{rr} + \sigma_{zz})], \quad (3.5)$$

$$\epsilon_{zz} = \frac{1}{E} [\sigma_{zz} - \Omega(\sigma_{rr} + \sigma_{\theta\theta})], \quad (3.6)$$

where σ is the stress, ϵ is the strain, E is the Young's modulus of the wall and Ω is Poisson's ratio for the wall of the cylinder, which is the ratio of its transverse to axial strain. Usually, vessels are assumed to be tethered in the longitudinal (z) direction, i.e. $\epsilon_{zz} = 0$ [24]. The compressive stress in the radial direction, σ_{rr} , is negligible compared with the circumferential tensile stress $\sigma_{\theta\theta}$. Therefore, from Hooke's law, we obtain:

$$\sigma_{\theta\theta} = \frac{E\epsilon_{\theta\theta}}{1 - \Omega^2}. \quad (3.7)$$

Substituting this into equation (3.3), using $\epsilon_{\theta\theta} = \frac{R-R_0}{R_0}$, where R_0 is the radius of the tube at zero transmural pressure, we find:

$$p - p_0 = \frac{Eh}{1 - \Omega^2} \left(\frac{1}{R_0} - \frac{1}{R} \right). \quad (3.8)$$

If the pressure is p_1 when the equilibrium radius is R_1 , it can be shown that equation (3.8) holds with p_0 replaced by p_1 and R_0 replaced by R_1 . Therefore, we can redefine p_0 to be the reference pressure at radius R_0 in equation (3.8). Biological tissue is practically incompressible [6], which implies $\Omega = \frac{1}{2}$. The forces on an element of the wall arising from the pressure difference and the elasticity of the wall act along the outward and inward normals respectively. The magnitudes of these forces per unit area are given by the left and right sides of equation (3.8) respectively, which holds when the wall is in equilibrium. When the wall is not in equilibrium, the net force per unit area in the direction of the outward normal is given by subtracting the elastic restoring force from the pressure difference. Using Newton's third law, we obtain the following equation of motion [24, 120]:

$$\rho_{\text{wall}} h \frac{d^2 R}{dt^2} = (p - p_0) - \frac{4Eh}{3} \left(\frac{1}{R_0} - \frac{1}{R} \right). \quad (3.9)$$

This equation may also be written in terms of the displacement of the wall in the direction of the outward normal, by substituting $\Delta R = R - R_0$.

3.2.2 The lattice-Boltzmann model

The lattice-Boltzmann model used in this study to simulate the fluid flow is the three-dimensional, 15-direction, incompressible lattice-Boltzmann scheme [88, 89] with a Bhatnagar-Gross-Krook (BGK) collision operator, which is a single-time relaxation model [16]. This model was described in section 2.1. For convenience we summarise it again here. Let $f_i(\mathbf{x}, t)$ be a non-negative real number describing the distribution function of the particle density at site \mathbf{x} at time t moving with microscopic velocity \mathbf{e}_i . The distribution functions evolve according to equation (2.4):

$$f_i(\mathbf{x} + \Delta t \mathbf{e}_i, t + \Delta t) - f_i(\mathbf{x}, t) = -\frac{1}{\tau} (f_i(\mathbf{x}, t) - f_i^{(eq)}(\rho(\mathbf{x}, t), \mathbf{v}(\mathbf{x}, t))),$$

where τ is the dimensionless relaxation time and $f_i^{(eq)}(\rho, \mathbf{v})$ is the local equilibrium distribution function for density ρ and velocity \mathbf{v} . For practical implementation, this equation is divided into two steps: collision and streaming, which are expressed by equations (2.5) and (2.6). The particle velocities, \mathbf{e}_i , for the D3Q15i model are given in equation (2.29) [17], i.e. $\mathbf{e}_0 = (0, 0, 0)$, $\mathbf{e}_i = c(0, 0, \pm 1)$, $c(0, \pm 1, 0)$, $c(\pm 1, 0, 0)$ for $i = 1, 2, \dots, 6$ and $\mathbf{e}_i = c(\pm 1, \pm 1, \pm 1)$ for $i = 7, 8, \dots, 14$, where $c = \Delta x / \Delta t$, where Δx is the lattice spacing. Equation (2.116) gives the equilibrium distributions:

$$f_i^{(eq)}(\rho, \mathbf{v}) = w_i \left(\rho + 3 \frac{\mathbf{e}_i \cdot \mathbf{v}}{c^2} + \frac{9}{2} \frac{(\mathbf{e}_i \cdot \mathbf{v})^2}{c^4} - \frac{3}{2} \frac{\mathbf{v} \cdot \mathbf{v}}{c^2} \right),$$

with $w_0 = 1$, $w_i = \frac{1}{9}$ for $i = 1, 2, \dots, 6$, and $w_i = \frac{1}{72}$ for $i = 7, 8, \dots, 14$.

The density and macroscopic velocity are calculated from the distribution functions by equation (2.13), i.e. $\rho = \sum_i f_i$, $\mathbf{v} = \sum_i f_i \mathbf{e}_i$. The pressure, p , and kinematic viscosity, ν , are given by equations (2.10) and (2.11) respectively, i.e. $p = \rho c_s^2$ and $\nu = \frac{c^2}{3} (\tau - \frac{1}{2}) \Delta t$, where the speed of sound is given by $c_s^2 = \frac{c^2}{3}$.

In all simulations in this chapter, Δx , the lattice length, and Δt , the time step, are set to one for convenience, so that $c = 1$. The density of the fluid ρ_0 is also set to one, so that $p_0 = c_s^2 = \frac{1}{3}$. All results in this chapter are given in lattice units, i.e. lengths are measured in lattice lengths, time is measured in lattice timesteps and $p_0 = 1$ lattice pressure unit.

3.3 Choice of boundary condition methods for simulations of a 3D cylinder

In this section, I compare the accuracy and stability of simulations of a 3D cylinder pointing along the x -axis with three different combinations of methods for applying pressure boundary conditions at the inlet and outlet and velocity boundary conditions at the walls and discuss their suitability for simulating fluid flow through elastic vessels in a general geometry. First, the time-extrapolation method developed by Mazzeo et al. [93] and described in section 2.9.6 is applied at all lattice sites that are adjacent to boundaries ¹.

¹The code and instructions for its use may be downloaded from <http://ccs.chem.ucl.ac.uk/~gary> as a zip archive and will be in the folder "Marcos_method_barycentric_v" when the archive has been unpacked. For the simulations reported in this section, INCOMPRESS was defined at compile time and the command-line argument "staircased" was 1.

Second, my own method involving extrapolation in time and space, described in section 3.3.1 is applied for all boundaries². Third, the extrapolation method by Zhao-Li et al. [10] and discussed in section 2.9.5 is used to determine the unknown distributions, f_i , at lattice sites adjacent to the wall, which I will define as edge sites, and the consistent method by Zou and He [9] is used to find the unknown f_i at the inlet or outlet, i.e. those for which the lattice vector \mathbf{e}_i is in the opposite direction to a link between a lattice site and the next one that crosses the inlet or outlet plane. For example, if the cylinder is oriented in the x -direction, the f_i for which $e_{ix} = 1$ are unknown at the inlet, then Zou and He's method is used to find the remaining f_i . The methods are abbreviated by the authors' names. The third method³ is called ZouHe+GZS, where I have used the authors' first names in [10]. At sites adjacent to both the wall and the inlet or outlet, the unknown f_i that cannot be determined by Zou and He's method are determined by the extrapolation method. The extrapolation method involves finding the relevant postcollisional distribution function, $f_i^+(x_w, t)$, at a solid site w , then this distribution function is streamed to site f , at which we are applying the boundary condition. The configuration of these sites is shown in figure 2.5. If the neighbouring site ff opposite site w is also solid, the method cannot be applied, as explained in section 2.9.5. Therefore, for the ZouHe+GZS method, bounceback is used to find $f_i(\mathbf{x}_f, t + \Delta t)$, i.e. $f_i(\mathbf{x}_f, t + \Delta t) = f_j(\mathbf{x}_f, t + \Delta t)$, where $\mathbf{e}_j = -\mathbf{e}_i$.

3.3.1 A new method for pressure and velocity boundary conditions

In this section, I propose a new method for applying pressure and velocity boundary conditions in a 3D vessel. It has similarities to the method proposed by Zhao-Li et al. [10] and described in section 2.9.5: the distribution functions at sites adjacent to a boundary are constructed by calculating the equilibrium and nonequilibrium components separately, and extrapolation is used to find the nonequilibrium distributions.

²The code and instructions for its use may be downloaded from <http://ccs.chem.ucl.ac.uk/~gary> as a zip archive and will be in the folder "BC_orig_dirs_fneq_unknown_2neighs" when the archive has been unpacked. For the simulations reported in this section, INCOMPRESS was defined at compile time and the command-line argument "staircased" was 0.

³The code and instructions for its use may be downloaded from <http://ccs.chem.ucl.ac.uk/~gary> as a zip archive and will be in the folder "Guo.Zheng.Shi" when the archive has been unpacked. For the simulations reported in this section, INCOMPRESS was defined at compile time.

At each edge site, the velocity is calculated from that at three neighbouring fluid lattice sites and a point on the wall itself using Barycentric coordinates to carry out the interpolation or extrapolation, as described by Hazewinkel [122, p. 342]. The velocity at the site is given by

$$\mathbf{v}^{(site)} = \sum_{i=1}^4 b^{(i)} \mathbf{v}^{(i)} \quad (3.10)$$

$$\sum_{i=1}^4 b^{(i)} = 1 \quad (3.11)$$

$$(3.12)$$

where $b^{(i)}$ is the Barycentric coordinate of the i th point in space (which may be a neighbouring lattice site or a point on the wall itself) and $\mathbf{v}^{(i)}$ is the velocity there. The $b^{(i)}$ are calculated by solving

$$A_{ij} b^{(j)} = x_j^{(site)} - x_j^{(4)}, \quad (3.13)$$

for $j = 1, 2, 3$, then finding $b^{(4)}$ from equation (3.11), where $x_j^{(i)}$ is the j th coordinate of the i th point and A_{ij} is a matrix given by

$$A_{ij} = x_j^{(i)} - x_j^{(4)}, \quad (3.14)$$

for $i = 1, 2, 3$, $j = 1, 2, 3$. At each lattice site that is adjacent to an inlet or outlet, which I will define as an inlet or outlet site respectively, the same method is applied to find the pressure at that lattice site, from that at three neighbouring sites and a point on the inlet or outlet itself.

For each boundary site, the three neighbouring lattice sites are chosen at the beginning of the simulation such that their position vectors are linearly independent. This ensures that the vectors $\mathbf{r}^{(i)} - \mathbf{r}^{(4)}$ are linearly independent and therefore the matrix \mathbf{A} is nonsingular, apart from the rare case where the point on the wall, inlet or outlet lies in the common plane of the three neighbouring lattice sites. If there is more than one suitable combination of these neighbours, the combination that will be used is chosen by the following criteria, in order of importance. First, the number of neighbours that are not themselves boundary sites is maximised. Second, the number of non-edge, non-inlet or non-outlet neighbours is maximised if the boundary site is an edge site or a non-edge inlet or outlet site respectively.

Third, $\mathbf{r}^{(neigh)} - \mathbf{r}^{(site)}$ is equal to one of the lattice vectors, \mathbf{e}_i , given in equation (2.29) or (2.30) and the indices of the first, then the second, then the third lattice vectors are minimised.

At this time, the velocity is unknown at each non-edge inlet or outlet site, the density is unknown at each non-inlet or non-outlet edge site and the nonequilibrium distribution is unknown. These quantities are determined by linear extrapolation from the fluid sites at positions $\mathbf{r}^{(site)} + \mathbf{e}_i$ and $\mathbf{r}^{(site)} + 2\mathbf{e}_i$. The vector \mathbf{e}_i is chosen by the following criteria, in order of importance. First, axis-aligned vectors are preferred. Second, the vector is preferred if the lattice site at $\mathbf{r}^{(site)} + \mathbf{e}_i$ is not a boundary site. Third, the vector with the smallest value of $\mathbf{e}_i \cdot \mathbf{n}$ is preferred, where \mathbf{n} is the inward normal to the wall if the boundary site we are looking at is an edge site and the inward normal to the inlet or outlet otherwise. Fourth, the direction with the lowest value of i is preferred.

The information that each boundary site requires from its neighbours to find the distribution functions at time $t + \Delta t$ is calculated from the distribution functions at its neighbours after streaming, i.e. at time $t + \Delta t$, except for the neighbours that are themselves boundary sites, in which case the distributions at time t are used, i.e. an extrapolation in time is carried out.

Rather than applying this method for the distribution functions that could not be determined by streaming, it was applied for all the distribution functions at the boundary sites because this gave rise to more accurate results in preliminary simulations of flow in a cylinder.

3.3.2 Simulation method

Steady flow in a cylinder is simulated using the D3Q15i lattice-Boltzmann model. The geometry of the system is approximated by a set of points on a cubic lattice that is inside the cylinder of radius R_0 . The pressure at the outlet is set to p_0 throughout the simulation. The flow fields are calculated at the beginning of each time step and the convergence of the simulation is checked by at each time step by comparing the velocity field to that at the beginning of the previous timestep. I choose to use the L^1 norm of the velocity flow

field to check whether the simulation has converged to a steady state sufficiently, i.e:

$$\frac{\sum_{sites} |\mathbf{v}(x, y, z, t) - \mathbf{v}(x, y, z, t - 1)|}{\sum_{sites} |\mathbf{v}(x, y, z, t)|} < tol, \quad (3.15)$$

where $tol = 10^{-8}$ for all simulations in this section. This convergence criterion is widely used [88, 102].

The pressure difference between the inlet and outlet is chosen to give rise to a particular maximum velocity, which is calculated by setting the distance from the centre of the tube, $r = 0$, in equation (1.12):

$$v_x = -\frac{1}{4\nu\rho} \nabla p (R^2 - r^2).$$

For all simulations in this section, I ensured that the length was greater than the entrance length for Poiseuille flow to ensure that the inlet boundary conditions do not affect the flow at the outlet. The entrance length is given by equation (1.14), i.e. $L_{entr} = 0.12ReR$ [69, 70], where Re is calculated from the average velocity over the cross-section of the cylinder. Integrating equation (1.12) with respect to r gives the flow rate:

$$Q = \int_0^R v(r)(2\pi r)dr = -\frac{\pi R^4}{8\nu\rho} \nabla p. \quad (3.16)$$

This is $\frac{\pi R^2}{2}$ times the maximum velocity. Therefore, the average velocity is half of the maximum velocity, so the entrance length is given by

$$L_{entr} = 0.06ReR, \quad (3.17)$$

if the Reynolds number is calculated from the maximum velocity given by equation (1.12).

Lattice-Boltzmann simulations may become unstable if the Mach number is too high or the dimensionless relaxation parameter, τ , is too low as discussed in section 2.5. For all simulations in this section, $v_x < 0.03c$, so the Mach number is less than 0.052, from equation (2.90). Therefore, the requirement that $Ma \ll 1$ for an accurate and stable simulation, discussed in section 2.8, is satisfied, which shows that any instability is caused by the value of τ being too low. The boundary conditions also affect the stability, as discussed in section 2.9. In this section, I test the stability of simulations that use the three combinations of boundary condition methods discussed earlier, by finding the value

of τ , τ_{min} , such that the simulation converges to a steady state while remaining stable for a given velocity, $v_x = 0.03c$ and the same simulation with $\tau = \tau_{min} - 0.1(\tau_{min} - 0.5)$ is unstable. The maximum Reynolds number that can be simulated accurately for a given system size can be readily calculated using equations (2.85) and (1.5).

Negative distribution functions indicate that a simulation has become unstable, as discussed in section 2.5. The same applies to the equilibrium part of the distribution functions and these were used to check for instability. The distribution functions may not become negative until a long time after the simulation has become unstable, in which case it would not converge to a steady state. In this section, a simulation at a value of $\tau = \tau_1 - 0.1(\tau_1 - 0.5)$ is deemed to be unstable if it does not converge within six times the number of timesteps required for the simulation with $\tau = \tau_1$.

When the steady state is reached, the velocity and pressure fields are compared with the analytical solution from Poiseuille flow. For the pressure, we expect that $p = p_0 + \nabla p(L-x)$, where L is the length of the cylinder, while equation (1.12) gives the analytical solution for the velocity. The simulation errors are measured with ϵ_1 and ϵ_∞ , i.e. the L^1 and L^∞ norms, which are given below for velocity and are calculated similarly for the pressure difference, $p - p_0$. The L^∞ norm depends only on the largest simulation error, while the simulation errors for each site are weighted equally in the L^1 norm.

$$\epsilon_1 = \frac{\sum_{\text{sites}} |\mathbf{v}(x, y, z) - \mathbf{v}'(x, y, z)|}{\sum_{\text{sites}} |\mathbf{v}'(x, y, z)|}, \quad (3.18)$$

$$\epsilon_\infty = \frac{\max_{\text{sites}} (|\mathbf{v}(x, y, z) - \mathbf{v}'(x, y, z)|)}{\max(|\mathbf{v}'(x, y, z)|)}, \quad (3.19)$$

where \mathbf{v}' is the analytical velocity. The L^∞ norm depends only on the largest simulation error, while the simulation errors for each site are weighted equally in the L^1 norm.

3.3.3 Stability of the simulations

Simulations of Poiseuille flow were performed for cylinders of two different radii. The maximum expected velocity was $0.03c$. The minimum values of τ at which the simulations were stable, τ_{min} , are given in table 3.1. These correspond to a maximum Reynolds number, which is calculated using equation (2.85), i.e. $\nu = \frac{\tau-0.5}{3}c^2\Delta t$, and $Re = \frac{2vR}{\nu}$. All the simulations shown are unstable if $\tau = \tau_{min} - 0.1(\tau_{min} - 0.5)$. For all simulations in

Method	$R = 5\Delta x$		$R = 10\Delta x$	
	τ_{min}	Re_{max}	τ_{min}	Re_{max}
Mazzeo	0.5015	600	0.5075	200
Doctors	0.67	5.29	0.70	9.00
ZouHe+GZS	0.530	30.0	0.522	81.8

TABLE 3.1: Minimum values of τ and corresponding maximum Reynolds number for which simulations of flow in a cylinder at radius R are stable if the maximum velocity is $0.03\frac{\Delta x}{\Delta t}$ when three different boundary condition methods are used. Re is calculated from the maximum velocity. The simulations are unstable if $\tau = \tau_{min} - 0.1(\tau_{min} - 0.5)$. The methods are abbreviated by their authors' names and described at the beginning of section 3.3 and in subsection 3.3.1. The lengths of the cylinders are $0.32ReR$, i.e. $5\frac{1}{3}$ times the entrance length.

this subsection, the length was set to $0.32ReR$, i.e. $5\frac{1}{3}$ times the entrance length given by equation (3.17).

3.3.4 Comparison of the accuracy of the simulations

Simulations of Poiseuille flow were performed for cylinders of three different radii at $Re = 1.0$, $\tau = 1.0$ using the three boundary condition methods described in this section and at $Re = 30.0$, $\tau = 0.53$ using the methods that were stable at these parameters. The accuracy of these simulations is expressed by the the L^1 and L^∞ norms for the pressure, velocity and stress flow fields. Linear regression on $\log(\epsilon)$ against $\log(\frac{\Delta x}{R})$ was used to find the value of n in the relationship $\epsilon \propto (\frac{\Delta x}{R})^n$ that fits the data best for each set of simulation errors. The results for $Re = 1.0$ and $Re = 30.0$ are given in tables 3.2 and 3.3.

3.3.5 Discussion

The simulation errors are higher at $Re = 30$ than at $Re = 1$ for both the Mazzeo and ZouHe+GZS methods. For the former, the errors in the velocity flow field become smaller as the resolution increases, as shown in tables 3.2 and 3.3, but the the reduction is less than first order in the lattice spacing, Δx and the L^1 and L^∞ norms remain above 0.1 at a radius of 20 lattice lengths. For the shear stress, the errors remain above 0.68. For the pressure, the errors become larger as the size of the simulation increases if $Re = 1.0$. For elastic vessels, the displacement of the wall is determined chiefly by the pressure. These inaccuracies are probably due to the fact that the stress is set to zero at the boundaries, as

Method	Type of error	Error for different system sizes			Order of Convergence
		$R = 5\Delta x$ $L = 50\Delta x$	$R = 10\Delta x$ $L = 100\Delta x$	$R = 20\Delta x$ $L = 200\Delta x$	
Mazzeo	velocity L^∞	3.88×10^{-1}	2.26×10^{-1}	1.69×10^{-1}	0.65
	velocity L^1	5.68×10^{-1}	3.30×10^{-1}	1.78×10^{-1}	0.82
	pressure L^∞	1.96×10^{-2}	4.30×10^{-2}	8.69×10^{-2}	-1.05
	pressure L^1	4.34×10^{-3}	1.02×10^{-2}	1.36×10^{-2}	-0.68
	stress L^∞	9.86×10^{-1}	9.95×10^{-1}	9.99×10^{-1}	-0.01
	stress L^1	7.41×10^{-1}	7.01×10^{-1}	6.81×10^{-1}	0.06
Doctors	velocity L^∞	7.06×10^{-2}	1.86×10^{-2}	5.66×10^{-3}	1.90
	velocity L^1	1.01×10^{-1}	2.78×10^{-2}	7.65×10^{-3}	1.86
	pressure L^∞	5.85×10^{-3}	1.47×10^{-3}	4.63×10^{-4}	1.95
	pressure L^1	1.29×10^{-3}	2.16×10^{-4}	3.72×10^{-5}	2.58
	stress L^∞	8.50×10^{-2}	4.33×10^{-2}	2.33×10^{-2}	0.95
	stress L^1	5.71×10^{-2}	2.43×10^{-2}	1.10×10^{-2}	1.21
ZouHe+GZS	velocity L^∞	7.69×10^{-2}	3.69×10^{-2}	1.78×10^{-2}	1.06
	velocity L^1	3.41×10^{-2}	4.29×10^{-3}	1.20×10^{-3}	2.41
	pressure L^∞	6.18×10^{-3}	5.90×10^{-3}	6.23×10^{-3}	-0.01
	pressure L^1	4.03×10^{-4}	1.82×10^{-4}	7.69×10^{-5}	-1.19
	stress L^∞	4.67×10^{-1}	4.67×10^{-1}	4.65×10^{-1}	0.00
	stress L^1	4.37×10^{-2}	1.74×10^{-2}	8.23×10^{-3}	-1.20

TABLE 3.2: Comparison of the accuracy of simulations of flow in a cylinder with radius R and length L at $Re = 1.0$, $\tau = 0.8$ for three different boundary condition methods. The methods are abbreviated by their authors' names and described at the beginning of section 3.3 and subsection 3.3.1. The order of convergence is the value of n for which the data fits the relationship $\epsilon \propto (\frac{\Delta x}{R})^n$.

explained in section 2.9.6. The method proposed in this study is much more accurate at $Re = 1, \tau = 0.8$: the L^1 errors in pressure, velocity and stress are 7.65×10^{-3} , 3.72×10^{-5} and 1.10×10^{-2} respectively. The errors in pressure and velocity are approximately of order Δx^2 , which matches the intrinsic accuracy of the LBM. The errors in stress are first order accurate in space. The velocity field for the ZouHe+GZS method is generally more accurate than the new method proposed in this study, although the L^∞ norm is higher at $R = 20\Delta x$. The L^1 and L^∞ norms for the pressure are of order Δx and 1 respectively, in contrast to the method in this study. The L^1 norm is approximately twice as high at $R = 20\Delta x$ as it is in my method. The ZouHe+GZS method generally produces the most accurate shear stress results, except at a very small number of lattice sites.

The Mazzeo method is stable at much lower values of τ than the other methods, as shown in table 3.1. A maximum Reynolds number of 600 or 200 can be obtained for a cylinder with radius 5 and 10 lattice lengths respectively, which is of the order of magnitude that

Method	Type of error	Error for different system sizes			Order of Convergence
		$R = 5\Delta x$ $L = 50\Delta x$	$R = 10\Delta x$ $L = 100\Delta x$	$R = 20\Delta x$ $L = 200\Delta x$	
Mazzeo	velocity L^∞	5.77×10^{-1}	3.07×10^{-1}	1.93×10^{-1}	0.79
	velocity L^1	7.24×10^{-1}	4.48×10^{-1}	2.54×10^{-1}	0.76
	pressure L^∞	1.12×10^{-1}	8.52×10^{-2}	8.41×10^{-2}	0.21
	pressure L^1	5.30×10^{-2}	2.68×10^{-2}	6.48×10^{-3}	1.52
	stress L^∞	9.99×10^{-1}	9.99×10^{-1}	1.00	0.00
	stress L^1	9.61×10^{-1}	9.56×10^{-1}	9.53×10^{-1}	0.01
ZouHe+GZS	velocity L^∞	1.33×10^{-1}	3.88×10^{-2}	1.66×10^{-2}	1.50
	velocity L^1	6.23×10^{-2}	1.78×10^{-2}	5.01×10^{-3}	1.81
	pressure L^∞	2.39×10^{-2}	8.22×10^{-3}	7.93×10^{-3}	0.80
	pressure L^1	1.47×10^{-2}	5.19×10^{-3}	7.73×10^{-4}	2.12
	stress L^∞	6.38×10^{-1}	5.42×10^{-1}	5.16×10^{-1}	0.15
	stress L^1	6.67×10^{-2}	2.52×10^{-2}	1.18×10^{-2}	1.25

TABLE 3.3: Comparison of the accuracy of simulations of flow in a cylinder with radius R and length L at $Re = 30.0$, $\tau = 0.53$ for the boundary condition methods described at the beginning of section 3.3. The method described in subsection 3.3.1 was unstable at these parameters. The order of convergence is the value of n for which the data fits the relationship $\epsilon \propto (\frac{\Delta x}{R})^n$.

would be required for blood flow simulations, as explained at the beginning of this chapter. However, the minimum value of τ is significantly higher at $R = 10\Delta x$ than at $R = 5\Delta x$, which suggests that it becomes much less stable as the system size is increased. For the method proposed in this study, the maximum Reynolds numbers are less than a tenth of that required for a simulation of cerebral blood flow. If the Mach number is kept constant, the Reynolds number can only be increased by increasing the radius of the cylinder. If the length is increased in the same proportion, the number of lattice sites would be proportional to Re^3 . The number of timesteps required for information to propagate is proportional to the size of the cylinder. Therefore, the computational cost is likely to scale as Re^4 . Therefore, increasing Re to 100 would result in a formidable increase in computational cost. Furthermore, if the length is to be kept longer than the entrance length, $0.06ReR$, there would be an additional factor $R \propto Re$ in the computational cost, so it would scale as Re^5 . Therefore, this method cannot reasonably be used for simulations of cerebral blood flow. If τ could be reduced further, the computational cost would scale as $Re \propto (\tau - 0.5)^{-1}$ for $\tau < 1$ since, in this regime, the distributions take more time to relax to equilibrium as τ is lowered. For the ZouHe+GZS method, the maximum Reynolds number achievable is 30 and 81.8 at $R = 5\Delta x$ and $10\Delta x$ respectively. A Reynolds number of 162.6 could be obtained at $R = 20\Delta x$ if the minimum value of τ is kept the same as it is at $R = 10\Delta x$. In

contrast to the other methods, the minimum value of τ is lower at $R = 10\Delta x$ than when $R = 5\Delta x$, which suggests that the maximum Reynolds number, $Re_{max} \propto \left(\frac{R}{\Delta x}\right)^n$, where $n > 1$.

Both Mazzeo's method and the method proposed in this study can simulate fluid flow in a complex geometry. However, the former does not take into account the distance from the edge sites to the wall, it would not be sensitive to displacements of less than one lattice length, which is required for simulations of blood flow through elastic arteries, as explained at the beginning of this chapter. It is possible that this could be improved by interpolation to find the velocity at the edge sites. The method proposed in section 3.3.1 takes into account the separation between each edge site and its point on the wall, which is ideal for simulating fluid flow through elastic systems. However, it is only stable at low Reynolds numbers. The ZouHe+GZS method takes into account the distances along the lattice vectors to the wall, but these may be difficult to calculate accurately for a moving wall since particular points on the wall will not necessarily move in the directions of the lattice vectors. The method is able to simulate flow in a complex geometry, but has the limitation that the inlet and outlet plane must be aligned with two axes. The pressure boundary condition can be changed to overcome this limitation, as discussed in section 3.4. For simulating blood flow through elastic vessels, the ZouHe+GZS method looks the most promising overall, considering its accuracy, stability and suitability for dealing with the motion of the wall. Therefore, this method is used for all simulations of fluid flow in elastic vessels in this chapter.

3.4 Choice of boundary condition methods for simulations of a 2D channel

Simulations of flow through a 2D elastic vessel at $Re = 450$ are required in chapter 5 to compare the results from the elastic model developed in that chapter and chapter 4 with results in [15] as explained in sections 5.2 and 5.3. However, in section 3.3, the highest Reynolds number that could be achieved for accurate simulations of a 3D cylinder was 81.8 at $R = 10\Delta x$ and it is therefore expected to be 163.6 at $R = 20\Delta x$. These simulations used the extrapolation method by Zhao-Li et al. [10] at the walls and the method by Zou and He [9] at the inlet and outlet. This combination of methods is again abbreviated by

ZouHe+GZS. Therefore, the accuracy and stability of simulations using this combination and the boundary conditions by Mazzeo et al. [93] (abbreviated by Mazzeo) are compared in this section. Since the computational cost is of order the number of lattice sites times the length of the channel, as discussed in section 3.4.4, it would scale as Re^3 in a 2D channel if the width is increased. However, if τ could be reduced, the computational cost would scale as Re^2 . Therefore, I attempt to reduce the minimum value of τ for simulations that use Zhao-Li et al. [10]’s method near the walls by using Mazzeo et al. [93]’s method to apply pressure boundary conditions at the inlet and outlet sites. Lattice sites adjacent to a wall and the inlet or outlet, which I will call the corner sites, must be treated very carefully, as explained in section 3.4.1. This combination is abbreviated as Mazzeo+GZS 4.

The simulations are carried out, and the stability is tested, in the same way as described in section 3.3.2, except that the D2Q9i model is used. The pressure difference between the inlet and outlet is chosen to give rise to a particular maximum velocity, which is calculated by setting $y = 0$ in the equation for Poiseuille flow in a 2D channel,

$$v_x = \frac{\nabla p}{2\nu\rho} (R^2 - y^2), \quad (3.20)$$

where $R = \frac{D}{2}$ is the half-width of the channel and y is measured relative to the centreline. For all simulations in this section, I ensured that the length was at least four times the entrance length, which is given by $0.06ReD$, where Re is calculated from the average velocity across the width. Integrating equation 3.20 with respect to y gives the flow rate:

$$Q = 2 \int_0^{D/2} v(y)dy = \frac{2\nabla p}{3\nu\rho} R^3 \quad (3.21)$$

This is $\frac{4}{3}R = \frac{2}{3}D$ times the maximum velocity, so the average velocity is $\frac{2}{3}$ of the maximum velocity, so the entrance length is given by

$$L_{entr} = 0.04ReD = 0.08ReR, \quad (3.22)$$

⁴The code for all simulations in this section and instructions for its use may be downloaded from <http://ccs.chem.ucl.ac.uk/~gary> as a zip archive and will be in the folder “Elastic_complex_geometry_rev_215” when the archive has been unpacked. For these simulations, INCOMPRESS and INC_FLUID were defined at compile time.

if the Reynolds number is calculated from the maximum velocity.

For the extrapolation method by Zhao-Li et al. [10], described in section 2.9.5, the normalised cut distance, δ , is required for each link from an edge site f to a neighbouring solid site w , as described in section 2.9.5. The normalised cut distance is given by equation (2.158), i.e. $\delta = \frac{(\mathbf{x}_b - \mathbf{x}_f) \cdot (\mathbf{x}_w - \mathbf{x}_f)}{|\mathbf{x}_w - \mathbf{x}_f|^2}$, where \mathbf{x}_f , \mathbf{x}_w and \mathbf{x}_b denote the position vectors of site f , site w and the point of intersection of the link with the wall respectively. For a 2D axis-aligned channel, δ is identical to the distance from the last row of lattice sites to the wall divided by the lattice spacing, for all the relevant links. Zhao-Li et al. [10] found that the minimum value of τ at which their simulations of an axis-aligned channel were stable varied with δ . Therefore, I also tested the effect of varying δ for the ZouHe+GZS combination.

When checking the convergence and simulation errors, the sums in equations (3.18), (3.19) and (3.15) are taken over the lattice sites that are not adjacent to the inlet or outlet and that lie beyond the entrance region. The tolerance for the convergence criterion is 10^{-8} .

3.4.1 Combination of a velocity and pressure condition at the corner sites

At sites adjacent to the both the wall and the inlet or outlet, the method by Mazzeo et al. [93] described in section 2.9.6 can be used to apply the pressure boundary condition, using equation (2.221), i.e.

$$f_i^+(\mathbf{x}_f, t) = f_i^{(0)}(\rho_{set}, \mathbf{v}(\mathbf{x}_f, t)).$$

This can then be combined with the method by Zhao-Li et al. [10] described in section 2.9.5 by carrying out streaming as usual, then using the latter to extrapolate to find the relevant distribution function at the site on the other side of the wall, labelled w in figure 2.5. The density required should be extrapolated from the prescribed density that was applied at the inlet or outlet, i.e. $\rho_f = \rho_{set}$. Equations (2.204), (2.205) and (2.202) can then be applied as usual to find $f_i^+(x_w, t)$, then this distribution function is streamed to the site at which we are applying the boundary condition, i.e. $f_i(\mathbf{x}_f, t + \Delta t) = f_i^+(\mathbf{x}_w, t)$. If the site labelled ff is solid, bounceback is used to find $f_i(\mathbf{x}_f, t + \Delta t)$, as explained in section 3.3. Some of the links from site f to its neighbours may intersect the inlet or outlet plane but not the wall. The distribution functions at site f that would be determined

Method	$R = 5.2\Delta x$		$R = 10.2\Delta x$	
	τ_{min}	Re_{max}	τ_{min}	Re_{max}
Mazzeo	0.506	156	0.5125	146.88
ZouHe+GZS	0.526	36	0.518	102
Mazzeo+GZS	0.524	39	0.5135	136

TABLE 3.4: Minimum values of τ and corresponding maximum Reynolds number for which simulations of flow in a channel with half-width R are stable if the maximum velocity is $0.03\frac{\Delta x}{\Delta t}$ for three different boundary condition methods. Re is calculated from the maximum velocity. The simulations are unstable if $\tau = \tau_{min} - 0.1(\tau_{min} - 0.5)$. The methods are abbreviated by their authors' names and described at the beginning of section 3.4 and in subsection 3.4.1. The lengths of the channels are $0.32ReR$, i.e. 4 times the entrance length.

by streaming from one of these neighbours are therefore unknown at this time. These distribution functions are given by equation (2.220), i.e.

$$f_i(\mathbf{x}_f, t + \Delta t) = f_i^+(\mathbf{x}_f, t).$$

3.4.2 Stability of the simulations

Simulations of Poiseuille flow were performed for channels with half-widths, $R = (5 + \delta)\Delta x$ and $R = (10 + \delta)\Delta x$ using the ZouHe+GZS combination of methods, with various values of δ , where $\delta\Delta x$ is the distance from the last row of lattice sites to the wall. The maximum expected velocity was $0.03c$. The minimum values of τ at which the simulations were stable, τ_{min} , are plotted on graph 3.2. These correspond to a maximum Reynolds number, which is calculated as explained in section 3.3.3 and plotted on graph 3.3. All the simulations shown are unstable if $\tau = \tau_{min} - 0.1(\tau_{min} - 0.5)$. For all simulations in this subsection, the length was set to $0.32ReR$, i.e. 4 times the entrance length given by equation (3.22). Stability tests were also carried out in the same way using the Mazzeo and Mazzeo+GZS methods at $R = 5.2\Delta x$ and $R = 10.2\Delta x$ and the results are compared with those from the ZouHe+GZS method in table 3.4.

Additional simulations were carried out with $R = 20.2\Delta x$ for the Mazzeo+GZS method. For that, the minimum value of τ was 0.508064, which corresponded to a Reynolds number of 450.

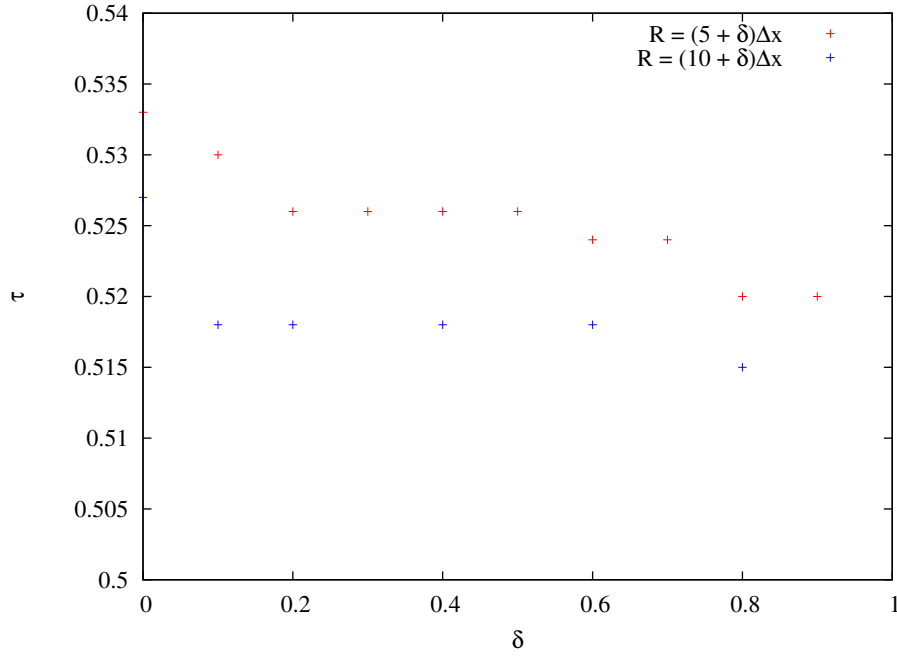


FIGURE 3.2: Minimum values of τ for which simulations of flow in a channel with the ZouHe+GZS method are stable for half widths R of $5.0\Delta x$ to $5.9\Delta x$ and $10.0\Delta x$ to $10.8\Delta x$. The maximum velocity is $0.03\frac{\Delta x}{\Delta t}$. The simulations are unstable if $\tau = \tau_{min} - 0.1(\tau_{min} - 0.5)$. The minimum value of τ is lower at $R \approx 10\Delta x$ than at $R \approx 5\Delta x$. As the distance from the last row of lattice sites to the wall, $\delta\Delta x$ is increased, the value of τ_{min} decreases somewhat. The effect of changing δ is less significant at $R \approx 10\Delta x$ than at $R \approx 5\Delta x$.

3.4.3 Comparison of the accuracy of the simulations

Simulations of Poiseuille flow were performed for channels of three different half-widths at $Re = 31.2$, $\tau = 0.53$ using the three boundary condition methods described in this section. The accuracy of these simulations is expressed by the the L^1 and L^∞ norms for the pressure and velocity flow fields. The relationship $\epsilon \propto (\frac{\Delta x}{R})^n$ was fitted to each set of simulation errors as explained in section 3.3.4. Table 3.5 shows the results.

3.4.4 Discussion

For all three combinations of boundary condition methods, the simulation errors in the velocity and the L^∞ norm for the pressure generally become smaller as the width of the channel increases, but the reduction in the error is of order Δx^n , where $n < 1$, in contrast to the results for the 3D simulations. For the L^1 norm for the pressure, the errors are at least first order in Δx . The order of convergence is lowest for the Mazzeo method

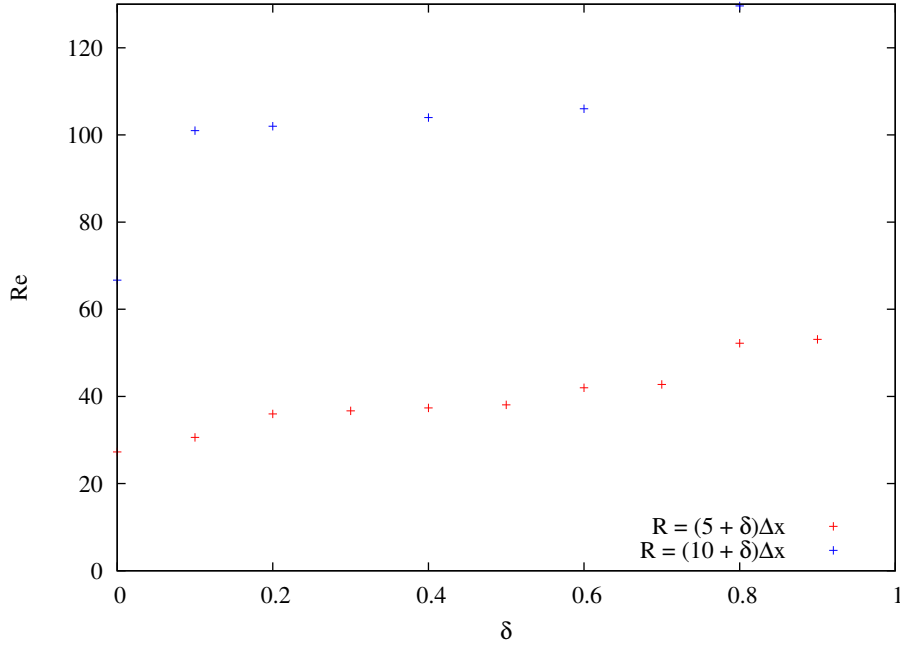


FIGURE 3.3: Maximum Reynolds numbers for which simulations of flow in a channel with the ZouHe+GZS method are stable for half widths R of $5.0\Delta x$ to $5.9\Delta x$ and $10.0\Delta x$ to $10.8\Delta x$. The values of Re correspond to the minimum values of τ in graph 3.2 and are calculated from the maximum velocity of $0.03\frac{\Delta x}{\Delta t}$. As the distance from the last row of lattice sites to the wall, $\delta\Delta x$ is increased, the maximum Reynolds number increases somewhat. The effect of changing δ is less significant at $R \approx 10\Delta x$ than at $R \approx 5\Delta x$.

and highest for the Mazzeo+GZS method, for which $n = 1.58$. None of the boundary condition methods achieve second-order accuracy in space. This may be because the distance from the wall to the last row of lattice sites is doubling as the system size doubles. Simulations with $R = 10.2\Delta x$ and $R = 20.2\Delta x$ will be needed to verify this. However, the results for the ZouHe+GZS method are accurate, with simulation errors between 10^{-2} and 10^{-3} at $R = 20\Delta x$. The errors for Mazzeo's method are 15 to 60 times higher. The Mazzeo+GZS method has somewhat smaller errors than the Mazzeo method and they achieve an acceptable accuracy, with L^1 norms of 0.0268 and 0.0125 for the pressure and velocity field when $R = 20\Delta x$, but these errors are still much higher than for the ZouHe+GZS method, rather than being similar to the ZouHe+GZS method as expected.

For the ZouHe+GZS method, increasing the distance from the last row of lattice sites to the wall when $R \approx 5\Delta x$ reduces τ_{min} somewhat, from 0.533 at $\delta = 0$ to 0.520 at $\delta = 0.9$, as shown in graph 3.2. The reduction in τ and the increase in width causes the Reynolds number to almost double, as shown in graph 3.2. At a half-width of 10 lattice lengths, τ_{min} decreases significantly as δ increases from 0 to 0.1, remains constant, then decreases

Method	Type of error	Error for different system sizes			Order of Convergence
		$R = 5.2\Delta x$ $L = 50\Delta x$	$R = 10.4\Delta x$ $L = 100\Delta x$	$R = 20.8\Delta x$ $L = 200\Delta x$	
Mazzeo	velocity L^∞	2.82×10^{-1}	1.91×10^{-1}	1.38×10^{-1}	0.52
	velocity L^1	3.33×10^{-1}	2.25×10^{-1}	1.75×10^{-1}	0.46
	pressure L^∞	2.36×10^{-1}	2.44×10^{-1}	1.52×10^{-1}	0.32
	pressure L^1	1.17×10^{-1}	5.71×10^{-2}	2.43×10^{-2}	1.13
ZouHe+GZS	velocity L^∞	6.08×10^{-3}	3.09×10^{-3}	4.31×10^{-3}	0.25
	velocity L^1	5.91×10^{-3}	4.04×10^{-3}	2.58×10^{-3}	0.60
	pressure L^∞	6.12×10^{-3}	2.71×10^{-3}	9.89×10^{-3}	-0.35
	pressure L^1	7.55×10^{-3}	1.09×10^{-3}	1.30×10^{-3}	1.27
Mazzeo+GZS	velocity L^∞	8.43×10^{-2}	6.53×10^{-2}	5.44×10^{-2}	0.32
	velocity L^1	2.80×10^{-2}	2.59×10^{-2}	2.68×10^{-2}	0.03
	pressure L^∞	1.62×10^{-1}	1.08×10^{-1}	1.22×10^{-1}	0.20
	pressure L^1	1.11×10^{-1}	4.15×10^{-2}	1.25×10^{-2}	1.58

TABLE 3.5: Comparison of the accuracy of simulations of flow in a channel with half-width R and length L at $Re = 31.2$, $\tau = 0.53$ for three different boundary condition methods. The methods are abbreviated by their authors' names and described at the beginning of section 3.4 and subsection 3.4.1. The order of convergence is the value of n for which the data fits the relationship $\epsilon \propto (\frac{\Delta x}{R})^n$.

slightly between $\delta = 0.6$ and $\delta = 0.8$. Since the stability of the GZS method changes very little for $\delta > 0.1$ at $R \approx 10\Delta x$, it was kept constant at $\delta = 0.2$ for the comparison of the three boundary condition methods. The results described here contrast with those in Zhao-Li et al. [10], for which the the minimum values of τ are much lower and increasing δ has a dramatic effect on them; they are 0.506, 0.50003 and less than $0.5 + 10^{-7}$ at $\delta = 0.1$, 0.2 and 0.3 respectively for a channel with $R \approx 16$. However, body forcing was used in that study, which implies that the use of a pressure boundary condition has significantly increased τ_{min} and therefore reduced the maximum Reynolds number that can be achieved.

The minimum value of τ for both the ZouHe+GZS and the Mazzeo+GZS methods appears to decrease as the width of the channel increases, as shown in figure 3.2 and table 3.4, so the maximum achievable Reynolds number increases as $(\frac{R}{\Delta x})^n$, with $n > 1$, but the opposite is true for the Mazzeo method. The value of τ_{min} decreases more for the Mazzeo+GZS method than the ZouHe+GZS method and is lower at $R = 10.2\Delta x$, reaching $\tau = 0.5135$. One further simulation showed that it decreases to 0.508064 at $R = 20.2\Delta x$, corresponding to $Re = 450$, as desired for the comparison of results of simulations of elasticity in a general two-dimensional geometry with those in Luo and Pedley [15]. Furthermore, since the Mazzeo method is used for the pressure boundaries, they need not be axis-aligned.

The Mazzeo+GZS method also achieves acceptable accuracy. It can be extended to three dimensions easily. Therefore, it is the most suitable of the combinations of boundary condition methods discussed in this section and section 3.3 for simulating cerebral blood flow through elastic arteries in a complex geometry at realistic parameters.

3.5 Simulation method

In this section, a method for simulating steady flow in an elastic cylinder is proposed⁵. The flow is simulated using the D3Q15i lattice-Boltzmann model. The geometry of the system is approximated by a set of points on a cubic lattice that is inside the cylinder when the pressure in the fluid is equal to the reference pressure p_0 , i.e. it is approximated by the set of points inside the cylinder of radius R_0 . No fluid nodes are moved, created or destroyed. The pressure at the outlet is set to p_0 throughout the simulation, while the pressure at the inlet is held constant at a pressure greater than p_0 . In the simulations presented in this study, the axis of the cylinder is aligned in the x direction and the geometry extends from $x = 0$ to $x = L$. The configuration of lattice sites in a quarter of one layer of a cylinder with radius $R_0 = 5$ is shown in figure 3.4.

As the cylinder deforms, every point on the wall moves in the direction of its outward normal, as explained in section 3.2.1. For each fluid node that is adjacent to the wall, f , which we will call an edge site, we store certain information about its nearest point on the wall, n . This includes the outward normal, \mathbf{n} , the displacement from site f to point n along \mathbf{n} when the cylinder has not been deformed, the change in displacement along \mathbf{n} , ΔR , and the velocity along \mathbf{n} , $\frac{d\Delta R}{dt}$, as shown in figure 3.4.

In order to couple the wall to the fluid, a no-slip boundary condition is applied at the wall rather than at the edge sites by using a boundary condition method based on that proposed by Zhao-Li et al. [10], which is described in sections 2.9.5 and 3.3. For this method, the normalised cut distance, δ , is required for each link from an edge site f to a neighbouring solid site w , as described in section 2.9.5. The normalised cut distance is given by equation (2.158) and described in section 2.9.1 and the beginning of section 3.4. At each edge site, the values of δ are stored for every link that points towards a solid

⁵ The code for all simulations reported in section 3.6, and instructions for its use, may be downloaded from <http://ccs.chem.ucl.ac.uk/~gary> as a zip archive and will be in the folder “Guo.Zheng-Shi”. For these simulations, INCOMPRESS and ELASTIC were defined at compile time.

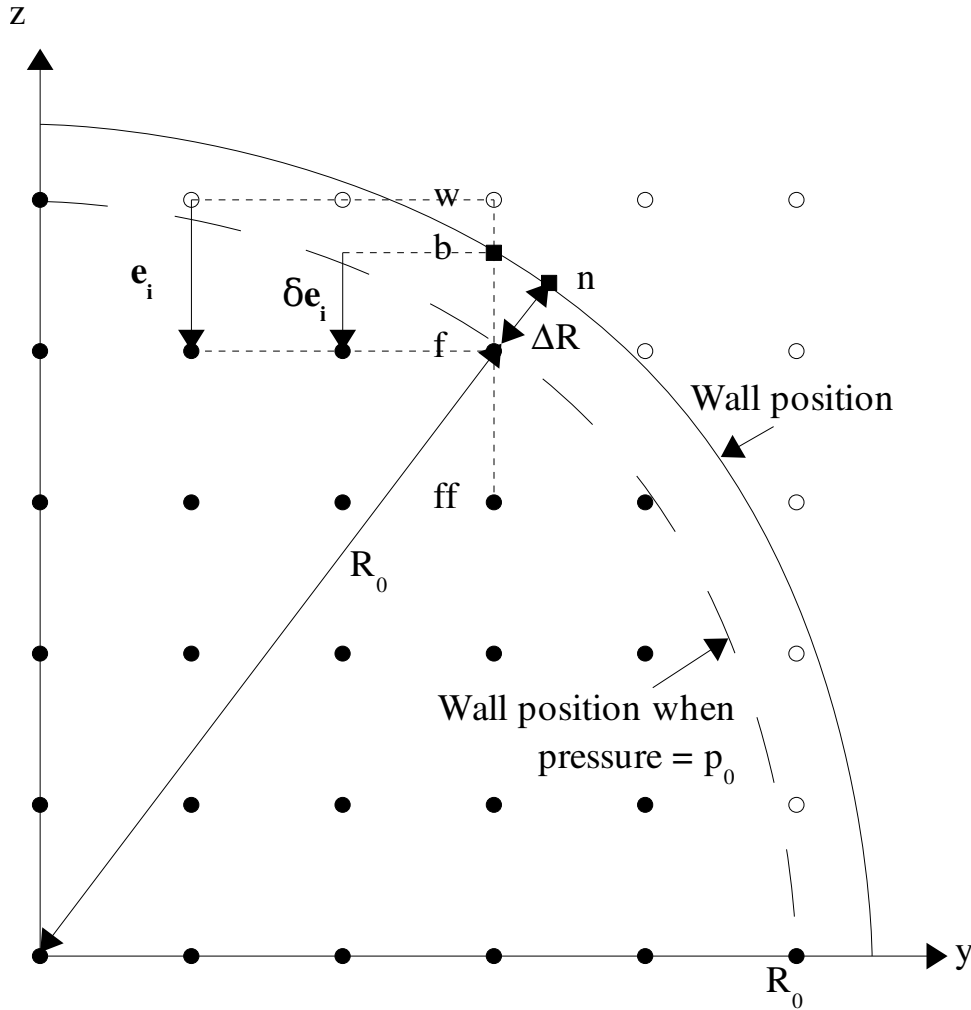


FIGURE 3.4: Diagram showing the configuration of fluid sites in a quarter of one layer of a circular cylinder. The filled circles are the fluid sites and the open circles are the solid sites. The link between an edge site, f , and one of its neighbouring solid sites, w , intersects the wall at point b . The nearest point to the edge site that lies on the wall is n . The fraction, δ , of the link between f and w that lies inside the cylinder is calculated from the displacement, ΔR , of point n from its equilibrium position at the reference pressure.

site, and the velocity is calculated at each point of intersection of a link with the wall, b . For each edge site, it is difficult to calculate δ and the velocity of the wall at point b , \mathbf{v}_b , exactly, because every point on the wall is displaced by a different amount from its position at the reference pressure in an elastic system. Therefore, we make the approximation that point b lies the same distance from its equilibrium position in the undeformed cylinder as the point n on the wall lies from its own, i.e. that it is also a distance $R_0 + \Delta R$ from the centre of the cylinder. Hence, for a cylinder pointing along the x axis, δ is estimated by

solving the following equation:

$$(y_f - \delta e_{iy})^2 + (z_f - \delta e_{iz})^2 = (R_0 + \Delta R)^2, \quad (3.23)$$

where e_{iy} and e_{iz} are the y and z components of the vector $\mathbf{x}_f - \mathbf{x}_w$. This approximation implies that the velocity of the wall at the point of intersection with the link, \mathbf{v}_b , is $d\Delta R/dt$ in the direction of the outward normal at point b . For a cylinder pointing along the x axis, the velocity at this point is given by

$$\mathbf{v}_b = \frac{d\Delta R}{dt} \left(\frac{1}{\sqrt{(y_f - \delta e_{iy})^2 + (z_f - \delta e_{iz})^2}} \right) (0, y - \delta e_{iy}, z - \delta e_{iz}). \quad (3.24)$$

Initially, the distribution functions everywhere are set to the equilibrium values with zero velocity and $p = p_0$. The displacement and velocity of the walls are zero everywhere, except at the inlet and outlet, where the displacement is set to the equilibrium value given by equation (3.9) with $\frac{d^2 R}{dt^2} = 0$.

At each timestep, the collision and streaming are carried out at all sites. The unknown distribution functions, f_i , at the edge sites are calculated by a boundary condition method based on that by Zhao-Li *et al* [10]. Pressure boundary conditions are then applied at the inlet and outlet using the method by Zou and He [9] to determine the f_i that point into the fluid. The procedure at sites adjacent to both the wall and the inlet or outlet is explained in section 3.3. The pressure and velocity flow fields at the end of the time step can then be calculated. At each edge site, the current displacement and velocity of its point on the wall are determined from those at the previous timestep by equation (3.9), assuming that the pressure at the wall is equal to the pressure at the edge site. This is followed by estimation of the values of δ required for the application of the boundary condition at the edge sites at the next timestep. Finally, the convergence of the simulation is checked by comparing the flow fields at the beginning of the timestep to those at the beginning of the previous timestep. We choose to use the L^1 norm of the velocity flow field to check whether the simulation has converged sufficiently, i.e.:

$$\frac{\sum_{sites} |\mathbf{v}(x, y, z, t) - \mathbf{v}(x, y, z, t - 1)|}{\sum_{sites} |\mathbf{v}(x, y, z, t)|} < tol, \quad (3.25)$$

where tol is the tolerance. This convergence criterion may also be used for pulsatile flow. In that case, the simulation is considered to be converged when the velocity as a function of space and time is the same during each pulsatile period.

3.5.1 Method for avoiding the creation and destruction of fluid nodes as the wall moves over a lattice site

As the wall moves, the fluid domain may expand to include site w in figure 3.4. In this case, we do not change w into a fluid node, as stated at the beginning of this section, but we simply allow the value of δ to increase beyond 1, i.e. we have $|\mathbf{x}_b - \mathbf{x}_f| > |\mathbf{x}_w - \mathbf{x}_f|$. This allows the value of $\Delta R > 1$. If $\delta > 1$, the extrapolation to find the velocity at site w in equation (2.204) to apply the velocity boundary conditions becomes an interpolation. By Taylor expanding \mathbf{v}_w and \mathbf{v}_b about \mathbf{x}_f , it can be shown that the error in the interpolation or extrapolation of \mathbf{v}_w is proportional to $(\Delta x)^2(1-\delta)$. We expect similar errors in the velocity field throughout the system. If the wall displacement ratio due to elasticity, $\Delta R/R_0$, remains constant and the lattice spacing is changed, the values of δ change approximately according to $\delta \propto \Delta R/(R_0 \Delta x)$. Therefore, we expect our simulations to be first-order accurate in space and in the value of $\Delta R/R_0$. If fluid nodes were created or destroyed, the velocity would be second-order accurate in space since the lattice-Boltzmann method and the scheme that is applied for the boundary conditions at the edge sites are second-order accurate, as explained in sections 2.8 and 2.9.5 respectively.

3.5.2 Oscillation of the walls

During a simulation, the walls oscillate about their equilibrium position according to equation (3.9). This influences the velocity flow field, which in turn influences the pressure exerted on the walls, so both the walls and the fluid oscillate while the oscillations are damped by the viscosity of the fluid. The simulation converges to a steady state when the oscillations die out. Since pressure boundary conditions are imposed at the inlet and outlet, the walls at the inlet and outlet oscillate indefinitely if the wall there does not start in its equilibrium position given by equation (3.9) with $\frac{d^2 R}{dt^2} = 0$; this prevents the simulation from converging due to the influence of the flow fields at the inlet and outlet

on the flow fields elsewhere. Hence, the walls at the inlet and outlet radii are initialised to their equilibrium positions.

The wall may undergo many oscillations before the simulation converges. Therefore, we have implemented an optional damping factor. This damping factor is removed when the simulation has almost converged, i.e. when equation (3.15) is satisfied for a tolerance three times higher than tol , in order to simulate a system in which the walls themselves do not provide any damping. Equation (3.9) with damping factor b is

$$\rho_{\text{wall}} h \frac{d^2 \Delta R}{dt^2} = (p - p_0) - \frac{4 E h}{3 R_0} \left(1 - \frac{R_0}{R_0 + \Delta R} \right) - b \frac{d \Delta R}{dt}. \quad (3.26)$$

A linear approximation to equation (3.26), valid for small displacements, i.e. $\Delta R \ll R_0$, is

$$\frac{d^2 \Delta R}{dt^2} + \frac{b}{\rho_{\text{wall}} h} \left(\frac{d \Delta R}{dt} \right) + \frac{4 E}{3 \rho_{\text{wall}} R_0^2} \Delta R - \frac{p - p_0}{\rho_{\text{wall}} h} = 0. \quad (3.27)$$

For a constant pressure, if we have light damping, the solution would be

$$\Delta R = \Re \left[A \exp \left(-\frac{bt}{2\rho_{\text{wall}} h} - i\omega t \right) \right], \quad (3.28)$$

where \Re means “the real part of”, with

$$\omega^2 = \omega_0^2 - \frac{b^2}{4\rho_{\text{wall}}^2 h^2}, \quad (3.29)$$

$$\omega_0^2 = \frac{4 E}{3 R_0^2 \rho_{\text{wall}}}. \quad (3.30)$$

The damping factor was chosen to be half that for critical damping, i.e. $b = \rho h \omega_0$. Therefore, equation (3.28) becomes

$$\Delta R = \Re[A \exp(-\omega_0 t/2 - i\omega t)]. \quad (3.31)$$

From equation (3.31), the amplitude of the oscillation decreases by a factor of 10^{-8} in a time $t = 37/\omega_0$. Therefore, if we have $tol = 10^{-8}$ it is expected that *any* simulation would converge in a number of timesteps approximately equal to $37/\omega_0$ except if the simulation with rigid walls with the same dimensions, relaxation parameter and Reynolds number requires more timesteps than this to converge, in which case the simulation with elastic walls would require approximately the same number of timesteps because the rate of

convergence is limited by that of the lattice-Boltzmann method rather than the oscillation of the walls. The additional damping factor also greatly enhances the stability of the simulation.

The period of oscillation of the wall, under constant pressure conditions, i.e. the period without taking into account the fluid, is $\Lambda' = 2\pi/\omega$. The period of oscillation without the additional damping factor, which we will call the free period, is shorter, and is given by

$$\Lambda = \frac{2\pi}{\omega_0} = \pi R_0 \sqrt{\frac{3\rho_{\text{wall}}}{E}}. \quad (3.32)$$

If the convergence rate is limited by the oscillation of the walls, the number of timesteps that we estimate will be required, $37/\omega_0$, is six times the free period of oscillation of the wall.

3.5.3 Solving the equation of motion

The displacement and velocity of the wall were calculated by integrating equation (3.26) numerically using a Runge-Kutta method adapted for solving second-order differential equations. This scheme finds the radius and velocity of one point on the wall at the current timestep from the same quantities at the previous timestep and the current pressure. Second-order equations can be expressed as two first-order equations with two dependent variables, i.e.

$$\frac{dy}{dt} = y' \quad (3.33)$$

$$\frac{dy'}{dt} = f(t, y, y') \quad (3.34)$$

where t is the independent variable, and y and $y' = dy/dt$ are the dependent variables.

The Runge-Kutta method could be developed for accuracy up to any order in the step size, but the lattice-Boltzmann method only simulates fluid flow accurate to second order in space and first order in time (see section 3.2.2), so a second-order method is sufficiently

accurate. The following iteration scheme for equations (3.33) and (3.34) guarantees second-order accuracy in the step size, h :

$$y_{t+h} = y_t + 0.5(a_1 + a_2) \quad (3.35)$$

$$y'_{t+h} = y'_t + 0.5(a'_1 + a'_2) \quad (3.36)$$

with

$$a_1 = hy'_t,$$

$$a'_1 = hf(t, y_t, y'_t),$$

$$a_2 = h(y'_t + a'_1),$$

$$a'_2 = hf(t + h, y_t + a_1, y'_t + a'_1).$$

In order to solve equation (3.26) to find the motion of the wall, we replace y with ΔR , y' with $u = \frac{d\Delta R}{dt}$ and h with Δt in equations (3.35) and (3.36). This gives:

$$R_{t+\Delta t} = R_t + 0.5(a_1 + a_2) \quad (3.37)$$

$$u_{t+\Delta t} = u'_t + 0.5(a'_1 + a'_2) \quad (3.38)$$

with

$$a_1 = \Delta t u_t$$

$$a'_1 = \Delta t \left(\frac{p - p_0}{\rho_{\text{wall}} h} - \frac{b u_t}{\rho_{\text{wall}} h} - \frac{4}{3} \frac{E}{\rho_{\text{wall}}} \left(\frac{1}{R_0} - \frac{1}{R_0 + \Delta R} \right) \right)$$

$$a_2 = \Delta t (u_t + a'_1)$$

$$a'_2 = \Delta t \left(\frac{p - p_0}{\rho_{\text{wall}} h} - \frac{b}{\rho_{\text{wall}} h} (u_t + a'_1) - \frac{4}{3} \frac{E}{\rho_{\text{wall}}} \left(\frac{1}{R_0} - \frac{1}{R_0 + \Delta R + a_1} \right) \right).$$

For the scheme to be valid, the free period of oscillation of the wall must be much larger than the timestep Δt . The period of oscillation is given by equation (3.32). The method was tested for various periods of oscillation, T , for the linear approximation to the equation of motion (equation (3.27)), with no damping and a constant pressure, i.e.

$$\frac{d^2 \Delta R}{dt^2} + \frac{4}{3} \frac{E}{\rho_{\text{wall}} R_0^2} \Delta R - \frac{p - p_0}{\rho_{\text{wall}} h} = 0. \quad (3.39)$$

The maximum relative error in displacement, $\epsilon_{\Delta R}$, and the maximum relative error in velocity, $\epsilon_{\mathbf{v}}$, were calculated as follows over 10 periods of oscillation:

$$\epsilon_{\mathbf{v}} = \frac{\max_{t=0}^{10T} |\mathbf{v}(t) - \mathbf{v}'(t)|}{\max_{t=0}^{10T} |\mathbf{v}'(t)|}, \quad (3.40)$$

$$\epsilon_{\Delta R} = \frac{\max_{t=0}^{10T} |\Delta R(t) - \Delta R'(t)|}{\max_{t=0}^{10T} |\Delta R'(t)|}, \quad (3.41)$$

where the primed quantities denote the analytical values. At $T = 1460\Delta t$, errors of $\epsilon_{\Delta R} = 1.9 \times 10^{-4}$ and $\epsilon_{\mathbf{v}} = 1.9 \times 10^{-4}$ were obtained. The errors were $O(\Delta t^2)$. From equation (3.32), we have $T > 1460\Delta t$ in the simulation of fluid flow in an elastic pipe in this study.

3.5.4 Comparison of numerical and analytical solutions

When the steady state is reached, the velocity and pressure fields and the displacements of the wall are compared with analytic solutions. The simulation errors are measured with ϵ_1 and ϵ_∞ , i.e. the L^1 and L^∞ norms, which are given by equations (3.18) and (3.19) respectively for the velocity. They are calculated similarly for the pressure difference, $p - p_0$, and the wall displacement, ΔR .

If the tube is long and thin, smooth under deformation and aligned along the x axis, the velocity at a displacement x from the inlet is equal to that of Poiseuille flow for a tube of radius $R(x)$. In three dimensions, the flow rate is given by:

$$Q(x) = \int_0^{R(x)} v_x(x, r)(2\pi r)dr = -\frac{\pi R^4(x)}{8\nu\rho} \frac{dp(x)}{dx}. \quad (3.42)$$

The flow rate can be expressed in terms of $R(x)$ using the expression for the pressure-radius relation, which comes from setting $\frac{d^2R}{dt^2} = 0$ in equation (3.9), giving

$$p(x) - p_0 = \frac{4}{3} \frac{Eh}{R_0} \left(1 - \frac{R_0}{R(x)} \right). \quad (3.43)$$

The flow rate is constant at all values of x in the tube, which allows us to find the functional form of $R(x)$. We can find dp/dx from equation (3.43), substitute it into equation (3.16),

then integrate with respect to x , as described by Fung [76], to obtain:

$$\left(\frac{18\nu Q}{\pi E h}\right)x = R^3(0) - R^3(x). \quad (3.44)$$

The radii of the tube at the inlet and outlet, $R(0)$ and $R(L)$ respectively, are determined from the pressure boundary conditions by equation (3.43). The flow rate can be found by substituting $R(0)$ and $R(L)$ into equation (3.44).

3.6 Results

A simulation of steady flow in a 3D elastic cylinder pointing along the x axis was performed and compared to a simulation with rigid walls with the same dimensions and Reynolds number. The simulation parameters were chosen such that the Reynolds number and maximum displacement of the wall relative to its position at the reference pressure are realistic for blood flow through large cerebral arteries, as explained in the introduction. We define the Reynolds number as $Re = 2v_{\max}R_0/\nu$, where v_{\max} is the maximum velocity, R_0 is the radius of the tube at the reference pressure and ν is the kinematic viscosity. We chose $Re = 120$, at which we expect the flow to be laminar, since the transition to turbulence occurs between $Re = 1500$ and $Re = 4000$ for flow in a cylinder [76]. The wall displacement at the inlet is 1.0 lattice length, which is 5% of R_0 , i.e. the cross-sectional area is 10% larger than at the reference pressure. In lattice units, the pressure difference between the inlet and outlet is $p(0) - p(L) = 5.4 \times 10^{-4}$, the relaxation parameter $\tau = 0.53$, the wall thickness $h = 4.0$, the Young's Modulus $E = 0.043$, the density of the fluid $\rho = 1.0$ and the density of the wall $\rho_{\text{wall}} = 7.8$. From equation (3.32), the free period of oscillation of the wall is 1500 timesteps. The tolerance for the convergence criterion in equation (3.15) was 1.0×10^{-8} . The damping factor was included in the simulation.

Figure 3.5 shows the difference between the numerical and analytical wall displacement ($\Delta R_{\text{numerical}} - \Delta R_{\text{analytical}}$) as a function of x . The mean of this difference over all edge sites at each value of x is plotted and the error bars show the range of this difference at each value of x . Figure 3.6 shows the difference between the numerical and analytical pressure ($p_{\text{numerical}} - p_{\text{analytical}}$). The mean of this difference over all sites at each value of x is plotted and the error bars show the range of this difference. The simulation errors are

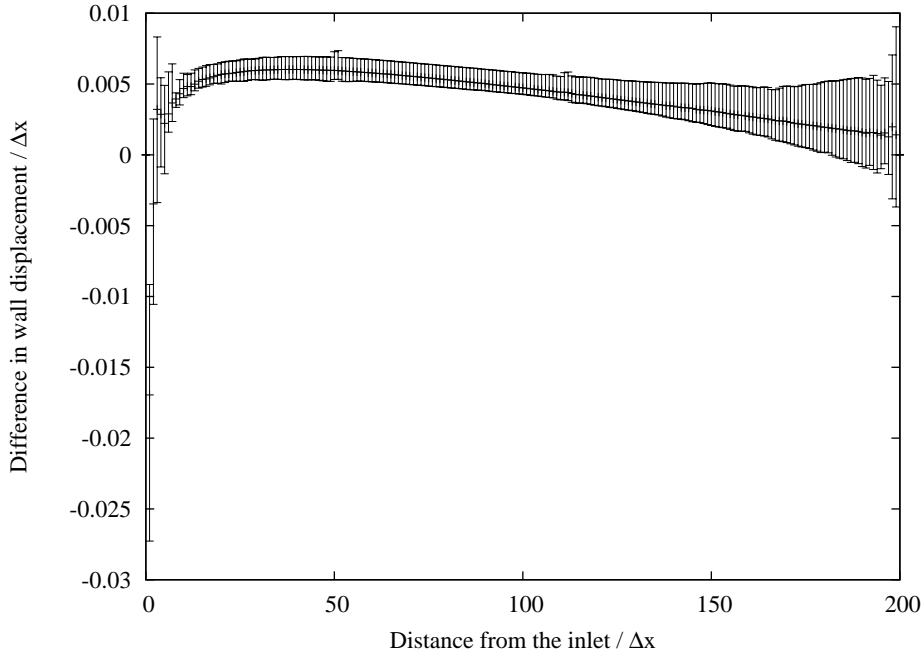


FIGURE 3.5: Difference between the numerical and analytical displacement ($\Delta R_{numerical} - \Delta R_{analytic}$) as a function of x in a simulation of fluid flow in a 3D elastic cylinder that includes a damping factor, with $\Delta R = 1.0$ lattice unit at the inlet and Reynolds number $Re = 120$. The mean difference in displacement over all edge sites at a particular value of x is shown by a cross, and its range over the same sites is shown as an error bar.

small compared with the difference between the inlet and outlet pressure and the maximum wall displacement respectively. The largest simulation errors, of 2.7%, occur near the inlet, where the cylinder is slightly narrower than the analytical solution predicts.

Figure 3.7 shows the x component of velocity, v_x , as a function of the distance from the centreline of the tube at four places along the length of the tube. The numerical results exhibit the expected Poiseuille flow and agree closely with the analytic solution. The maximum numerical value of v_x is 2.79×10^{-2} in lattice units and it occurs at coordinate $(200, 0, 0)$. The maximum analytical velocity of 3.00×10^{-2} lattice units occurs at the same place. The maximum absolute values of velocity in the y and z directions are both 1.98×10^{-4} in lattice units. The velocity is slightly lower than that predicted by the analytical solution at all four locations along the length of the tube. This is because the cylinder is narrower than the analytical solution predicts near to the inlet, which restricts the flow. The maximum error in the wall displacement is 2.7% and the flow velocity is proportional to the square of the radius of the cylinder, so this would account for a difference of 5.4% in the velocity.

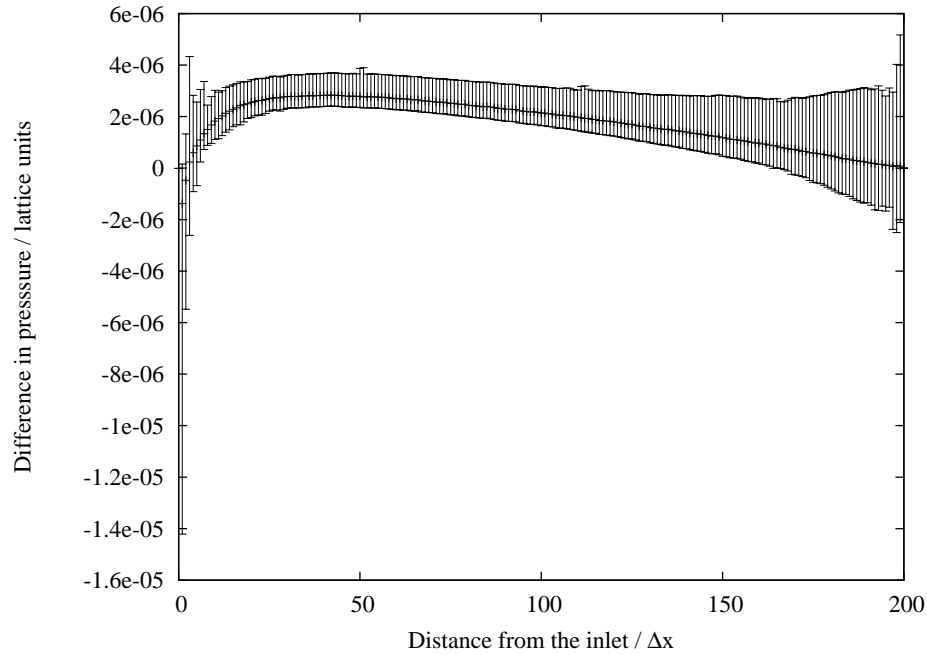


FIGURE 3.6: Difference between the numerical and analytical pressure ($p_{numerical} - p_{analytical}$) as a function of x in a simulation of fluid flow in a 3D elastic cylinder that includes a damping factor, with $\Delta R = 1.0$ lattice unit at the inlet and Reynolds number, $Re = 120$. The mean difference in pressure from the analytical solution over all edge sites at a particular value of x is shown by a cross, and its range over the same sites is shown by an error bar.

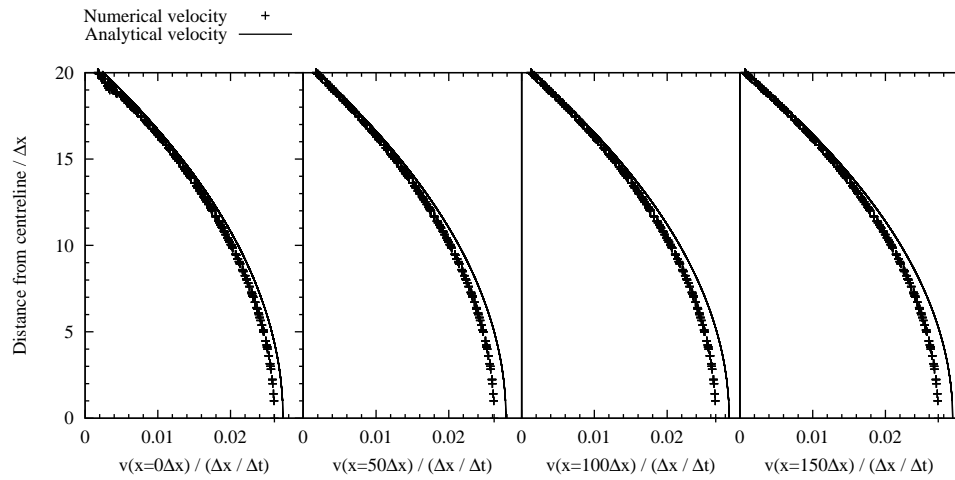


FIGURE 3.7: Velocity of flow in the x direction at four values of x in a simulation of fluid flow in a 3D elastic cylinder that includes a damping factor, with $\Delta R = 1.0$ lattice unit at the inlet and Reynolds number $Re = 120$. The crosses are the numerical results and the line is the analytical solution. The numerical velocity is slightly lower than the analytical velocity because the cylinder is slightly narrower than the analytical solution predicts near the inlet, which restricts the flow.

TABLE 3.6: Relative errors in velocity, pressure and wall displacement for a simulation of fluid flow in a 3D elastic cylinder that includes a damping factor, with $\Delta R = 1.0$ lattice unit at the inlet and Reynolds number $Re = 120$, and for a simulation with rigid walls with the same dimensions and Reynolds number.

Quantity and type of error	Simulation error	
	Rigid walls	Elastic walls with damping factor
velocity ϵ_1	4.87×10^{-3}	5.79×10^{-2}
velocity ϵ_∞	1.69×10^{-2}	7.12×10^{-2}
pressure difference ϵ_1	3.15×10^{-3}	6.39×10^{-3}
pressure difference ϵ_∞	9.21×10^{-3}	2.61×10^{-2}
wall displacement ϵ_1	0	8.40×10^{-3}
wall displacement ϵ_∞	0	2.74×10^{-2}

TABLE 3.7: Comparison of computational cost between the simulation of fluid flow in a 3D elastic cylinder that includes a damping factor, with $\Delta R = 1.0$ lattice unit at the inlet, and the simulation for rigid walls with the same Reynolds number.

Quantity measured in simulation	Rigid walls	Elastic walls with damping factor
Site updates per second	2.42×10^6	2.07×10^6
Timesteps until convergence	64737	62522
Wall clock time for the simulation	6760s	7630s

For the velocity, wall displacement and pressure relative to the reference pressure ($p - p_0$), the ϵ_1 and ϵ_∞ errors were calculated using equations (3.18) and (3.19). These relative errors, and the error for a simulation with rigid walls with the Reynolds number $Re = 120$, are shown in table 3.6. Comparing the simulations with rigid and elastic walls, it can be seen that taking into account wall elasticity introduces errors of less than 6% in the velocity, less than 2% in the density and less than 3% in the wall displacement.

Table 3.7 compares the computational cost of the simulation with elastic walls to that of the simulation with rigid walls with the same Reynolds number, Re . We ran these simulations on a 2.5GHz Intel Q3900 quad-core machine, using OpenMP to parallelise the program [123], and having compiled the program with the optimisation flag -O3. The wall clock time was measured by taking the difference in the return values of the function `time()` from the standard C library at the beginning and end of the simulation. The number of site updates per second was 14% lower when elasticity was included, so only 17% more work was needed for each timestep. The simulation time was 12% longer than that for a simulation with rigid walls and it required 3% fewer timesteps.

3.7 Discussion

For three-dimensional simulations of fluid flow in elastic pipes, the ϵ_1 simulation errors in velocity, pressure difference and wall displacement are 6%, 0.6% and 0.8% respectively and the ϵ_∞ errors are 7%, 3% and 3% respectively, which shows that the pressure field and the shape of the wall are calculated very accurately. While the relative errors in velocity are slightly larger, the simulation method is sufficiently accurate to reveal the patterns in the velocity field and the accuracy is comparable with possible errors in geometry due to the finite resolution of, for example, medical imaging techniques.

The simulation errors are higher than those for the simulation with rigid walls for the same dimensions and Reynolds number, but the differences in both types of relative error are less than 6%, 2% and 3% for the velocity, pressure difference and wall displacement respectively. The reason for the larger errors is that the wall is generally further from the sites at which the boundary condition method is applied.

The method satisfies the requirement, explained at the beginning of this chapter, that the calculation at every site depends only on information from nearest neighbours. No more communication between processors is required for a simulation with elastic walls than one with rigid walls. On 4 cores, 14% fewer site updates per second were achieved compared with the simulation for rigid walls. This is because, in addition to the lattice-Boltzmann method and boundary conditions, the Runge-Kutta method was applied to calculate the position and velocity of the wall, and the fractions of the links between fluid sites adjacent to boundaries and their neighbouring solid sites were recalculated at every time step.

While the number of timesteps required for convergence was 42 times the free period of oscillation of the wall, it was approximately equal to the number of timesteps for a comparable simulation with rigid walls, as predicted in section 3.5.2. This shows that the rate of convergence is limited by that of the lattice-Boltzmann method rather than the oscillation of the wall.

The Reynolds number and maximum wall displacement in the simulation were reasonably realistic for blood flow through the largest cerebral arteries. For these parameters, the simulation is accurate and the computational cost is little more than that for a comparable

simulation with rigid walls, which shows that the method described in this study may be suitable for simulating cerebral blood flow.

In physical units, the density of the wall was $\rho_{\text{wall}} = 7800\text{kg m}^{-3}$, while for cerebral arteries, we would expect $\rho_{\text{wall}} = 1000\text{kg m}^{-3}$. The free period of oscillation of the wall decreases as ρ_{wall} decreases, which reduces the accuracy of the Runge-Kutta method used to calculate the position and velocity of the wall and could cause instability. This does indeed happen if $\rho_{\text{wall}} = 1000\text{kg m}^{-3}$ for the simulation described in this paragraph. However, it is sensible to choose a slightly higher value of ρ_{wall} because the cerebral arteries are surrounded by other tissues in the brain, which are likely to increase the free period of oscillation of the wall.

The method is sensitive to relatively small displacements of the wall, which were less than 5% of the original radius of the cylinder in this study. The fluid domain can, and does, expand to include sites that were initially solid. In this case, we continue to treat these sites as solid sites and simply apply the boundary condition method at the same fluid sites, taking into account the increased displacement of the wall. As explained in section 2.9.5, we expect that this method for dealing with the walls would introduce relative errors proportional to the ratio of wall displacement to the initial radius of the cylinder and that, for the same relative wall displacement, the error would be first order in space. For relatively large wall displacements, allowing creation or destruction of fluid nodes may improve the accuracy because the sites at which the boundary conditions are applied would be closer to the walls. However, this may increase the computational cost considerably (see section 3.1) because information from different sites would be needed as the simulation progresses, unless one is able to set up the necessary buffers to pass information between processors on a multicore machine. This could be done by setting up buffers for the extra lattice sites that may be needed during the simulation and indexing the sites, including these extra ones, at the beginning of the simulation.

Although the method developed for simulating fluid flow in elastic pipes can be used in a complex geometry, the equation of motion for an element of the wall would need to be modified. The elastic restoring force would depend on the strain and the principal radii of curvature rather than only the radius. In simulations of flow through pipes that bend significantly, two principal radii of curvature would be needed. The equation of motion could be derived by considering an element of the wall in the same manner as in section

3.2.1, and we expect it to have a similar form to the current equation of motion. Therefore, it may not be significantly more computationally intensive to solve.

We may require information from nearby points to calculate the normal, strain and radii of curvature when simulating the flow in complex geometries. We track the motion of one point on the wall for each lattice site that is adjacent to the wall, as described in section 3.5. Therefore, when updating a lattice site and its point on the wall, we can minimise the computational cost by only using information from neighbouring lattice sites and their points on the wall, so that the amount of communication between processors would not increase significantly. While the calculation of the normal, strain and radii of curvature will increase the computational cost at the edge sites slightly, we anticipate that this will have a minor effect on the overall computational cost of the simulation because the majority of lattice sites in the simulation are not adjacent to the wall. For simulations running in parallel on multicore machines, we can take into account the relative computational costs of edge sites and non-edge sites when dividing the computational domain between the processors.

3.8 Conclusions

A new method has been proposed for simulating viscous fluid flow in elastic pipes using the lattice-Boltzmann method. It is based on estimating the distances from sites at the edge of the simulation box to the wall in the lattice directions, from the displacement of the closest point on the wall and its curvature. The nonequilibrium extrapolation method [10] is then applied as it would be in a simulation with rigid walls, making use of these distances. The method is capable of simulating flow in a three-dimensional vessel with curved boundaries.

The simulation method has been tested in a cylinder and the numerical results for the pressure, velocity and wall displacement are in good agreement with the analytical solutions. The maximum relative errors in velocity, pressure difference and wall displacement are 7%, 3% and 3% respectively. The simulation errors are higher than those for the simulation with rigid walls for the same dimensions and Reynolds numbers, but the differences are less than 6%, 2% and 3% for the velocity, pressure difference and wall displacement respectively.

The method is promising for simulations of cerebral blood flow because, at a realistic Reynolds number, wall displacement and wall density, as well as being accurate, its computational cost is little more than the cost for a comparable simulation with rigid walls. This is because it requires a similar number of timesteps and the computational effort per timestep is such that 14% fewer site updates are achieved per second. The algorithm for calculating the flow fields at each lattice site depends only on information from the nearest neighbours, and no fluid nodes are created or destroyed, so it is suitable for use in large simulations running in parallel on multicore machines. No more information needs to be communicated between lattice sites than in a simulation with rigid walls.

The simulation method proposed is also sensitive to small displacements of the wall, therefore it may be especially useful for simulations of complex, branching geometries, such as the cerebral vasculature. This simulation method could also be applied in studies of the bladder and urinary tract or for designs of piping systems in engineering projects.

In situations where the density of the wall is very low, or the free period of oscillation of the wall is very short, the simulation may become unstable due to the limitations of the Runge-Kutta method. This could be improved by using several timesteps for calculating the displacement and velocity of the wall during each timestep for the lattice-Boltzmann method.

Chapter 4

A new method for simulating fluid flow through elastic systems with a general geometry

In the previous chapter, a method for simulating fluid flow through elastic vessels was developed that has could be used for modelling cerebral blood flow. The theory in section [3.2.1](#) assumes that the system is axisymmetric and that the radius of the vessel varies slowly along its length, so that the $\sigma_{r\theta} = \sigma_{z\theta} = \sigma_{zr} = 0$, where r and θ are the radial and circumferential directions and z is the axis of symmetry. The model can be used for individual arteries provided that they are locally almost axisymmetric, and the directions of their axes vary slowly along their length. Given the positions of a point on the wall and its neighbours, it would be straightforward to estimate the normal to the wall (the radial direction) and the principal radius of curvature, R_0 , and its direction (the circumferential direction) at that point. The z direction is perpendicular to the other two directions. For aneurysms, one could follow the method of section [3.2.1](#) assuming spherical symmetry.

However, the model would not be valid at the branches between arteries or at the edges that connect arteries to aneurysms because there is no symmetry about any of the axes. It is also possible that the axes of the blood vessels may change too quickly for the model to be valid. Therefore, the full theory of linear elasticity is required to simulate blood flow through such complex geometries accurately. In this chapter, I develop a scheme

for simulating fluid flow through elastic vessels in two dimensions with this theory. The theory required is discussed in section 4.1 and the method is explained in sections 4.2 to 4.4. Section 4.3 explains how the neighbours to each point on the wall are chosen, while section 4.4 explains how the surface normals, stress tensor and distances from the wall to the adjacent lattice sites along the lattice vectors are calculated. The work required to extend the method to three dimensions is discussed in section 4.5. Section 4.6 reviews some experimental and computational work on an extensively studied system of fluid flow through compliant vessels. The results from the scheme developed here are compared with those from computational studies of the same system in section 4.7. Conclusions for this chapter are presented in section 4.8.

4.1 Theory of Linear Elasticity in Two and Three Dimensions

In this section, I outline the theory of linear elasticity in the case of a general geometry, based on Landau and Lifshitz [121, chapter 1] unless otherwise stated. We use the summation convention for subscripts throughout this section.

4.1.1 The Strain Tensor

In this subsection, the strain tensor is defined in terms of the derivatives of the displacement field.

The deformation of a body is described mathematically in the following way. Let the position of a point in the body be defined by the vector \mathbf{r} , denoted x_i before deformation and \mathbf{r}' , denoted x'_i after deformation. The displacement of a point due to the deformation is given by the vector $u_i = x'_i - x_i$. The displacement vector is a function of the original position in the body. Let dl and dl' be the distance between two points in the body that are very close together before and after deformation respectively. We have

$$dl'^2 = (dx_i + du_i)^2 \tag{4.1}$$

$$= dx_i^2 + 2du_i dx_i + du_i^2 \tag{4.2}$$

$$dl'^2 = dl^2 + 2 \frac{\partial u_i}{\partial x_k} dx_i dx_k + \frac{\partial u_i}{\partial x_k} \frac{\partial u_i}{\partial x_l} dx_k dx_l. \tag{4.3}$$

Splitting the second term by swapping suffixes i and k and swapping suffixes i and l in the third term gives

$$dl'^2 = dl^2 + \left(\frac{\partial u_i}{\partial x_k} + \frac{\partial u_k}{\partial x_i} + \frac{\partial u_l}{\partial x_k} \frac{\partial u_l}{\partial x_i} \right) dx_i dx_k. \quad (4.4)$$

The strain tensor, ϵ_{ik} is defined as

$$dl'^2 = dl^2 + 2\epsilon_{ik} dx_i dx_k. \quad (4.5)$$

Therefore, it can be expressed in terms of the spatial derivatives of the displacement as

$$\epsilon_{ik} = \frac{1}{2} \left(\frac{\partial u_i}{\partial x_k} + \frac{\partial u_k}{\partial x_i} + \frac{\partial u_l}{\partial x_i} \frac{\partial u_l}{\partial x_k} \right). \quad (4.6)$$

For small deformations, the strain tensor is given by

$$\epsilon_{ik} = \frac{1}{2} \left(\frac{\partial u_i}{\partial x_k} + \frac{\partial u_k}{\partial x_i} \right). \quad (4.7)$$

The relative change in volume in 3D or area in 2D during a deformation can be derived by considering an infinitesimal element with area or volume dV before deformation and dV' afterwards. We take the principal axes of the strain tensor as the coordinate axes. Therefore:

$$dV' = dV \prod_{i=1}^{N_D} (1 + \epsilon^{(i)}), \quad (4.8)$$

where N_D is the number of dimensions and $\epsilon^{(i)}$ is the i th principal value of the strain tensor. Neglecting higher-order terms, we have

$$dV' = dV \left(1 + \sum_{i=1}^{N_D} \epsilon^{(i)} \right) \quad (4.9)$$

The sum of the principal values of a tensor is equal to the sum of the diagonal components. Therefore

$$\frac{dV' - dV}{dV} = \epsilon_{ii}. \quad (4.10)$$

4.1.2 The stress tensor

In this subsection, the force per unit volume is derived in terms of the stress tensor and the constraints on it at the boundaries of an elastic body.

The force per unit volume, F_i , is given by the divergence of the stress tensor with respect to the coordinates of the deformed body, i.e.

$$F_i = \frac{\partial \sigma_{ik}}{\partial x'_k} \quad (4.11)$$

We can find the acceleration of a point in the body by dividing by the density there.

When the deformations are small, the derivatives of the stress tensor with respect to x_i and x'_i differ only by higher-order quantities, so we may therefore make the approximation that

$$F_i = \frac{\partial \sigma_{ik}}{\partial x_k}. \quad (4.12)$$

Furthermore, when the deformations are small, $\frac{dV' - dV}{dV} \ll 1$, so the acceleration of a point in the body is given by

$$\frac{d^2 u_i}{dt^2} = \frac{F_i}{\rho_0}, \quad (4.13)$$

where ρ_0 is the density of the body before deformation and $\frac{d^2 u_i}{dt^2} = \frac{dv_i}{dt} = \frac{\partial v_i}{\partial t} + v_j \frac{\partial v_i}{\partial x_j}$, is the convective derivative of the velocity field \mathbf{v} in the elastic material.

From equation (4.12), it follows that the force on any volume can be written as an integral of the stress over the closed surface, i.e.

$$\int_V F_i dV = \int_V \frac{\partial \sigma_{ik}}{\partial x_k} dV = \oint_S \sigma_{ik} ds_k, \quad (4.14)$$

where ds_k are the components of the surface element vector directed along the outward normal. Let us consider an element of an elastic body of finite area but infinitesimal thickness at the surface, as shown in figure 4.1. If the outward normal to the surface is \mathbf{n} , the force on the surface is given by $\oint_S (\tau \cdot \mathbf{n} - \sigma \cdot \mathbf{n})$, where τ is the external stress. The acceleration of this element must be finite, but its volume is infinitesimal, which implies that we must have

$$\sigma \cdot \mathbf{n} = \tau \cdot \mathbf{n}, \quad (4.15)$$

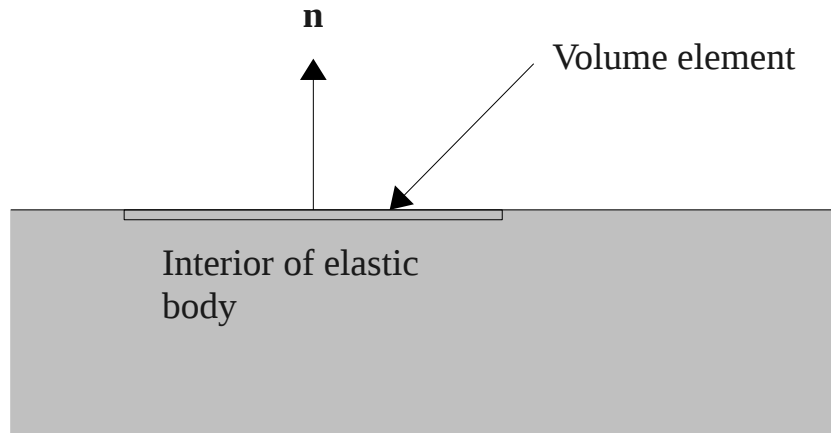


FIGURE 4.1: A volume element at the boundary of the elastic body.

whether or not the elastic body is in equilibrium.

4.1.3 Calculating the Free Energy

In this subsection, the Helmholtz free energy is expressed in terms of the strain tensor. This expression can be used to derive Hooke's law.

We consider the free energy of a body, W , as a function of the strain tensor, ϵ_{ik} . The strain tensor for an elastic body is given by equation (4.7). We take the undeformed state to be the state of the body in the absence of external force and at the same temperature. Then for $\epsilon_{ik} = 0$, the internal stresses are also zero, i.e. $\sigma_{ik} = 0$. Since

$$\sigma_{ik} = \frac{\partial W}{\partial \epsilon_{ik}}, \quad (4.16)$$

it follows that there is no linear term in the expansion of W in powers of ϵ_{ik} . Next, since the free energy is a scalar, each term in the expansion of W must also be a scalar. Two independent scalars of the second degree can be formed from the components of ϵ_{ik} . Therefore, expanding W in powers of ϵ_{ik} , we therefore have as far as terms of the second order

$$W = W_0 + \frac{1}{2} \lambda \epsilon_{ii}^2 + \mu \epsilon_{ik} \epsilon_{ik}, \quad (4.17)$$

where λ and μ are called Lamé coefficients.

Any deformation can be represented as the sum of a pure shear and a hydrostatic compression. To do so, we use the identity

$$\epsilon_{ik} \equiv \left(\epsilon_{ik} - \frac{1}{N_D} \delta_{ik} \epsilon_{ll} \right) + \frac{1}{N_D} \delta_{ik} \epsilon_{ll}. \quad (4.18)$$

Since the relative change in volume in 3D or area in 2D in a deformation is given by equation (4.10), $\frac{dV'-dV}{dV} = \epsilon_{ii}$, the first term on the right of equation (4.18) is a pure shear, since the sum of its diagonal terms is zero because $\delta_{ii} = N_D$. The second term is a hydrostatic compression. Substituting this into equation (4.17), we have

$$W = \mu \left(\epsilon_{ik} - \frac{1}{N_D} \delta_{ik} \epsilon_{ll} \right)^2 + \frac{2}{N_D} \mu \delta_{ik} \epsilon_{ik} \epsilon_{ll} - \frac{1}{N_D^2} \mu \delta_{ik} \delta_{ik} \epsilon_{ll}^2 + \frac{1}{2} \lambda \epsilon_{ii}^2 \quad (4.19)$$

$$\Rightarrow W = \mu \left(\epsilon_{ik} - \frac{1}{N_D} \delta_{ik} \epsilon_{ll} \right)^2 + \mu \left(\frac{2}{N_D} - \frac{N_D}{N_D^2} + \frac{1}{2} \lambda \right) \epsilon_{ll}^2 \quad (4.20)$$

$$\Rightarrow W = \mu \left(\epsilon_{ik} - \frac{1}{N_D} \delta_{ik} \epsilon_{ll} \right)^2 + \frac{1}{2} K \epsilon_{ll}^2 \quad (4.21)$$

with

$$K = \lambda + \frac{2}{N_D} \mu, \quad (4.22)$$

where we have dropped the term W_0 since it will be of no interest in what follows. K and μ are called respectively the *bulk modulus* or *modulus of hydrostatic compression* and the *shear modulus* or *modulus of rigidity*.

The free energy must be a minimum in equilibrium, therefore we have $K > 0$ and $\mu > 0$.

4.1.4 Hooke's law

In this subsection, Hooke's law is derived for a general geometry, based on Landau and Lifshitz [121, chapter 1].

We can find the stress in terms of the strain by first finding the total differential dW .

$$dW = K \epsilon_{ll} d\epsilon_{ll} + 2\mu \left(\epsilon_{ik} - \frac{1}{N_D} \delta_{ik} \epsilon_{ll} \right) d \left(\epsilon_{ik} - \frac{1}{N_D} \delta_{ik} \epsilon_{ll} \right) \quad (4.23)$$

We have $\left(\epsilon_{ik} - \frac{1}{N_D} \delta_{ik} \epsilon_{ll} \right) \delta_{ik} = \epsilon_{ii} - \frac{1}{N_D} \epsilon_{ll} N_D = 0$. Therefore:

$$dW = K \epsilon_{ll} d\epsilon_{ll} + 2\mu \left(\epsilon_{ik} - \frac{1}{N_D} \delta_{ik} \epsilon_{ll} \right) d\epsilon_{ik} \quad (4.24)$$

Using equation (4.16), the stress tensor is given by

$$\sigma_{ik} = K\delta_{ik}\epsilon_{ll} + 2\mu\left(\epsilon_{ik} - \frac{1}{N_D}\delta_{ik}\epsilon_{ll}\right) \quad (4.25)$$

To find the converse formula, we find the sum of the diagonal terms. This is zero for the second term on the right side of equation (4.25). Therefore

$$\epsilon_{ii} = \frac{\sigma_{ii}}{N_D K}, \quad (4.26)$$

Substituting this expression into equation (4.25), we find

$$\sigma_{ik} = \frac{\delta_{ik}\sigma_{ll}}{N_D} + 2\mu\epsilon_{ik} - 2\mu\frac{\delta_{ik}\sigma_{ll}}{N_D^2 K} \quad (4.27)$$

$$\Rightarrow \epsilon_{ik} = \frac{\delta_{ik}\sigma_{ll}}{N_D^2 K} + \frac{1}{2\mu}\left(\sigma_{ik} - \frac{1}{N_D}\delta_{ik}\sigma_{ll}\right) \quad (4.28)$$

The coefficients of the components of the strain tensor are consistent in Hooke's law in 2D and 3D if we express it in terms of the Lamé coefficients, since they then do not depend on the number of dimensions. Substituting equation (4.22) into equation (4.25), we find

$$\sigma_{ik} = \left(\lambda + \frac{2\mu}{N_D}\right)\delta_{ik}\epsilon_{ll} + 2\mu\left(\epsilon_{ik} - \frac{1}{N_D}\delta_{ik}\epsilon_{ll}\right) \quad (4.29)$$

$$\Rightarrow \sigma_{ik} = \lambda\delta_{ik}\epsilon_{ll} + 2\mu\epsilon_{ik}. \quad (4.30)$$

4.1.5 Expressing Hooke's law in terms of the Young's modulus and Poisson's ratio

In this subsection, we define the Poisson's ratio, Ω and Young's modulus, E in terms of the bulk and shear moduli and express Hooke's law in equation (4.25) in terms of Ω and E .

We first consider a simple extension or compression of a rod. Let the rod be along the y or z axis in two or three dimensions respectively, and let forces be applied to its ends which stretch it in both directions. The force per unit area is p . Since the deformation is homoeogeneous, i.e. ϵ_{ik} is constant through the body, the stress tensor σ_{ik} is also constant,

and so it can be determined at once from the boundary conditions. They are given by

$$\sigma_{ik}n_k = 0, \quad (4.31)$$

where n_k is the outward normal to the boundary. There is no external force on the sides of the rod, so all components of the stress tensor there are zero apart from σ_{yy} or σ_{zz} in two and three dimensions respectively. On the end surface, we have $\sigma_{zz} = p$. From the inverse of Hooke's law (equation (4.28)), all components ϵ_{ik} with $i \neq k$ are zero. For the remaining components, we find

$$\left(\frac{1}{N_D^2 K} + \frac{N_D - 1}{2N_D \mu} \right) p = \begin{cases} \epsilon_{yy}, & 2D \\ \epsilon_{zz}, & 3D \end{cases} \quad (4.32)$$

$$\left(\frac{1}{N_D^2 K} - \frac{1}{2N_D \mu} \right) p = \begin{cases} \epsilon_{xx}, & 2D \\ \epsilon_{xx} = \epsilon_{yy}, & 3D \end{cases} \quad (4.33)$$

The component ϵ_{yy} or ϵ_{zz} in 2D or 3D respectively gives the relative lengthening of the rod. The reciprocal of the coefficient of p is called the Young's modulus, E . We have

$$E = \begin{cases} \frac{p}{\epsilon_{yy}}, & 2D \\ \frac{p}{\epsilon_{zz}}, & 3D \end{cases} \quad (4.34)$$

$$\Rightarrow \frac{1}{E} = \frac{2\mu + N_D(N_D - 1)K}{2N_D^2 K \mu} \quad (4.35)$$

$$\Rightarrow E = \frac{2N_D^2 K \mu}{N_D(N_D - 1)K + 2\mu} \quad (4.36)$$

The ratio of transverse compression to longitudinal extension is called Poisson's ratio, Ω :

$$\Omega = \frac{N_D K - 2\mu}{N_D(N_D - 1)K + 2\mu}. \quad (4.37)$$

Rearranging equation (4.37) gives:

$$N_D(N_D - 1)\Omega K + 2\Omega\mu = N_D K - 2\mu \quad (4.38)$$

$$\Rightarrow 2\mu(\Omega + 1) = (1 - (N_D - 1)\Omega)N_D K \quad (4.39)$$

$$\Rightarrow 2\mu = \frac{1 - (N_D - 1)\Omega}{\Omega + 1} N_D K. \quad (4.40)$$

Since K and μ are always positive, Poisson's ratio can vary between -1 (for $K/\mu = 0$)

and $\frac{1}{N_D-1}$ (for $\mu/K = 0$). For incompressible materials, the bulk modulus is infinite, so $\mu/K = 0$ and we have a Poisson's ratio of $\frac{1}{N_D-1}$. Substituting the Poisson's ratio into equation (4.36) gives:

$$E = \frac{N_D^3 K^2 \left(\frac{1}{\Omega+1}\right) (1 - (N_D - 1)\Omega)}{N_D(N_D - 1)K + N_D K \left(\frac{1}{\Omega+1}\right) (1 - (N_D - 1)\Omega)} \quad (4.41)$$

$$\Rightarrow E = \frac{N_D^2 K (1 - (N_D - 1)\Omega)}{(N_D - 1)(\Omega + 1) + (1 - (N_D - 1)\Omega)} \quad (4.42)$$

$$\Rightarrow K = \left(\frac{(N_D - 1)(\Omega + 1) + 1 - (N_D - 1)\Omega}{N_D^2 (1 - (N_D - 1)\Omega)} \right) E \quad (4.43)$$

$$\Rightarrow K = \frac{N_D E}{N_D^2 (1 - (N_D - 1)\Omega)} \quad (4.44)$$

$$\Rightarrow K = \frac{E}{N_D (1 - (N_D - 1)\Omega)} \quad (4.45)$$

Substituting this into equation (4.40) gives

$$\mu = \frac{E}{2(1 + \Omega)} \quad (4.46)$$

Substituting equations (4.45) and (4.46) into equation (4.25) gives Hooke's law in terms of the Young's modulus and Poisson's ratio.

$$\sigma_{ik} = \frac{E}{N_D(1 - (N_D - 1)\Omega)} \delta_{ik} \epsilon_{ll} + \frac{E}{1 + \Omega} \left(\epsilon_{ik} - \frac{1}{N_D} \delta_{ik} \epsilon_{ll} \right) \quad (4.47)$$

$$= \frac{E}{1 + \Omega} \left(\epsilon_{ik} + \left(\frac{1 + \Omega}{N_D(1 - (N_D - 1)\Omega)} - \frac{1}{N_D} \right) \delta_{ik} \epsilon_{ll} \right) \quad (4.48)$$

$$= \frac{E}{1 + \Omega} \left(\epsilon_{ik} + \left(\frac{1 + \Omega - 1 + (N_D - 1)\Omega}{N_D(1 - (N_D - 1)\Omega)} \right) \delta_{ik} \epsilon_{ll} \right) \quad (4.49)$$

$$= \frac{E}{1 + \Omega} \left(\epsilon_{ik} + \frac{\Omega}{1 - (N_D - 1)\Omega} \delta_{ik} \epsilon_{ll} \right) \quad (4.50)$$

4.1.6 Equations of motion and its boundary conditions for an isotropic elastic medium

In this subsection, an equation of motion for an elastic medium is developed along with its boundary conditions.

We first express Hooke's law in terms of the displacement field by substituting the expression for the strain tensor (equation (4.7)) into that for Hooke's law (equation (4.50)):

$$\sigma_{ik} = \frac{E}{2(1 + \Omega)} \left[\frac{\partial u_i}{\partial x_k} + \frac{\partial u_k}{\partial x_i} + \left(\frac{\Omega}{1 - (N_D - 1)\Omega} \right) \delta_{ik} \frac{\partial u_l}{\partial x_l} \right] \quad (4.51)$$

Applying equation (4.12) to find the force per unit volume gives:

$$F_i = \frac{E}{2(1 + \Omega)} \left[\frac{\partial^2 u_i}{\partial x_k^2} + \frac{\partial^2 u_k}{\partial x_i \partial x_k} + \left(\frac{2\Omega}{1 - (N_D - 1)\Omega} \right) \frac{\partial^2 u_l}{\partial x_i \partial x_l} \right]. \quad (4.52)$$

Changing suffix l to k and applying equation (4.13) produces the equation of motion, given in Landau and Lifshitz [121, chapter 3]:

$$\frac{d^2 u_i}{dt^2} = \frac{E}{2(1 + \Omega)} \left[\frac{\partial^2 u_i}{\partial x_k^2} + \left(\frac{1 + (3 - N_D)\Omega}{1 - (N_D - 1)\Omega} \right) \frac{\partial^2 u_k}{\partial x_i \partial x_k} \right], \quad (4.53)$$

where $\frac{d^2 u_i}{dt^2} = \frac{dv_i}{dt} = \frac{\partial v_i}{\partial t} + v_j \frac{\partial v_i}{\partial x_j}$, is the convective derivative of the velocity field \mathbf{v} in the elastic material.

The boundary condition on the stress tensor, given by equation (4.15), can be expressed in terms of the derivatives of displacement by substituting equation (4.51) into it:

$$\tau_{ik} n_k = \frac{E}{2(1 + \Omega)} \left[\frac{\partial u_i}{\partial x_k} n_k + \frac{\partial u_k}{\partial x_i} n_k + \left(\frac{\Omega}{1 - (N_D - 1)\Omega} \right) \frac{\partial u_l}{\partial x_l} n_i \right]. \quad (4.54)$$

The equation can be rearranged such that both sides are dimensionless as follows:

$$\left(\frac{2(1 + \Omega)(1 - (N_D - 1)\Omega)}{E} \right) \tau_{ik} n_k = \Omega \frac{\partial u_k}{\partial x_k} n_i + (1 - (N_D - 1)\Omega) \left(\frac{\partial u_i}{\partial x_k} + \frac{\partial u_k}{\partial x_i} \right) n_k. \quad (4.55)$$

4.2 Scheme for simulating fluid flow through an elastic vessel in a general geometry

In this section, I describe a scheme for the two-dimensional simulation of the wall of an elastic fluid-filled vessel and the fluid inside that vessel. The vessel may have any geometry and the wall has a finite thickness. This scheme is used throughout this chapter and the next. It applies the theory of linear elasticity, which is valid where the strains are small. It also uses the following approximations, discussed in section 4.1.2, that are valid in the same

regime: the density remains equal to that of the undeformed body; the spatial derivatives of the stress tensor are approximately equal to those with respect to the coordinates of the body before deformation.

4.2.1 Simulation setup

The simulation requires the initial shape of the inside surface of the vessel, and, if it is initially strained, its shape in the unstrained state. We first label each lattice site in our system as fluid if it is inside the vessel and solid if it is outside. Lattice sites that are adjacent to the wall will have one or more neighbouring solid sites and they are labelled as edge sites. We place a pair of points on the wall for each lattice site that is adjacent to it: one on the inner surface of the wall and one on the outer surface. The positions of these points are chosen such that the point on the inner surface is the closest point to the lattice site, except for the simulations described in section 5.4 and thereafter, and the vector joining the two points is normal to the surface. The configuration of points in the wall is shown in figure 4.2. For each point on the wall, we choose which of its nearest neighbouring points we will use to calculate the force per unit area at each point, and hence find its acceleration. The selection of neighbouring points is discussed in section 4.3.

4.2.2 Procedure at each time step

First, we carry out a lattice-Boltzmann timestep to find the distribution functions, f_i at each lattice site at time $t + \Delta t$ from those at time t . From these, we can calculate the pressure, velocity and stress flow fields at time $t + \Delta t$. The motion of the wall influences the fluid through a no-slip condition. This is applied via a lattice-Boltzmann boundary condition based on that proposed by Zhao-Li et al. [10], which was described in section 2.9.5. We consider the lattice vector from an edge site f to a neighbouring solid site w . This vector intersects the wall at point b , as shown in figure 4.2. We require the velocity of the wall at point b , \mathbf{v}_b to calculate the distribution functions at the edge site $f_i(\mathbf{x}_f, t + \Delta t)$. For simulations of fluid flow through elastic vessels of a general geometry, we make the approximation that $\mathbf{v}_b = \mathbf{v}_n$, where \mathbf{v}_n is the velocity of the point on the inside surface

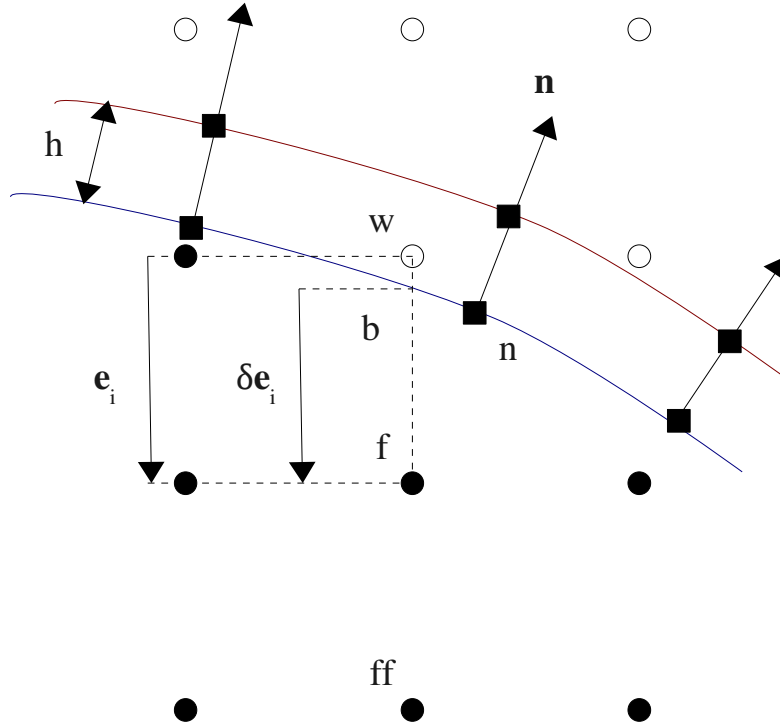


FIGURE 4.2: Configuration of points on the wall and nearby lattice sites. The filled circles are the fluid sites and the open circles are the solid sites. The link between an edge site, f , and one of its neighbouring solid sites, w intersects the wall at point b . Site ff is the fluid site opposite site w . There is a pair of points (shown by filled squares) for each edge site: one on the inside surface of the wall (the blue line) and one on the outside surface of the wall (the red line). The separation between these two points is $\mathbf{n}h$, where \mathbf{n} is the outward normal and h is the thickness of the wall. The point on the inner surface is chosen to be the closest point to the edge site.

that belongs to the lattice site f . The error from this approximation error is first order in the spacing between the points on the inside surface of the wall.

Second, we integrate the equation of motion (equation (4.53)) numerically at each point on the wall using a Runge-Kutta method adapted for solving second-order differential equations, which is the same method as the one used for simulations in an axisymmetric vessel, which is explained in section 3.5.3. The spatial derivatives of displacement in this equation are estimated from the displacement at the point in question and its neighbours and the boundary condition on the stress tensor (equation (4.55)), as explained in the next subsection. For a point on the inner surface of the wall, the external stress is equal to the stress in the fluid at that point and may therefore vary with time. Therefore,

the acceleration at our point depends explicitly on time, its displacement and that of its neighbours, i.e. we have:

$$\frac{d^2\mathbf{u}}{dt^2} = f(t, \mathbf{u}, \mathbf{u}'). \quad (4.56)$$

Such a second-order equation can be expressed as two first-order equations with two dependent variables, i.e.

$$\frac{d\mathbf{u}}{dt} = \mathbf{u}', \quad (4.57)$$

$$\frac{d\mathbf{u}'}{dt} = f(t, \mathbf{u}, \mathbf{u}'), \quad (4.58)$$

where t is the independent variable and \mathbf{u} and $\mathbf{u}' = d\mathbf{u}/dt$ are the dependent variables. The following iteration scheme for equations (4.57) and (4.58) guarantees second-order accuracy in the step size, Δt :

$$\mathbf{u}_{t+\Delta t} = \mathbf{u}_t + 0.5(a_1 + a_2), \quad (4.59)$$

$$\mathbf{u}'_{t+\Delta t} = \mathbf{u}'_t + 0.5(a'_1 + a'_2), \quad (4.60)$$

with

$$a_1 = \Delta t \mathbf{u}'_t,$$

$$a'_1 = \Delta t f(t, \mathbf{u}_t, \mathbf{u}'_t),$$

$$a_2 = \Delta t (\mathbf{u}'_t + a'_1),$$

$$a'_2 = \Delta t f(t + h, \mathbf{u}_t + a_1, \mathbf{u}'_t + a'_1).$$

If we know the displacement and velocity of the wall at time t , we can calculate the displacement at time $t + \Delta t$, but the velocity at time $t + \Delta t$ depends on the displacements of the neighbouring points at time $t + \Delta t$. Therefore, $\mathbf{u}_{t+\Delta t}$ must be calculated for every point before we can calculate $\mathbf{u}'_{t+\Delta t}$ anywhere.

4.2.3 Finding the Derivatives of Displacement

In this section, I describe the scheme for calculating the derivatives of the displacement, which are required for the equation of motion and its boundary conditions.

For each component of the displacement field, u_i , there are N unknown first- and second-order spatial derivatives of displacement, where

$$N = 2N_D + \frac{N_D(N_D - 1)}{2}, \quad (4.61)$$

where N_D is the number of dimensions. Therefore, we have NN_D unknown derivatives in total. Since $N_D = 2$ for all simulations in this chapter, $N = 5$, i.e. there are 5 derivatives for each component of \mathbf{u} : $\frac{\partial}{\partial x}$, $\frac{\partial}{\partial y}$, $\frac{\partial^2}{\partial x^2}$, $\frac{\partial^2}{\partial y^2}$ and $\frac{\partial^2}{\partial x \partial y}$. We therefore have $NN_D = 10$ unknown derivatives in total. The boundary condition on the stress tensor (equation (4.55)) gives us N_D constraints on them. Taylor expanding the displacement about a point \mathbf{r}_0 up to second order to give the displacement at a neighbouring point \mathbf{r} also produces N_D constraints for these derivatives:

$$u_i(\mathbf{r}) - u_i(\mathbf{r}_0) = \frac{\partial u_i}{\partial x_j} \Delta x_j + \frac{1}{2} \frac{\partial^2 u_i}{\partial x_j \partial x_k} \Delta x_j \Delta x_k, \quad (4.62)$$

where $\Delta x_i = x_i - x_{0,i}$. Therefore, we combine the N_D constraints from the boundary condition with the Taylor expansions of $(N-1)$ neighbouring points, which give $(N-1)N_D$ constraints, to give us a system of NN_D equations for NN_D constraints. Since $N_D = 2$ and $N = 5$, we require four neighbouring points. The selection of neighbouring points is discussed in section 4.3. Our closed system of equations can be written as

$$\mathbf{U} = \mathbf{M}\mathbf{D}, \quad (4.63)$$

where \mathbf{U} and \mathbf{D} are vectors with NN_D elements and M is an $NN_D \times NN_D$ matrix, as follows:

$$\mathbf{D} = \begin{pmatrix} \frac{\partial u_i}{\partial x_j} \text{ for } j = 1, 2, \dots, N_D \\ \vdots \\ \frac{\partial u_i}{\partial x_j \partial x_k} \text{ for } k = j = 1, 2, \dots, N_D \\ \vdots \\ \frac{\partial u_i}{\partial x_j \partial x_k} \text{ for } k > j, j = 1, 2, \dots, N_D \\ \text{for } i = 1, 2, \dots, N_D \end{pmatrix}, \quad (4.64)$$

$$\mathbf{U} = \begin{pmatrix} u_{1,i} - u_{0,i} \\ u_{2,i} - u_{0,i} \\ \vdots \\ u_{N-1,i} - u_{0,i} \\ \text{for } i = 1, 2, \dots, N_D \\ \vdots \\ \frac{2(1+\Omega)(1-(N_D-1)\Omega)}{E} \tau_{ij} n_j \\ \text{for } i = 1, 2, \dots, N_D \end{pmatrix}, \quad (4.65)$$

$$\mathbf{M} = \begin{pmatrix} \mathbf{M}_D & \mathbf{0} & \cdots & \mathbf{0} \\ \mathbf{0} & \mathbf{M}_D & \cdots & \mathbf{0} \\ \mathbf{0} & \mathbf{0} & \ddots & \mathbf{0} \\ \mathbf{0} & \mathbf{0} & \mathbf{0} & \mathbf{M}_D \\ & & & \mathbf{M}_S \end{pmatrix}, \quad (4.66)$$

where \mathbf{M}_D and \mathbf{M}_S are sub-matrices with dimensions $(N - 1) \times N$ and $N_D \times (NN_D)$ respectively and $\mathbf{0}$ is a sub-matrix whose elements are 0. They contain the coefficients of the derivatives in vector \mathbf{D} in the Taylor expansions of \mathbf{u} about position \mathbf{r}_0 and in the boundary condition given by equation (4.55) respectively. Column j of matrix \mathbf{M} is a coefficient of D_j .

In order to solve equation (4.63) we need to invert the matrix \mathbf{M} and multiply it by the vector \mathbf{U} . It would be very computationally expensive to invert the entire matrix at every timestep for every point on the wall. Fortunately, the matrix \mathbf{M}_D is constant throughout the simulation because it consists entirely of combinations of the separations between the point we are looking at and its neighbours when the wall is not strained. Therefore, we can rearrange matrix \mathbf{M} such that it is only necessary to invert a $N_D \times N_D$ matrix at each timestep as follows. Columns $l, l + N, \dots, l + (N_D - 1)N$ are removed from matrix \mathbf{M} ; the remaining columns are shifted in order to fill the gaps; then the empty columns $(N - 1)N_D, (N - 1)N_D + 1, \dots, NN_D$ are replaced by the columns whose indices were $l, l + N, \dots, l + (N_D - 1)N$ respectively before they were removed. The same operation must be performed on the rows of \mathbf{D} . Matrix \mathbf{M}_D is now split into matrix \mathbf{L} and vector \mathbf{q} with dimensions $(N - 1) \times (N - 1)$ and $(N - 1) \times 1$ respectively, while matrix \mathbf{M}_S is split into matrices \mathbf{R} and \mathbf{S} with dimensions $N_D \times (N - 1)$ and a $N_D \times N_D$ respectively.

We now have:

$$\mathbf{M} = \begin{pmatrix} \mathbf{P} & \mathbf{Q} \\ \mathbf{R} & \mathbf{S} \end{pmatrix}, \quad (4.67)$$

where \mathbf{P} , \mathbf{Q} , \mathbf{R} and \mathbf{S} are sub-matrices and

$$\mathbf{P} = \begin{pmatrix} \mathbf{L} & \mathbf{0} & \cdots & \mathbf{0} \\ \mathbf{0} & \mathbf{L} & \cdots & \mathbf{0} \\ \mathbf{0} & \mathbf{0} & \ddots & \mathbf{0} \\ \mathbf{0} & \mathbf{0} & \mathbf{0} & \mathbf{L} \end{pmatrix}, \quad (4.68)$$

$$\mathbf{Q} = \begin{pmatrix} \mathbf{q} & \mathbf{0} & \cdots & \mathbf{0} \\ \mathbf{0} & \mathbf{q} & \cdots & \mathbf{0} \\ \mathbf{0} & \mathbf{0} & \ddots & \mathbf{0} \\ \mathbf{0} & \mathbf{0} & \mathbf{0} & \mathbf{q} \end{pmatrix}. \quad (4.69)$$

It can be readily checked that the inverse of matrix \mathbf{M} is given by Bernstein [124, p. 44]:

$$\mathbf{M}^{-1} = \begin{pmatrix} \mathbf{P}^{-1} + \mathbf{P}^{-1}\mathbf{Q}(\mathbf{S} - \mathbf{R}\mathbf{P}^{-1}\mathbf{Q})^{-1}\mathbf{R}\mathbf{P}^{-1} & -\mathbf{P}^{-1}\mathbf{Q}(\mathbf{S} - \mathbf{R}\mathbf{P}^{-1}\mathbf{Q})^{-1} \\ -(\mathbf{S} - \mathbf{R}\mathbf{P}^{-1}\mathbf{Q})^{-1}\mathbf{R}\mathbf{P}^{-1} & (\mathbf{S} - \mathbf{R}\mathbf{P}^{-1}\mathbf{Q})^{-1} \end{pmatrix}. \quad (4.70)$$

The matrices \mathbf{P} and \mathbf{Q} are constant throughout the simulation, so its inverse and the matrix $\mathbf{P}^{-1}\mathbf{Q}$ only need to be calculated once at the beginning of the simulation. It is only necessary to invert the matrix $\mathbf{S} - \mathbf{R}\mathbf{P}^{-1}\mathbf{Q}$, which is a $N_D \times N_D$ matrix. From equation (4.68), it can be shown that the inverse of matrix \mathbf{P} is

$$\mathbf{P}^{-1} = \begin{pmatrix} \mathbf{L}^{-1} & \mathbf{0} & \cdots & \mathbf{0} \\ \mathbf{0} & \mathbf{L}^{-1} & \cdots & \mathbf{0} \\ \mathbf{0} & \mathbf{0} & \ddots & \mathbf{0} \\ \mathbf{0} & \mathbf{0} & \mathbf{0} & \mathbf{L}^{-1} \end{pmatrix}. \quad (4.71)$$

Using equation (4.69), we have:

$$\mathbf{P}^{-1}\mathbf{Q} = \begin{pmatrix} \mathbf{L}^{-1}\mathbf{q} & \mathbf{0} & \cdots & \mathbf{0} \\ \mathbf{0} & \mathbf{L}^{-1}\mathbf{q} & \cdots & \mathbf{0} \\ \mathbf{0} & \mathbf{0} & \ddots & \mathbf{0} \\ \mathbf{0} & \mathbf{0} & \mathbf{0} & \mathbf{L}^{-1}\mathbf{q} \end{pmatrix}. \quad (4.72)$$

We choose the value of l that maximises the condition number of matrix \mathbf{L} , in order to minimise the error in \mathbf{L}^{-1} .

4.3 The choice of neighbouring points

We find the derivatives of displacement at a point on the wall using its displacement and that of some of its neighbouring points. Four neighbours are required for a 2D simulation, but there are five possible neighbouring points to choose from, as shown in figure 4.3. The validity of the calculation of the derivatives depends strongly on our choice of neighbouring points. This section describes and explains which neighbouring points were chosen for simulations of fluid flow through elastic systems.

I initially chose to use neighbours 1, 2, 3 and 4 since they are placed symmetrically about the normal to the wall (figure 4.3). However, this choice causes instability, as illustrated by the following situation. We have a rectangular piece of elastic material that we stretch in the x -direction such that $\epsilon_{xx} = 0.01$. It contracts in the y -direction due to the Poisson effect. We choose $\Omega = 0.5$, therefore $\epsilon_{yy} = -0.005$. We then fix its corners. We place eight points on this rectangle, which is shown by the dotted line in figure 4.4. Points C, D, E and F should not move. However, in simulations of this situation, the points reached a configuration similar to that shown by the solid line in figure 4.4 due to the limits of numerical precision (the movements of points C, D, E, and F have been vastly exaggerated). However, instead of returning to equilibrium, the left hand side of the material continues to contract and the right hand side continues to expand, so the simulation is unstable with respect to this configuration.

A test of the calculation of derivatives at point C was performed on this configuration. Since $\mathbf{r} = (x, y)$ represents the position of a point in an elastic material before deformation

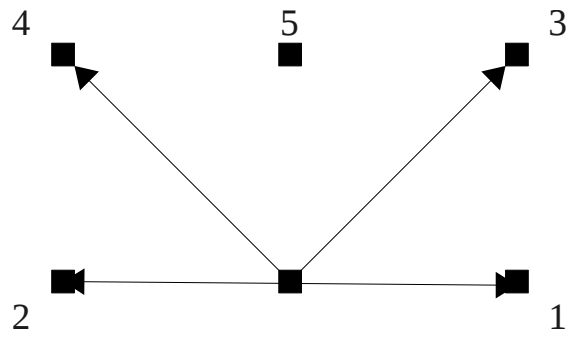


FIGURE 4.3: A possible selection of the four neighbours that are used to calculate the spatial derivatives of displacement at a point on the wall. This selection gives rise to instability.

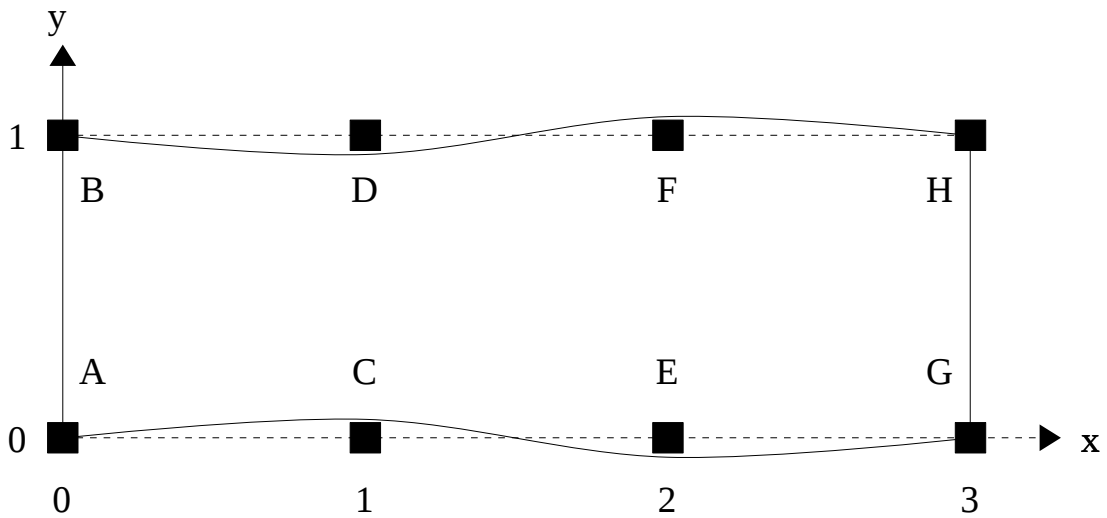


FIGURE 4.4: This elastic rectangle (the dotted line) is unstable with respect to the shape defined by the continuous lines if, for each point represented by a square, an unsuitable combination of neighbouring points is used to calculate the spatial derivatives of displacement there.

and \mathbf{u} represents the displacement after deformation, the coordinates marked in figure 4.4 are the values of $\mathbf{r} + \mathbf{u}$ on our elastic rectangle, nondimensionalised with respect to the spacing between the points. From the definition of strain and taking point 0 to be at the origin before stretching, we have $x = \frac{x+u_x}{\epsilon_{xx}}$, and $y = \frac{y+u_y}{\epsilon_{yy}}$. To reach the configuration shown by the solid line, we then add displacements $(0, 7 \times 10^{-10})$, $(0, -7 \times 10^{-10})$, $(0, 7 \times 10^{-10})$ and $(0, -7 \times 10^{-10})$ to points C, D, E and F respectively. The values of \mathbf{r} and \mathbf{u} for all eight points are shown in table 4.1. Setting the stress at the walls to zero and applying the algorithm explained in section 4.2.3 gives the derivatives shown in table 4.2. If we substitute these derivatives into the Taylor expansion of displacement about point C (equation (4.62)), we find that the resulting values of $\mathbf{r} + \mathbf{u}$ correspond exactly to those in table 4.1, but we obtain $(1, 1 + 7 \times 10^{-10})$ instead of $(1, 1 - 7 \times 10^{-10})$ for point D due to the positive value of $\frac{\partial^2 u_y}{\partial y^2}$. This is because we used points A, B, E and F in the calculation but ignored point C and therefore biased the derivatives. Point C “thinks” that the material has been stretched in the y -direction. Applying equation (4.53) gives an acceleration of $\frac{E}{2\rho(1+\Omega)(1-\Omega)}(-3.517325 \times 10^{-10}, 1.70 \times 10^{-9})$. We would expect the acceleration in the y -direction to be negative by inspection of figure 4.4. Therefore, the simulation is unstable.

Point	x	y	u_x	u_y
A	0	0	0	0
B	0	$\frac{1}{0.995}$	0	$\frac{-0.005}{0.995}$
C	$\frac{1}{1.01}$	0	$\frac{0.01}{1.01}$	7.0×10^{-10}
D	$\frac{1}{1.01}$	$\frac{1}{0.995}$	$\frac{0.01}{1.01}$	$\frac{-0.005}{0.995} - 7.0 \times 10^{-10}$
E	$\frac{1}{2}$	0	$\frac{0.02}{1.01}$	7.0×10^{-10}
F	$\frac{1}{2}$	$\frac{1}{0.995}$	$\frac{0.02}{1.01}$	$\frac{-0.005}{0.995} - 7.0 \times 10^{-10}$
G	$\frac{1}{3}$	0	$\frac{0.03}{1.01}$	0
H	$\frac{1}{3}$	$\frac{1}{0.995}$	$\frac{0.03}{1.01}$	$\frac{-0.005}{0.995}$

TABLE 4.1: Unstrained positions of points, (x, y) , and their displacements, \mathbf{u} , from these positions for the piece of elastic material shown in figure 4.4.

I conclude that when calculating the derivatives at a point, it is important to use the displacement of the corresponding point on the opposite wall. One could choose the neighbours in one of the two ways shown in figure 4.5, but there is still a risk of biasing the derivatives by not including one of the neighbours. Therefore, I decided to calculate the derivatives of displacement using both sets of neighbours and averaging them. Repeating the test on point C in the last paragraph, we obtain an acceleration of $\frac{E}{2\rho(1+\Omega)(1-\Omega)}(-3.517325 \times 10^{-10}, -6.62 \times 10^{-9})$. The acceleration in the y -direction is negative, i.e. towards the equilibrium position, which indicates that the simulation is stable

Derivative	Neighbour choice shown in:			
	Figure 4.3		Figure 4.5	
	u_x	u_y	u_x	u_y
$\frac{\partial}{\partial x}$	1.00000×10^{-2}	-3.53500×10^{-10}	1.00000×10^{-02}	$-3.535000 \times 10^{-10}$
$\frac{\partial}{\partial y}$	3.53500×10^{-10}	-5.00000×10^{-3}	3.535000×10^{-10}	$-5.000000 \times 10^{-03}$
$\frac{\partial^2}{\partial x^2}$	0.00000	-2.14221×10^{-9}	$0.000000 \times 10^{+00}$	$-2.142210 \times 10^{-09}$
$\frac{\partial^2}{\partial y^2}$	-7.03465×10^{-10}	1.38604×10^{-9}	$-7.034650 \times 10^{-10}$	$-2.772070 \times 10^{-09}$
$\frac{\partial^2}{\partial x \partial y}$	1.43138×10^{-26}	7.03465×10^{-10}	$0.000000 \times 10^{+00}$	7.034650×10^{-10}

TABLE 4.2: Spatial derivatives of displacement at point C in figure 4.4 for both choices of neighbouring points.

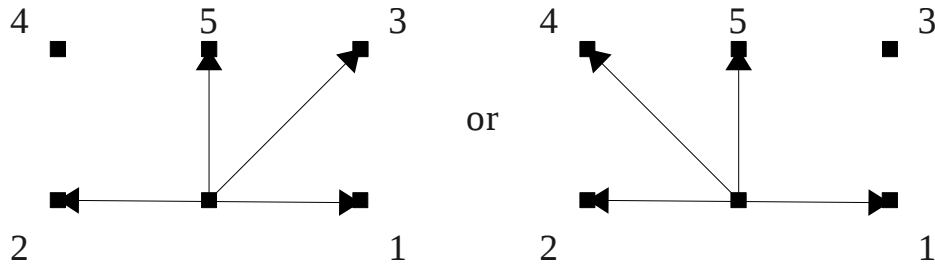


FIGURE 4.5: The final selections of the four neighbours that are used to calculate the spatial derivatives of displacement at a point on the wall. This is stable with respect to the situation in figure 4.4.

with respect to the configuration shown in figure 4.4.

4.4 Calculation of the surface normals, normalised cut distances and stress tensor

The methods used for the simulations reported in this chapter to calculate the normal to each point on the elastic wall, the stress tensor at the inner surface and the normalised cut distances at each lattice site adjacent to the wall are described in this section. The nomenclature of the relevant lattice sites and points is given in figure 4.2.

The normalised cut distance, δ , is the distance from site f to point b expressed as a fraction of the length of the lattice vector $\mathbf{x}_w - \mathbf{x}_f$, and it could be estimated as the distance along the lattice vector to its point of intersection with one of the two lines passing through point n and its neighbours on the inner surface of the wall. The relative error of this estimate

is first-order in space, for the following reason. If the lattice site is at the origin and the point of intersection is (x, y) , then Taylor expanding y about point n gives

$$y = y_n + (x_b - x_n) \left(\frac{dy}{dx} \right)_n + \frac{(x_b - x_n)^2}{2} \left(\frac{d^2y}{dx^2} \right)_n + \dots \quad (4.73)$$

We are ignoring the 3rd term in the Taylor expansion, giving us an absolute error of order $(\Delta x)^2$, where Δx is the spacing between adjacent lattice points, which is approximately equal to the spacing between adjacent wall points. The magnitude of the cut distance is of order Δx , therefore the relative error is of order Δx .

If we approximate the inner surface of the wall between the points as a circle passing through point n and its two neighbours and choose our axes such that the x-axis is the tangent to this circle for the purposes of this discussion, we have $\frac{d^2y}{dx^2} = \frac{1}{r}$, where r is the radius of the circle. Therefore, the error in y is third-order in space, so the relative error in the normalised cut distance is second-order in space, which matches the accuracy of the LBM (see chapter 3.2.2). When the point and its neighbours are collinear, we simply find the point of intersection between the straight line on which they lie and the lattice vector.

A line that passes through a circle will intersect that circle in two places. The normalised cut distance was chosen to be the distance from the lattice site to the nearest point of intersection. The normal to the point on the wall that points away from the fluid was approximated by the normal to the circle described above. This normal may point towards or away from the centre of the circle, depending on the curvature of the wall. We choose the normal that is closer to that at the previous timestep. At the beginning of the simulation, we set the normal to point away from the fluid domain. Therefore, our normal will always point away from the fluid domain except in the extreme case where the orientation of the wall changes by approximately π radians in one time step.

The stress at point n on the inner surface of the wall is approximated to be equal to the stress at point b , which is calculated by linear extrapolation from the lattice sites f and ff , i.e. $(\tau_{ij})_b = (1 + \delta)(\tau_{ij})_f - \delta(\tau_{ij})_{ff}$. The site f may be have several fluid neighbours, so there are several possible positions of intersection b , each with a different value of δ . We want to use one close to point n . Therefore, for each neighbour, $fneigh$, of site f , the scalar product between the lattice vector $\mathbf{x}_f - \mathbf{x}_{fneigh}$ and the separation between site f and its point on the wall, $\mathbf{x}_n - \mathbf{x}_f$, was evaluated and site ff was chosen to be the site

$fneigh$ for which this scalar product is a maximum, provided that $fneigh$ is a fluid site. If the wall moves inwards past site f , the site $fneigh$ for which the scalar product is a maximum may be solid, in which case site ff was chosen to be the lattice site opposite site $fneigh$, i.e. $\mathbf{x}_{ff} = \mathbf{x}_f + (\mathbf{x}_f - \mathbf{x}_{fneigh})$.

The acceleration of a point on the wall depends on the derivatives of displacement (equation (4.53)) and these in turn depend on the stress tensor, τ_{ij} , and outward normal there (equations (4.63) to (4.65)). Clearly, the normal at a point depends on its displacement and that of its neighbours, but the extrapolation of the stress tensor also depends on these displacements because it depends on the value of δ . Since we must calculate the acceleration as a function of the displacements of a point and its neighbours and as a function of these displacements plus the a_1 Runge-Kutta coefficient (see equation (4.59) (4.60)), it follows that the normal, the values of δ and the stress at the inner surface of the wall must be calculated as functions of these two sets of displacements during each time step. The stress at the outer surface is a parameter of the simulation.

4.5 Work required to extend the simulation method to three dimensions

In this section, I discuss how the simulation method could be extended to three dimensions.

The general scheme described in section 4.2 can be readily extended to 3D by using $N_D = 3$ for all equations in that section. For each point on the wall there are $N = 9$ unknown spatial derivatives of the displacement field at each point on the elastic wall, from equation (4.61). Each point on the wall therefore requires eight neighbouring points. If a pair of points is placed on the wall for each lattice site that is adjacent to the wall, there are many different ways of choosing the neighbours to each point. For each point, the neighbours could be chosen from all points on the wall or points belong to lattice sites adjacent to the one that the current point belongs to. The calculation of the derivatives of the displacement field at a point would need to be tested for different choices of neighbouring points. In particular, it could be important to always include the corresponding point on the opposite surface of the elastic wall (inner or outer) in the set of neighbours to ensure the simulation remains stable.

The circle passing through a point and two of its neighbours on the same surface could be assumed to lie approximately on the surface around that point, as described in section 4.4. The tangent to the circle will then be a good approximation to a tangent of the actual surface. Another tangent can be found by drawing a circle through the point and its other two neighbours on the same surface. The normal is then the vector product of the tangents. The normalised cut distances could be calculated by finding a curved surface that contains these two circles, but this is not straightforward.

4.6 Review of studies of a Starling resistor

The collapse of compressed tubes occurs naturally in several physiological applications. Experiments have shown that the system is a non-linear dynamical system of great complexity, in which self-excited oscillations arise in particular regions of parameter space and that some combinations of parameters are unattainable.

Bertram et al. [125] carried out a systematic mapping of the types of instability occur in different regions of parameter space. They studied elastic tubes of four different lengths with three values of the resistance of the downstream rigid tube and plotted the flow rate against the pressure drop between the upstream and downstream ends of the elastic tube ($p'_u - p'_d$ in figure 4.6) for several positive values of the difference between the external pressure and that at the downstream end of the elastic tube, $p_e - p'_d$. The behaviour of the Starling resistor at each value of the pressure drop and flow rate, which was called an operating point, was classified as steady flow, regular or irregular self-excited oscillations or small-amplitude, broadband noise-like fluctuations. They noted that at the lowest downstream resistance, repetitive oscillations were most prevalent, many operating points were unattainable at the intermediate resistance and many points were stable at the highest resistance. There were distinct bands of low, intermediate and high frequency oscillations in the parameter space studied, corresponding to different modes of oscillation. Within each band, the frequency increased smoothly with the flow rate and pressure drop and did not depend strongly on the tube length. However, the length of the elastic tube affected the mode of oscillation that occurred. There were also some regions of hysteresis, where the behaviour depended on the direction of approach.

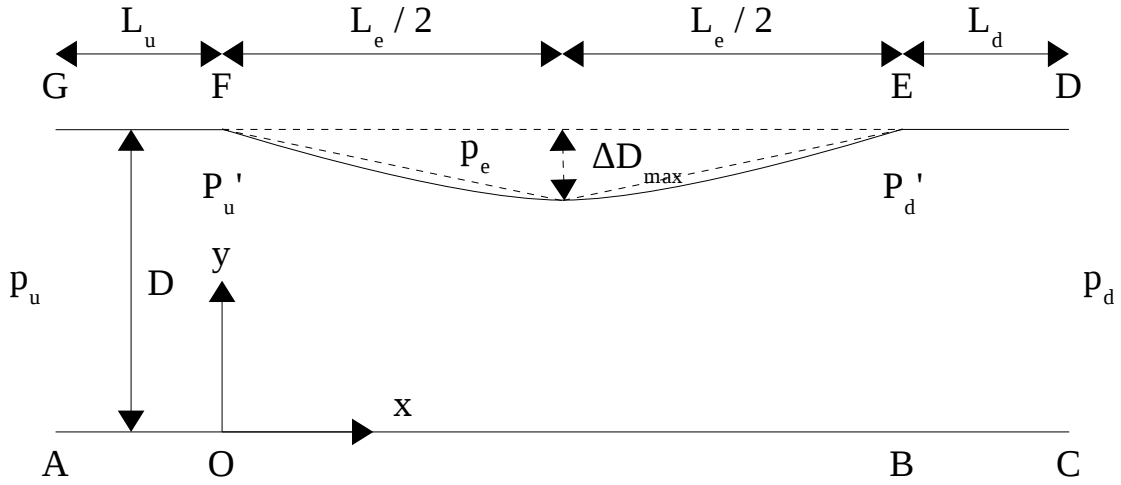


FIGURE 4.6: Diagram of a 2D Starling resistor, which is a channel with a collapsible segment through which fluid flows. The dimensions are marked as well as the pressure at the inlet and outlet and the pressure applied to the outside of the wall. The maximum deformation is ΔD_{max} . The length of the elastic segment after deformation can be estimated by applying Pythagoras' theorem to the dotted triangles.

In order to understand the behaviour of the system, Lowe, Luo and Pedley [11, 13, 15, 19] have carried out a series of computational studies of flow through a two-dimensional Starling resistor, which is a channel in which part of one wall is replaced with an elastic segment under tension and to which a uniform external pressure may be applied, as shown in figure 4.6. A Poiseuille flow may be imposed upstream. Let D be the width before deformation and L_u , L_e and L_d be the lengths of the upstream, elastic and downstream sections of the wall respectively. The pressure at the outlet is p_d while that applied externally is p_e . In their studies, the channel was oriented in the x -direction. The Reynolds number was calculated from the average velocity of flow at the inlet for all studies discussed in this section.

Lowe and Pedley [11] considered Stokes flow, which is the flow in the limit as $Re \rightarrow 0$. The membrane was assumed to be thin and massless. They simulated the system with an iterative method, in which the flow fields were calculated for a given wall shape using a finite-element method, which is itself iterative, then the wall shape was calculated from the pressure along the wall as follows. The membrane equation, $p_e - p = T/R$, was rearranged to find the radius of curvature, R , at each point on the wall in terms of the tension. The curvature at each point was expressed in terms of the position of the point and its nearest neighbours. This system of equations was then solved using the Newton-Raphson method.

The tension at each point was calculated by integrating the stress on the wall from the fluid. In this study, the lengths of the wall segments were $L_u = L_d = 2D$ and $L_e = 10D$.

Simulations were carried out at various values of the tension and $p_e - p_d$. For each value of the tension, the wall was distended everywhere at low external pressures, distended upstream and collapsed downstream at intermediate external pressures and completely collapsed at high external pressures. The pressure at which the two transitions should occur was predicted analytically in the limit of high tension and the computations for different pressures at the highest value of tension showed that the transitions occurred close to the analytical predictions.

As the tension was lowered, the variation in channel width along the channel increased, as one would expect. The shape of the wall also became more asymmetric. For intermediate external pressures, the point at which the wall changes from being distended to collapsed moved downstream as the tension was reduced. The pressure gradient increased significantly due to the narrowing of the channel. This caused the wall to bulge at the upstream end for external pressures at which it would have been collapsed at lower tensions. Therefore, the differences between the external pressures at which the transitions occurred became wider. At the highest tension, the variation in tension along the membrane was $6 \times 10^{-4}T$ for all pressures tested, but this variation became more significant as the tension was reduced. There was a limiting tension, below which no converged solution could be found.

In the studies by Luo and Pedley [13, 15, 19], the following physical parameters were used: $\eta = 10^{-3}\text{Nm}^{-1}\text{s}$, $\rho_f = 10^3\text{kgm}^{-2}$, $D = 10^{-2}\text{m}$, $L_e = 5 \times 10^{-2}\text{m}$, $p_e - p_d = 0.93\text{Nm}^{-1}$, $T = T_0/\beta$, where $T_0 = 1.610245\text{N}$ and β is a dimensionless parameter.

Luo and Pedley [13] considered steady flow at a non-zero Reynolds number under the same assumptions as [11], except that the tension in the membrane was assumed to be uniform, i.e. the shear stress was not included in the fluid-membrane interaction. The simulation method was very similar to that in [11]. The length of the upstream and downstream segments were $L_u = 0.02\text{m}$ and $L_d = 0.07\text{m}$ respectively. L_d was chosen to be long enough for the flow pattern to recover from the constriction so that constant pressure condition is applicable at the outlet.

They found that at $Re = 1$, the wall deflection increases as β increases, i.e. the tension decreases. This continued until $\beta = \beta_c = 65$, beyond which no converged solution was found. At $Re = 100$ and $Re = 500$, the maximum deflection only increased up to a point. The point of maximum deflection moved downstream significantly as β increased and continued to do so after the deflection reached its maximum. The upstream end of the membrane bulged out when β was increased to β_b and the authors were unable to find a converged solution beyond $\beta = \beta_c$. They obtained $\beta_b = 129, \beta_c = 130$ and $\beta_b = 30, \beta_c = 31$ for $Re = 100$ and 500 respectively. For $Re = 100$ and $Re = 500$, flow separation occurred at the downstream end of the membrane before the deflection reached its maximum, which was shown by the negative vorticity there. A singularity in the vorticity was expected at the upstream end of the segment at $\beta = \beta_b$, but it occurred later due to the finite resolution, being approached rapidly as β was increased to β_c .

Luo and Pedley [13] suggest that the breakdown in their model may be due to the bulging of the membrane at the upstream end and the singularities that develop there rather than a purely numerical problem. A one-dimensional analysis was then performed to investigate this. They used a constant flow rate, neglected viscosity, and assumed that the flow separation begins at the point of maximum deflection and a steady solution existed for all values of the tension. The tension reductions required for the membrane to bulge outwards agreed well with those from the 2D simulations. At this point, the pressure drop no longer increased with flow rate, which corresponded to the onset of self-excited oscillations that had been observed in experiments in a different region of parameter space [125]. This suggested that the origin of the breakdown was physical, but this was still uncertain.

Rast [126] also carried out steady state simulations, but the critical values for tension differed significantly, which showed that there is a numerical breakdown in the methods for finding steady solutions. For example, at $Re = 300$, the value of $\frac{TD}{\rho_f Q^2}$, where Q is the flow rate, is reduced to 0.15, whereas in Luo and Pedley [19], we have $\beta_c = 190$, so $\frac{TD}{\rho_f Q^2} = 0.94$ at the critical tension. Furthermore, Luo and Pedley [19] state that $\beta_b = 40$ at $Re = 300$. The fact that this is significantly less than β_c shows that the membrane bulging alone does not cause a breakdown in the simulation. While Rast [126] can achieve a lower tension than [13], his numerical method reaches a limit when the wall at the downstream end of the membrane becomes almost vertical, which occurs when the tension is very low.

Rast [126] found that the wall exhibited similar behaviour to that described in [11] as the tension was lowered. The spatial variation in the tension in the membrane was taken into account as in [11] and the other assumptions about it were the same. Flow separation was observed at $Re = 100$ and $Re = 300$ and the eddies were observed to increase in length with Re , but the length remained of $O(D)$, not $O(Re)$. The complexity of the flow increases as the channel becomes narrower. At $Re = 300$, the wall was found to be collapsed everywhere until the tension was lowered below a certain value, when it became distended upstream. The point at which the channel became collapsed moved downstream as the tension was reduced. The same behaviour was observed by Luo and Pedley [19]. However, since Rast [126] was able to lower the tension further, he found that the curvature of the wall changed sign twice at $\frac{TD}{\rho_f Q^2} = 0.15$, i.e. $\beta = 1193$. The spatial variation in tension was $0.5T$ at the lowest tension, which is much larger than that reported in any simulations in [11], so it is expected that using a uniform tension would change the results significantly. This might explain why the channel width never fell below $0.6D$ in [126], whereas it reached $0.5D$ in [19] under the assumption of constant tension in the membrane.

While Luo and Pedley [19, 1996] presented results for steady flow simulations, the main focus was on unsteady flow. They used $L_u = 5 \times 10^{-2}\text{m}$, $L_d = 0.3\text{m}$. The elastic wall was modelled under the same assumptions as in their previous study Luo and Pedley [13, 1995], and its tension was assumed to remain constant with time. In contrast to their previous study, the iteration scheme was solved for the fluid and the wall simultaneously as follows. The equations for the unknown flow fields in space were discretized and combined. The resulting equation was then integrated with respect to time with an implicit finite difference scheme: an equation involving the unknowns in two subsequent timesteps was obtained, then solved using the Newton-Raphson method. This method is an extension of that developed in [126] for simulating steady flow.

Each simulation was initialised to its steady solution for the desired Reynolds number, but a slightly different tension from that desired in order to impose a small disturbance on the actual steady solution. The points on the wall were assumed to move only in the direction normal to the wall's initial shape. The simulations approached the steady state solution for values of $\beta < \beta_u$, but were unstable and underwent self-excited oscillations for $\beta \geq \beta_u$ for Reynolds numbers between 100 and 500, but were stable for all β at $Re = 1$. The value of β_u decreased as Re increased.

The behaviour of the system was studied in detail for three different values of β at $Re = 300$, where $\beta_u = 27.5$. Self-excited oscillations were observed. The motion of one point on the wall was tracked over time and instantaneous streamlines were recorded at different times throughout one period of oscillation of the wall. When $\beta = 30$, the oscillations had a period of $\frac{12.71Q}{D^2}$ and an amplitude of $0.2D$. When β was increased to 32.5, the wall oscillation was composed of one slow oscillation with a period of $\frac{20.75D^2}{Q}$ and one oscillation at twice the frequency, i.e. a period doubling bifurcation occurred. At $\beta = 35$, there was a triple peak in the position of the point on the wall. These double peak and triple peak phases were observed in measurements of the pressure and cross-sectional area of a tube by Bertram et al. [125] and are shown in figures 9a and 9c of that study. When β was increased further still, the wall was sucked under the rigid wall on the right [19], in agreement with experimental observations in another study. The qualitative agreements with experimental observations provide evidence that their simple model is sufficient to explain the observed phenomena.

Luo and Pedley [13, 1995] also found that for a constant value of β , the pressure difference between the inlet and outlet of the channel only increases with Re up to the point where the membrane bulges out, then it remains approximately constant, i.e. pressure-drop limitation occurs. Oscillations have often been experimentally observed when this occurs, as shown by figure 2 in [125]. Luo and Pedley [19]'s results at $Re = 300$ also show that oscillations would definitely be present in the pressure-drop limitation regime. They state that the location of unstable points agrees with the experimentally observed conditions at which steady flow gives way to self-excited oscillations. However, their results seem to show that instability occurs somewhat earlier, at $\beta = 27.5$ for $Re = 300$.

In the self-excited regime, vorticity waves were found downstream of the elastic section with associated eddies that sometimes split in two. These were similar to the vorticity waves found in several computational studies, including [127], with a prescribed moving indentation in the channel wall. The energy dissipation rates upstream and downstream of the point of greatest constriction were very different in the self-excited and steady regimes, which suggests that the mechanism of oscillation depends strongly on the details of energy dissipation and flow separation.

Luo and Pedley [15] studied the effects of wall inertia at $Re = 300$ using the same ratios of length to width as [19]. The ratio of the mass of the wall to the mass of the fluid below,

i.e. $\frac{\rho_w h}{\rho_f D}$, where h is the thickness of the wall, was varied, as well as the value of β . The wall was, however, treated as a thin membrane. The position of the point on the wall close to that of maximum deformation and the pressure there was examined. For $\beta = 30$, the results for $\frac{\rho_w h}{\rho_f D} = 0.01$ were very similar to those obtained by [19] with a massless wall. At $\frac{\rho_w h}{\rho_f D} = 0.1$, for $\beta = 30, 32.5$ and 35 , high-frequency flutter was superposed on the low-frequency self-excited oscillations for both the position of the point on the wall and the pressure. The flutter grows with time from a small amplitude until it dominates the slower mode. As the value of β increased, the oscillations became more complex, with a flutter frequency six times that of the oscillation at $\beta = 30$, a period bifurcation at $\beta = 32.5$ and a very complex oscillation at $\beta = 35$. Flutter also occurred at $\beta = 25$, which is outside the regime at which self-excited oscillations arise when the wall is massless, which shows that the inertia of the wall alone can cause instability. The critical value of tension below which self-excited oscillations arose decreased as the mass was increased. At $\frac{\rho_w h}{\rho_f D} = 1$, the flutter frequency was comparable to the normal self-excited oscillations and they suggest that the mechanism of the generation of oscillations may therefore be different when the wall has more inertia. A direct quantitative comparison of the model with experiment was not possible because the experiments are three dimensional and the wall has a finite thickness. However, flutter has been observed in many different experiments. [15] have picked one study to compare the ratios of the flutter frequency to that of the self-excited oscillations and this ratio is 6 in [15] for $\frac{\rho_w h}{\rho_f D} = 0.1$ and between 4 and 8 in the study.

When the external pressure and upstream pressure are increased by the same amount relative to that at the downstream end of the elastic membrane, the flow rate increases up to a limiting rate. This is called flow limitation.

Many studies have discussed whether flow limitation is related to self-excited oscillations. The simulations by Luo and Pedley [15] show that the occurrence of flow limitation is not a sufficient condition for self-excited oscillations at a fixed inflow rate.

Jensen and Heil [12] analysed high-frequency self-excited oscillations. They carried out an asymptotic analysis in the limit of high tension, i.e. $\frac{TD}{\rho_f Q^2} \gg Re$, and found the boundaries of stability. Numerical simulations confirmed these stability boundaries. All simulations were carried out at $Re > 300$ and $10^3 \leq \frac{TD}{\rho_f Q^2} \leq 10^5$, therefore $3 \times 10^5 \leq \frac{TD}{\eta Q} \leq 3 \times 10^7$, which is much higher than the maximum value of 10^5 used by Lowe and Pedley [11] and Luo and Pedley [13, 15, 19]. By investigating self-excited oscillations in a different region

of parameter space, Jensen and Heil [12] showed that self-excited oscillations can grow by extracting energy from the mean flow faster than it is lost through viscous dissipation. The oscillations are closely related to the normal modes of the system, which have a frequency set by a balance between the membrane tension and the inertia of the fluid.

4.7 Comparisons with the study by Lowe and Pedley

In this section, the method described in this chapter is validated by comparing the results of several simulations of a Starling resistor to the results reported in Lowe and Pedley [11] for the same sets of parameters ¹.

The length of the Starling resistor was parallel to the x -axis. At the beginning of each simulation, the elastic wall was initialised to be a rectangular piece of material of length L_e and thickness h that had been uniformly stretched in the x -direction to achieve the desired tension, T , and allowed to contract in the y -direction due to the Poisson effect. The corners were fixed during the simulation. The spacing between adjacent pairs of points was equal to the lattice spacing Δx . The coordinates of each point were measured relative to the bottom left of the wall and calculated from the initial strain as follows, given that the strain is uniform and defined by equation (4.7), with $\epsilon_{xy} = 0$:

$$(x, y) = \left(\frac{x'}{1 + \epsilon_{xx}}, \frac{y'}{1 + \epsilon_{yy}} \right), \quad (4.74)$$

where (x, y) and $(x', y') = (x + u_x, y + u_y)$ are its coordinates before and after stretching respectively and $\epsilon_{yy} = -\Omega\epsilon_{xx}$, where Ω is the Poisson ratio. The initial strain, Young's modulus and thickness of the wall are constrained by

$$T = E\epsilon_{xx}h. \quad (4.75)$$

From equation (4.74), the natural length of the elastic material is given by

$$L_0 = \frac{L_e}{1 + \epsilon_{xx}}. \quad (4.76)$$

¹The code for these simulations and instructions for its use may be downloaded from <http://ccs.chem.ucl.ac.uk/~gary> as a zip archive and will be in the folder "Elastic_complex_geometry_rev_118". For these simulations, INCOMPRESS and ELASTIC were defined at compile time.

The flow was simulated using the D2Q9i lattice-Boltzmann model. The lattice sites that were initially inside the channel were regarded as fluid sites and those outside were regarded as solid. No fluid nodes were moved, created or destroyed as the wall moved. The centreline of the channel was placed on a row of lattice points, as shown in figure 4.7. Its width was chosen such that the lattice points nearest to the wall lie a distance of 0.25 lattice points from it unless otherwise stated. The distribution functions were initially set to the equilibrium ones with zero velocity and $p = p_0 = 0$. Pressure boundary conditions $p = p_u$ and $p = p_d = p_0 = 0$ were applied at the inlet and outlet respectively using the method by Zou and He [89], which was described in section 2.9.2, with pressure p_0 at the outlet.

In all simulations reported here the ratios of the lengths of the elastic and rigid sections are given by $\frac{L_u}{D} = 2$, $\frac{L_e}{D} = 10$ and $\frac{L_d}{D} = 2$.

4.7.1 The wall parameters

In Lowe and Pedley's study [11], the wall is assumed to be a thin membrane for which the tension is fixed at the downstream end, whereas in the present study, the tension will change as the wall deforms since we are using the full theory of linear elasticity. The strain was chosen to minimise the anticipated relative change in tension, while ensuring that $\epsilon_{xx} \ll 1$, as required by the theory (section 4.1).

The wall shapes in [11] that are compared with the results from this study are qualitatively similar to that in figure 4.6 and the maximum change in the channel width, $\Delta D_{max} < 0.02D$. Therefore, equations (4.75) and (4.76) hold approximately if we replace subscript x with subscript t , which denotes a tangential component, i.e. $T \approx E\epsilon_{tt}h$, with $\epsilon_{tt} \approx \frac{L-L_0}{L_0}$, where L is the current length of the wall. Expressing the tension in terms of this gives

$$T \approx Eh \frac{L - L_0}{L_0}. \quad (4.77)$$

If the wall has length L_1 initially and tension T_1 initially and length L_2 and tension T_2 after deformation, the relative change in tension during the simulation is

$$\frac{T_2 - T_1}{T_1} = \frac{L_2 - L_1}{L_1 - L_0}. \quad (4.78)$$

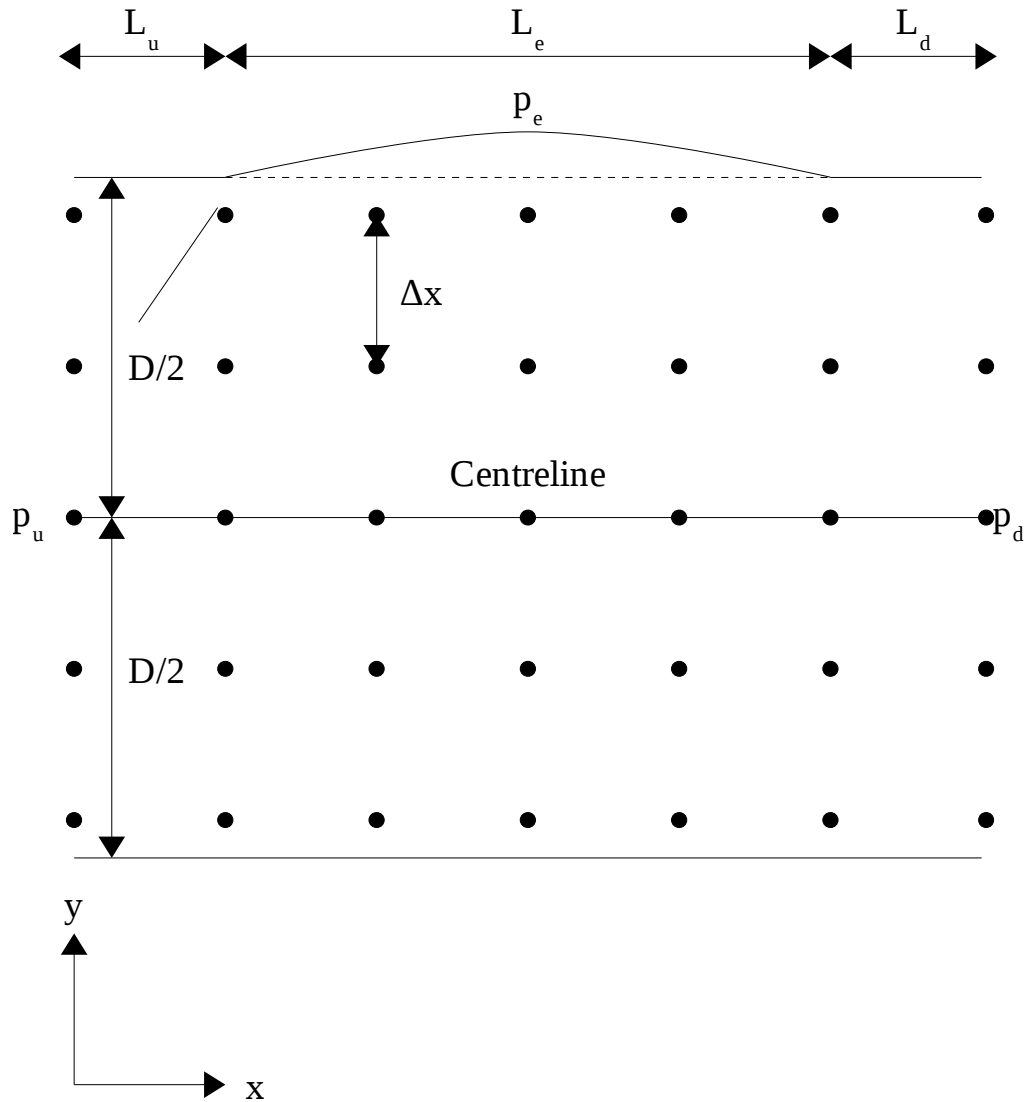


FIGURE 4.7: Diagram to show the setup of the simulations of the Starling resistors for which the wall profiles were compared to those obtained by Lowe and Pedley [11]. The solid circles are the fluid lattice sites and the centreline of the channel is placed on a row of lattice sites. The channel is aligned with the x -axis. The inlet, outlet and external pressures are p_u , p_d and p_e respectively. The width of the channel is D and the lengths of the upstream and downstream rigid sections of the wall and the elastic section are L_u , L_d and L_e respectively. For clarity, the lattice resolution is coarser than the resolution used in the simulations.

If the maximum change in the channel width during deformation, ΔD_{max} , is small, L_2 can be estimated using Pythagoras' theorem on the dotted triangles shown in figure 4.6 to give $L_2 \approx \sqrt{L_1^2 + 4\Delta D_{max}^2}$. The Taylor expansion in ΔD_{max} is $L_2 \approx L_1 \left(1 + \frac{2\Delta D_{max}^2}{L_1^2}\right)$. Substituting into equation (4.78) gives:

$$\frac{T_2 - T_1}{T_1} \approx \frac{L_1}{L_1 - L_0} \left(\frac{2\Delta D_{max}^2}{L_1^2} \right). \quad (4.79)$$

$$\Rightarrow \frac{T_2 - T_1}{T_1} \approx \frac{1}{\epsilon_{xx}} \left(\frac{2\Delta D_{max}^2}{L_1^2} \right). \quad (4.80)$$

from equation (4.76). Since $\Delta D_{max} < 0.02D$ and $L_1 = L_e = 10D$, we have $\frac{T_2 - T_1}{T_1} < \frac{8 \times 10^{-6}}{\epsilon_{xx}}$. In all simulations in this chapter, $\epsilon_{xx} = 0.01$, so the fractional change in tension during the simulation is less than 8×10^{-4} .

The numerical scheme allows for any Poisson's ratio except $\Omega = \frac{1}{N_D - 1}$, which would make the coefficient of the second term in equation (4.53) infinite. Therefore, $\Omega = 0.5$ was chosen, which is well away from this critical value. The simulations were carried out with a variety of different wall thicknesses. There are some issues surrounding the choice of the wall density, which will be discussed in section 5.1. In this section, the density was set such that the following parameter, $\Gamma = 250$ lattice-Boltzmann timesteps:

$$\Gamma = 2\pi h \sqrt{\frac{\rho_w}{E}} \quad (4.81)$$

Substituting equation (4.75) into this and rearranging gives

$$\rho_w = E \left(\frac{\Gamma}{2\pi h} \right)^2. \quad (4.82)$$

4.7.2 The flow parameters

For the simulations in this section, the tension is given by $\frac{TD}{\eta Q} = 10^5$, where η is the dynamic viscosity and Q is the flow rate. The last two quantities could therefore be chosen freely provided that the Reynolds number is of order one or less so that it is sensible to compare Lowe and Pedley's results from computation of Stoke's flow with my own. The dimensionless relaxation parameter was chosen to be, $\tau = 0.56$, therefore from equation (2.11), $\eta = \nu \rho_f = \rho_f \frac{\tau - 0.5}{3} = 0.02 \rho_f \frac{\Delta x^2}{\Delta t}$, where ν is the dynamic viscosity, and the density of the fluid, $\rho_f = 1$ in lattice units. Lowe and Pedley applied a Poiseuille flow at the inlet,

therefore

$$Q = \frac{2}{3}v_{max}D, \quad (4.83)$$

where v_{max} is the maximum flow velocity. We define $Re = \frac{\rho_f v_{max} D}{\eta}$, therefore

$$Q = \frac{2Re\eta}{3\rho_f}. \quad (4.84)$$

The pressure difference, $p_u - p_d$, that was applied was calculated using the following equation for Poiseuille flow:

$$p_u - p_d = \frac{12\eta LQ}{D^3}, \quad (4.85)$$

with $L = L_u + L_e + L_d$. Since $\Delta D_{max} < 0.02D$, this is a reasonable approximation. Lowe and Pedley state the pressure difference $p_e - p'_d$, where p'_d is the pressure at the right-hand end of the elastic wall. For Poiseuille flow, the pressure gradient is constant along the length, therefore we have $p_u - p'_d = \frac{L_u + L_e}{L}(p_u - p_d)$, where $\frac{L_u + L_e}{L} = 6/7$, from the lengths stated earlier in this section. Adding $p_e - p_u$ to both sides of the equation and rearranging gives

$$p_e - p_d = (p_e - p'_d) + \frac{1}{7}(p_u - p_d). \quad (4.86)$$

4.7.3 Convergence of the simulation

At each timestep, the convergence of the simulation is checked by comparing the flow fields at the end of the timestep to those at the beginning. The simulation is considered to be converged when the L^1 norms of the velocity flow field and the wall displacement from its initial (stretched) position are both below a chosen tolerance. The L^1 norm of the velocity

field is given in equation (3.15), i.e. $\frac{\sum_{x=0}^L \sum_{y=-R_0}^{R_0} |\mathbf{v}(x,y,t) - \mathbf{v}(x,y,t-1)|}{\sum_{x=0}^L \sum_{y=-R_0}^{R_0} |\mathbf{v}(x,y,t)|} < tol$. The tolerance is

2.0×10^{-8} for all simulations in this section.

Since we calculate the acceleration of the wall explicitly, both the walls and the fluid oscillate during each simulation, as explained in section 3.5.2. The simulation converges when the oscillations die out. In order to help the simulation converge to a steady state, I apply damping to each point on the wall by adding the term

$$-b \frac{d\mathbf{u}}{dt} \quad (4.87)$$

to its acceleration. The damping factor, b , is chosen to be 0.2 times the critical damping factor for the lowest frequency mode of oscillation of the wall, i.e. $b = 0.4\omega_0$, where ω_0 is the angular frequency of oscillation without damping. In this mode, the entire wall moves inwards or outwards together and forms a standing wave with a wavelength, λ of twice its length. If we consider the wall as a stretched string oscillating in free space, the wave speed, c , is given by

$$c^2 = \frac{T}{\rho_w h}. \quad (4.88)$$

Therefore the period of the wave is given by

$$\Lambda = \frac{2\pi}{\omega_0} = 2L_e \sqrt{\frac{\rho_w h}{T}}. \quad (4.89)$$

4.7.4 Results and Discussion

A computation of a Starling resistor with a width of $D = 10.5\Delta x$ was carried out, where Δx is the lattice spacing, $Re = 0.15$, $h = \Delta x = \frac{D}{10.5}$, and $\Delta p^* = (p_e - p_d) \left(\frac{D^2}{\eta Q} \right) = 24$. The dark red solid line in figure 4.8 shows the inner surface of the wall when the simulation reached a steady state, where the x and y coordinates measured relative to the left hand end of the inner wall and nondimensionalised on D . The top part of figure 3 in [11] is superimposed on this graph since their raw data was not available for comparison. The black solid line shows their results for $\Delta p^* = 24$. The maximum displacements in the y -direction in Lowe and Pedley's and the present study are $\Delta D_{max} = 7.5 \times 10^{-3}D$ and $\Delta D_{max} = 5.7016 \times 10^{-3}D$ and these occur at $x = 4D$ and $x = 4.48D$ respectively. I suspected that the poor agreement between the results was due to the bending stiffness of the wall, which is ignored in Lowe and Pedley's simulation. I therefore reduced the wall thickness, first to $h = \frac{D}{21}$, then to $h = \frac{D}{42}$. The results for the latter are shown by the red solid line. It is clear that the wall bulged out more, resulting in better agreement with Lowe and Pedley's results. When considering the bending stiffness, the most important ratio is $\frac{h}{L_e}$, but $L_e \propto D$ in this study, so I report the ratio $\frac{h}{D}$. After reducing the thickness of the wall, I increased the resolution of the lattice, first to $D = 20.5\Delta x$, while $h = 0.25\Delta x$. The results for the latter, are shown by the dark green solid line. It is clear that the agreement with Lowe and Pedley's results is better at $D = 40.5\Delta x$ than at $D = 10.5\Delta x$, which is probably at least partly due to a further reduction in the ratio $\frac{h}{D}$. Figure 4.9 shows the results for $\Delta p^* = 24$ for all five values of $\frac{h}{D}$ and it is clear that the wall bulges out further

as $\frac{h}{D}$ decreases. However, the wall profiles for $h = \frac{D}{82}$ and $h = \frac{D}{162}$ are very close, so it cannot be clearly determined which agrees most closely with Lowe and Pedley's results since we do not have the exact data for these.

The simulations with $D = 10.5\Delta x$ and $D = 20.5\Delta x$ converged to the desired tolerance within a time equal to 6 times the free period of lowest frequency mode of the wall, i.e. within 6Λ . However, this was not the case at the highest spatial resolution, $D = 40.5\Delta x$. This may be because, for the same Reynolds number, the maximum fluid velocity in the x -direction, v_x , is lower in lattice units, whereas the amplitude of the oscillation of the wall's velocity during an oscillation is the same. Since we impose no-slip conditions, the L^1 norm of the velocity field is larger. The amplitude of the velocity of the wall is approximately $\omega_0\Delta D$, from equation (4.89). From equation (4.89), we have $\omega_0 = \frac{\pi}{L}\sqrt{\frac{T}{\rho_w h}}$. Therefore $\omega = \frac{2\pi^2}{L\Gamma}\sqrt{\frac{hT}{E}}$ from equation (4.82), then $\omega_0 = \frac{2\pi^2 h}{L\Gamma}\sqrt{\epsilon_{xx}}$ from equation (4.75). Since $\Delta D \propto D$, the amplitude of the velocity oscillation is proportional to $D\frac{h}{L\Gamma}$. This amplitude is the same in lattice units for the simulations with $h = 0.25\Delta x$. Therefore, the Reynolds number was changed to 1.5 for simulations with $D = 40.5\Delta x$ throughout this section, since this was expected to speed up the convergence.

However, the simulations still did not converge to the desired tolerance; the L^1 norm for the velocity of the fluid decreased, then increased again later on in each simulation. The L^1 norms for the wall displacement continued to decrease for a longer period, but that also began to increase under the influence of the fluid. The results for $D = 40.5\Delta x$ in this section are those for $Re = 1.5$ taken at $t = 10^7\Delta t = 7.76\Lambda$. The reason why this happens is still unknown.

Graphs 4.10 and 4.11 show my results for $\frac{TD}{\eta Q} = 10^5$ with $\Delta p^* = 84$ and 224 respectively for $h = \frac{\Delta x}{4}$ at three different values of the lattice resolution, Δx . The deformation of the wall increases when the lattice resolution increases and therefore $\frac{h}{D}$ decreases, as it did when $\Delta p^* = 24$, probably due to the reduced effect of the bending stiffness. The wall profiles for the highest and lowest resolutions are shown in red and dark green on graph 4.8 respectively, with dashed and dotted lines for $\Delta p^* = 84$ and 224 respectively, and compared with Lowe and Pedley's results, which are shown by the black dashed and dotted lines respectively. The agreement with their results is better at the $h \approx \frac{D}{40}$ than at $h \approx \frac{D}{10}$, which suggests that it improves as $\frac{h}{D}$ decreases. However, as in the case with

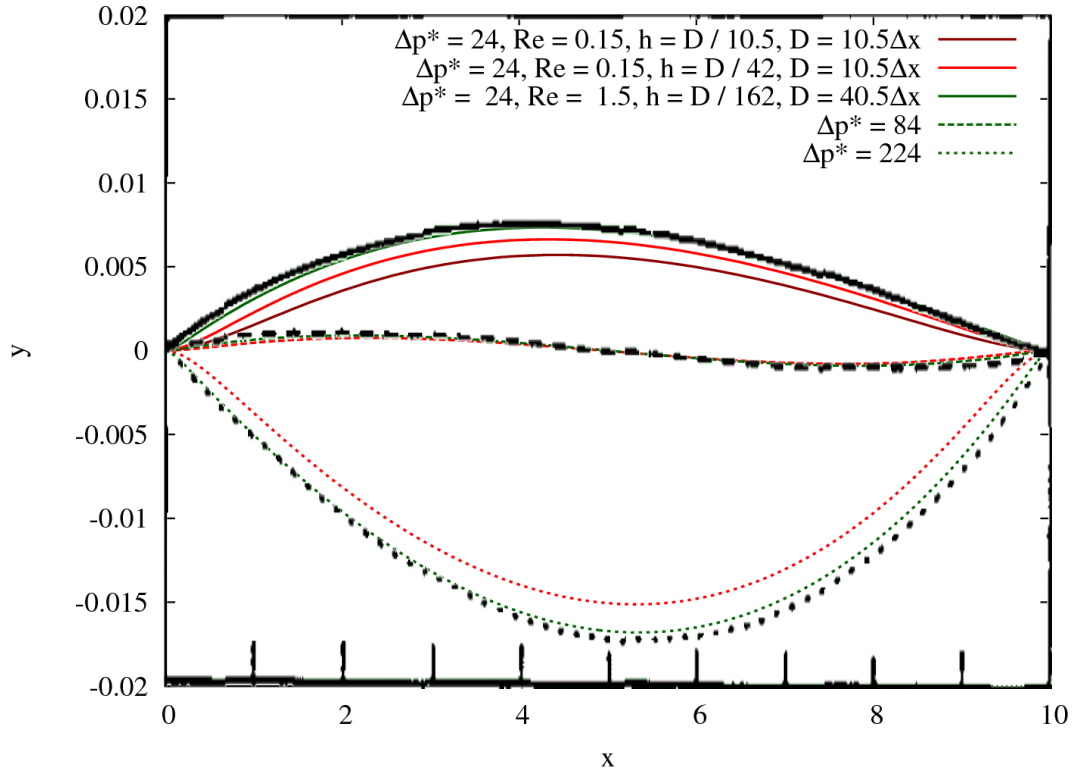


FIGURE 4.8: Comparison of the wall profiles obtained in the present study at $\frac{TD}{\eta Q} = 10^5$ with those obtained by Lowe and Pedley [11] and shown in figure 3 of that study. The results for $\Delta p^* = 24, 84$ and 224 are represented by the solid, dashed and dotted lines respectively. For each pressure, the black lines show Lowe and Pedley's results, while the dark red, red and dark green lines show the results of the present study for $D = 10.5\Delta x$, $h = \frac{D}{10.5}$, $Re = 0.15$; $D = 10.5\Delta x$, $h = \frac{D}{42}$, $Re = 0.15$; and $D = 40.5\Delta x$, $h = \frac{D}{162}$, $Re = 1.5$ respectively, except that $D = 42\Delta x$ and $h = \frac{D}{168}$ instead of $D = 40.5\Delta x$ for $\Delta p^* = 224$. We have $\tau = 0.56$.

$\Delta p^* = 0$, we cannot be sure whether the result with $h \approx \frac{D}{20}$ or $h \approx \frac{D}{40}$ agrees more closely with Lowe and Pedley's result, since the wall profiles for these results are very similar.

For $\Delta p^* = 224$, the simulations with $D = 20.5\Delta x$ and $D = 40.5\Delta x$ were unstable. This was probably because the maximum inward displacement of the wall was expected to be $\Delta D = 0.018D$, which is more than the initial separation of $0.25\Delta x$ between the row of lattice sites adjacent to the wall and the wall itself when $D = 20.5\Delta x$ and $D = 40.5\Delta x$. Using lattice resolutions such that the initial separation between the wall and the adjacent row of lattice sites is $0.5\Delta x$ from the wall and Δx from the wall, i.e. greater than ΔD , so $21\Delta x$ and $D = 42\Delta x$ respectively, improves the situation. This issue is discussed further in section 5.5.

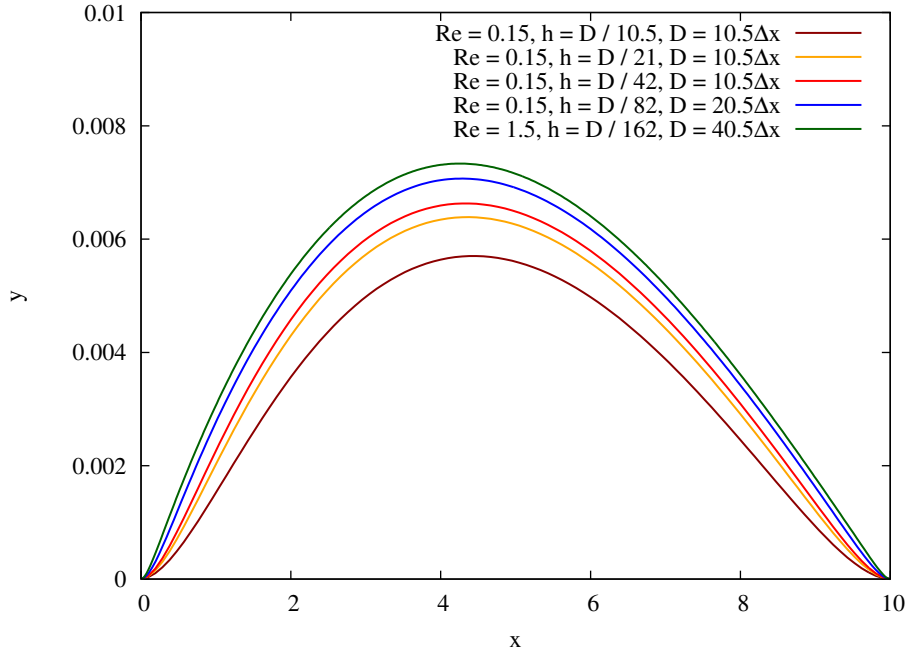


FIGURE 4.9: Wall profiles obtained in the present study for $\frac{TD}{\eta Q} = 10^5$ and $\Delta p^* = 24$ at different lattice resolutions and wall thicknesses. From the least to the most distended wall profile, we have $Re = 0.15, h = D/10.5, D = 10.5\Delta x$; $Re = 0.15, h = \frac{D}{21}, D = 10.5\Delta x$; $Re = 0.15, h = \frac{D}{42}, D = 10.5\Delta x$; $Re = 0.15, h = \frac{D}{82}, D = 20.5\Delta x$; and $Re = 1.5, h = \frac{D}{162}, D = 40.5\Delta x$. We have $\tau = 0.56$.

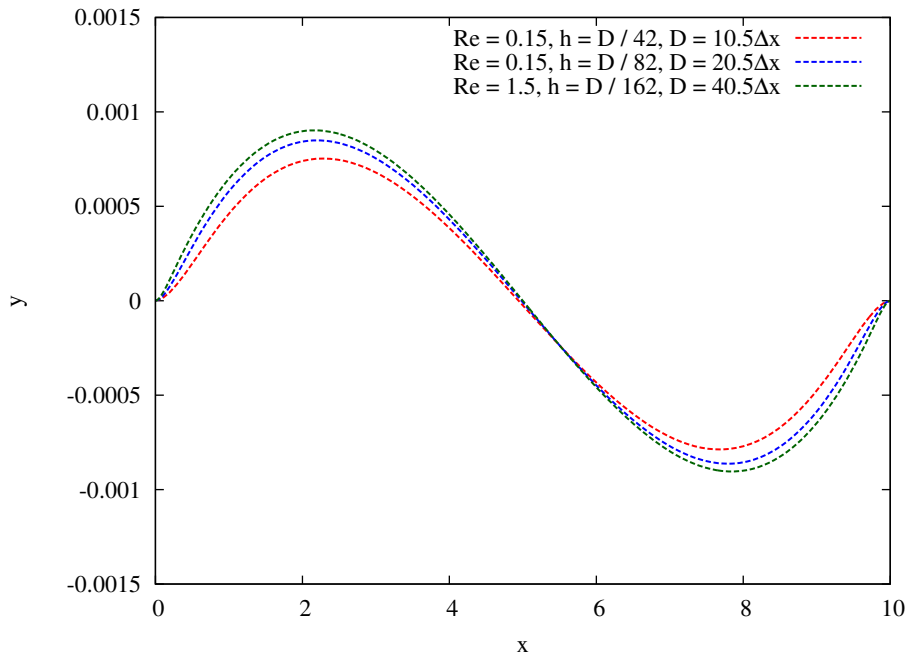


FIGURE 4.10: Wall profiles obtained in the present study for $\frac{TD}{\eta Q} = 10^5$ and $\Delta p^* = 84$ at different lattice resolutions and wall thicknesses. The red, blue and dark green lines show the wall profiles for $Re = 0.15, h = \frac{D}{42}, D = 10.5\Delta x$; $Re = 0.15, h = \frac{D}{82}, D = 20.5\Delta x$; and $Re = 1.5, h = \frac{D}{162}, D = 40.5\Delta x$ respectively. We have $\tau = 0.56$.

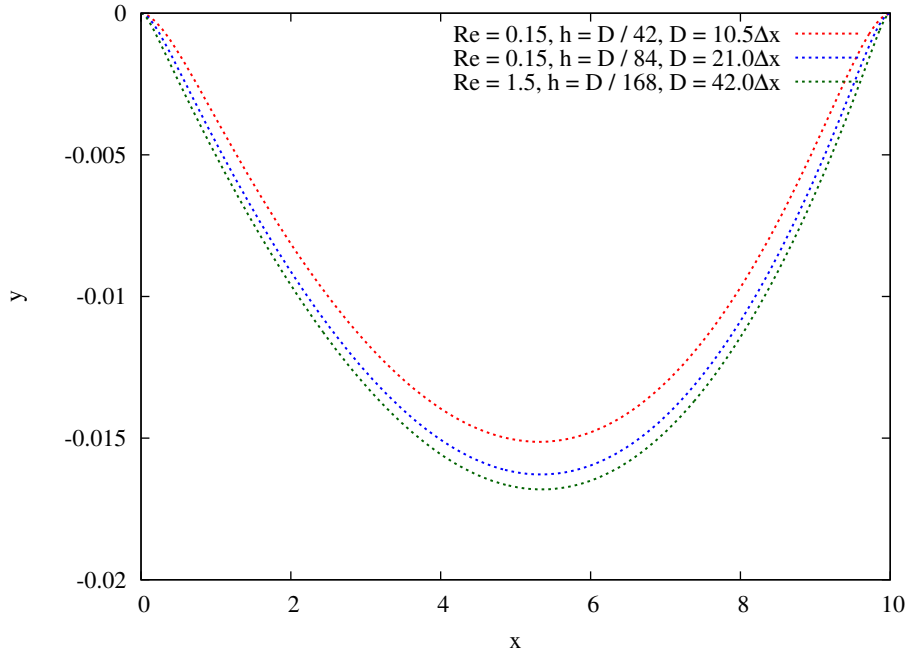


FIGURE 4.11: Wall profiles obtained in the present study for $\frac{TD}{\eta Q} = 10^5$ and $\Delta p^* = 224$ at different lattice resolutions and wall thicknesses. The red, blue and dark green lines show the wall profiles for $Re = 0.15$, $h = \frac{D}{42}$, $D = 10.5\Delta x$; $Re = 0.15$, $h = \frac{D}{84}$, $D = 21\Delta x$; and $Re = 1.5$, $h = \frac{D}{168}$, $D = 42\Delta x$ respectively. We have $\tau = 0.56$.

Lowe and Pedley [11] predicted analytically that, at $\frac{TD}{\eta Q} = 10^5$, the transition from the elastic section being completely distended to being partially distended should occur at $\Delta p^* = 64$ and that the transition to it being fully collapsed should occur at $\Delta p^* = 104$. They carried out computations at $\Delta p^* = 63.5$ and $\Delta p^* = 64.5$ to examine the first transition and $\Delta p^* = 103.5$ and $\Delta p^* = 104.5$ to examine the second transition and presented the results in figure 4 of their study. Their computations for the first and second transition are compared with my own in graphs 4.12 and 4.13 respectively. For $h = \frac{D}{42}$ and $h = \frac{D}{82}$, the wall is less distended at $\Delta p^* = 64.5$ than at $\Delta p^* = 63.5$, but the transition occurs when $\Delta p^* > 64.5$. However, when the resolution is increased such that $h = \frac{D}{162}$, the transition occurs when $63.5 < \Delta p^* < 64.5$, in agreement with Lowe and Pedley's results. In contrast to the simulations described earlier in this section, the agreement with Lowe and Pedley's results is significantly better at $h = \frac{D}{162}$ than at $h = \frac{D}{82}$. The resolution may be insufficient to capture such a small collapsed section near the end of the wall when $h = \frac{D}{42}$, $D = 10.5\Delta x$ or $h = \frac{D}{82}$, $D = 20.5\Delta x$, since the width of the collapsed section is $0.15D$. Alternatively, the improved agreement may be due to the reduction in the bending stiffness. A similar situation occurs for the second transition, in which a tiny portion

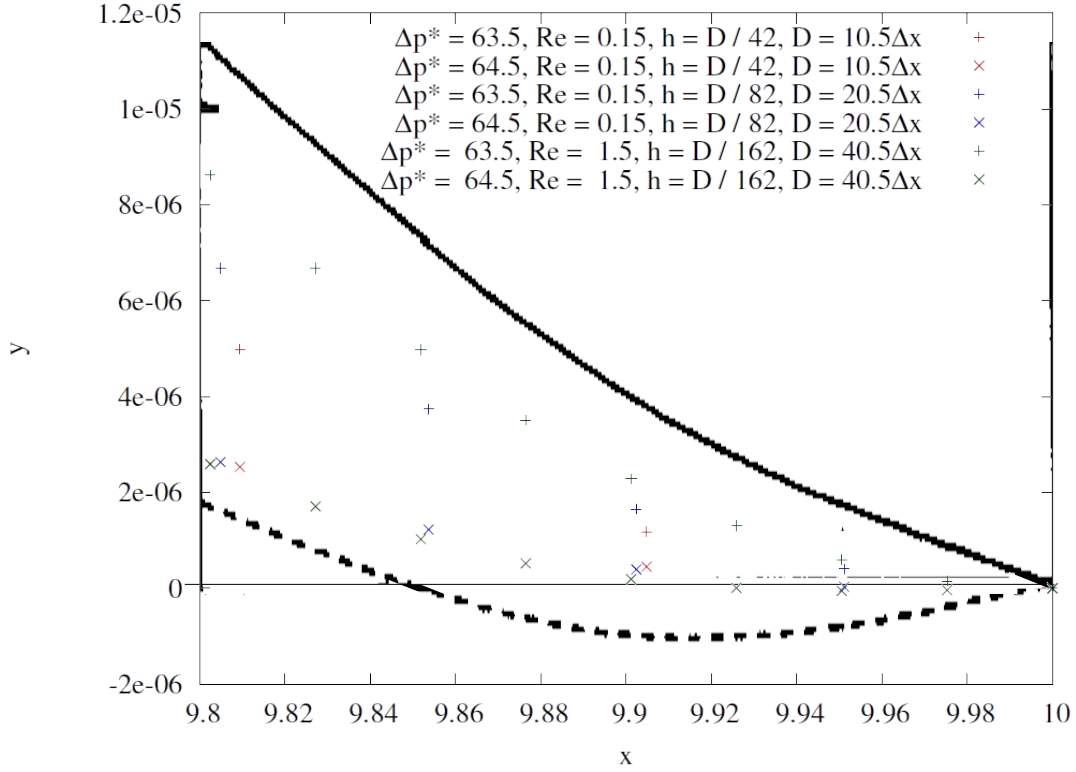


FIGURE 4.12: Comparison of the wall profiles near the wall's right-hand end obtained in the present study at $\frac{\tau D}{\eta Q} = 10^5$ (the points marked by '+' and 'x' for $\Delta p^* = 63.5$ and $\Delta p^* = 64.5$ respectively) with those obtained by Lowe and Pedley [11] and shown in figure 4 of their study, at the same external pressures (the black solid and dashed lines respectively). For each pressure, the red, blue and dark green points show the results when $D = 10.5\Delta x$, $h = \frac{D}{42}$, $Re = 0.15$, $D = 20.5\Delta x$, $h = \frac{D}{82}$, $Re = 0.15$ and $D = 40.5\Delta x$, $h = \frac{D}{162}$, $Re = 1.5$ respectively. The wall undergoes a transition from a fully to partially distended state for $63.5 < \Delta p^* < 64.5$ for the higher resolution and in [11]. We have $\tau = 0.56$.

of the wall is distended at $\Delta p^* = 103.5$. The transition occurs for $\Delta p^* < 103.5$ when $h = \frac{D}{42}$, $D = 10.5\Delta x$ and $h = \frac{D}{82}$, $D = 20.5\Delta x$, but it occurs for $63.5 < \Delta p^* < 64.5$ when $h = \frac{D}{162}$. While the wall profiles I obtain around these two transitions look significantly different to Lowe and Pedley's, even for the highest resolution, the difference is small compared to the maximum displacement of the entire wall shown in figure 4.8.

The Starling resistor differs from blood vessels in at least two ways. First, the ends of the elastic walls are fixed in a Starling resistor, but not in a blood vessel. Second, the elastic forces on the wall are caused by the stretching of the wall in the same plane as the axis of the length of the channel, whereas for blood flow through elastic vessels, the largest contribution to the forces comes from the stretching of the wall in the circumferential

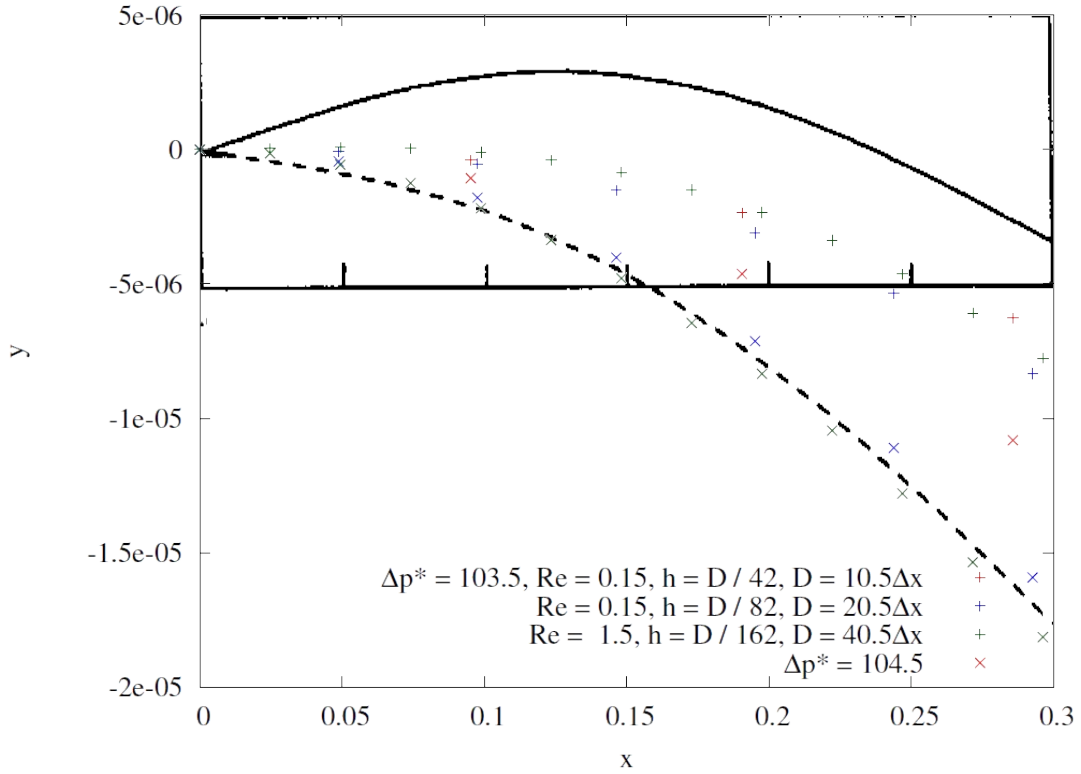


FIGURE 4.13: Comparison of the wall profiles near the wall's left-hand end obtained in the present study at $\frac{TD}{\eta Q} = 10^5$ (the points marked by '+' and 'x' for $\Delta p^* = 63.5$ and $\Delta p^* = 64.5$ respectively) with those obtained by Lowe and Pedley [11] and shown in figure 4 of their study, at the same external pressures (the black solid and dashed lines respectively). For each pressure, the red, blue and dark green points show the results when $D = 10.5\Delta x$, $h = \frac{D}{42}$, $Re = 0.15$, $D = 20.5\Delta x$, $h = \frac{D}{82}$, $Re = 0.15$ and $D = 40.5\Delta x$, $h = \frac{D}{162}$, $Re = 1.5$ respectively. The wall undergoes a transition from a partially to fully collapsed state for $103.5 < \Delta p^* < 104.5$ for the higher resolution and in [11]. We have $\tau = 0.56$.

direction, which is perpendicular to this plane, as explained in section 3.2, particularly for axisymmetric vessels. Therefore, it is desirable to validate the method developed in this chapter for a system with characteristics that are more similar to blood vessels, but the method needs to be extended to three dimensions to accomplish this.

4.8 Conclusions

A model for time-dependent 2D simulations of fluid flow through elastic systems in a general geometry has been developed in this chapter, which uses the full theory of linear elasticity. The general scheme can be readily extended to 3D, but the selection of points

on the wall to be used for the calculation of forces on the wall and the determination of the points of intersection of the lattice vectors with the wall are more difficult to extend, as discussed in section 4.5. The force at a point on the elastic wall depends on the derivatives of the displacement field, which are estimated from the displacement of a point and its neighbours for this model. In contrast, the model described in chapter 3 did not take into account the displacement of the neighbouring points when calculating the force at a point, but it used the assumption that the blood vessels are axisymmetric instead. Therefore, the model described in this chapter can be used for simulations of cerebral blood flow in more complex geometries, including blood vessels involving branches or aneurysms. For both models, the Poisson's ratio can be chosen freely except that we cannot have $\Omega = \frac{1}{2}$, whereas the model described by Buxton et al. [119] restricts the Poisson's ratio to $\frac{1}{4}$.

The steady-state behaviour of the model has been validated by comparing the wall profiles resulting from simulations of a 2D Starling resistor in which the fluid to those reported in [11]. The agreement with their results improved as the ratio of the wall thickness, h , to the channel width, D , was decreased, becoming very close at $h = \frac{D}{162}$. This is because the effect of the bending stiffness, which is ignored in [11], decreased as $\frac{h}{D}$ decreased, since the length of the elastic portion of the wall, $L_e = 10D$, for all simulations in this chapter. The spatial resolution became finer as $\frac{h}{D}$ decreased, which might also have contributed to the improved agreement with [11]. The deformation of the wall increased as the bending stiffness was reduced, as we would expect. Starling resistors have different characteristics from blood vessels, as described in section 4.7.4, but they provide a useful system for which to validate the model. Furthermore, the model needs to be extended to three dimensions in order to validate it for systems that are more similar to blood vessels.

The dynamics of the model still need to be tested. While the simulations at $h = \frac{D}{162}$ initially converged to steady states that agreed closely with those in [11], the velocity and wall displacement fields began to diverge towards the end of the simulation. The convergence of the schemes proposed in this thesis is investigated further in section 5.10.

The computational cost of the method is likely to be greater than that for the method in chapter 3 because the calculation of the acceleration at each point on the wall depends on information from the neighbouring points instead of being independent of them, while the equation of motion is also more complicated. However, since information is only required from the nearest neighbours, the method is well suited to computation on parallel

machines. The calculation of the acceleration of each point on the wall requires two inversions of 10×10 or 27×27 matrices in 2D and 3D respectively. The computational cost of this has been minimised by decomposing the matrix into blocks such that only 2×2 or 3×3 matrices must be inverted. The performance will be tested in chapter 5.

Chapter 5

Dynamic simulations of fluid flow through elastic systems

In the previous chapter, a method for simulating time-dependent fluid flow through elastic systems in a general geometry was developed and the steady state behaviour was validated. In this chapter, the dynamics of the model for a 2D Starling resistor are studied, the model is adapted in several ways in order to be able to deal with larger displacements of the wall and lower wall densities, and its computational cost is evaluated. Section 5.1 contains discussion of the limitations on the density of the wall, the improvement to the method that allows lower densities to be used, and a simple test of the dynamics of the model in 2D. Section 5.2 explains how simulations were set up to attempt to compare the dynamics with results from existing computational studies. Sections 5.3 to 5.6 describe attempts at these comparisons and how the method was adapted to deal with the problems that arose. Section 5.3 describes why it was necessary to change the method of calculating the normalised cut distances, then describes this change. Section 5.4 describes how the points on the elastic wall were initially evenly spaced and why this is important. In section 5.5, I describe the remaining issues with the normalised cut distances and conclude that it is necessary to create and destroy fluid nodes as the wall moves. I describe how this is done in section 5.6. Results for simulations using this method are presented in section 5.7 and its computational cost is evaluated in section 5.8. The simulation of fluid flow through large elastic systems on multicore machines using the methods developed in 3 to 5 is discussed in section 5.9. In section 5.10, changes are made to the method of calculating the

velocity imposed on the fluid. In section 5.11, I describe how viscoelasticity was included. Section 5.12 describes a comparison of the dynamics with a previous computational study. Conclusions for this chapter are presented in section 5.13.

5.1 The density of the wall

In this section, the minimum temporal resolution that the simulation method can cope with is determined and the limitations this places on the density of the wall are discussed. The method is then improved by dividing each lattice-Boltzmann timestep into a number of sub-timesteps which are used to integrate the equation of motion of the wall. Results are presented for simulations of a Starling resistor at a variety of wall densities to test the dynamics of the simulation when this improvement to the method is applied.

5.1.1 Limitations on the density of the wall caused by the temporal resolution

When we simulate a piece of elastic material by integrating the equations of motion explicitly for a number of points on the wall (equation (4.53)), as described in section 4.2, we expect many modes of oscillation. A full analysis of the normal modes is beyond the scope of this work. However, we know that the modes of oscillation with the shortest periods will be those for which neighbouring points move in opposite directions. In this section, we consider the case where a point on the inner surface and its corresponding point on the outer surface move in opposite directions and estimate the order of magnitude of the period of this oscillation. For the purpose of this discussion, we fix the point on the outside and model the point on the inside as a mass on a spring. The relevant mass is then of order $m = \rho_w \Delta x h$, where ρ_w , Δx and h are the density of the wall, the spacing between adjacent pairs of points on the wall and its thickness respectively. The spring constant is $\frac{E \Delta x}{h}$, where E is the Young's modulus. Therefore the period of oscillation is of order Γ , as given by equation (4.81).

$$\Gamma = 2\pi h \sqrt{\frac{\rho_w}{E}}.$$

In a Starling resistor, we expect motion to be dominated by the mode of oscillation in which the entire wall moves inwards or outwards together to form a standing wave with

a wavelength of $2L_e$, where L_e is the length of the elastic section of the wall. This is the lowest frequency mode of oscillation and its frequency is given by equation (4.89), i.e.

$$\Lambda = \frac{2\pi}{\omega_0} = 2L_e \sqrt{\frac{\rho_w h}{T}},$$

where T is the tension in the wall, provided that the mass of the wall is much greater than that of the fluid below it, so that the inertia of the fluid is ignored. Since we integrate the equations of motion of the wall explicitly in time as explained in chapter 4, section 4.2.2, the temporal resolution must be sufficient for the simulation to be stable. In this section, we determine whether the minimum temporal resolution required is determined by the shortest or the dominant mode of oscillation.

I carried out six computations ¹ of the elastic section of the wall of a Starling resistor, i.e. simulations that did not include the fluid. Most of the parameters are the same as in section 4.7, i.e. the thickness of the wall is $0.25\Delta x$, its initial strain is given by $\epsilon_{xx} = 0.01$, $\epsilon_{yy} = -0.005$, $\epsilon_{xy} = 0$ and the Poisson ratio, $\Omega = 0.5$. A constant pressure gradient was applied on the inside of the wall, such that the internal pressure was given by $p = p_e + 4.8 \times 10^{-7}(L_u + L_e - x)\rho_f \frac{\Delta x}{\Delta t^2}$, where ρ_f is a reference density. It was enforced through the boundary condition on the stress tensor in the wall, given by equation (4.55). The tension was $T = 0.4\rho_f \frac{\Delta x^3}{\Delta t^2}$. The results are shown in table 5.1. I ran the simulations for approximately four times the expected period of oscillation of the entire wall, Λ .

If a fluid with density ρ_f and dynamic viscosity $\eta = 0.02\rho_f \frac{\Delta x^2}{\Delta t}$ were present, the pressure gradient would drive a Poiseuille flow at $Re = 0.15$ in a channel of constant width $D = 10\Delta x$, which approximately match the parameters used section 4.7. The value of $\frac{TD}{\eta Q} = 10^5$, where Q is the flow rate, would also match that used in section 4.7.

The amplitudes of the oscillations described earlier in this section were then examined as follows. The change in separation in the y -direction between each point on the inner surface of the wall and its corresponding point on the outer surface since the beginning of the simulation was calculated at each timestep. The change in this separation is similar, but not identical to, the change in thickness of the wall. A discrete Fast Fourier Transform

¹The code for these simulations and instructions for its use may be downloaded from <http://ccs.chem.ucl.ac.uk/~gary> as a zip archive and will be in the folder "Elastic_complex_geometry_rev_142". For these simulations, INCOMPRESS and INC_FLUID were not defined at compile time.

$L_e/\Delta x$	ρ_w/ρ_f	$\Gamma/\Delta t$	$\Gamma_o/\Delta t$	$\Lambda/\Delta t$
5	63326	250	105.3	3979
5	15831	125	52.63	1989
8	63326	250	104.4	6366
8	15831	125	53.33	3183
10	63326	250	108.1	7958
10	15831	125	54.05	3979

TABLE 5.1: Parameters of computations of the elastic section of the wall of a Starling resistor for which a constant pressure gradient is applied at the lower surface. L_e is the length of the elastic wall and Λ is the expected period of oscillation of the entire wall. Γ is the expected period of oscillation of the separation between each point on the inner surface and its neighbour on the outer surface. Γ_o is the period of the dominant frequency of oscillation of the y -component of this separation, which was the same for every pair of points for each simulation.

(FFT) of the change in separation was then taken with respect to time for each pair of points for $0 \leq t < \Lambda_r$, $\Lambda_r \leq t < 2\Lambda_r$, $2\Lambda_r \leq t < 3\Lambda_r$ and $3\Lambda_r \leq t < 4\Lambda_r$ using the function `fft` from the NumPy library for Python [128], where Λ_r is Λ rounded to two significant figures. This results in a complex amplitude for each frequency in the FFT. Graphs 5.1 to 5.3 show the modulus of the complex amplitude of the dominant frequency for the simulations described above, $|A_k|_{max}$, for each pair of points on the wall for the four periods of time plotted against the initial x -ordinate of each pair of points. The range in frequencies for the FFT is given by

$$\frac{-0.5}{\Delta t} \leq \xi < \frac{0.5}{\Delta t}. \quad (5.1)$$

The separation between adjacent frequencies is

$$\Delta\xi = \frac{1}{\Lambda_r}. \quad (5.2)$$

The Fourier transform is given by

$$A_k = \sum_{t/\Delta t=0}^{\Lambda_r/\Delta t-1} a_t \exp\left(-2\pi i \frac{kt}{\Lambda_r}\right) \quad k = -\frac{\Lambda_r}{2\Delta t}, -\frac{\Lambda_r}{2\Delta t} + 1, \dots, \frac{\Lambda_r - \Delta t}{2\Delta t}, \quad (5.3)$$

where $k = \xi\Lambda_r$ and t is the number of timesteps since the start of the period over which we take the FFT, a_t is the change in separation between the points at time t and A_k is the complex amplitude for frequency ξ . The reciprocal of the dominant frequency for each simulation is given in table 5.1. For each simulation, this frequency was the same for every

pair of points, as we would expect. This period is shorter than Γ , probably because this estimate of the period of oscillation of the separation between adjacent points on the wall is highly simplified: it does not treat the modes of oscillation properly or take into account the Poisson ratio.

Figures 5.1 to 5.3 show that, for $\Gamma = 125\Delta t$, for all three lengths of the elastic wall, and for every pair of points apart from the fixed ones at the end of the wall, $|A_k|_{max}$ became significantly larger for each successive period, Λ_r , over which it was measured, showing that the simulation was unstable. For $\Gamma = 250\Delta t$, $|A_k|_{max}$ fluctuated but did not increase over time. For example, for $L_e = 10\Delta x$, the value $|A_k|_{max}$ for some pairs of points on the wall was largest during the fourth period, but this was not the case for other points. These results show that the minimum temporal resolution is determined by the shortest modes of oscillation and is independent of the period of the longest modes of oscillation and that $\Gamma = 250\Delta t$ provides adequate temporal resolution for a wall thickness, $h = 0.25\Delta x$. Therefore, $\Gamma = 250\Delta t$ was chosen for all simulations in this section and section 4.7.

The choice of $\Gamma = 250\Delta t$ required $\rho_w = 4.0 \times 10^6 \rho_f$, $2.0 \times 10^6 \rho_f$ and $10^6 \rho_f$ in chapter 4, for an initial channel width $D = 10\Delta x$, $20\Delta x$ and $40\Delta x$ respectively, whereas ideally we want the density of the wall to be of the same order of magnitude or less than that of the fluid because, for many of the existing computations of flow in a Starling resistor with which we could compare simulation results [11–13, 15, 19], the ratio of the mass of the elastic section of the wall to that of the fluid below it, $\frac{h}{D} \left(\frac{\rho_w}{\rho_f} \right)$, is much less than one. For simulations of blood flow, the densities of the wall and the fluid should be equal as explained in section 3.7. This is not important for the steady state, but it would be important for a comparison of the dynamics. However, the temporal resolution of the method for simulating the elastic wall would then be insufficient for the simulations to be stable.

5.1.2 Subdivision of the lattice-Boltzmann timesteps

The situation has been improved as follows. The lattice-Boltzmann timestep is carried out first, then the equation of motion of the elastic wall is integrated using a number, Ψ ,

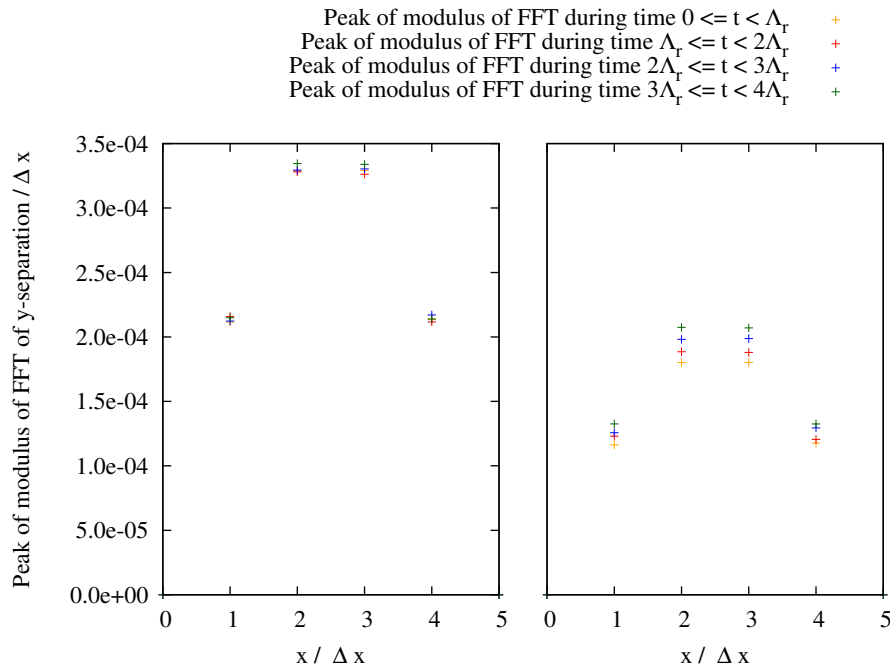


FIGURE 5.1: Modulus of the amplitude of the dominant frequency of oscillation of the separation in the y -direction between each point on the lower surface at initial position x and its corresponding point on the upper surface, for simulations of the elastic sections of the walls of two Starling resistors. The elastic sections have length $L_e = 5\Delta x$ and thickness $0.25\Delta x$. The pressure applied on the lower surface is given by $p = p_e + 4.8 \times 10^{-7}(L_e - d)\rho_f \frac{\Delta x}{\Delta t^2}$, where ρ_f is a reference density, Δt is the timestep and p_e is the pressure applied on the upper surface. The tension is $T = 0.4\rho_f \frac{\Delta x^3}{\Delta t^2}$. The graph on the left shows results for $\rho_w/\rho_f = 63326$, which gives rise to $\Gamma = 250\Delta t$, $\Lambda_r = 4000\Delta t$, while the graph on the right has $\rho_w/\rho_f = 15831\Delta t$, therefore $\Gamma = 125\Delta t$, $\Lambda_r = 2000\Delta t$, where Λ_r is the period of the mode of oscillation in which the wall forms a standing wave with wavelength $2L_e$, which is given by equation (4.89), rounded to two significant figures.

of shorter sub-timesteps². Therefore, Δt , the length of the timestep, is replaced with $\frac{\Delta t}{\Psi}$ in equations (4.59) and (4.60). At each sub-timestep, the stress in the fluid is estimated by linear interpolation between the stress at times t_0 and $t_0 + \Delta t$, where t_0 is the time at the start of the lattice-Boltzmann timestep. The stress at the inner surface of the wall is then extrapolated as explained in section 4.4.

Since we calculate the acceleration of the wall explicitly, both the walls and the fluid oscillate during each simulation, as explained in section 3.5.2. If all the simulation parameters are constant, the simulation converges to a steady state when the oscillations die out due to the viscosity of the fluid. The subdivision of each timestep involves a change to the

²The code for this and instructions for its use may be downloaded from <http://ccs.chem.ucl.ac.uk/~gary> as a zip archive and will be in the folder “Elastic_complex_geometry_rev_142” when the archive has been unpacked. For the tests described in this section, INCOMPRESS and INC_FLUID were not defined at compile time.

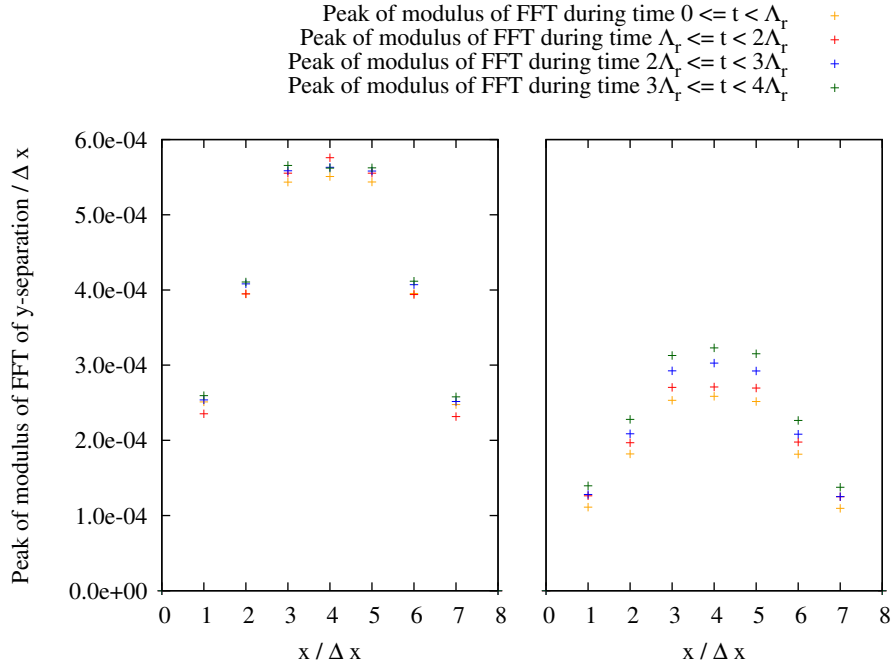


FIGURE 5.2: Modulus of the amplitude of the dominant frequency of oscillation of the separation in the y -direction between each point on the lower surface at initial position x and its corresponding point on the upper surface, for simulations of the elastic sections of the walls of two Starling resistors. The elastic sections have length $L_e = 8\Delta x$ and thickness $0.25\Delta x$. The pressure applied on the lower surface is given by $p = p_e + 4.8 \times 10^{-7}(L_e - d)\rho_f \frac{\Delta x}{\Delta t^2}$, where ρ_f is a reference density, Δt is the timestep and p_e is the pressure applied on the upper surface. The tension is $T = 0.4\rho_f \frac{\Delta x^3}{\Delta t^2}$. The graph on the left shows results for $\rho_w/\rho_f = 63326$, which gives rise to $\Gamma = 250\Delta t$, $\Lambda_r = 6400\Delta t$, while the graph on the right has $\rho_w/\rho_f = 15831\Delta t$, therefore $\Gamma = 125\Delta t$, $\Lambda_r = 3200\Delta t$, where Λ_r is the period of the mode of oscillation in which the wall forms a standing wave with wavelength $2L_e$, which is given by equation (4.89), rounded to two significant figures.

check on the convergence of the simulation described in section 4.7.3. It is still checked once per lattice-Boltzmann timestep, but the L^1 norm of the wall displacement from its initial position is now calculated for each sub-timestep. If simulations are performed with identical parameters apart from Ψ , the L^1 norm for the wall displacement at a given time is expected to be smaller for the simulations with a larger value of Ψ , but the L^1 norm for the velocity of the fluid would be the same. The L^1 norm of the velocity field is given in equation (3.15), i.e.

$$\frac{\sum_{x=0}^L \sum_{y=-R_0}^{R_0} |\mathbf{v}(x, y, t) - \mathbf{v}(x, y, t-1)|}{\sum_{x=0}^L \sum_{y=-R_0}^{R_0} |\mathbf{v}(x, y, t)|} < tol.$$

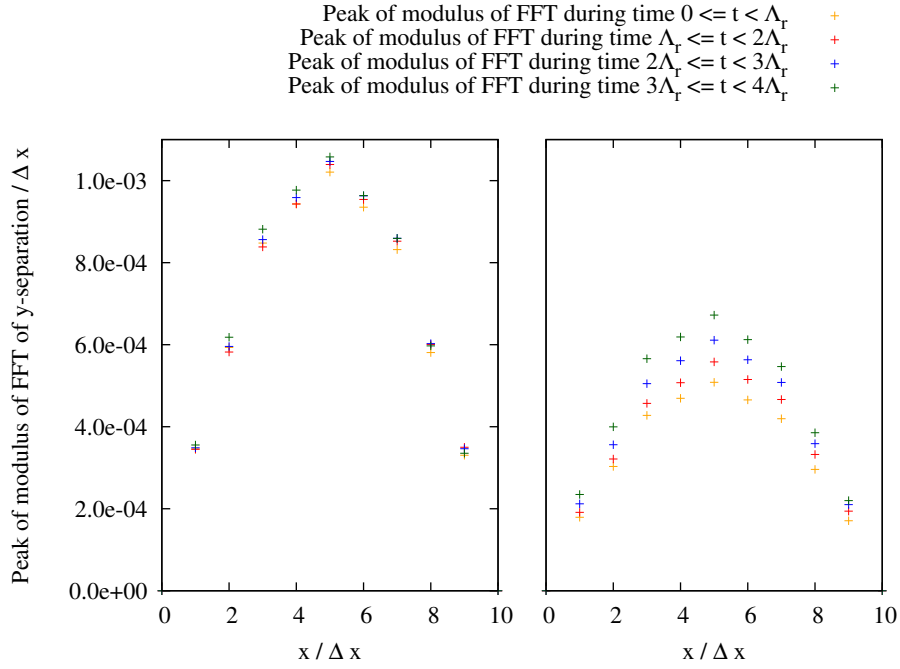


FIGURE 5.3: Modulus of the amplitude of the dominant frequency of oscillation of the separation in the y -direction between each point on the lower surface at initial position x and its corresponding point on the upper surface, for simulations of the elastic sections of the walls of two Starling resistors. The elastic sections have length $L_e = 10\Delta x$ and thickness $0.25\Delta x$. The pressure applied on the lower surface is given by $p = p_e + 4.8 \times 10^{-7}(L_e - d)\rho_f \frac{\Delta x}{\Delta t^2}$, where ρ_f is a reference density, Δt is the timestep and p_e is the pressure applied on the upper surface. The tension is $T = 0.4\rho_f \frac{\Delta x^3}{\Delta t^2}$. The graph on the left shows results for $\rho_w/\rho_f = 63326$, which gives rise to $\Gamma = 250\Delta t$, $\Lambda_r = 8000\Delta t$, while the graph on the right has $\rho_w/\rho_f = 15831\Delta t$, therefore $\Gamma = 125\Delta t$, $\Lambda_r = 4000\Delta t$, where Λ_r is the period of the mode of oscillation in which the wall forms a standing wave with wavelength $2L_e$, which is given by equation (4.89), rounded to two significant figures.

The tolerance is set to 2.0×10^{-8} for all simulations in this section for both the fluid and the wall displacement.

The boundary conditions on the fluid are less straightforward. If the velocity of the fluid next to the wall is set to the instantaneous velocity of the wall, we would obtain spurious results for the fluid because its temporal resolution would be insufficient to resolve the results of the modes of oscillation of the wall with very short periods. Furthermore, the fluid behaviour we are interested in happens on the timescale of the oscillation of the entire wall. One possible approach to finding the long-term velocity of the wall at time t is to find the average velocity between times $t - \Delta t$ and t , i.e. $\mathbf{v} = (\mathbf{u}(t) - \mathbf{u}(t - \Delta t))/\Delta t$, but this does not take into account the long-term acceleration of the wall. We apply the

following equation of uniformly accelerated motion:

$$\mathbf{u}(t_0) - \mathbf{u}(t_1) = (t_1 - t_0)\mathbf{u}'(t_1) - 0.5(t_1 - t_0)^2\mathbf{u}'', \quad (5.4)$$

where t_0 and t_1 are two times. If we first substitute in $t_0 = t$, $t_1 = t - \Delta t$, then substitute $t_0 = t$, $t_1 = t - 2\Delta t$ to obtain a second equation, then eliminate the acceleration, \mathbf{u}'' , we find that the long-term velocity of the wall is:

$$\mathbf{v} = 1.5\mathbf{u}(t) - 2\mathbf{u}(t - \Delta t) + 0.5\mathbf{u}(t - 2\Delta t) \quad (5.5)$$

We can therefore reduce the density and we only need to satisfy the criterion

$$\Gamma\Psi \geq 250\Delta t, \quad (5.6)$$

provided Λ remains greater than L_e/c_s so that the slow-flow condition described in section 2.6 is satisfied, as required for accurate lattice-Boltzmann simulations. That is, the characteristic timescale over which the flow fields change, which is equal to Λ , is greater than the advection time for information to travel a distance L_e through the fluid. Therefore, from equation (4.89) we have

$$2\sqrt{\frac{\rho_w h}{T}} > \frac{1}{c_s}, \quad (5.7)$$

where $c_s = \frac{\Delta x}{\Delta t\sqrt{3}}$ from equation (2.90). For the parameters used in this chapter and the last, with $D = 10\Delta x$, $Re = 0.15$ and $h = 0.25\Delta x$, the density can be reduced to $\rho_w = 0.4\rho_f$ and this minimum density is directly proportional to Re .

I repeated the simulations described in table 5.1 with $\Gamma = 25\Delta t$ but used a timestep of $\Delta t' = 0.1\Delta t$. For each simulation, the displacement of every point on the wall at time t was equal to the displacement for the corresponding simulation with $\Gamma = 250\Delta t$ at time $10t$, for every value of t that is an integer multiple of Δt , correct to three significant figures, which showed that the timesteps had been subdivided correctly.

5.1.3 Testing the dynamics of a Starling resistor with subdivision of the timesteps.

Some simulations of a 2D Starling resistor including the fluid ³ were carried out with various wall densities to verify that they are stable provided the density is chosen such that $\Lambda > \frac{L_e}{c_s}$ and $\Gamma\Psi \geq 250\Delta t$ and to test the dynamics in a simple way. Since the mass of the wall was much greater than the mass of the fluid below it for these simulations, i.e. $\rho_w h \gg \rho_f D$, I expected the wall to perform oscillations with period Λ that are damped by the viscosity of the fluid.

These were set up as described in section 4.7. The lengths of the first rigid section, the elastic section and the second rigid section of the wall were $L_u = 5D$, $L_e = 10D$ and $L_d = 30D$ respectively. The external pressure, p_e , was given by $\frac{D^2(p_e - p_d)}{\rho_{fluid} Q^2} = 1.40133$, where p_d is the pressure at the outlet. These parameters match those used by Jensen and Heil [12]. The spatial resolution was chosen such that $D = 10.4\Delta x$, therefore the wall lay a distance of $0.2\Delta x$ from the nearest row of lattice points. Since $\Lambda > \frac{L_e}{c_s}$ is required, as explained in section 5.1.2, simulations are expected to be stable if $\Lambda > 175\Delta t$. The wall thickness, $h = 0.25\Delta x$. Its Poisson ratio and initial strain were the same as in section 4.7. The inlet pressure, p_u , was calculated for Poiseuille flow at $Re = 30$ as described in that section. The computations were carried out for a time $t \approx 4.5\Lambda$.

The displacement of the point that began at the centre of the inner surface of the wall over time for the computation with $\rho_w = 3896.96803\rho_f$, corresponding to $\Lambda = 331$, $\Gamma = 0.25$, with $\Psi = 1000$, is shown in graph 5.4. The simulation is stable and the amplitude of the motion of the wall decreases over time due to the viscosity of the fluid, as we expect. The results for all simulations with $\Lambda > 175$, and $\Gamma\Psi = 250$ were qualitatively similar, except that the effect of the damping was insignificant at higher values of ρ_w . This is because the mass of the elastic portion of the wall was greater but the damping forces for a given set velocity profile of the wall were the same. The simulations with $\Lambda < 175$ were unstable, i.e. the amplitude of oscillation of the wall increased over time, because the wall profile changes on a scale faster than the lattice-Boltzmann method can transfer the information

³The code for these simulations and instructions for its use may be downloaded from <http://ccs.chem.ucl.ac.uk/~gary> as a zip archive and will be in the folder “Elastic_complex_geometry_rev_142”. For these simulations, INCOMPRESS and INC_FLUID were defined at compile time.

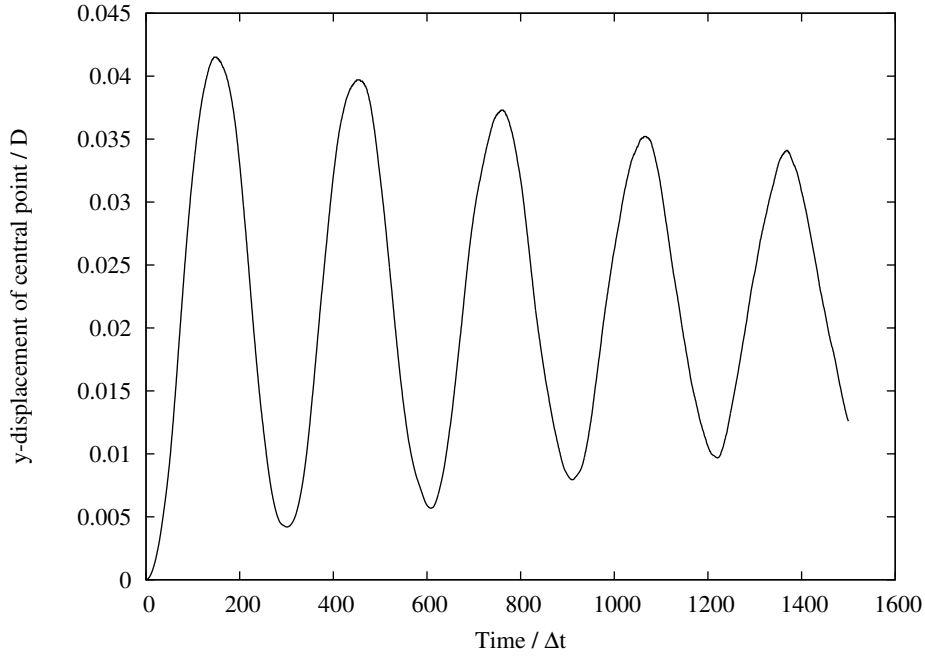


FIGURE 5.4: y -displacement of the central point on the inner surface of the elastic wall in a simulation of a Starling resistor with $L_u = 5D$, $L_e = 10D$ and $L_d = 30D$, $D = 5.2\Delta x$, $h = 0.25\Delta x$, $v_{max} = 0.03\frac{\Delta x}{\Delta t}$, $Re = 30.0$, $\frac{D^2(p_e - p_d)}{\rho_{fluid}Q^2} = 1.40133$, $\Psi = 1000$ and $\rho_w = 3896.968603\rho_f$, corresponding to $\Gamma = 0.25\Delta t$, $\Lambda = 331\Delta t$.

about the flow fields from one end of it to the other. An example of this is shown in graph 5.5.

The average period of oscillation of each simulation over the first four periods of oscillation was measured from graphs of the wall displacement over time. The densities of the wall, the observed periods of oscillation and the expected ones, Λ , as well as whether the simulation was stable, are given in table 5.2 for the simulations with $\Gamma\Psi = 250$. The periods agree fairly closely, which shows that the dominant motion is a standing wave described in section 5.1.1 and its period is controlled by the inertia of the wall, which is expected since for the first five entries in the table, the ratio of the mass of the elastic section wall to that of the fluid below it, $\frac{h}{D}\left(\frac{\rho_w}{\rho_f}\right)$, is more than 25. The periods are all slightly shorter than expected by approximately the same factor in these simulations, but the period appears to be directly proportional to the density of the wall, as expected. This is probably because additional forces are needed to deform the wall owing to the bending stiffness or the expansion or compression of the wall in the direction of its normal due to the nonzero pressures on either side. On the other hand, we would expect the damping from the fluid to increase the period of oscillation, but this effect may be much smaller than that of the

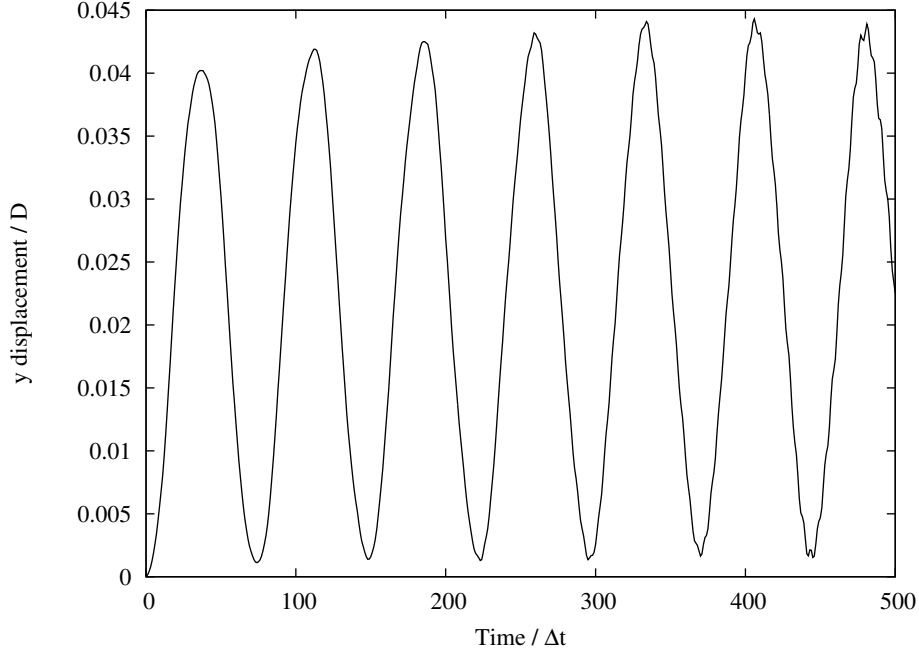


FIGURE 5.5: y -displacement of the central point on the inner surface of the elastic wall in a simulation of a Starling resistor with $L_u = 5D$, $L_e = 10D$ and $L_d = 30D$, $D = 5.2\Delta x$, $h = 0.25\Delta x$, $v_{max} = 0.03\frac{\Delta x}{\Delta t}$, $Re = 30.0$, $\frac{D^2(p_e - p_d)}{\rho_{fluid}Q^2} = 1.40133$, $\Psi = 4138$ and $\rho_w = 227.5830679\rho_f$, corresponding to $\Gamma = 0.060\Delta t$, $\Lambda = 80\Delta t$. The simulation is unstable because Λ is shorter than the advection time $\frac{L_e}{c_s}$ for information to travel a distance L_e through the fluid.

expansion or compression of the wall because the mass of the elastic section of the wall is much greater than the mass of the fluid below it.

While the simulation with $\rho_w = 3.56363503 \times 10^9 \rho_f$, corresponding to $\Lambda = 3.31 \times 10^5 \Delta t$, $\Gamma = 250\Delta t$ with $\Psi = 1$ is stable, a simulation with $\rho_w = 9.742421508 \times 10^8 \rho_f$, corresponding to $\Lambda = 1.655 \times 10^5 \Delta t$, $\Gamma = 125\Delta t$ with $\Psi = 1$ is unstable. This confirms that it is necessary to sub-divide each lattice-Boltzmann timestep into Ψ sub-timesteps for the elastic wall such that $\Gamma\Psi \geq 250\Delta t$ for a simulation of a Starling resistor to be stable.

The results in this section show that the density of the wall can be reduced provided that $\Lambda > \frac{L_e}{c_s}$ and $\Gamma\Psi > 250\Delta t$. Simple tests of the dynamics have shown that the model behaves correctly.

ρ_w/ρ_f	$\Lambda/\Delta t$	Observed period / Δt	$\Gamma/\Delta t$	Ψ	stability
3.89696803×10^9	331000	308000	2.5×10^2	1	stable
3.89696803×10^7	33100	30800	2.5×10^1	10	stable
3.89696803×10^5	3310	3080	2.5	100	stable
3.89696803×10^3	331	305	2.5×10^{-1}	1000	stable
1.08902054×10^3	175	157	1.32×10^{-1}	1892	stable
2.275830679×10^2	80	74	6.04×10^{-2}	4138	unstable

TABLE 5.2: Comparison of observed and expected periods of oscillation of points at the centre of the elastic wall for simulations with $L = 10D$, $h = 0.024D$, $v_{max} = 0.03$, $Re = 30.0$, $\tau = 0.53$, $\Delta p' = 1.40133$, $\Gamma\Psi = 250\Delta t$.

5.2 Setting up a comparison of the dynamics of the Starling resistor simulation with previous computational studies

In this section, I describe how 2D simulations of Starling resistors were set up to attempt to validate the dynamics of the model in this study by comparing the results with computations in previous studies under the same parameters. Since the simulation method is best suited to wall movements that are small compared with the channel width, I searched for results that satisfied this criterion and chose to use those shown in figure 4 of [15], for which the wall moves by less than $0.1D$. However, that simulation was started from a steady state solution for a slightly different wall tension, and in that steady state solution, the wall deformation was large. In order to keep the deformation during my own simulations significantly smaller than the channel width, it was necessary to begin the simulations from a state expected to be close to the steady state, as described in the rest of this section.

The simulations described in sections 5.3 to 5.5 were set up as described in section 4.7, except that the wall shape was initialised to correspond approximately with one of the steady solutions given in [13] or [19], the lattice site types were set according to this new wall shape and the wall was held in its initial position until the fluid had converged according to the criterion expressed by equation (3.15). The initialisation of the positions of the wall points is described in the rest of this section.

The coordinates of eleven points were estimated by measuring from the graphs in [13] or [19]. The inner surface of the wall consisted of the straight lines joining these points. The sum of the lengths of these lines, L , was compared to the natural length of the elastic wall

to estimate the tangential strain by $\epsilon_{tt} = \frac{L-L_0}{L_0}$. The thickness of the wall was estimated by assuming that the normal strain, $\epsilon_{nn} = -\Omega\epsilon_{tt}$, so that $h = h_0(1 + \epsilon_{nn})$. The outer surface of the wall was constructed by shifting all the line segments of the inner surface by $h\mathbf{n}$, where \mathbf{n} is the outward normal to the surface, except for the segments at the ends of the wall. The line segments at the ends of the outer surface were those joining the coordinates $(0, h)$ to (L_e, h) measured relative to the bottom left corner of the wall. An example of the wall shape in which we have five points on the inner surface is shown in figure 5.6. If a pair of adjacent line segments of the outer surface meet at a separation $\Delta\mathbf{r}$ from where the corresponding line segments of the inner surface meet and these line segments have normals \mathbf{n}_{AB} and \mathbf{n}_{BC} , then we must have

$$\Delta\mathbf{r} \cdot \mathbf{n}_{AB} = \Delta\mathbf{r} \cdot \mathbf{n}_{BC} = h. \quad (5.8)$$

Therefore

$$\Delta\mathbf{r} = \frac{h}{2}(\mathbf{n}_{AB} + \mathbf{n}_{BC}). \quad (5.9)$$

For each lattice site, the nearest point on the inner surface was sought starting with the line segment for which $x''_{start} \leq x_{site} \leq x''_{end}$, where x''_{start} and x''_{end} are the x ordinates of the left and right ends of the line segment and x_{site} is that of the site. The nearest point on the line passing through the points at the ends of this line segment, \mathbf{r}''_{start} and \mathbf{r}''_{end} , is given by $\mathbf{r}''_{start} + l(\mathbf{r}''_{end} - \mathbf{r}''_{start})$, where l is found by solving $(\mathbf{r}''_{start} - \mathbf{r}_{site} + l(\mathbf{r}''_{end} - \mathbf{r}''_{start})) \cdot \mathbf{n} = 0$, where \mathbf{n} is its normal. If $l < 0$ this point was to the left of the start of the line segment and hence the closest point on the inner surface lay on one of the other line segments. The procedure above was therefore repeated with successive line segments to the left of the current one until $l > 0$. If $l > 1$ for the initial line segment, the procedure was repeated with successive line segments to the right of the current one until $l < 1$. The cases for the line segment AB with $0 < l < 1$, $l < 0$ and $l > 1$ are shown in figure 5.6. If a pair of line segments meet such that the wall is convex, we may have $l > 1$ for one segment and $l < 0$ for the other. In this case, the point on the inner surface is placed at the corner between the two segments. An example of this is shown in the diagram, where point B is the nearest point to the lattice site in the region bounded by the dashed lines starting from point B .

For each point at the corner between two line segments on the inner surface of the wall,

its corresponding point on the outer surface was placed at the corner between the two corresponding line segments of the outer surface. For each point that lies on a line segment on the inner surface but not at a corner, its outer point is placed at a separation of $\mathbf{n}h$ from it, where \mathbf{n} is the normal to the line segment. This usually places the point on the corresponding line segment on the outer surface, but it has a flaw: a lattice site's nearest point on the outer surface may lie at one of the outer surface's corners even if its nearest point on the inner surface does not lie on one of the inner surfaces corners. In figure 5.6, this problem will occur if we have a point on the inner surface between point B and one of the arrows joining the inner and outer surfaces. The position of the point on the outer wall is shown by a diamond. However, the flaw in the algorithm is not relevant to the findings described in sections 5.3 to 5.5.

When the points had been placed on the wall, it was assumed that the x -ordinates of the points on the inner surface of the wall before it had been deformed by the stress from the fluid were the same as those afterwards, i.e. $x'' = x'$. For each point on the outer surface of the wall, it was assumed that x' was equal to that for the corresponding point on the inner surface. The coordinates of the wall before stretching were given by equation (4.74), i.e. $(x, y) = (\frac{x'}{1+\epsilon_{xx}}, \frac{y'}{1+\epsilon_{yy}})$.

5.3 Change to the method for calculation of the normalised cut distances

In this section, I describe a simulation that was carried out starting from a nonflat wall ⁴ and the reason why it was necessary to change the method of calculating the normalised cut distances.

I decided to begin with a steady state solution given in figure 4 of [13] instead of figure 4 of [15] because the former has $Re = 1.5$ instead of $Re = 450$ ⁵, because their resulting flow fields were more straightforward in that simulation. The physical parameters are given

⁴The code for this simulation and instructions for its use may be downloaded from <http://ccs.chem.ucl.ac.uk/~gary> as a zip archive and will be in the folder "Elastic_complex_geometry_rev_176" when the archive has been unpacked. For this simulation, INCOMPRESS, INC_FLUID and MOVE.WALL were defined at compile time.

⁵The Reynolds numbers for these simulations are quoted as 1 and 300 in Luo and Pedley's publications because they calculate them using the average velocity of fluid flow at the inlet whereas I calculate them using the maximum velocity.

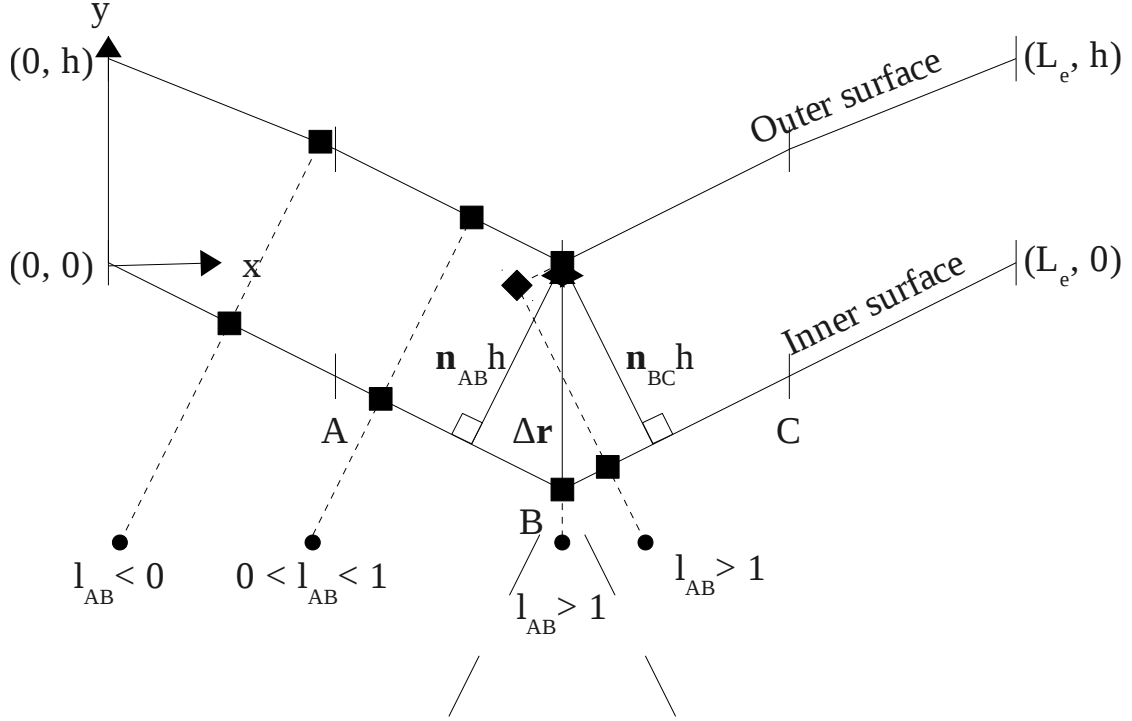


FIGURE 5.6: Example of the simulation setup when we begin with a nonflat wall. In this example, the inner wall is divided into four segments, separated by vertical lines. The squares show the points we place on the elastic wall, while the circles represent some of the lattice sites. For each lattice site, the value of l_{AB} shows where the straight line that includes segment AB comes closest to the lattice site. If $l_{AB} < 0$ or $l_{AB} > 1$, the line comes closest beyond the ends of the line segment AB . The dotted lines join each point on the inner surface to its corresponding point on the outer surface. The thickness of the wall is h and the normal is \mathbf{n} . Point B is the nearest point to the lattice site in the region bounded by the dashed lines. The diamond shows the point corresponding to that on the inner surface between corners B and C is not on the outer wall since the algorithm that places the points is slightly flawed.

in section 4.6, i.e. $\eta = 10^{-3}\text{Nm}^{-1}\text{s}$, $\rho_f = 10^3\text{kgm}^{-2}$, $D = 10^{-2}\text{m}$, $L_{elastic} = 5 \times 10^{-2}\text{m}$, $p_e - p_d = 0.93\text{Nm}^{-1}$, $T = T_0/\beta$, where $T_0 = 1.610245\text{N}$. I used $\beta = 15$, which is the lowest value in figure 4 of [13], since the simulations at high values of β become more challenging [13]. The lengths of the upstream and downstream rigid section and the elastic section were given by $L_u = 2D$, $L_d = 7D$ and $L_e = 5D$ respectively. The strain and Poisson ratio were given by $\epsilon_{xx} = 0.01$, $\epsilon_{yy} = -0.005$ and $\Omega = 0.5$, the same as in section 4.7. The lattice resolution was $\Delta x = \frac{D}{10}$, and the thickness was $\frac{D}{40}$. The lattice timestep is $\Delta t = 0.02\text{s}$, leading to $\tau = 0.56$ from equation (2.128). The density of the wall is $\rho_w = 4000\rho_f$, which leads to $\Gamma = 0.758\Delta t$ (from equation (4.81)). For each lattice-Boltzmann timesteps, 500 timesteps were used for the elastic wall, i.e. $\Psi = 500$ which satisfies the requirement that

$\Gamma\Psi \geq 250$. The parameters also satisfy the requirement that the period of oscillation of the wall, $\Lambda > \frac{L}{c_s}$. The initial positions of the points at the ends of the line segments that form the initial inner surface of the wall were measured from figure 4(a) of [13], They are given in table 5.3 and plotted in figure 5.7.

$\frac{x''}{D}$	$\frac{y''}{D}$
-5.8824×10^{-11}	0.0000
4.7059×10^{-1}	-9.0909×10^{-2}
1.0000	-1.8182×10^{-1}
1.5294	-2.3636×10^{-1}
2.0588	-2.7273×10^{-1}
2.5000	-2.7273×10^{-1}
3.0294	-2.5455×10^{-1}
3.4706	-2.0000×10^{-1}
4.0000	-1.6364×10^{-1}
4.5294	-7.2727×10^{-2}
5.0000	0.0000

TABLE 5.3: Positions of the ends of the line segments that form the inner surface of the elastic wall measured relative to its bottom left corner for the simulations started close to the steady state found in figure 4 of [13]. The inner surface is formed by the line segments joining these points. The double prime denotes the positions of the points after the wall has been stretched along the x -direction, then deformed due to the internal and external stress.

The configuration of lattice sites surrounding the one at $(1.1D, -0.2D)$ is shown in figure 5.8. The point belonging to this lattice site is point B and its neighbours are points A and C. At the beginning of the simulation, these points are collinear with coordinates $(1.0019D, -0.18201D)$, $(1.1008D, -0.19220D)$ and $(1.1110D, -0.19326D)$, so we have $\delta = 0.7636$ for lattice direction 1, i.e. $(1, 0)$. During the simulation, these points move so that they are not collinear, and therefore the cut distances are calculated by approximating the inner surface of the wall as a circle passing through a point and its neighbours, as explained in chapter 4, section 4.4. In this simulation, the wall was allowed to move at time $t = 7364\Delta t$ and the simulation failed at time $t = 7367\Delta t$ when the lattice vector $(1, 0)$ no longer intersected the circle between the three points, which were then at coordinates $(1.0045D, -0.17986D)$, $(1.1032D, -0.19140D)$ and $(1.1134D, -0.19269D)$. This lattice vector would have intersected the line joining the last two points if they were joined with a straight line. Furthermore, if we have a point at or near a corner between two line segments and two neighbouring points on those line segments, drawing a circle between the three points artificially concentrates the curvature at the corners if the points are close together, as shown in figure 5.9. Lastly, the circle passing through a point and its neighbours will

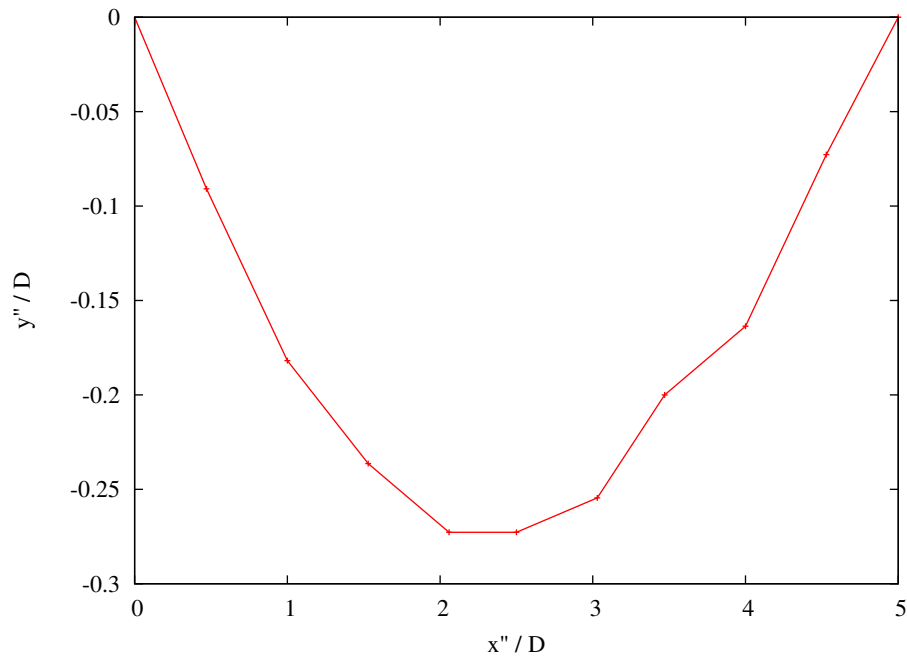


FIGURE 5.7: Initial inner surface of the elastic wall for the simulations started close to the steady state found in figure 4 of [13]. The double prime denotes the coordinates of the points after the wall has been stretched along the x -direction, then deformed due to the internal and external stress.

not generally be consistent with the circle passing through one of the neighbours and its own neighbouring points.

In order to solve these problems, the normalised cut distances were estimated as the distance along the lattice vector to its point of intersection with one of the two straight lines that join a point on the inner surface of the wall to its neighbours. The lattice vector may intersect the wall beyond the neighbours, in which case we are assuming that the tangent to the wall does not change, which is reasonable if the radius of curvature of the wall is much greater than the spacing between the points on the wall. The method for calculating the normal at a point on the wall remained the same.

5.4 Initial spacing between the points on the elastic wall

In this section, I discuss why it is necessary to space the points on the elastic wall moderately evenly and how the simulation method was adapted to deal with this issue.

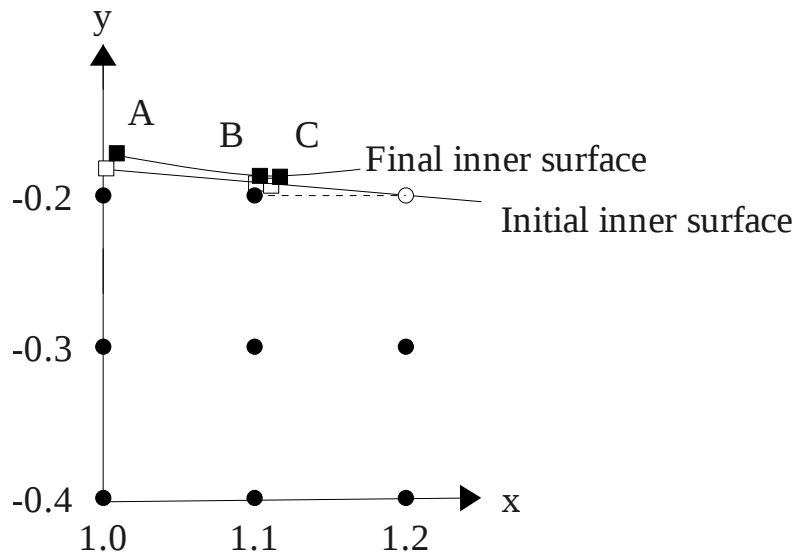


FIGURE 5.8: Configuration of lattice sites and surrounding the one at $(1.1D, -0.2D)$. The filled circles represent fluid sites, while the open circles represent solid sites. Point B on the inner surface of the wall belongs to the aforementioned lattice site and its neighbours are A and C . The open and filled squares represent the points' positions when the wall began to move and when the distance from the lattice site to the wall along the vector $(1, 0)$ became undefined. The movements of the three points have been exaggerated for clarity.

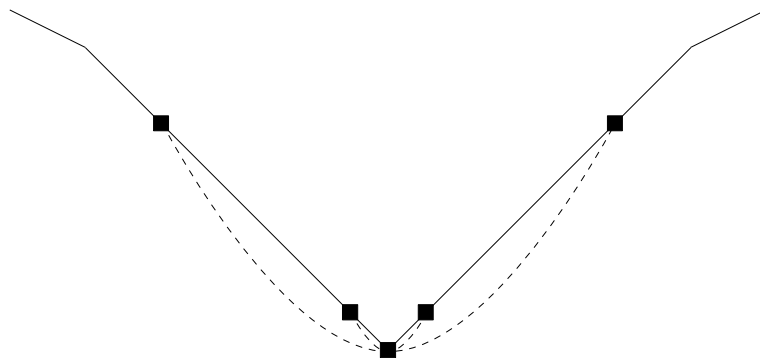


FIGURE 5.9: If an elastic wall is represented by line segments, one point is placed at the corner between them and its neighbouring points are placed on them, the radius of the circle passing through the three points is smaller if the neighbours are closer to the original point. It is therefore inappropriate to approximate the surface between a point and its neighbours as a circle.

The simulation was carried out as described in the last section ⁶. The wall was allowed to move after time $t = 7364\Delta t$. The results at this time, $t = 7371.2\Delta t$ and $t = 7371.42\Delta t$ are shown in figure 5.10. The wall does not move inwards or outwards significantly but its shape becomes smoother, which is exactly what we would expect if the steady state solution agrees with the one in figure 4 of [13]. However, point P moved 16 times further during the last $0.22\Delta t$ than it did during the $7.2\Delta t$ since the wall began to move, reaching a final y -ordinate of $-0.16353D = -1.6353\Delta x$, which shows that it was accelerating rapidly away from its equilibrium position, i.e. the simulation was unstable.

The instability occurs because the aforementioned point was initially much closer to one of its neighbours on the inner surface than the other; the initial coordinates of the point and its two neighbours on the inner surface were $(4.9849D, -2.3326 \times 10^{-3}D)$, $(4.8872D, -1.7426 \times 10^{-2}D)$ and $(5D, 0)$ respectively. The algorithm for placing the points, described in section 5.2, was modified to ensure that adjacent points on the inner surface were separated by at least $0.5\Delta x$, as described in the next paragraph. This prevented the problem described in this section. The wall profiles at $t = 7364\Delta t$ and $t = 7375\Delta t$ are plotted in figure 5.11 ⁷.

If the wall slopes gently such that it is almost parallel to a row of lattice sites and it crosses that row, the wall's normal will be almost parallel with a lattice vector. Since the separation between a lattice site and its point on the wall is perpendicular to the wall, as explained in section 5.2, the point belonging to the last fluid site in the row that the wall crosses will be very close to this fluid site and to the point belonging to the fluid site below. In figure 5.12, A is the former lattice site and B is the latter. The point on the wall that became unstable in the simulation described earlier belonged to a lattice site of type B at $(49.849\Delta x, -2.3326 \times 10^{-2}\Delta x)$ while site A was at $(50\Delta x, 0)$. The gradient of the wall was 0.1545. To remedy this situation, each point on the wall that lay less than $0.5\Delta x$ from a lattice site belonging to a neighbouring point was moved along its line segment

⁶The code for this simulation and instructions for its use may be downloaded from <http://ccs.chem.ucl.ac.uk/~gary> as a zip archive and will be in the folder "Elastic_complex_geometry_rev_176" when the archive has been unpacked. For this simulation, INCOMPRESS, INC_FLUID and MOVE_WALL were defined at compile time.

⁷The code for this simulation and instructions for its use may be downloaded from <http://ccs.chem.ucl.ac.uk/~gary> as a zip archive and will be in the folder "Elastic_complex_geometry_rev_181". For this simulation, INCOMPRESS, INC_FLUID and MOVE_WALL were defined at compile time.

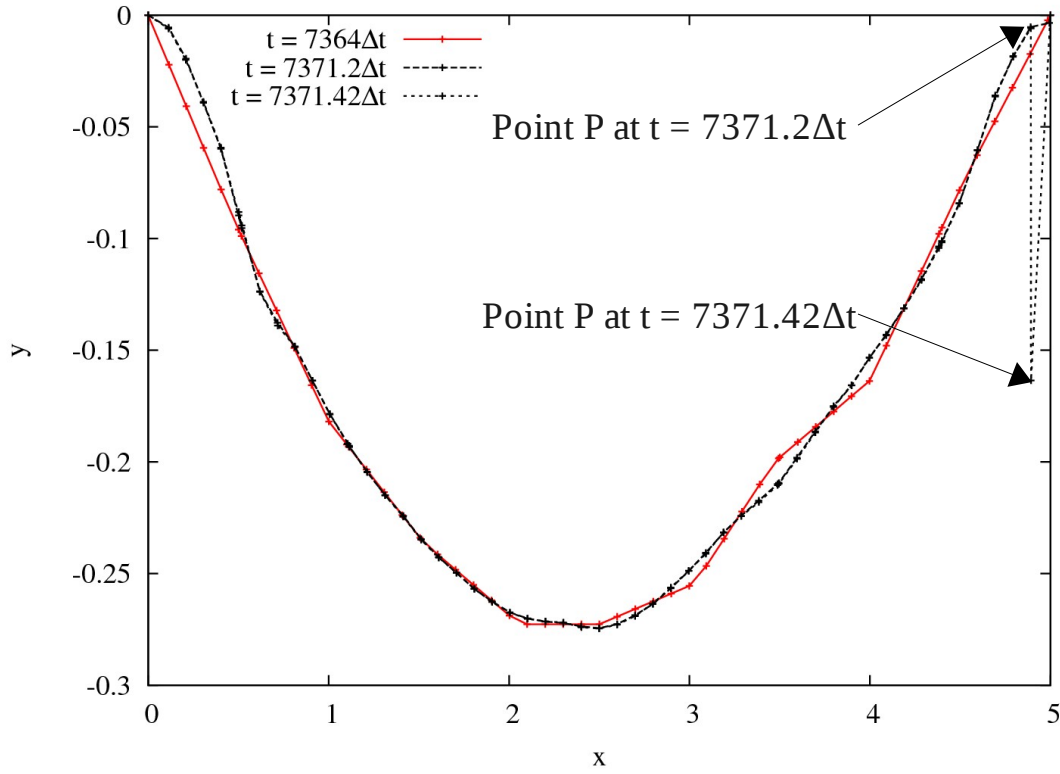


FIGURE 5.10: Profile of the inner surface of the elastic wall in a Starling resistor for which the initial state is expected to be close to the steady state. The physical parameters are $Re = 1.5$, $\eta = 10^{-3}\text{Nm}^{-1}\text{s}$, $\rho = 10^3\text{kgm}^{-2}$, $D = 10^{-2}\text{m}$, $L_{elastic} = 5 \times 10^{-2}\text{m}$, $p_e - p_d = 0.93\text{Nm}^{-1}$, $T = T_0/\beta$, where $T_0 = 1.610245\text{N}$ and $\beta = 15$. The red line shows the wall's position at the time that it began to move, $t = 7364\Delta t$, while the black dashed and dotted lines show its position at $t = 7371.2\Delta t$ and $t = 7371.42\Delta t$. Point P on the wall accelerates rapidly away from its equilibrium position, because it was initially much closer to one of its neighbours on the inner surface than the other.

until the length of projection of $(\mathbf{r}_{point} - \mathbf{r}_A)$ along the line's tangent reached $0.5\Delta x$, since we expect the spacing of points on the wall to be of order Δx .

5.5 Causes and effects of negative or undefined normalised cut distances

In this section, remaining issues with the normalised cut distances are discussed, including the effect of a negative normalised cut distance and cases in which they are undefined.

The lattice-Boltzmann computation for the Starling simulation described in the previous section became unstable at $t = 7376\Delta t$ for the lattice site at $(35\Delta x, -2\Delta x)$, i.e. some of

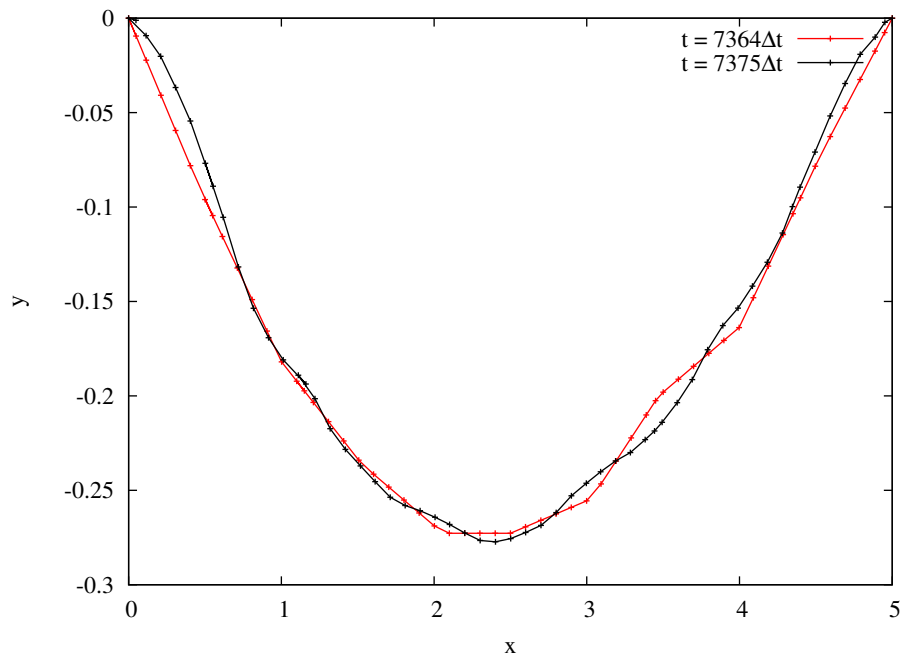


FIGURE 5.11: Simulation of the same Starling resistor as in figure 5.10, but with more evenly spaced initial points. The wall positions at $t = 7364\Delta t$ and $t = 7375\Delta t$ are represented by the red and black lines respectively.

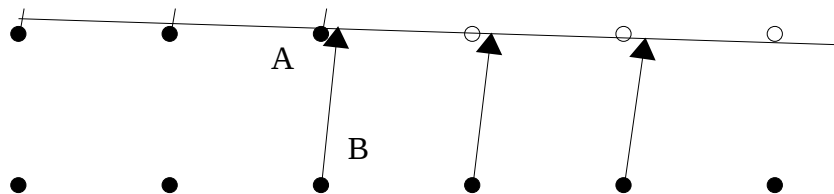


FIGURE 5.12: Configuration of lattice sites and their points on an elastic segment of the inner surface of the wall if the wall slope is gentle. The filled and open circles represent fluid and solid sites respectively. For each site adjacent to the wall, one point is placed on its inner surface. The separation between lattice sites and their points are shown by arrows. The points belonging to lattice sites *A* and *B* are much closer together than the other points.

the equilibrium distributions were negative. This site is an edge site, so the nonequilibrium extrapolation method described in chapter 3, section 2.9.5 was applied to determine the distribution functions for the lattice directions pointing away from its solid neighbours. This involved constructing the distribution functions at the solid neighbours from estimates of their velocities, densities and nonequilibrium distributions at time $t = 7375\Delta t$. The velocities are given by equation (2.204), i.e. $\mathbf{v}_b + (\delta - 1)\mathbf{v}_f + \left(\frac{1-\delta}{1+\delta}\right)(2\mathbf{v}_b(t) + (\delta - 1)\mathbf{v}_{ff})$ for $\delta < 0.75$, where $\mathbf{v}_b = \mathbf{v}(\mathbf{x}_b, t)$, $\mathbf{v}_f = \mathbf{v}(\mathbf{x}_f, t)$ etc. and f represents the edge site, w represents a neighbouring solid site, ff represents the neighbouring fluid site opposite the solid neighbour, point b is the point of intersection between the lattice vector $\mathbf{x}_w - \mathbf{x}_f$ and the wall and $\delta = \frac{(\mathbf{x}_b - \mathbf{x}_f) \cdot (\mathbf{x}_w - \mathbf{x}_f)}{|\mathbf{x}_w - \mathbf{x}_f|^2}$, from equation (2.158). For the site at $(35, -2)$ at $t = 7375\Delta t$, the x -components of \mathbf{v}_f , \mathbf{v}_{ff} and \mathbf{v}_b are $-0.08\frac{\Delta x}{\Delta t}$, $0.11\frac{\Delta x}{\Delta t}$ and $-0.04\frac{\Delta x}{\Delta t}$ respectively and $\delta = -1.19$ when the solid neighbour at $(34, -2)$ is considered. Therefore, $\mathbf{v}_w = 3.81$, which is much greater than the speed of sound $c_s = \frac{1}{\sqrt{3}}$, so the lattice-Boltzmann simulation breaks down, as explained in section 2.5. This occurs despite the fact that \mathbf{v}_f , \mathbf{v}_{ff} and \mathbf{v}_b were much less than c_s and shows that negative value of δ may cause the simulation to become unstable. From equation (2.204), we see that $\mathbf{v}_w \rightarrow \pm\infty$ in the limit as $\delta \rightarrow -1$. Figure 5.11 shows that the lattice site at $(35, -2)$ was inside the wall at time $t = 7364\Delta t$ but outside at $t = 7375\Delta t$, which caused the value of δ to be negative. The simulation shows that a small movement of the wall inwards can cause instability if it crosses a lattice site and we do not change it into a solid site.

One could allow for a certain amount of inward motion of the wall by setting lattice sites that lie within a certain distance of the wall to be solid in addition to those that lie outside. However, small outward movements of the wall may also cause problems if it crosses a row of lattice sites. For example, in figure 5.13, the wall becomes convex, so the lattice vector from site A in direction $(-1, 0)$ no longer intersects the two line segments coming from point P , which belongs to lattice site A , so its value of δ for this direction is undefined. To solve this problem, it is necessary to find the true point of intersection of the lattice vector with the wall, by searching through all the line segments of which the wall's inner surface is composed instead of extending the line segments coming from point P until they intersect the lattice vector, as explained in section 5.3. This would only solve the problem if the wall crosses the row of lattice sites again. For simulations of systems other than a Starling resistor oriented in the x -direction, this may not be the case. Therefore, it is necessary to change the lattice site types from fluid to solid or vice versa as the wall moves.

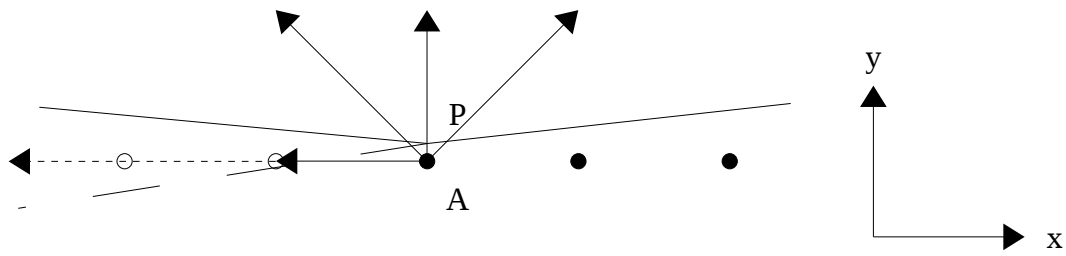


FIGURE 5.13: Configuration of lattice sites around a region of the inner surface of the wall that is initially concave (the dashed line), but becomes convex (the solid line). The filled and open circles represent fluid and solid sites respectively. Point P belongs to site A . The distances along the lattice vectors shown by arrows are required to impose the boundary conditions at site A . The distance along vector $(-1, 0)$ becomes undefined as the wall moves.

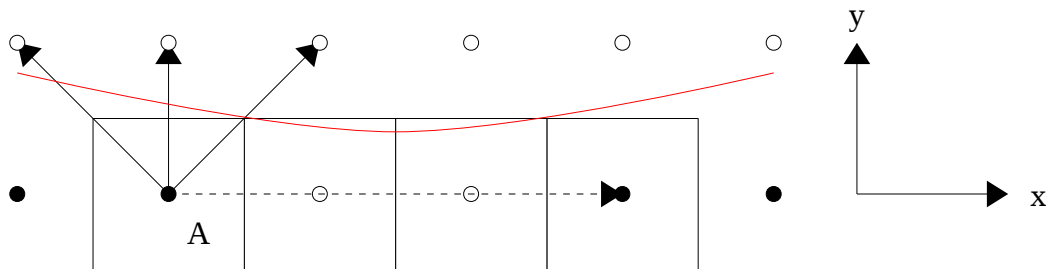


FIGURE 5.14: Configuration of lattice sites that could occur around a region of the inner surface of the wall that is convex if the rules in Fang et al. [14] are applied, i.e. a site cannot be a fluid site if the wall (shown in red) does not cross unit square centred on the site. The filled and open circles represent fluid and solid sites respectively. The distances along the lattice vectors shown by arrows are required to impose the boundary conditions at site A . The distance along vector $(1, 0)$ is undefined.

Fang et al. [14]’s method for applying no-slip boundary conditions required the normalised cut distances, like the present study, as described in section 2.9.5. Although Fang et al. [14] changed the site types as the wall moved, the normalised cut distances could have become undefined if the wall was convex, because a lattice site was only considered to be fluid if it was inside the wall and the wall did not cross the unit square on the lattice site. For example, in figure 5.14, the lattice vector from site A in direction $(1, 0)$ does not intersect the wall. The normalised cut distance in this direction is therefore undefined. In a less extreme case, the wall could cross the row of lattice sites, but the normalised cut distance to the wall, δ , may be greater than 1.5, violating their requirement that $0.5 < \delta < 1.5$.

5.6 Adaptations of the simulation method when fluid nodes are created or destroyed

In this section, I describe the changes to the procedure at each time step that are required to deal with the creation and destruction of fluid sites as the wall moves.

After the lattice-Boltzmann method had been applied, the distribution functions, f_i , at each solid lattice site are set to the average of the f_i over all neighbouring fluid sites in case that site is about to become a fluid site due to the motion of the wall during the timestep. This algorithm conserves the mass of the fluid approximately, as explained in section 5.6.4 and causes the flow fields at this site to be set to the average of the flow fields of the surrounding fluid sites when it becomes a fluid site. The equation of motion of the wall is then integrated as usual.

Some of the lattice sites are changed from solid to fluid, or vice-versa, as appropriate to the new wall profile. For each lattice site, an array of neighbouring site types has always been maintained throughout the simulation because it was needed at the edge sites in order to apply the boundary conditions and it is now needed for the solid sites in order to set their distribution functions. This array of neighbouring site types is updated after the site types have been set. As before, a site is an edge site if one or more of its neighbours that lie on the same side of the inlet or outlet plane are solid. The array of neighbouring sites is used at every time step to determine whether this is the case.

At the beginning of the simulation, there is one point on the wall for each edge site. The number of points on the wall remains constant, but, since fluid nodes are created or destroyed, the number of edge sites may change, so there is no longer exactly one pair of wall points for each edge site. Each point on the inner surface of the wall requires the stress at a fluid lattice site. Therefore, the next stage in the procedure is to search for the nearest fluid site. Since the lattice-Boltzmann simulation is only valid if the wall moves by less than one lattice length in a timestep, it is expected that the lattice site that was used at the last time step or at least one of its neighbours will be fluid. Therefore, the search is only carried out among these lattice sites in order to minimise the computational cost of this step. The simulation exits if a fluid site is not found.

Finally, a wall point is assigned to each edge site so that its displacement at different times may be used to apply the lattice-Boltzmann boundary condition at the edge site, as explained in section 5.1 and section 4.2.2. The following algorithm is used to avoid searching through all the points to find the nearest one for every edge site. The inner surface of the wall is traversed from one end to the other and the types of lattice sites immediately surrounding each line segment of the wall formed by joining a point on the inner surface to its nearest neighbour on the same surface are checked, i.e. the lattice sites for which

$$\min(x_0, x_1) - \Delta x \leq x \leq \max(x_0, x_1) + \Delta x, \quad (5.10)$$

$$\min(y_0, y_1) - \Delta x \leq y \leq \max(y_0, y_1) + \Delta x \quad (5.11)$$

are checked, where (x, y) are the coordinates of a lattice site and (x_0, y_0) and (x_1, y_1) are the coordinates of the points on the wall. An example of this is shown in figure 5.15. For each edge site that is found, the position of the wall point that was assigned to the site at the previous timestep is compared with the positions of the wall points at the ends of the line segment. The nearest of these three points on the inner surface of the wall is assigned to that lattice site. This procedure requires a list of the indices of the points on the inner surface of the wall as it is traversed from one end to the other. This ordered list is set up at the beginning of the simulation.

5.6.1 Algorithm for updating the site types

If a fluid lattice site has some solid neighbours at time t , we know that the wall's inner surface intersects the lattice vectors from the fluid site that point towards those neighbours, but not those that point towards the other neighbours. When the position of the wall at time $t + \Delta t$ has been determined, we can determine which of the lattice vectors are intersected by its inner surface at time $t + \Delta t$. From this information, we can establish whether the wall's inner surface has crossed the lattice site. If it has, the site now lies outside this surface, so it becomes solid. The same argument applies for establishing whether a solid site that has some fluid neighbours should become a fluid site.

I devised a number of tests for the algorithm that updates the site types, which involved a fluid site surrounded by different combinations of fluid and solid neighbours and different

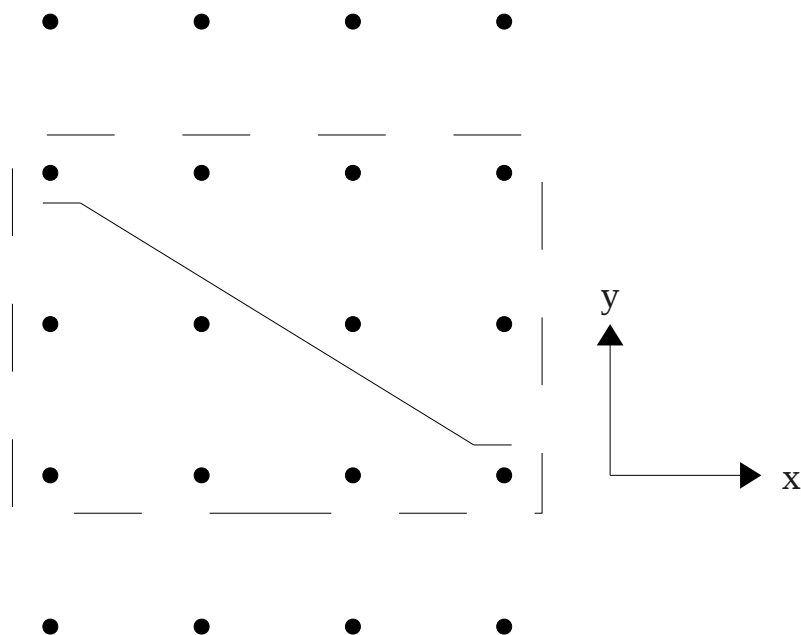


FIGURE 5.15: In order to find the nearest wall point to each edge site or to find the distances from lattice sites along their vectors to the points of intersection with the wall, the lattice sites immediately surrounding the line segment that joins a point on the wall to its neighbour are checked. The circles represent lattice sites. Those that need to be checked when we look at the central line segment (the solid line) are inside the dashed rectangle.

wall configurations. This set of tests was expanded to include cases in which an algorithm failed to updated the site types correctly during some preliminary simulations, which are not reported here, despite having passed the existing tests. The final set of seventeen test cases are shown in figures 5.16 and 5.17. The same set of tests with the opposite site types was carried out to check that the algorithm changes a solid site to a fluid when appropriate. The tests do not include sets of configurations that are rotations of one another because the algorithms are symmetric under rotation. For all the algorithms tested, if the wall's inner surface passed through a lattice site, that site was defined to be a fluid site.

Three algorithms were tested. For the first one, the lattice site type is changed if some of the links joining this site to neighbouring sites of the same type are intersected by the wall's inner surface and either there are no neighbours of the opposite type or the links joining this site to neighbours of the opposite type are not cut, because this shows that the fluid site is now on the same side of the wall as sites of the opposite type. This method

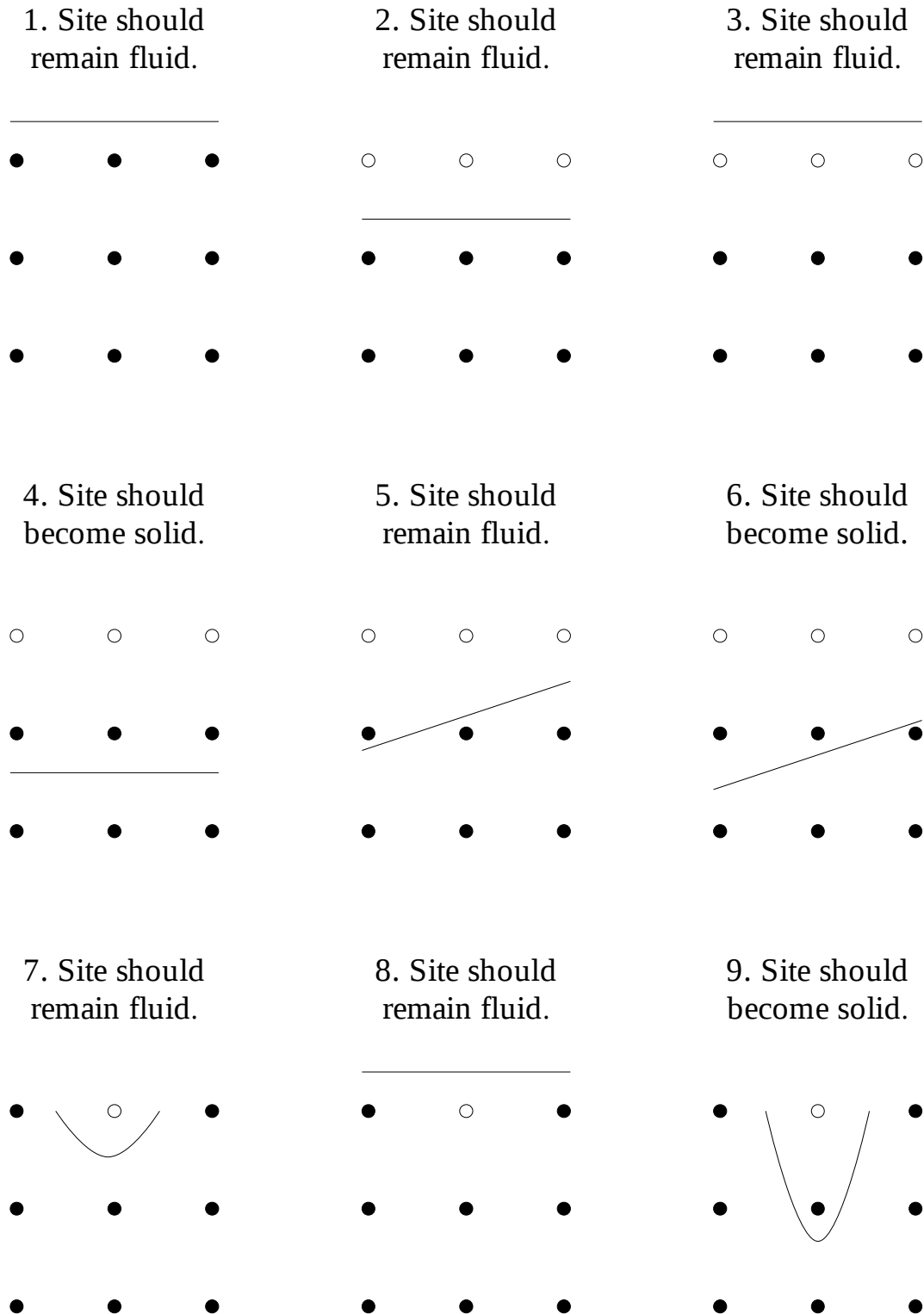
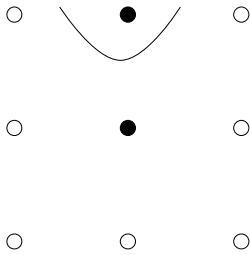
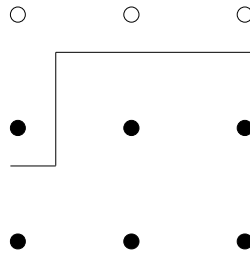


FIGURE 5.16: The first nine of seventeen tests for the algorithm that changes lattice sites from fluid to solid or *vice versa*. Each test consists of a central fluid site, its neighbours and a part of the inner surface of the wall that passes nearby, which is represented by a solid line. The filled and open circles represent fluid and solid sites respectively.

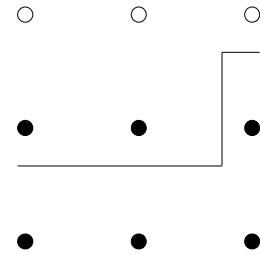
10. Site should become solid.



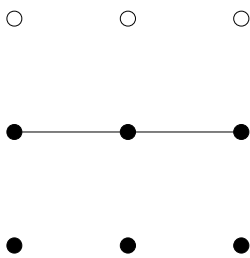
11. Site should remain fluid.



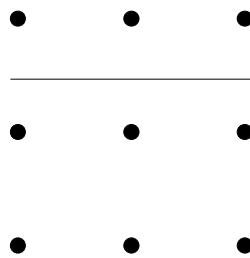
12. Site should become solid.



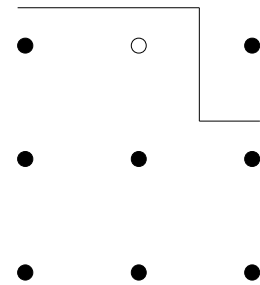
13. Site should remain fluid.



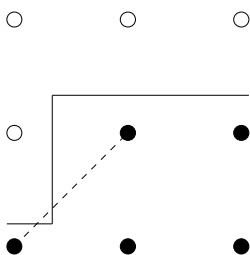
14. Site should remain fluid.



15. Site should remain fluid.



16. Site should remain fluid.



17. Site should become solid.

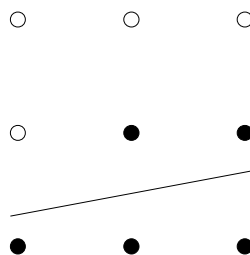


FIGURE 5.17: The last eight of seventeen tests for the algorithm that changes lattice sites from fluid to solid or *vice versa*. Each test consists of a central fluid site, its neighbours and a part of the inner surface of the wall that passes nearby, which is represented by a solid line. The filled and open circles represent fluid and solid sites respectively. For case 16, the link, shown by the dotted line, from the central fluid site to one of its neighbours, is cut twice by the inner surface of the wall.

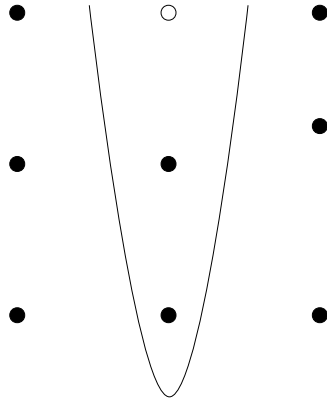


FIGURE 5.18: The algorithm that changes lattice sites from fluid to solid or *vice versa* will fail in this test case because the wall has moved by more than one lattice site during one timestep. The solid line shows the new position of the wall's inner surface. The filled and open circles represent fluid and solid sites respectively.

works for all cases except 14 and 15. For the second algorithm, the site type is changed if there exist some links that point towards neighbours of the same type and in the opposite direction to neighbours of the opposite type and the wall's inner surface intersects all of these links. It works for all but the last test case. The final algorithm, which I have used for the remaining simulations in this chapter, is a refinement of the second: the site type is changed if there exists one link that fits the description in the last sentence and the wall intersects it or if there exist two or more of these links and the wall's inner surface intersects two or more of them. This algorithm works in all seventeen test cases.

In test case 16, the lattice vector in direction $(-1, -1)$ points towards a fluid site but away from a solid site, but from the diagram it is clear that we should not change the central site to a solid site. This is why the wall's inner surface is required to intersect two or more of the links of this type before the central site should be changed. The algorithm will fail if we have two or more of these double intersections, but this can only occur if the wall bends by more than 90° over a distance of the order of the lattice spacing. It may also fail if the wall moves by more than one lattice length in one timestep, as shown in figure 5.18, but we already forbid this. A lattice site should never be completely surrounded by sites of the opposite type. If this happens, the simulation exits.

If the simulation method is to be extended to 3D, an algorithm is needed to determine whether the wall has crossed a particular lattice site given the set of lattice vectors that

the wall intersects, as in the 2D case. However, the algorithm may be different from the one used in 2D and more test cases would be required to check it.

5.6.2 Algorithm for calculating the normalised cut distances

Since the site types are now updated according to the position of the wall at every lattice-Boltzmann timestep, the links between a fluid site and a neighbouring solid site are always intersected by the wall. Therefore, normalised cut distances cannot be greater than one or negative, i.e. $0 < \delta < 1$, unlike the situation in which the lattice site types are not updated. The normalised cut distances along all other links are irrelevant for applying the boundary conditions at the edge sites since the wall does not pass through them. For the same reason, they are also irrelevant for updating the lattice site types. Therefore, the normalised cut distances along all links are first set to an undefined value. The inner surface of the wall is then traversed from one end to the other and the lattice sites immediately surrounding each line segment of the wall formed by joining a point on the inner surface to its nearest neighbour on that surface are identified, as described by equations (5.10) and (5.11) and figure 5.15. If one of the links between a lattice site and its neighbours is cut by the line segment, the distance from that lattice site along the link to the point of intersection is calculated. If a link is cut twice, as shown by case 16 of figure 5.17, the normalised cut distance will depend on the order in which the points on the wall are traversed. However, this is not important because in that case, the sites at the ends of this link will either both be fluid or both be solid, so the normalised cut distance will not be used to apply the boundary condition.

5.6.3 Extrapolation of the stress

The method for extrapolating to find the stress at the inner wall that is described in section 4.4 will fail in certain cases. For example, if the wall is approximately parallel to the x -direction, but the separation between a point on the wall, n , and its edge site, f , has a nonzero x -component, the neighbouring fluid site will be chosen such that $\mathbf{x}_f - \mathbf{x}_{ff}$ is one of the diagonal directions. The lattice link between sites f and p , where site p is defined by $\mathbf{x}_p - \mathbf{x}_f = \mathbf{x}_f - \mathbf{x}_{ff}$, may not be intersected by the wall, so the normalised cut distance for this link at site f may remain undefined, as explained in section 5.6.2. This

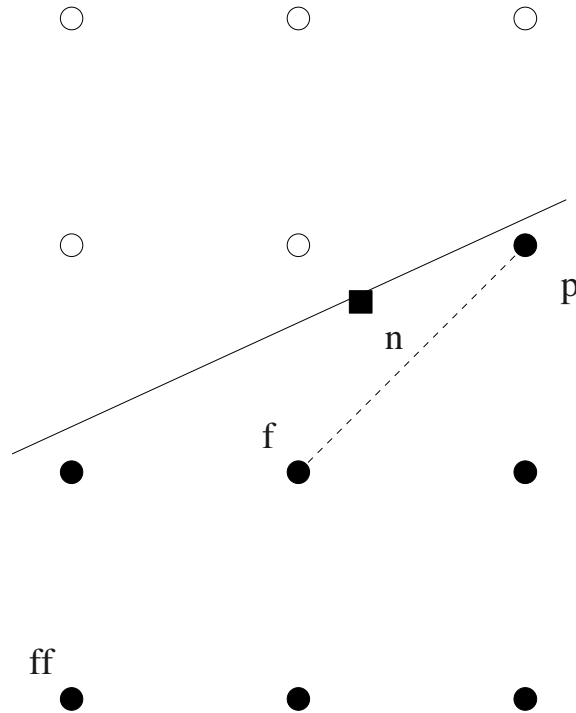


FIGURE 5.19: If the stress at a point on the wall, n , is estimated as described in section 4.4, the method will fail in the case shown above since site f for its choice of site ff , the normalised cut distance, δ , for the link from site f to site p is not intersected by the wall, so δ remains undefined, where site p is defined by $\mathbf{x}_p - \mathbf{x}_f = \mathbf{x}_f - \mathbf{x}_{ff}$. The solid line is the inner surface of the wall, the filled circles are fluid sites and the open circles are solid sites.

is illustrate in figure 5.19. To avoid this problem, the stress tensor at a point on the inner surface is set to the stress tensor at the nearest fluid lattice site.

5.6.4 Conservation of mass

We can show analytically that the mass is conserved as lattice sites are created or destroyed for fluid that is contained in a channel with the walls moving at velocity \mathbf{v} and that is not driven by body forcing or a pressure gradient [14] as follows. For the purposes of this discussion, we will refer to a solid site that has a fluid neighbour as a boundary site and any other solid site as a solid site. In the discussions of the boundary condition, this site is labelled w in figures 3.4 and 4.2.

After a period of time, all fluid nodes have density ρ_0 and velocity \mathbf{v} and the same, time-independent distribution functions, f_i . The boundary sites also have these distribution functions. Without loss of generality, we assume that $v_y < 0$. We consider the mass of the fluid arriving at and leaving a boundary site between time t_0 , when it becomes a boundary site, and t_1 , when it becomes a fluid site. The boundary sites we consider are shown in figure 5.20.

For a flat wall, we only need to consider site A , since all boundary sites will be of this type. Recalling that all fluid and boundary nodes share the same and time-independent distribution functions, f_i , the increment in density at site A during one timestep of length Δt , is

$$d\rho = f_4 + f_7 + f_8 - f_2 - f_5 - f_6 = -\rho_0 v_y \quad (5.12)$$

where we have used equations (2.2) and (2.3) for the D2Q9 lattice-Boltzmann model and taken $\Delta x = \Delta t = 1$. The density at time t_1 is given by

$$\rho_A(t_1) = \sum_{t=t_0}^{t_1} d\rho_0 v \Delta t = \rho_0, \quad (5.13)$$

since the wall must move one lattice length between times t_0 and t_1 . When the boundary node becomes a fluid node, the density will be ρ_0 , since each distribution function is set to the average of those at the surrounding fluid sites. Therefore, no perturbation occurs when site A becomes a fluid site. A similar result can be obtained for the reverse process. Therefore, the total mass of fluid at the fluid sites at time t_0 is equal to that at t_1 because the number of fluid sites is the same at these times. Although this total is different at other times because the number of fluid sites varies, the mass is conserved if one takes into account the mass of the fluid that accumulates at the boundary sites.

For a nonflat wall, a given site will be of type C when it first becomes a boundary site, then type B , then A , then D ; such sites are illustrated in figure 5.20. The streaming between boundary nodes B and D must also be considered to ensure that the increase in density on node B behaves the same as the other nodes. The density increment for site B

during one timestep is then given by equation (5.12). For nodes C and D , we have

$$\begin{aligned} d\rho_D &= f_1(\mathbf{x}_D - \mathbf{e}_1) + f_4(\mathbf{x}_D - \mathbf{e}_4) + f_5(\mathbf{x}_D - \mathbf{e}_5) + f_7(\mathbf{x}_D - \mathbf{e}_7) \\ &\quad + f_8(\mathbf{x}_D - \mathbf{e}_8) - f_2(\mathbf{x}_D) - f_3(\mathbf{x}_D) - f_5(\mathbf{x}_D) - f_6(\mathbf{x}_D) - f_7(\mathbf{x}_D) \end{aligned} \quad (5.14)$$

$$= f_1 + f_4 + f_8 - f_2 - f_3 - f_6 \quad (5.15)$$

$$d\rho_C = f_8 - f_6 \quad (5.16)$$

The total increment in density of sites C and D is

$$d\rho = f_4 + f_7 + f_8 - f_2 - f_5 - f_6 + f_1 + f_5 + f_8 - f_3 - f_6 - f_7 = \rho_0(v_x - v_y). \quad (5.17)$$

If we set $v_x = 0$, we obtain equation (5.12) again. Since it applies throughout the downward movement of the wall through one lattice length, the mass entering the wall is equal to ρ_0 and therefore no perturbation occurs when a boundary site becomes a fluid site. For the case with $v_x \neq 0$, we may have to consider the streaming of the distribution functions between neighbouring boundary sites.

In the case where the density of the fluid varies in space, it is much more difficult to calculate the net mass of fluid entering the wall to justify the distribution functions that we set at a newly created fluid site. However, since we apply Zhao-Li et al. [10]'s method at the boundaries, which is described in section 2.9.5, the calculation of the distribution function at a boundary site that points towards a fluid site is calculated from the density at that fluid site, f . In the case where $\mathbf{v} \ll \frac{\Delta x}{\Delta t}$ and $f_i^{(neq)} \ll f_i^{(eq)}$ in the fluid, that distribution function $f_i \propto \rho$ and the same applies for the distribution functions coming from the fluid. Therefore, the net mass of the fluid entering the wall is the average of the densities of the fluid sites surrounding a boundary site multiplied by Δx^2 . Consequently, setting each f_i at the boundary site to the average value of f_i at the surrounding fluid sites gives rise to the correct mass of the fluid. This argument does not take into account the changes in the number of fluid neighbours over time, but provides some justification for setting the distributions as described above and would be correct in the case of a flat wall, where every boundary site always has three neighbours.

The boundary condition method described in Fang et al. [14] and section 2.9.5 uses a second-order extrapolation of the density to calculate the distribution functions that

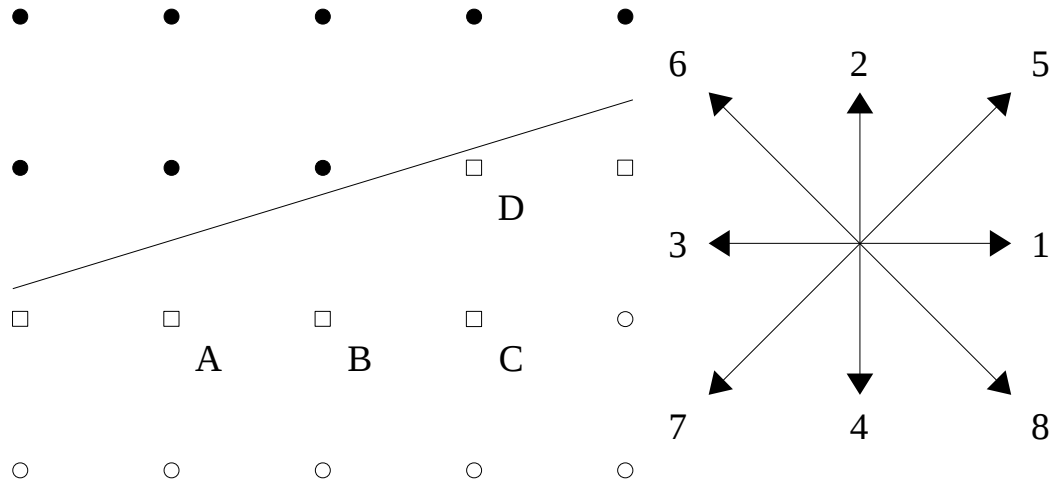


FIGURE 5.20: The configuration of lattice sites around a nonflat vessel wall. The filled circles represent fluid sites; the open squares represent sites that are solid but have fluid neighbours, which are defined as boundary sites in section 5.6.4; and the open circles represent solid sites. For the boundary sites, there are four possible combinations of neighbouring fluid sites. The boundary sites with these combinations are labelled *A*, *B*, *C* and *D*. The indexing of the lattice links is shown on the right hand side of this figure.

stream from boundary sites to fluid sites, so using the argument above, the mass of the fluid leaving the wall is the average of the extrapolated values of the densities over all directions pointing towards the fluid sites. If the same were true for the mass of the fluid entering the wall, then setting each f_i to the average of the extrapolated values over all directions pointing towards fluid sites, as in [14], which would give rise to the correct density. They have shown that it gives rise to the correct density in the case where the density and velocity of the fluid are constant. They calculated the amount of mass in the unit square that each boundary site is responsible for, which was centred on the boundary site, as described in section 2.9.5. They used this calculation to check the conservation of mass for by running simulations in cases in which the density varied in space and the velocity of the wall varied with time. This would be more difficult in the current study, since there is no straightforward definition of the area that a boundary site is responsible for.

5.7 Results for a Starling resistor with a large wall displacement

In this section, results are presented for a Starling resistor in which the wall is expected to move by several lattice lengths during the simulation ⁸. The parameters mostly matched those used in [11] and section 4.7, i.e. $\frac{TD}{\eta Q} = 10^5$, $L_u = 2D$, $L_e = 10D$, $L_u = 2D$. The density of the wall was $\rho_w = 4000\rho_f$, which leads to $\Gamma = 2.48\Delta t$ (from equation (4.81) and $\Lambda = 3162\Delta t$ from equation (4.89)). For each lattice-Boltzmann timestep, 250 timesteps were used for the elastic wall, i.e. $\Psi = 250$, which satisfies the requirement that $\Gamma\Psi \geq 250$ described at the end of section 5.1. The parameters also satisfy the requirement that $\Lambda > \frac{L_e}{c_s}$. The resolution was chosen such that $D = 10\Delta x$ and the thickness of the wall, $h = 0.25\Delta x$. The dimensionless relaxation parameter, $\tau = 0.56$ and $Re = 1.5$. The external pressure is given by $p_e - p_d = 0.0058125$ in lattice units, therefore, $\Delta p^* = (p_e - p_d) \left(\frac{D^2}{\eta Q} \right) = 1453.125$, much higher than highest value the value of $\Delta p^* = 224$ used in section 4.7. If we let $\Delta x = 5 \times 10^{-4}\text{m}$, $\Delta t = 1.25 \times 10^{-3}\text{s}$ and $\rho_f = 1000\text{kgm}^{-2}$ in physical units, the kinematic viscosity $\nu = 4 \times 10^{-6}\text{m}^2/\text{s}$ and $D = 5 \times 10^{-3}\text{m}$, which are in the regime of typical parameters for cerebral blood flow, described in section 1.6. We also obtain $p_e - p_d = 0.93\text{N/m}$, which matches that used in [13] and section 5.3. The tension, $T = 0.32\text{N}$, which corresponds to $\beta = 5.032$.

The simulation was set up as in described in chapter 4, section 4.7 and the wall was initially flat, since it was no longer necessary to begin the simulation close to the expected steady state because the method can cope with wall movements of several lattice lengths. Furthermore, initialising the wall in that way also has the effect of creating a fairly abrupt change in thickness near the ends of the wall, as shown in figure 5.6, which may cause waves in the thickness of the wall with large amplitudes that might hinder the convergence of the simulation. The wall was held in position until the fluid had converged, as described in section 5.2. For the simulation described here, the wall was allowed to move after $t = 7740\Delta t$, and the simulation was stopped at time $t = 25000\Delta t$. These two times are separated by more than five times the free period of oscillation of the wall.

⁸The code for this simulation and instructions for its use may be downloaded from <http://ccs.chem.ucl.ac.uk/~gary> as a zip archive and will be in the folder “Elastic_complex_geometry_rev_215” when the archive has been unpacked. For this simulation, INCOMPRESS, INC_FLUID and MOVE_WALL were defined at compile time.

The displacement of the point that began at the centre of the inner surface of the wall over time is shown in graph 5.21. The amplitude of the oscillation of this point decreases due to the damping of the fluid, as we would expect. However, the oscillation becomes less sinusoidal over time and the period of oscillation, estimated by measuring the times between the peaks, is not constant, unlike the simulations in section 5.1.3. This may be due to increasing amounts of noise due to an instability. The periods of the first four oscillations are $3380\Delta t$, $3570\Delta t$, $3150\Delta t$ and $3680\Delta t$. Three of these are slightly longer than Λ , in contrast to the simulations in section 5.1.3. However, we would expect different behaviour of the model since the simulation method is now significantly different, most notably by the creation and destruction of fluid nodes.

The wall profile was checked at intervals of approximately one quarter of the apparent period of oscillation. Figures 5.22 and 5.23 show the wall shape during the first and fourth period respectively. From these, it is clear that the entire wall moves inwards or outwards together, as we would expect for simulations at a low Reynolds number.

The results in this section indicate that the model appears to behave correctly in the early stages of simulations in which the wall displacement is several lattice points. However, increasing amounts of noise suggest that an instability is present. The noise may be due to an assumption that is made when the no-slip and no-penetration boundary conditions are applied to the fluid: The velocity of the wall at a point of intersection, b , of the wall and the lattice link from an edge site is assumed to be equal to the velocity of the point on the wall, n , that belongs to the lattice site, as explained at the beginning of section 4.2.2. Further work is required to check this and to validate the dynamics more rigorously by raising Re to 300 to compare the results with those in figure 4 of [15].

5.8 Computational cost of the simulation

The computational cost of the simulation method developed in this chapter is discussed in this section.

First, the wall clock time required to simulate one lattice-Boltzmann timestep for a Starling resistor for which the wall moves at all times, was compared with the same quantity for a channel with rigid walls with the same dimensions and flow parameters. The parameters

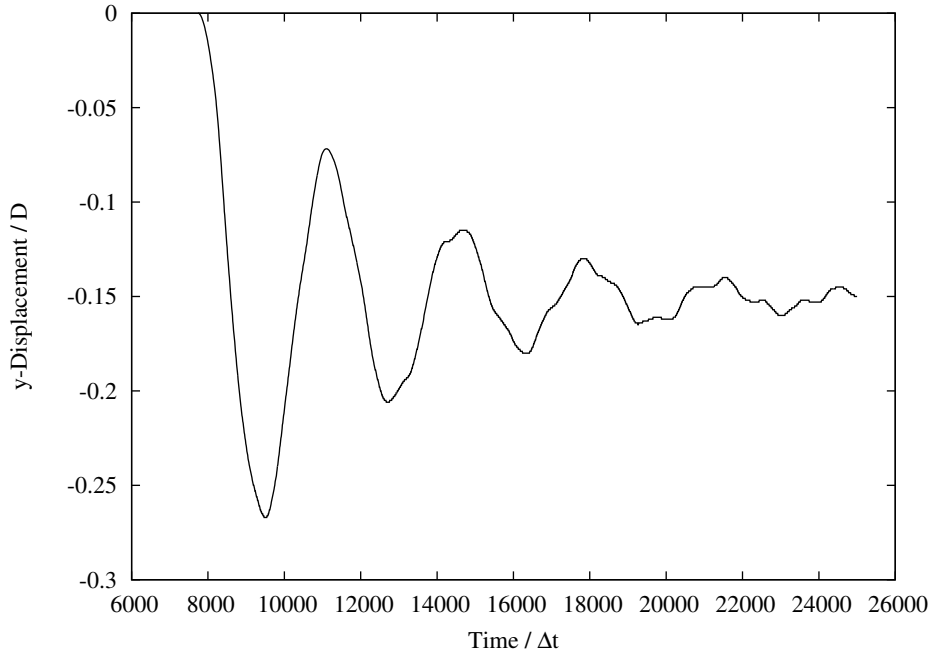


FIGURE 5.21: Displacement of the central point on the wall in the y -direction over time for a simulation of a Starling resistor with the parameters used in [11], except for the external pressure, which is given by $(p_e - p_d) \left(\frac{D^2}{\eta Q} \right) = 1453.125$. We have $\frac{TD}{\eta Q} = 10^5$ and the lengths of the upstream and downstream rigid sections and the elastic section are $L_u = 2D$, $L_d = 2D$, $L_e = 10D$. The resolution is given by $D = 10\Delta x$, the wall thickness, $h = 0.25\Delta x$, $Re = 1.5$ and $\tau = 0.56$. If we let $\Delta x = 5 \times 10^{-4}\text{m}$, $\Delta t = 1.25 \times 10^{-3}\text{s}$ and $\rho_f = 1000\text{kgm}^{-2}$ in physical units, $p_e - p_d = 0.93\text{N/m}$, which matches that used in [13], and $T = 0.32\text{N}$, which corresponds to $\beta = 5.032$. The central point performs oscillations that are damped by the viscosity of the fluid. However, the amount of noise appears to increase over time, suggesting that there is an instability. This may be due to an assumption that is made when the no-slip and no-penetration boundary conditions are applied to the fluid.

were the same as those used in section 5.7. The flow fields and distribution functions that had been obtained from the simulation in that section at the time the flow fields had converged, i.e. at $t = 7740\Delta t$, were used to initialise the simulation of the Starling resistor in this section so that the wall would be allowed to move immediately. For the simulation of the channel with rigid walls, the tolerance for the convergence criterion was set to zero so that the simulation would continue until the required number of timesteps had been carried out. For both simulations, the compiler option `-O3` was used to compile the code, but OpenMP [123] was not used to parallelise the program, in contrast to the simulations in section 3.6. The wall clock time was measured by taking the difference in the return values of the function `time()` from the standard C library at the beginning and end of the simulation. No information about the flow fields was written to output files during the

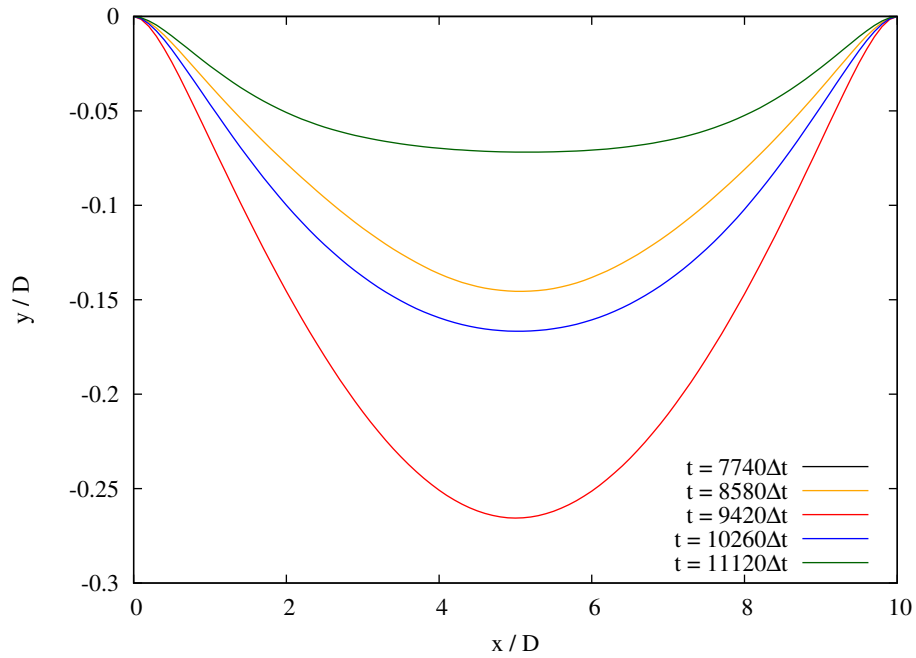


FIGURE 5.22: Wall profiles for a Starling resistor with the same parameters as those used for figure 5.21 at intervals of time separated by one quarter of the apparent period of oscillation of the wall during its first period of oscillation. The entire wall moves inwards or outwards together and there are no points of inflexion.

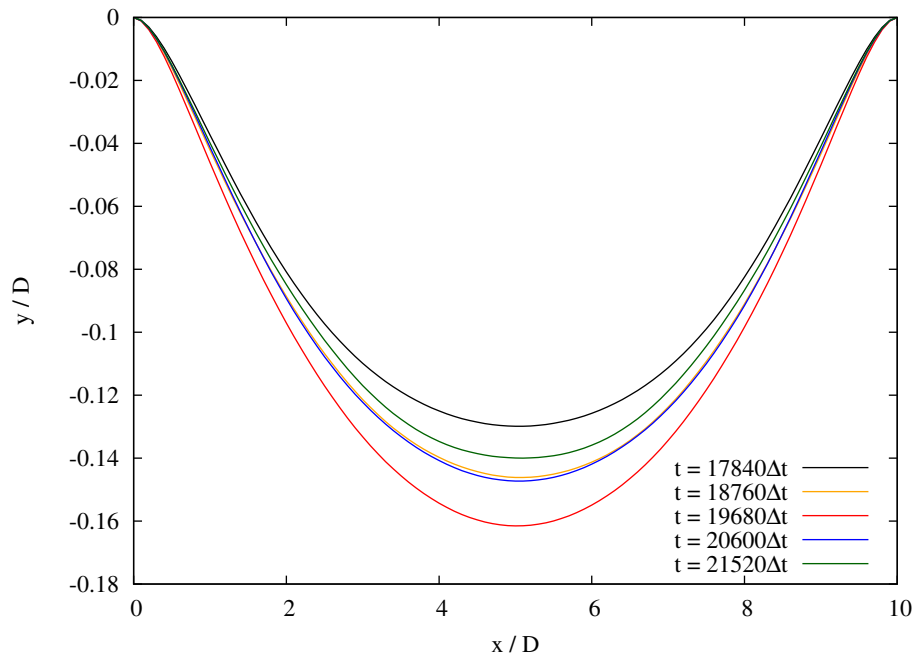


FIGURE 5.23: Wall profiles for a Starling resistor with the same parameters as those used for figure 5.21 at intervals of time separated by one quarter of the apparent period of oscillation of the wall during its fourth period of oscillation. The entire wall moves inwards or outwards together and there are no points of inflexion.

two simulations.

The simulations with rigid and elastic walls took 173 ± 1 s for 5×10^5 timesteps and (1145 ± 1) s for 10^4 timesteps respectively; therefore they took $(3.46 \pm 0.02) \times 10^{-4}$ s and $(1.145 \pm 0.001) \times 10^{-1}$ s per lattice-Boltzmann timestep respectively. For this simulation, the computational cost is a factor $C = 331 \pm 2$ higher when elastic walls are used compared with rigid walls. This factor is much greater than that for the method for simulating an axisymmetric system described in chapter 3 and for which $C = 1.17$, as shown in section 3.6. However, the 2D Starling resistor that I have simulated differs significantly from the 3D simulations carried out in chapter 3, as explained in section 4.7.4. Furthermore, the computational cost depends strongly on the simulation parameters, as discussed in the next paragraph.

The calculations required for moving the wall are expected to require a time

$$\gamma_e \propto \Psi \frac{L_e}{\Delta x} \quad (5.18)$$

per timestep, since the number of moving points on the elastic wall is proportional to its length. For the simulation of the fluid itself, we have

$$\gamma_f \propto \frac{LD}{\Delta x^2}, \quad (5.19)$$

where L is the total length of the channel, i.e. $L = L_u + L_e + L_d$. The ratio of the computational cost of a simulation with elastic walls to that of the same simulation with rigid walls is given by

$$\Phi = \frac{\gamma_f + \gamma_e}{\gamma_f} = 1 + k \frac{\Psi L_e \Delta x}{LD}, \quad (5.20)$$

where k is a constant which we can determine from the results in this section. Since $C = 331$, $L_e = 100\Delta x$, $L = 140\Delta x$ and $\Psi = 250$, $k = 18.48$. Since we must satisfy equation (5.6) for the simulation to be stable, we have

$$\Phi_{min} = 1 + 18.48 \frac{L_e \Delta x}{LD} \left(\max \left(1, \frac{250}{\Gamma} \right) \right). \quad (5.21)$$

Substituting equation (4.81) into this gives

$$\Phi_{min} = 1 + 18.48 \frac{L_e \Delta x}{LD} \left(\max \left(1, \frac{125}{\pi h} \sqrt{\frac{E}{\rho}} \right) \right). \quad (5.22)$$

The computational cost can be compared with the simulation in chapter 3 as follows. Following the arguments in section 5.1.1, the period of the oscillation of a point on the inner surface and its corresponding point on the outer surface should obey equation (4.81) in 3D as well as in 2D, and equation (5.6) should still apply, giving rise to equation (5.22). We should note that the dimensions of both ρ and E are different in 2D and 3D. The computational costs of both the lattice-Boltzmann method (LBM) and the method for dealing with the elasticity would be higher in 3D than in 2D. We assume that the ratio of the computational cost of the latter at each point on the wall that of the LBM at each lattice site is the same in 2D and 3D. We then need to replace L_e with $2\pi R_0 L$ in equation (5.22), where R_0 is the radius of the cylinder before deformation, since the number of pairs of points on the wall depends on the surface area of the cylinder and the elastic section takes up the entire length of the cylinder. The number of lattice sites is approximately $\pi R_0^2 L$ instead of LD . Making these replacements gives:

$$\Phi_{min} = 1 + 36.96 \frac{\Delta x}{R_0} \left(\max \left(1, \frac{125}{\pi h} \sqrt{\frac{E}{\rho}} \right) \right). \quad (5.23)$$

Substituting the parameters used in section 3.6 into this, i.e. $R_0 = 20\Delta x$, $h = 4\Delta x$, $\rho = 7.8$ and $E = 0.043$ in lattice units, we obtain $C = 2.848$. The computational cost is therefore expected to be more reasonable for realistic blood flow parameters than for simulations of Starling resistors, but it is higher than that of the simple method described in chapter 3.

5.9 Computational issues regarding simulations of fluid flow through large elastic systems on multicore machines

In this section, I discuss the simulation of fluid flow through large elastic systems using the methods developed in chapters 3 to 5, including how they could be parallelised to run on

multicore machines, the amount of communication required between the processors and the memory requirements.

The lattice-Boltzmann method was used for all simulations of fluid flow in this thesis because it is much more suitable for computation on multicore machines than finite-element or finite-volume fluid solvers, mainly because the distribution functions at each lattice site only require information from its nearest neighbours, as described in section 2.2, which reduces the amount of communication between neighbouring processors. Furthermore, it can take place on a simple Cartesian grid, whereas mesh generation for continuum solvers is a complicated process. This advantage becomes even more important in simulations with moving boundaries because the mesh would need to be constantly updated for a continuum solver. Since the lattice sites are divided among the processors at the beginning of the simulation, the communication costs can be further reduced by setting up buffers to store information that is sent to or received from neighbouring processors and by partitioning the domain such that each processor deals with the same number of lattice sites, as explained in section 2.3. Applying these techniques minimises the communication costs and therefore results in a linear speed up as the number of processors used to run the simulation is increased.

For all simulations of fluid flow through elastic systems in this thesis, a boundary condition method based on that by Zhao-Li et al. [10] and described in sections 2.9.5 and 3.3, was applied at the lattice sites adjacent to the wall. For each distribution function that is determined this way, this method requires the pressure, velocity and one of the pre-collision distribution functions from a neighbouring fluid site. This information can be communicated along with the distribution functions during the streaming step.

For the simulation method developed to deal with fluid flow in axisymmetric elastic systems, each point on the wall belongs to a particular edge site, as described in section 3.5. Therefore, when the lattice sites are divided between the processors, each edge site can be allocated to the same processor as its lattice site. Furthermore, each point moves independently of the others. Therefore, no more communication between processors is required for this method than for simulations with rigid walls. Since no fluid nodes are created or destroyed, the aforementioned techniques for running the simulation in parallel could be applied.

The method developed in this chapter, parts of which are the same as that described in the previous chapter, is more complex. Consequently, it would be more challenging to develop an efficient parallel computation from it for several reasons. These problems are explained, along with some possible solutions, in the following paragraphs.

Firstly, several communication steps would be needed during each lattice-Boltzmann timestep and each elastic wall timestep. Each point on the wall requires information from its nearest neighbouring points twice during each timestep because the displacement of every point must be calculated before the velocity of any of them can be, as explained in section 4.2.2. The lattice-Boltzmann timestep must also be complete before the wall moves because the stress at the boundary at the beginning and end of the timestep is required for the calculation of the wall motion. When it is complete, the distribution functions at each solid site with fluid neighbours are set in case that solid site becomes a fluid site, as explained in section 5.6. The positions of the wall point at the end of each time step are needed to calculate the lattice sites' normalised cut distances, as explained in section 5.6.2, and to find their nearest wall points, for which the velocity is used to find the distribution functions at each edge site, as explained in section 4.2.2. This information must be passed to the lattice sites before the next time step begins. In order to determine whether a lattice site needs to change from being fluid to solid or *vice versa*, the neighbouring site types before the update are required, as explained in section 5.6.1, which necessitates another communication step. When this update is complete, another communication is needed to determine which lattice sites are edge sites. Some of these communication steps are independent and could be done concurrently to reduce the computational cost, for example the distribution functions at each solid site could be set at the same time as each site checks whether each of its neighbours are fluid or solid.

Secondly, since lattice sites are created or destroyed, the number of lattice sites that pass information from their processor to neighbouring processors would change during the simulation, which would make it difficult to set up buffers to store the information that is sent or received. This problem could be solved by setting up buffers at the beginning of the simulation for lattice sites that could potentially become fluid sites during the simulation and letting these sites send and receive information from their neighbours, even though this is only meaningful when they become fluid sites. This would also help to distribute

the lattice sites evenly between the processors. The buffers for passing information between the points on the wall on one processor and neighbouring processors would be more straightforward to set up because the number of points on the wall remains constant. The total number of fluid lattice sites and potential fluid lattice sites is constant. Therefore, the lattice sites and points on the wall can remain evenly distributed among the processors throughout the simulation, similarly to the method described in chapter 3.

Finally, in contrast to the simulation method described in chapter 3, each point on the wall does not belong to a particular lattice site. Therefore, information at a point on the wall may need to be shared between a point and a lattice site residing on a different processor. Some of the phases of communication between processors described in the previous paragraph would be unnecessary if this were not the case. A point will share information with different lattice sites during the simulation, although the lattice site must be the same as or a nearest neighbour of the one used at the previous time step, as explained in section 5.6, which might help to reduce the computational cost. Each segment of the wall that joins a point on the wall to one of its neighbours affects the lattice sites surrounding that segment of the wall, which may or may not be nearest neighbours of one another. However, all communication within the wall or the fluid domain only takes place between points or lattice sites that are neighbours of one another.

While the lattice-Boltzmann method is more suitable than continuum fluid solvers for execution on multicore machines, it is much more memory intensive because, in addition to the pressure and velocity at time t and $t + \Delta t$, the distribution functions at those times also need to be stored at each lattice site. Therefore, for the D3Q15 model, 38 floating point numbers are required at each site: 15 distribution functions, three components of velocity and one pressure at the times t and $t + \Delta t$. This requires 304 bytes if double precision is used. Lattice-Boltzmann simulations achieve a linear speed up with the number of processors until there are too few lattice sites per processor, such that the proportion of lattice sites that need to communicate with those on neighbouring processors becomes too high. For example, the lattice-Boltzmann solver HemeLB [92, 93] scales linearly up to 1024 cores for geometries with 4.7 million lattice sites as described in section 2.3, i.e. while there are more than 4600 lattice sites per core. For such a simulation, 1.4×10^6 bytes are required for each core. The processor requires more time to load information from some parts of the memory than others. For memory intensive simulations, the speed

of the simulation may be limited by the time required to retrieve data from the memory rather than the time required for the calculations themselves.

For the simulations of flow through axisymmetric elastic systems described in chapter 3, the following information is stored for each edge site, as explained in section 3.5: the normalised cut distances, the normal to the nearest point on the wall, its current displacement from the edge site and that before deformation and its velocity. This requires 21 double precision numbers for each edge site, i.e. 168 bytes. For a simulation of a blood vessel of radius R , the fraction of lattice sites that are edge sites is approximately $\frac{2\pi R}{\pi R^2} = \frac{2}{R}$. For a resolution such that $R = 20$ lattice units, one tenth of the sites are edge sites and therefore the difference in memory requirements between simulations with rigid and elastic walls is negligible.

For the simulation method developed in this chapter, the normalised cut distances must be stored for every lattice site because the lattice sites can change type during the simulation so that any lattice site could become an edge site. Each site also requires the index of its nearest point on the wall, as explained in section 5.6, and this can be stored as a 4-byte integer. Therefore, 124 bytes of storage would be needed at each lattice site for a 3D simulation, in addition to the 304 bytes needed for 3D LBM simulations in systems with rigid walls. Some storage is also needed for types of the neighbouring lattice sites, as explained in section 5.6.1, but since a site can only be a solid, fluid or edge site, it is unnecessary to use an integer for every neighbour. At each point on the wall, storage is required for its current position vector and that before deformation, its velocity, and the a_1 and a'_1 Runge-Kutta coefficients, which are needed because the displacement at time $t + \Delta t$ must be calculated for every point before the velocity at that time can be calculated for any of them, as explained in section 4.2.2. Each point also requires the stress tensor at these times, as explained in section 5.1.2. Since it is symmetric, it has six distinct components in three dimensions. Therefore, 27 double precision numbers must be stored for each point, requiring 216 bytes. Each point would also require the index of the nearest lattice point and the indices of its neighbours, for which there are nine in three dimensions, as explained in section 4.2.3. Therefore, at least ten integers are required, taking the storage requirement to 256 bytes per point on the wall. At the beginning of the simulation, there is a pair of points on the wall for each edge site, as explained in section 4.2.1. Therefore, for a blood vessel with a radius of 20 lattice units, there are one fifth as many wall points as edge sites. Therefore, we require an average of $428 + \frac{256}{5} \approx 480$ bytes

per lattice site, which is 50% more than what we would require for a lattice-Boltzmann simulation with rigid walls.

5.10 Change to the method for applying velocity boundary conditions to the fluid

In order to compare the time-dependent behaviour of the simulations in this study with those in [15], it is necessary to find the steady state solution at the parameters used there, as discussed in section 5.2. If the simulation is valid, it should be possible to achieve convergence to a steady state because the viscosity of the fluid should damp the oscillations. In this section, a simulation is carried out⁹ to check whether such convergence is obtained, then changes are made to the velocity imposed on the fluid, \mathbf{v}_b , at each point of intersection with a lattice link from an edge site to its neighbouring solid site, in order to improve the convergence properties of the model developed in this study.

The parameters of the simulation were the same as those used in the last section, except that the external pressure was given by $\Delta p^* = (p_e - p_d) \left(\frac{D^2}{\eta Q} \right) = 24$, so that the parameters matched those used for one of the computations reported in [11], as explained in section 4.7.2. The simulation is started from the steady state solution for the flow fields for a channel of the same dimensions with rigid walls. The L^1 norms for both the velocity field of the fluid and displacement of the wall decreased, then increased again, as shown in figure 5.24, which indicates that an instability arose. The velocity flow field begins to diverge at approximately $t = 4000\Delta t$, whereas the wall displacement field begins to diverge at $10000\Delta t$. This suggests that the calculation of the velocity at the boundary of the fluid is invalid, rather than the calculation of the wall motion. This could cause instability in the fluid, which subsequently causes instability in the wall motion. Nevertheless, the wall shape has been checked at $t = 10000\Delta t$, where the L^1 norm of the wall displacement reaches its minimum value. The wall shape is shown by the dark green line in figure 5.28. It agrees closely with that achieved in section 4.7.4 for the same parameters except that $D = 10\Delta x$ in this section and $D = 10.5\Delta x$ there. That wall profile is shown by the red

⁹The code for this simulation and instructions for its use may be downloaded from <http://ccs.chem.ucl.ac.uk/~gary> as a zip archive and will be in the folder “Elastic_complex_geometry_rev_215” when the archive has been unpacked. For this simulation, INCOMPRESS, INC_FLUID and MOVE_WALL were defined at compile time.

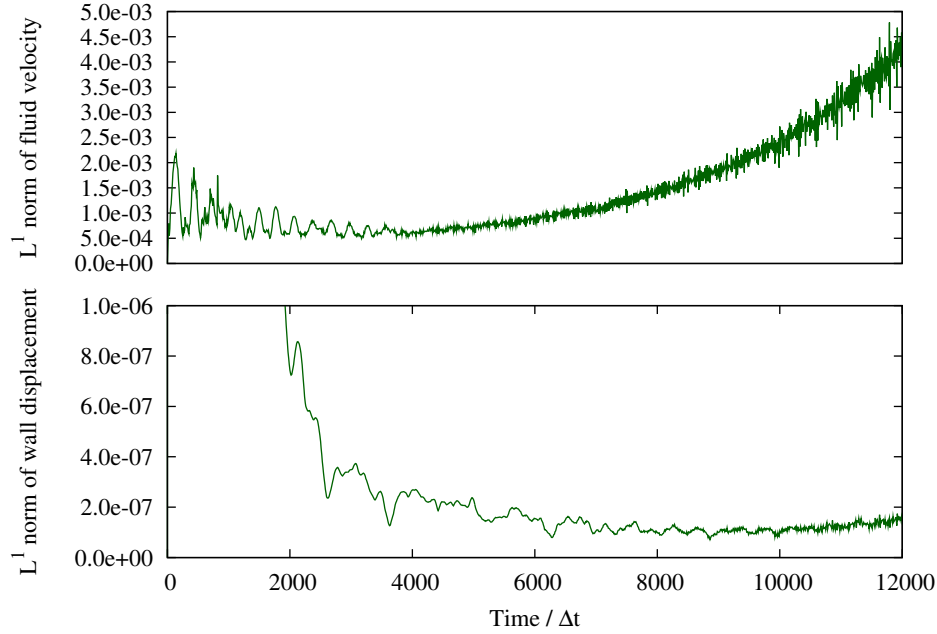


FIGURE 5.24: L^1 norms of the fluid velocity and wall displacement, calculated from equation (3.15), during a simulation of a Starling resistor with $\frac{TD}{\eta Q} = 10^5$, $\Delta p^* = (p_e - p_d) \left(\frac{D^2}{\eta Q} \right) = 24$, $D = 10\Delta x$, $Re = 0.15$, $\tau = 0.56$, $h = 0.25\Delta x$. The velocity flow field and wall displacement field begin to diverge at $t = 4000\Delta t$ and $t = 10000\Delta t$ respectively.

line in figures 5.28 and 4.8. The latter shows that the numerical solution agreed closely with the Lowe and Pedley [11]’s solution.

A plausible explanation for the divergence in the velocity field of the fluid is as follows. At the point of intersection, b , of the wall and the link from an edge site, f , to a neighbouring solid lattice site, w , velocity \mathbf{v}_b is imposed on the fluid, as explained in section 4.2.2 and illustrated in figure 4.2. The velocity \mathbf{v}_b is set equal to the long-term velocity, \mathbf{v}_n of the nearest point on the inner surface of the wall, n , to lattice site f , as explained at the beginning of section 5.6. This long-term velocity is calculated by making the approximation that the acceleration is uniform between times $t - 2\Delta t$ and t because the temporal resolution of the fluid simulation is Δt , as explained in section 5.1.2. This results in equation 5.5. Therefore we have:

$$\mathbf{v}_b(t) = \mathbf{v}_n(t) = 1.5\mathbf{u}_n(t) - 2\mathbf{u}_n(t - \Delta t) + 0.5\mathbf{u}_n(t - 2\Delta t), \quad (5.24)$$

where \mathbf{u}_n is the displacement of point n . However, point b lies between point n and its neighbours on the inner surface of the wall, as shown in figure 5.26. Therefore, the error

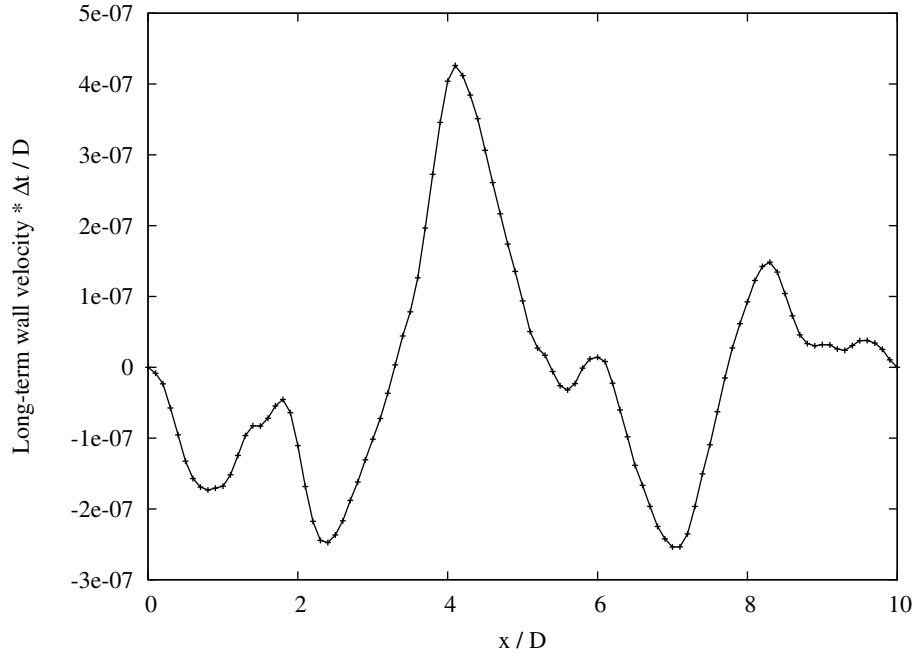


FIGURE 5.25: Long term-velocity of the wall, as defined in section 5.1.2, for a simulation of a Starling resistor at $t = 8002\Delta t$, calculated from equation (5.5), with the same parameters as figure 5.24. The differences between velocities of neighbouring points are significant, causing the velocity imposed at the boundary of the fluid to be inaccurate.

in the approximation that $\mathbf{v}_b = \mathbf{v}_n$ is of order the difference in velocity between a point and its neighbours. At the beginning of the simulation, the motion is dominated by the mode of oscillation in which the entire wall moves inwards or outwards together to form a standing wave with wavelength $\lambda = 2L_e$, where L_e is the length of the elastic section of the wall. At a time $t = 10000\Delta t$, the overall wall profile changes very little, but other modes of oscillation with shorter wavelengths are still present. Therefore, the error in \mathbf{v}_b is larger relative to the maximum velocity of the wall. This inaccuracy could prevent the velocity flow field from converging to a steady state.

To test this explanation, the long-term velocity of each point on the wall \mathbf{v}_n at time $t = 8002\Delta t$, which was defined in section 5.1.2, has been calculated and plotted in figure 5.25. This velocity changes significantly over a shorter distance than L_e and the maximum difference in velocity between adjacent points is $7.6 \times 10^{-8} \frac{D}{\Delta t}$ for the points at $x = 3.7D$ and $x = 3.8D$, which is 18% of the maximum velocity, $4.26 \times 10^{-7} \frac{D}{\Delta t}$. This suggests that the error in the approximation $\mathbf{v}_b = \mathbf{v}_n$ may be preventing convergence of the computation.

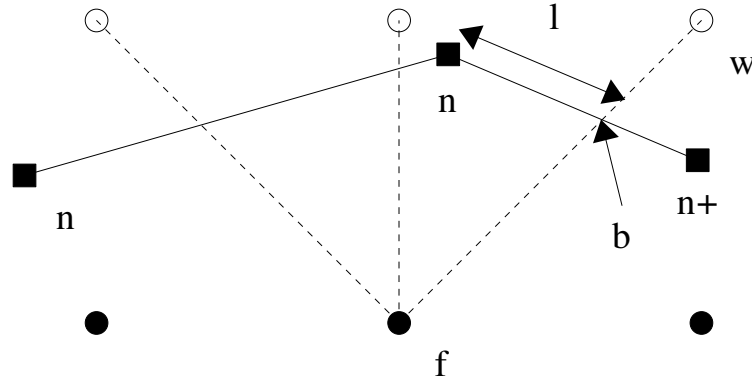


FIGURE 5.26: A link between an edge site f and a neighbouring solid site w , shown by a dotted line, intersects the inner surface of the wall at point b , which lies between points n and $n+$ on the wall, for which the motion is calculated. Interpolating between these two points to find the velocity at point b , \mathbf{v}_b is more accurate than assuming that $\mathbf{v}_b = \mathbf{v}_n$. The normalised distance from point n to point b , l , is required for the interpolation.

The accuracy of the estimate of the \mathbf{v}_b has been improved by using linear interpolation of the velocity between the points on the inner surface of the wall for which the line segment that joins them intersects the link between the lattice sites at point b , as shown in figure 5.26. That is,

$$\mathbf{v}_b = (1 - l)\mathbf{v}_n + l\mathbf{v}_{n+}, \quad (5.25)$$

where l is the normalised distance from point n to point b along the line segment between points n and $n+$, i.e.

$$l = \frac{(\mathbf{x}_b - \mathbf{x}_n) \cdot (\mathbf{x}_{n+} - \mathbf{x}_n)}{|\mathbf{x}_{n+} - \mathbf{x}_n|^2}, \quad (5.26)$$

where l lies within the range $0 \leq l < 1$.

The simulation described in this section was repeated with interpolation to find \mathbf{v}_b ¹⁰. The behaviour of the L^1 norms for the velocity of the fluid and the wall displacement changed very little. These L^1 norms are shown by the dark red lines in figure 5.27. The L^1 norms increase more slowly, reaching 3.74×10^{-3} and 1.31×10^{-7} respectively, instead of 4.22×10^{-3} and 1.46×10^{-7} . This shows that the instability remains, but it is less severe.

¹⁰The code for this simulation and instructions for its use may be downloaded from <http://ccs.chem.ucl.ac.uk/~gary> as a zip archive and will be in the folder “Elastic_complex_geometry_rev.225” when the archive has been unpacked. For this simulation, INCOMPRESS, INC_FLUID and MOVE_WALL were defined at compile time.

Although interpolating between the points on the wall to find the velocity at the boundary should have improved the accuracy and stability of the simulation, the method for calculating the long-term velocity of a point on the wall, \mathbf{v}_n may be causing the instability. The alternatives, which are described in section 5.1.2 are to set \mathbf{v}_n equal to the average velocity of the wall over one timestep, i.e.

$$\mathbf{v}_n(t) = \mathbf{u}_n(t) - \mathbf{u}_n(t - \Delta t) \quad (5.27)$$

or to set it equal to the instantaneous velocity of the wall ¹¹. The simulation described in the previous paragraph was repeated with these two methods and the L^1 norms for the former and latter methods of finding \mathbf{v}_n are shown by the orange and blue lines in figure 5.27 respectively. For both of these alternative methods for calculating \mathbf{v}_n , the simulation divergences later on. If \mathbf{v}_n is set equal to the average velocity of the wall, the divergence occurs at $t \approx 11000\Delta t$ and does not occur before $t = 20000\Delta t$ for the wall displacement. The L^1 norms are much lower at $t = 200000\Delta t$ than they are for the other methods. Therefore, this method is used for the remaining simulations in this thesis.

The wall shape at $t = 10000\Delta t$ is shown by the orange line in figure 5.28 and it agrees very closely with the wall shapes obtained using the current method without the adjustments to the calculation of the velocity at the boundary of the fluid. The agreement of the wall profiles between the various simulation methods used in this thesis provides evidence that the simulation method produces accurate steady state solutions.

5.11 Inclusion of viscoelastic behaviour

In this section, I explain how a damping factor can be included in the equation of motion of the wall in order to enable simulations of a Starling resistor to converge to a steady state and to include viscoelastic behaviour in the simulation, if this is desired. This damping factor is removed when comparing the dynamics of the system with numerical or analytical results for a system without a damping factor.

¹¹The code for the former and latter methods and instructions for its use may be downloaded from <http://ccs.chem.ucl.ac.uk/~gary> as a zip archive and will be in the folders “Elastic_complex_geometry_rev_226” and “Elastic_complex_geometry_rev_227” respectively when the archive has been unpacked. For the simulations reported in this section, INCOMPRESS, INC.FLUID and MOVE_WALL were defined at compile time.

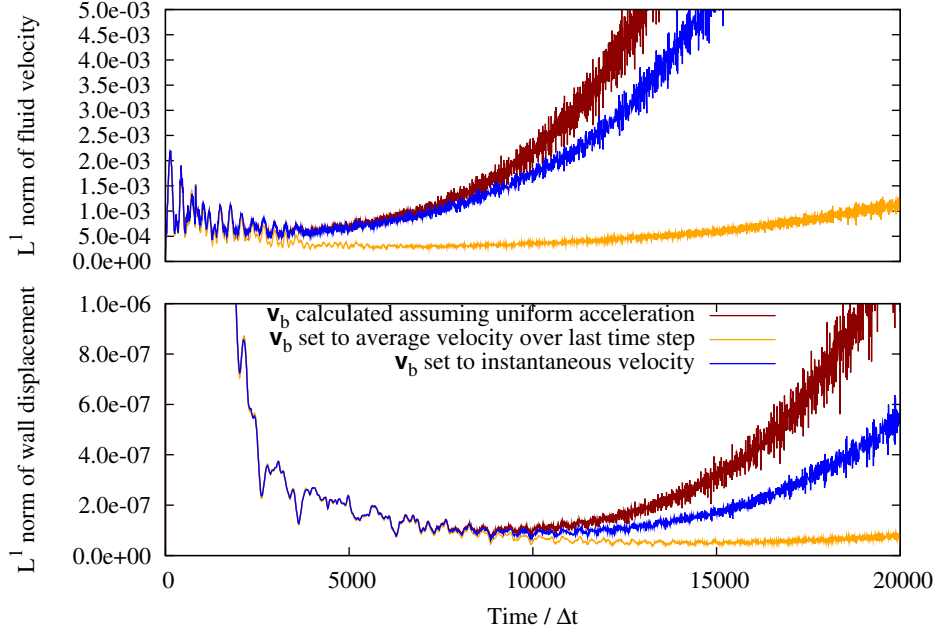


FIGURE 5.27: L^1 norms of the fluid velocity and wall displacement during three simulations of a Starling resistor for which different methods involving spatial interpolation are used to calculate the velocity to impose at the boundary of the fluid domain. The parameters are $\frac{TD}{\eta Q} = 10^5$, $\Delta p^* = (p_e - p_d) \left(\frac{D^2}{\eta Q} \right) = 24$, $D = 10\Delta x$, $Re = 0.15$, $\tau = 0.56$, $h = 0.25\Delta x$. For all three methods, the simulation begins to diverge instead of reaching a steady state, but the divergence is much less severe if the velocity at the boundary of the fluid is set equal to the average velocity of the wall over the last time step.

Any real elastic material exhibits viscoelastic behaviour, such that the stress depends on the strain rate as well as the strain. The viscosity has bulk and shear components like the elastic modulus [121]. A full treatment of this behaviour in the simulations described in this thesis would be very complex. Therefore, the following term is added to the acceleration of each point on the wall:

$$\sum_{neighs} b \left(\frac{\partial \mathbf{u}_{neigh}}{\partial t} - \frac{\partial \mathbf{u}_{point}}{\partial t} \right), \quad (5.28)$$

where the sum is taken over neighbours 1 to 5 in figure 4.3. Since this term depends on the relative velocities of the neighbouring points, the stress depends on the strain rate. This damping term is more realistic than that given by equation (4.87), which depended only on the absolute velocity of the point. It does not allow the bulk and shear viscosity to be varied independently, but it can be used to help simulations converge to a steady state.

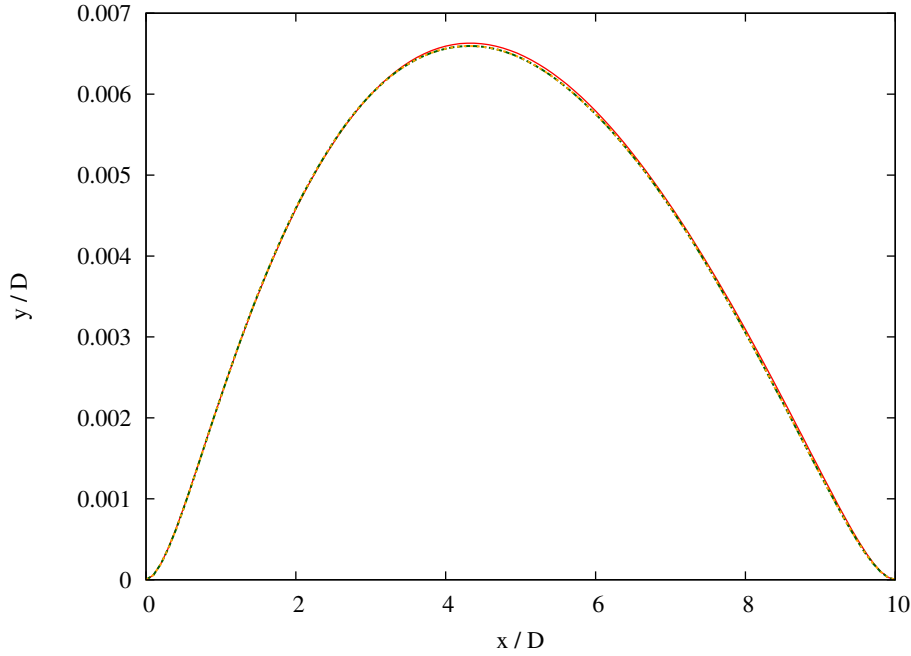


FIGURE 5.28: Wall profile obtained by simulations of a Starling resistor with three different methods. The red line show the results for the method described in chapter 4, while the dark green and orange line show the results for the current method before and after adjustments were made to the calculation of the velocity field at the boundary of the fluid. The very close agreement between these profiles and the comparison of them with [11]’s solution shown in figure 4.8 provides evidence that the current simulation method gives accurate results for the steady state. The parameters are $\frac{T D}{\eta Q} = 10^5$,

$$\Delta p^* = (p_e - p_d) \left(\frac{D^2}{\eta Q} \right) = 24, D = 10\Delta x, Re = 0.15, \tau = 0.56, h = 0.25\Delta x.$$

The simulation described in section 5.10 that used interpolation of the average velocities of points on the wall to set the velocities at the boundary of the fluid was repeated ¹² with a damping factor of 0.1 times the critical damping factor calculated from the expected period of oscillation of the separation between the inner and outer surfaces of the wall, Γ , which is given by equation (4.81), as explained in section 5.1.1. For damped harmonic motion, the critical damping factor is $2\omega_0$, where ω_0 is the angular frequency of the free period of oscillation. Therefore, I have used $b = 0.1b_{crit} = 0.2\omega_0 = \frac{0.4\pi}{\Gamma}$. The fluid velocity and wall displacement fields converged to a steady state such that their L^1 norms were 1.8×10^{-5} and 1.5×10^{-8} at $t = 20000\Delta t$ respectively, which are much lower than those achieved without damping at $t = 20000\Delta t$, and 1.0×10^{-8} and 6.2×10^{-11} respectively at $t = 85220\Delta t$. The maximum difference between the positions of the points on the wall

¹²The code for this simulation and instructions for its use may be downloaded from <http://ccs.chem.ucl.ac.uk/~gary> as a zip archive and will be in the folder “Elastic_complex_geometry_rev_226” when the archive has been unpacked. For this simulation, INCOMPRESS, INC_FLUID and MOVE_WALL were defined at compile time.

obtained from this simulation and from the simulation described at the end of the last section at $t = 10000\Delta t$, for which the wall shape is shown by the orange line in figure 5.28, is $1.4 \times 10^{-5}D$.

5.12 Comparison of the dynamics with results from a previous study

In this section, I describe simulations of the Starling resistor shown in figure 5.29 with the same parameters as those used for figure 4 of [15], which were intended to help validate the dynamics of the model described in this study, as discussed in section 5.2¹³. In that study, the parameters were as follows. The width of the channel was $D = 10^{-2}\text{m}$ and the lengths of the first rigid section of the wall, the elastic section, and the second rigid section were $L_u = 5D$, $L_e = 5D$ and $L_d = 30D$ respectively. The tension in the wall was $1.610245\text{N}/\beta$, $\beta = 25$ and the external pressure was $p_e - p_d = 0.93\text{Nm}^{-1} + \frac{12 \times 23\eta Q}{D^2}$, where the second term is the pressure required to drive Poiseuille flow through a channel of length $23D$, where Q is the flow rate and η is the dynamic viscosity. It was used by Luo and Pedley [15, 19] to ensure that their simulation parameters matched those in Luo and Pedley [13]. The viscosity and density of the fluid are $\eta = 10^{-3}\text{Nm}^{-1}\text{s}$ and 10^3kgm^{-2} . The Reynolds number at the inlet was 450¹⁴. The length of the Starling resistor was along the x -axis.

β	y -ordinate at $x = 3.5D$	Reference
20	-0.30D	Figure 7(a), [13]
25	-0.524D	Figure 20(a), [19]
30	-0.545D	Figure 20(a), [19]

TABLE 5.4: y -ordinate of the point on the wall at $x = 3.5D$, measured relative to the left-hand end of the elastic wall, for the steady state solutions obtained by [13, 19] at different values of the tension, $T = \frac{1.610245\text{N}}{\beta}$.

Figure 4 of [15] shows the y -ordinate of the point with $x = 3.5D$ relative to the left-hand end of the elastic wall. The simulation shown there was started from a perturbation on the steady state, i.e. the steady state for a slightly different value of β , which I have

¹³The code for these simulations and instructions for its use may be downloaded from <http://ccs.chem.ucl.ac.uk/~gary> as a zip archive and will be in the folder “Elastic_complex_geometry_rev_236” when the archive has been unpacked. For these simulations, INCOMPRESS, INC_FLUID and MOVE_WALL were defined at compile time.

¹⁴The Reynolds number quoted in Luo and Pedley [15] is 300 because it is calculated from the average velocity of fluid flow at the inlet, whereas I calculate it from the maximum velocity.

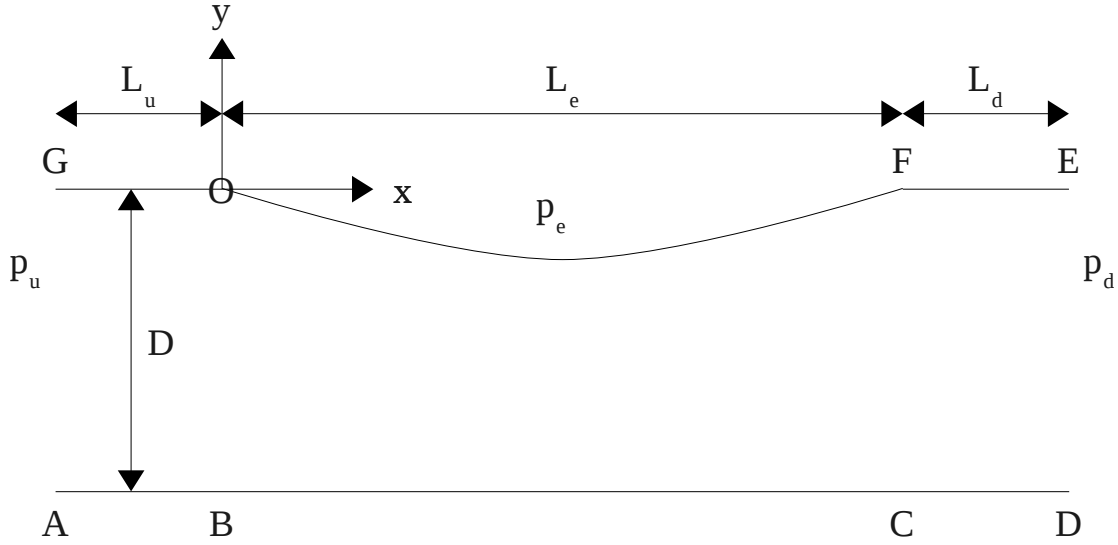


FIGURE 5.29: Diagram of a 2D Starling resistor, which is a channel with a collapsible segment through which fluid flows. The dimensions are marked as well as the pressure at the inlet and outlet and the pressure applied to the outside of the wall.

estimated from the y -ordinates at $x = 3.5D$ for the steady-state solutions obtained by Luo and Pedley [13, 19] at several different values of β . These y -ordinates are given in table 5.4 and measured relative to point O in figure 5.29. Since $y = -0.425D$ when the simulation shown in figure 4 of [15] was started, I estimate that $\beta = 22$.

In order to carry out the comparison with figure 4 of [15], it is necessary to initialise the wall position and fluid velocity to a small perturbation on the steady state at $\beta = 25$. This perturbed solution should ideally be equal to the steady state solution for $\beta = 22$. To that end, a simulation was carried out with the method developed in this chapter, with $\beta = 22$. The simulation was set up as described in section 4.7. The initial strain of the wall was given by $\epsilon_{xx} = 0.01$, $\epsilon_{yy} = -0.005$, $\epsilon_{xy} = 0$ and the Poisson ratio, $\Omega = 0.5$. The thickness of the wall is $h = 0.3125\Delta x$. The pressure difference between the inlet and outlet was chosen to drive a Poiseuille flow in a channel of width D at $Re = 450$. The resolution is given by $\Delta x = 2 \times 10^{-4}\text{m}$, $\Delta t = 1.333 \times 10^{-4}\text{s}$.

In order to achieve stability at $Re = 450$, the Mazzeo+GZS combination of boundary conditions was used, as described in section 3.4.1, except that the method by Mazzeo et al. [93] was used to impose a Poiseuille flow profile at the inlet $Re = 450$ instead of a constant pressure. The boundary conditions therefore matched those used by Luo and Pedley [15].

The half-width is chosen to be $D = 25.2\Delta x$ so that the distance from the last row of lattice points to the wall is $0.2\Delta x$, as described in section 3.4.2. The dimensions of the channel are therefore 2% larger than those in [15], since I keep $L_u = L_e = 5D$ and $L_d = 30D$.

The density of the wall was $\rho_w = 100\rho_f$. Therefore, the expected period of oscillation of the entire wall, calculated from equation (4.89), was $\Lambda = 6986\Delta t$. Since $L_e = 252\Delta x$, this satisfies the requirement that $\Lambda > \frac{L_e}{c_s}$, which was explained in section 5.1.2. The expected period of the oscillation of the separation between the inner and outer surfaces of the wall, $\Gamma = 2.722\Delta t$, therefore $\Psi = 100$ wall timesteps were used per lattice-Boltzmann timestep, satisfying $\Gamma\Psi > 250\Delta t$. A damping factor of $b = \frac{0.4\pi}{\Gamma}$ was applied, as discussed in section 5.11, to help the simulation to converge.

The wall was held in position until the fluid had converged, as described in section 5.2, such that the L^1 norm for the difference in the velocity field between the current and previous time steps reached 1.0×10^{-7} . In order to avoid having to wait for the oscillations of the wall to die away, the simulation was restarted with the points on the wall initialised to their positions at a previous point in time, t_1 , which is estimated to be the time when the wall was close to its steady state.

When the fluid had converged during the first part of the simulation, in which the wall was flat, the velocity and pressure fields were compared with the analytic solution for a rectangular channel. The simulation errors were measured with the L_1 and L_∞ norms for the difference between the analytical and numerical solutions, which are calculated using equations 3.18 and 3.19 respectively. The L_1 and L_∞ norms were 1.09×10^{-3} and 2.79×10^{-2} respectively for the velocity field and 1.28×10^{-2} and 5.05×10^{-2} respectively for the pressure field, which shows that the fluid was simulated accurately.

The wall profiles obtained during the first simulation at various times are shown in figure 5.30. The wall does not complete an oscillation, despite the period of oscillation of the wall in the absence of fluid being $\Lambda \approx 7000\Delta t$. This is probably because the ratio of the mass of the wall to the mass of the fluid, $\frac{\rho_w h}{\rho_f D} = 0.625$, so the period of oscillation is not dominated by the inertia of the wall. The wall becomes unstable, such that at $t = 36039\Delta t$ after it was released, it crosses itself, which is unphysical, and it intersects some of the links between lattice sites more than once, which causes the algorithm for calculating the normalised cut distances, described in section 5.6.2, to fail.

The simulation was then restarted with the wall fixed held its position at $t = 33076\Delta t$. This wall profile, along with the resulting steady state solution for the fluid, was used as the initial state for the comparison with figure 4 of [15], since it was smooth and collapsed everywhere, in common with the steady state solutions for $Re = 450$, $\beta < 30$ shown in figure 5(b) of [19], and $y = -0.289D$ at $x = 3.5D$, which is comparable with the initial y -ordinate of the point at $x = 3.5D$ in the simulation shown in figure 4 [15]. Since $y = -0.524D$ at $x = 3.5D$ for the steady state solution at $\beta = 25$, this perturbation is somewhat larger than the one used by [15], but it still permits a comparison with their results. In order to carry out the comparison, the parameters were changed to the values used in figure 4 of [15] i.e. $\beta = 25$ and the ratio of the mass of the wall to that of the fluid below it, $\frac{\rho_w h}{\rho_f D} = 0.1$, which required $\rho_w = 16.064\rho_f$. This gives $\Gamma = 1.163\Delta t$, therefore $\Psi = 220$ wall timesteps were used per lattice-Boltzmann timestep, satisfying $\Gamma\Psi > 250\Delta t$.

The y -ordinate of the point at $x = 3.5D$ at $t = 0$, $t = 100\Delta t$, $t = 200\Delta t$, $t = 300\Delta t$, $t = 400\Delta t$ and $t = 454\Delta t$ is shown in figure 5.31. The fluid simulation became unstable at $t = 454\Delta t$. The wall began to move outwards, i.e. away from the steady state solution expected, at time $t = 400\Delta t$. This result shows that the model I have proposed is unstable under the parameters used by [15], for which the tension is very low compared to the previous simulations in this thesis; we have $\frac{TD}{\eta Q} = 2.46 \times 10^3$, compared with 10^5 in section 4.7. Figure 4 in [15] shows results for a much longer time: $t = \frac{20D^2}{Q} = \frac{30D^2}{Rev} = 6.667s = 50000\Delta t$, from equation (4.84). Therefore, this figure is shown separately as figure 5.32 in this section.

5.13 Conclusions

The method for simulating fluid flow through elastic vessels that was developed in chapter 4 has been improved in several ways. Many sub-timesteps for the elastic wall are carried out for each lattice-Boltzmann timestep, so that the minimum density of the wall that is required to achieve sufficient temporal resolution is limited only by the fact that the period of oscillation of the wall needs to be greater than the shortest timescale over which the LBM can cope with major changes in the flow fields. The method also allows the wall to move over lattice sites, so that it can simulate systems in which the displacement of the wall is large. Some simple tests of the dynamics of the model in a Starling resistor

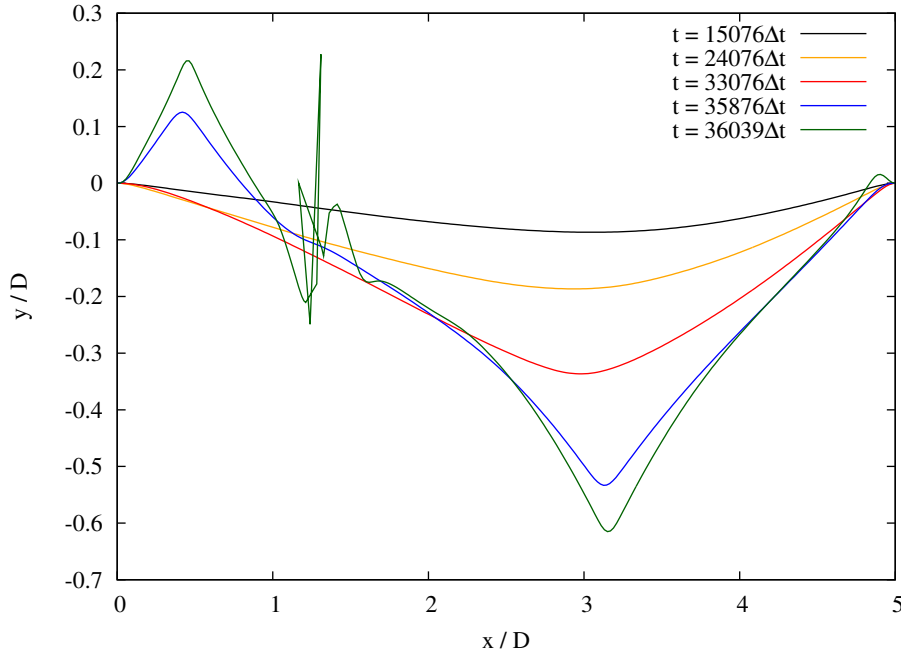


FIGURE 5.30: Wall profiles obtained during a simulation of a Starling resistor for which the wall was initially flat. The times are measured relative to time when wall was released. The parameters approximately match those for the steady state solution used for figure 4 of [15]. We have $D = 0.01008\text{m}$, $L_u = 5D$, $L_e = 5D$, $L_d = 30D$, $\rho_f = 1000\text{kgm}^{-2}$, $\rho_w = 100\rho_f$, $\eta = 10^{-3}\text{Nm}^{-1}\text{s}$, $Re = 450$, $T = 1.610245\text{N}/22$, $p_e - p_d = 0.93\text{Nm}^{-1} + \frac{12 \times 23\eta Q}{D^2}$. The resolution is given by $\Delta x = 2 \times 10^{-4}\text{m}$, $\Delta t = 1.333 \times 10^{-4}\text{s}$, therefore $\tau = 0.510$. The thickness of the wall is $h = 0.3125\Delta x$.

have shown that the elastic portion of the wall performs oscillations approximately equal to the free period of oscillation of a stretched string under the same tension, as expected, and these oscillations are damped by the viscosity of the fluid. However, noise is present in the oscillations and the amplitude of the noise appears to increase over time. The simulation does not converge to a steady state. In an attempt to improve this situation, the method for imposing the velocity at the boundary of the fluid has been improved, but the simulations do not converge to a steady state unless damping is included.

The dynamics of the simulation have been compared with those in [15], but the fluid simulation became unstable under the parameters used there. The wall moved towards the steady state at first, then away from it. This shows that the model I have proposed is unstable under the parameters used by [15]. For these parameters, the tension is very low compared to the previous simulations in this thesis; we have $\frac{TD}{\eta Q} = 2.46 \times 10^3$, compared with 10^5 in section 4.7, and hence we would expect sudden large movements of the wall to be more likely. Such rapid divergence of the wall position and flow fields did not occur for

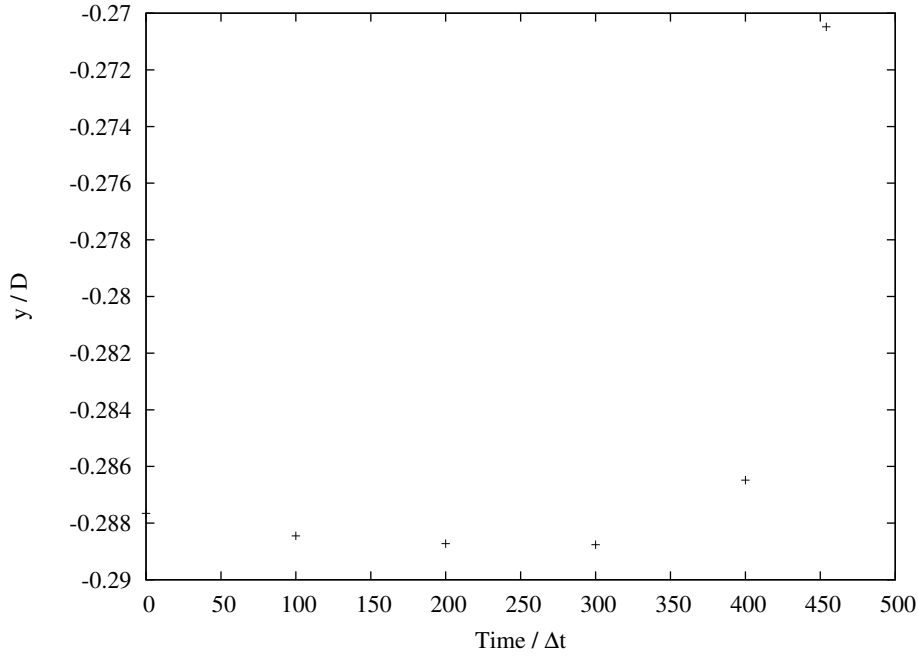


FIGURE 5.31: Wall position y at $x = 3.5D$ as a function of time for a simulation of a Starling resistor for which the wall profile was initialised to that shown in figure 5.30 at time $t = 33076$ and the parameters were approximately equal to those used for figure 4 of [15]. They are given by $D = 0.01008\text{m}$, $L_u = 5D$, $L_e = 5D$, $L_d = 30D$, $\rho_f = 1000\text{kgm}^{-2}$, $\rho_w = 16.064\rho_f$, $\eta = 10^{-3}\text{Nm}^{-1}\text{s}$, $Re = 450$, $T = 1.610245\text{N}/25$, $p_e - p_d = 0.93\text{Nm}^{-1} + \frac{12 \times 23\eta Q}{D^2}$. The resolution is given by $\Delta x = 2 \times 10^{-4}\text{m}$, $\Delta t = 1.333 \times 10^{-4}\text{s}$. The thickness of the wall is $h = 0.3125\Delta x$.

the simulations reported elsewhere in this thesis, where the tension was higher. It would therefore be sensible to attempt further validations of the dynamics at a higher tension.

The method also needs to be extended to 3D in order carry out meaningful simulations of cerebral blood flow, but some work is required to extend the methods for selecting the points on the wall to be used for the calculation of forces on the wall and the determination of the points of intersection of the lattice vectors with the wall, as discussed in section 4.5. A significant effort is also needed to extend the algorithm for deciding whether the wall has crossed a particular site to 3D, as discussed in section 5.6.1.

The ratio of the computational cost of a simulation with elastic walls to that of the same simulation with rigid walls is higher for the simulation of a Starling resistor presented in section 5.7 than for that of an elastic cylinder in section 3.6, but the systems being simulated and their parameters are very different. The expected ratio for the elastic cylinder in 3D, under the same parameters as in section 3.6, is estimated to be 3, which is

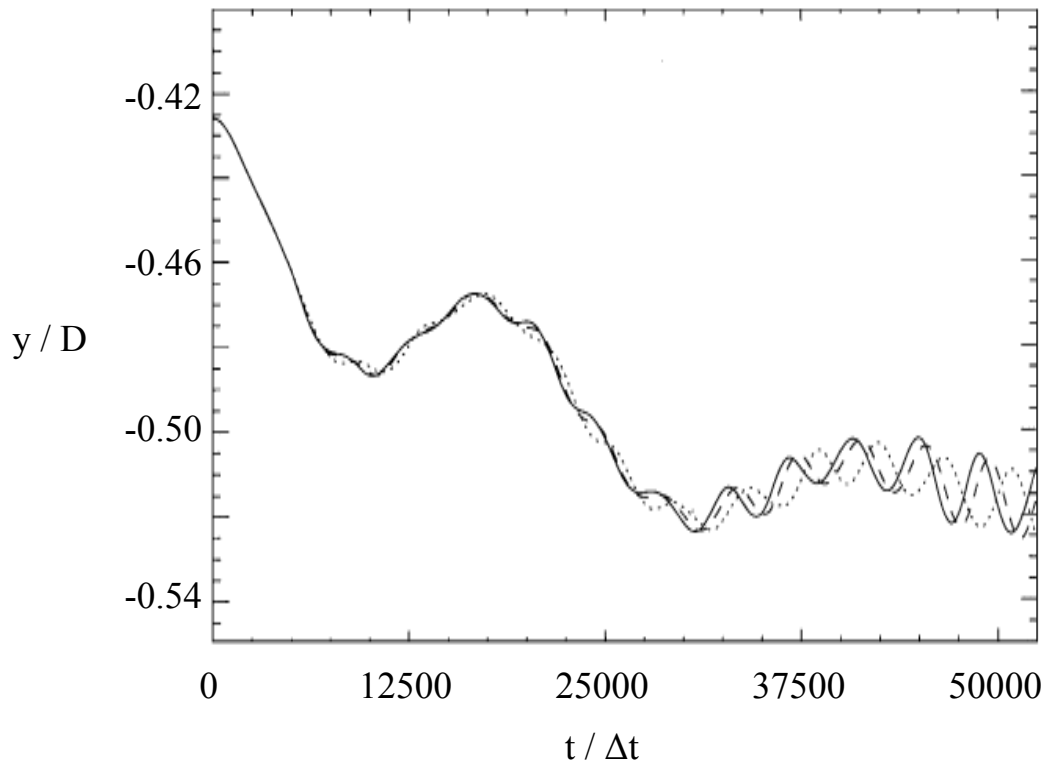


FIGURE 5.32: Wall position y at $x = 3.5D$ as a function of time from figure 4 of [15], with error tolerances of 10^{-5} , 10^{-6} , 10^{-7} and 10^{-8} for their numerical methods for the dotted, dashed, dash-dotted and solid lines respectively.

reasonable considering that the model neither makes any assumptions about the geometry nor requires the wall displacement to be small. However, it would be more challenging to develop an efficient parallel implementation for this method than that for axisymmetric systems described in chapter 3, because several communication steps are needed during each timestep for the wall and the lattice-Boltzmann method, and each point on the wall does not belong to a particular edge site.

Chapter 6

Conclusions and Future Work

In this thesis, I have discussed models of cerebral blood flow and how they have helped to improve our understanding of cerebrovascular diseases. Three-dimensional (3D) computational fluid dynamics (CFD) simulations of patient-specific vasculature can now be performed. I then explained how such simulations could be used to plan neurosurgery by simulating the effects of different procedures on cerebral blood flow. The majority of CFD simulations of blood flow use finite-element or finite volume simulations, which are computationally costly for simulations in complex geometries at high resolutions. The lattice-Boltzmann method, its computational efficiency and its scalability for simulations in parallel were then discussed, along with existing simulations of cerebral blood flow using this method, including some that are capable of carrying out simulations quickly enough for use in neurosurgery.

Most 3D CFD simulations of cerebral blood flow do not include arterial elasticity, which is important for simulating cerebral blood flow. There are also only a few published schemes for simulating fluid flow through elastic vessels with the lattice-Boltzmann method. The majority of these studies only include simulations of flow through a simple channel in which the wall is divided into segments that move independently [14, 117, 118, 120]. However, the method by Buxton et al. [119] is capable of simulations in a complex geometry.

I have developed a method for simulations of fluid flow through an axisymmetric elastic vessel in three dimensions. The steady-state solutions for the wall displacement and the pressure and velocity flow fields in a cylinder achieved good agreement with the analytical

solution. The simulations were carried out at realistic parameters for cerebral blood flow, in contrast to the existing methods for simulations of the cerebral blood flow. The method is sensitive to displacements of the wall of fractions of a lattice lengths, in common with [14, 117, 118], but not [120]. It is capable of carrying out time-dependent simulations in common with the former three studies, but not the latter one. The Poisson ratio of the wall material can also be chosen freely, in contrast to the other studies. Each point on the wall moves independently. In contrast to the existing studies, no fluid nodes are created or destroyed. The method is computationally efficient, requiring little more computational effort than a simulation with rigid walls at realistic parameters for cerebral blood flow simulations. It requires the inlet and outlet to be axis-aligned due to the pressure boundary condition method, but this could be adapted.

A somewhat similar method was developed for simulations of fluid flow through elastic vessels in a more complex geometry in two dimensions. It uses the full theory of linear elasticity. Therefore, the motion of each point on the wall depends on that of the other points, which is more realistic than the method described in the last paragraph. It can therefore be used in complex geometries with branches, bulges in the wall, or rapid variations of the channel width along its length. These features occur in blood vessels, where aneurysms correspond to bulges in the wall in a two-dimensional simulation. The steady-state behaviour was validated by comparing the wall profiles resulting from simulations of a 2D Starling resistor, which is a channel in which part of the wall is replaced with an elastic segment under tension, to those reported in [11]. In contrast to most simulations of Starling resistors [11, 13, 15, 19, 126], the wall has a finite thickness and the Young's modulus and Poisson ratio can be varied independently. I discovered that it is essential to create and destroy fluid sites during simulations of fluid flow through vessels with moving boundaries if the boundary crosses any lattice sites.

Simulations of a cylinder and a two dimensional channel have been performed for several different combinations of lattice-Boltzmann boundary condition methods that were suitable for simulating fluid flow in a complex geometry to assess the efficacy of them for simulations of fluid flow through elastic vessels. A combination of the pressure boundary condition developed by Zou and He [9] and the velocity condition by Zhao-Li et al. [10] was found to be suitable in both cases, except that the pressure boundary condition requires the inlet and outlet to be aligned with the axes. For the two-dimensional simulations,

it was difficult to raise the Reynolds number beyond 200. Two dimensional simulations of a channel with the pressure boundary condition method replaced by that proposed by Mazzeo et al. [93] were tried. The accuracy was less good, but still acceptable. The method was more stable, reaching a Reynolds number of 450 for a channel that is 40 lattice lengths wide, which is sufficient for the comparison of the dynamics of the system with simulations by Luo and Pedley [15].

The method for simulating flow in a complex geometries was then improved in several ways. The density of the wall had been restricted by the minimum temporal resolution required for a stable simulation, which was determined by the period of oscillation of a mode in which each point moves in the opposite direction to its neighbour. Many sub-timesteps for the elastic wall are carried out for each lattice-Boltzmann timestep, so that the minimum density required is limited only by the condition that the period of oscillation of the wall, and consequently the flow fields, must be greater than the advection time for the LBM, as described in section 2.6. Lattice sites were created and destroyed as the wall moved. Therefore, the method would be able to simulate elastic vessels in which the wall is displaced by several lattice sites.

Simple tests of the dynamics have shown that when the mass per unit length of the wall is much greater than that of the fluid in the channel, the elastic wall performs oscillations equal to the expected period of oscillation of a membrane under tension. When the mass of the wall is reduced, the oscillation is damped significantly due to the viscosity of the fluid, as expected. However, noise is present in the oscillations and the amplitude of the noise appears to increase with time. In an attempt to improve this situation, the method for imposing the velocity at the boundary of the fluid has been improved, but the simulations do not converge to a steady state unless damping is included in the wall. More work is required to identify the source of the noise that arises in the simulation.

The dynamics were compared with the results shown in [15], but the simulation became unstable at the parameters used there. This could be because the ratio $\frac{TD}{\eta Q}$, where T , D , η and Q are the tension, the channel width before deformation, the viscosity of the fluid and the flow rate respectively, is much lower than it is for simulations reported elsewhere in this thesis, and therefore we would expect instability to be more likely. It would therefore be sensible to attempt further validations of the dynamics at a higher tension.

The simulations of Starling resistors with this method were significantly more computationally costly than simulations of fluid flow through an elastic cylinder with the method for axisymmetric systems. The computational cost for such a simulation with the latest method has been estimated and it is expected to require three times the computational effort of the same simulation with rigid walls. It would also be more challenging to develop an efficient parallel implementation for this method.

Most parts of the method can be readily extended to three dimensions, but a significant effort is needed to extend the algorithms for calculating the distances from the wall to the lattice sites adjacent to it along the lattice vectors, selecting the points on the wall that are used to calculate the forces on the wall, and deciding whether the wall has crossed a particular site.

The method should then be parallelised so that it can be used in simulations of cerebral blood flow. It could be combined with an interactive simulation tool such as HemeLB [92, 93], which was described in section 2.3, in order to carry out patient-specific simulations of cerebral blood flow that include the effects of arterial elasticity. It would then be interesting to compare the pressure, velocity and stress flow fields obtained by simulations of blood flow where elasticity is included to where it is not. The effect of the geometry and the other flow fields on the wall displacement in complex geometries can then be investigated.

The Young's modulus is constant in my method, whereas in reality it depends on the radius of the arteries [24]. However, it would be relatively easy to modify the method to take the spatial variation of the Young's modulus as a set of input parameters. The same applies to the thickness of the wall. The elasticity is also nonlinear [76], but the variation of the Young's modulus with strain could readily be included in the simulation. However, the non-constant Young's modulus gives rise to a linear pressure-radius relationship in large arteries [76] and one might question why I did not simply use that. It is because the relationship would not determine the behaviour of the arterial walls at aneurysms or branches.

Many studies have demonstrated the feasibility of blood flow simulation in patient-specific vascular geometries for estimating the risk of cerebrovascular diseases, for example, the rupture of an aneurysm [3, 20, 25]. Such simulations are also promising for assessing the effect of surgical procedures on blood flow. For example, the tool described by Axner [85]

allows the vascular geometry to be edited to simulate surgical procedures such as occluding an artery or inserting a bypass. More recently, simulations of stent placement have been carried out, for which a very high spatial resolution is required to resolve the stent struts [33–35]. These studies assume that the arterial walls are rigid. However, the elasticity is likely to affect the flow fields because the flow fields are sensitive to small changes in the geometry [25, 37, 71]. Hoi et al. [74] found that similar CFD models with a small difference in volume gave rise to significantly different results for the wall shear stress, which gives further evidence that the inclusion of elasticity would affect the flow fields significantly. Mihalef et al. [43], and Jeays et al. [44] simulated blood flow through vessels with moving boundaries, where the wall motion during a cardiac cycle was derived from medical images, which would improve the accuracy of the flow fields. However, it is also very important to model the stress inside the blood vessel walls accurately, particularly when assessing the risk of rupture of an aneurysm, and the constitutive relations of the tissue must be applied [78]. The method that I have developed for the fully coupled simulation of fluid flow through elastic vessels could be incorporated into blood flow simulations such as those described above for this purpose and for the investigation of the vessel wall displacement during the cardiac cycle. This change and further improvements to cerebral blood flow models would render the simulations sufficiently realistic for a surgeon to use to assess whether patients are at risk from cerebrovascular disease and to assess the effects of different treatment procedures.

Bibliography

- [1] B. Hillen, T. Gaasbeek, and H. W. Hoogstraten. A mathematical model of the flow in the posterior communicating arteries. *Journal of Biomechanics*, 15(6):441–448, 1982.
- [2] L.A. Bortolotto and M.E. Safar. Blood pressure profile along the arterial tree and genetics of hypertension. *Brazilian Archives of Cardiology*, 86(3):166–169, 2006. URL <http://www.ncbi.nlm.nih.gov/pubmed/16612446>.
- [3] J.R. Cebal, M.A.. Castro, J.E. Burgess, R.S. Pergolizzi, M.J. Sheridan, and C.M. Putman. Characterization of cerebral aneurysms for assessing risk of rupture by using patient-specific computational haemodynamics models. *American Journal of Neuroradiology*, 26(10):2550–2559, 2005. URL <http://www.ajnr.org/cgi/content/abstract/26/10/2550>.
- [4] T. Hassan, E.V. Timofeev, M. Ezura, T. Saito, A. Takahashi, K. Takayama, and T. Yoshimoto. Haemodynamic analysis of an adult vein of Galen aneurysm malformation by use of 3D image-based computational fluid dynamics. *American Journal of Neuroradiology*, 24(6):1075–1082, 2003. URL <http://www.ajnr.org/cgi/content/abstract/24/6/1075>.
- [5] B. Hillen, H. W. Hoogstraten, and L. Post. A mathematical model of the flow in the circle of willis. *Journal of Biomechanics*, 19(3):187–194, 1986.
- [6] J. Alastruey, K. H. Parker, J. Peir, S. M. Byrd, and S. J. Sherwin. Modelling the circle of Willis to assess the effects of anatomical variations and occlusions on cerebral flows. *Journal of Biomechanics*, 40(8):1794–1805, 2007. doi: 10.1016/j.jbiomech.2006.07.008. URL <http://dx.doi.org/10.1016/j.jbiomech.2006.07.008>.

-
- [7] M. Bouzidi, M. Firdaouss, and P. Lallemand. Momentum transfer of a lattice-Boltzmann fluid with boundaries. *Physics of Fluids*, 13:3452–3459, 2001.
- [8] R. Verberg and J. Ladd. Lattice-Boltzmann model with sub-grid scale boundary conditions. *Physical Review Letters*, 84:2148–2150, 2000.
- [9] Q. Zou and X. He. On pressure and velocity boundary conditions for the lattice-Boltzmann BGK model. *Physics of Fluids*, 9:1591–1598, June 1997.
- [10] G. Zhao-Li, Z. Chu-Guang, and S. Bao-Chang. An extrapolation method for boundary conditions in lattice-Boltzmann methods. *Physics of Fluids*, 14:2007–2010, 2002.
- [11] T.W. Lowe and T.J. Pedley. Computation of Stokes flow in a channel with a collapsible segment. *Journal of Fluids and Structures*, 9:885–905, 1995.
- [12] O.E. Jensen and M. Heil. High-frequency self-excited oscillations in a collapsible-channel flow. *Journal of Fluid Mechanics*, 481:235–268, 2003.
- [13] X. Y. Luo and T. J. Pedley. A Numerical Simulation of Steady Flow in a 2-D Collapsible Channel. *Journal of Fluids and Structures*, 9(2):149 – 174, 1995. ISSN 0889-9746. doi: DOI:10.1006/jfls.1995.1008. URL <http://www.sciencedirect.com/science/article/pii/S0889974685710080>.
- [14] H. Fang, Z. Wang, Z. Lin, and M. Liu. Lattice-Boltzmann method for simulating the viscous flow in large distensible blood vessels. *Physical Review E*, 65(5):051925, May 2002. doi: 10.1103/PhysRevE.65.051925.
- [15] X.Y. Luo and T.J. Pedley. The effects of wall inertia on flow in a two-dimensional collapsible channel. *Journal of Fluid Mechanics*, 363:253–280, 1998.
- [16] Y.H. Qian, D. D’Humières, and P. Lallemand. Lattice BGK models for Navier-Stokes equations. *Europhysics Letters*, 17:479, February 1992.
- [17] S. Succi. *Lattice-Boltzmann equation for fluid dynamics and beyond*. Oxford Science Publications, 2001.
- [18] D. Kandhai, A. Koponen, A. Hoekstra, M. Kataja, J. Timonen, and P. M. A. Sloot. Implementation aspects of 3D lattice-BGK: boundaries, accuracy, and a new fast relaxation method. *Journal of Computational Physics*, 150(2):482–501, 1999. ISSN 0021-9991. doi: <http://dx.doi.org/10.1006/jcph.1999.6191>.

- [19] X. Y. Luo and T.J. Pedley. A numerical simulation of unsteady flow in a two-dimensional collapsible channel. *Journal of Fluid Mechanics*, 314:191–225, 1996.
- [20] M. Shojima, M. Oshima, K. Takagi, R. Torii, M. Hayakawa, K. Katada, A. Morita, and T. Kirino. Magnitude and role of wall shear stress on cerebral aneurysms: computational fluid dynamics study of 20 Middle Cerebral Artery Aneurysms. *Stroke*, 35:2500–2505, 2004.
- [21] L. Jou, G. Wong, B. Dispensa, M.T. Lawton, R.T. Higashida, W.L. Young, and D. Saloner. Correlation between lumenal geometry changes and haemodynamics in fusiform intracranial aneurysms. *American Journal of Neuroradiology*, 26:2357–2363, 2005.
- [22] L. Boussel, V. Rayz, C. McCulloch, A. Martin, G. Acebedo-Bolton, M.T. Lawton, R.T. Higashida, W.S. Smith, W.L. Young, and D. Saloner. Aneurysm growth occurs at regions of low wall shear stress. *Stroke*, 39:2997–3002, 2008.
- [23] P Michael Conn. *Neuroscience in medicine*. Humana Press, 2nd edition, 2003.
- [24] M.S. Olufsen. Structured tree outflow condition for blood flow in larger systemic arteries. *American Journal of Physiology - Heart and Circulatory Physiology*, 276(1):H257–268, 1999. URL <http://ajpheart.physiology.org/cgi/content/abstract/276/1/H257>.
- [25] J.R. Cebral, M.A. Castro, S. Appanaboyina, C.M. Putman, D. Millan, and A.F. Frangi. Efficient pipeline for image-based patient-specific analysis of cerebral aneurysm haemodynamics: technique and sensitivity. *IEEE Transactions on Medical Imaging*, 24(4):457–467, April 2005. ISSN 0278-0062. doi: 10.1109/TMI.2005.844159.
- [26] M.D. Guglielmi, F. Vinuela, .J. Dion, and G. Duckwiler. Electrothrombosis of saccular aneurysms via endovascular approach. Part 2: Preliminary clinical experience. *Journal of Neurosurgery*, 75:8–14, 1991.
- [27] J.L. Brisman, J.K. Song, Y. Niimi, and A. Berenstein. Treatment options for wide-necked intracranial aneurysms using a self-expandable hydrophilic coil and a self-expandable stent combination. *American Journal of Neuroradiology*, 26:1237–1240, 2005.

- [28] R. Vanninen, H. Manninen, and A. Ronkainen. Broad-based intracranial aneurysms: Thrombosis induced by stent placement. *American Journal of Neuroradiology*, 24: 263–266, 2003.
- [29] M. E. Clark, M. Zhao, F. Loth, N. Alperin, L. Sadler, K. Guppy, and F.T. Charbel. A patient-specific computer model for prediction of clinical outcomes in the cerebral circulation using MR flow measurements. In *MICCAI '99: Proceedings of the Second International Conference on Medical Image Computing and Computer-Assisted Intervention*, pages 368–377, London, UK, 1999. Springer-Verlag. ISBN 3-540-66503-X.
- [30] S. Tateshima, Y. Murayama, J. Villablanca, T. Morino, K. Nomura, K. Tanishita, and F. Vinuela. In vitro measurement of fluid-induced wall shear stress in unruptured cerebral aneurysms harboring blebs. *Stroke*, 34(1):187–192, 2003. doi: 10.1161/01.STR.0000046456.26587.8B. URL <http://stroke.ahajournals.org/cgi/content/abstract/34/1/187>.
- [31] D.A. Steinman. Image-based computational fluid dynamics modelling in realistic arterial geometries. *Annals of Biomedical Engineering*, 30(4):483–497, 2002.
- [32] A. Bernardini, I. Larrabide, H. Morales, G. Pennati, L. Petrini, S. Cito, and A.F. Frangi. Influence of different computational approaches for stent deployment on cerebral aneurysm haemodynamics. *Royal Society Interface Focus*, 1:338–348, 2011.
- [33] M. Kim, I. Larrabide, M.C. Villa-Uriol, and A.F. Frangi. Haemodynamic alterations of a patient-specific intracranial aneurysm induced by virtual deployment of stents in various axial orientations. In *Proceedings of IEEE International Symposium on Biomedical Imaging*, 2009.
- [34] H. Morales, M. Kim, M.C. Villa-Uriol, E. Vivas, and A.F. Frangi. Influence of coil packing rate and configuration on intracranial aneurysm haemodynamics. In *IFMBE Proceedings, Volume 25/4*, pp. 2291–2294, 2010.
- [35] H. Tahir, A.G. Hoekstra, E. Lorenz, P.V. Lawford, D.R. Hose, J. Gunn, and D.J.W. Evans. Multi-scale simulations of the dynamics of in-stent restenosis: impact of stent deployment and design. *Royal Society Interface Focus*, 1:365–373, 2011.

-
- [36] L.D. Landau and E.M. Lifshitz. *Fluid mechanics, 2nd edition*. Pergamon Press, 1987.
- [37] M.A. Castro, C.M. Putman, and J.R. Cebral. Patient-specific computational fluid dynamics modelling of anterior communicating artery aneurysms: a study of the sensitivity of intra-aneurysmal flow patterns to flow conditions in the carotid arteries. *American Journal of Neuroradiology*, 27(10):2061–2068, 2006. URL <http://www.ajnr.org/cgi/content/abstract/27/10/2061>.
- [38] Ansys Fluent. URL <http://www.ansys.com/Products/Simulation+Technology/Fluid+Dynamics/ANSYS+FLUENT>.
- [39] B. Hillen, B. A. Drinkenburg, H. W. Hoogstraten, and L. Post. Analysis of flow and vascular resistance in a model of the circle of Willis. *Journal of Biomechanics*, 21(10):807–814, 1988.
- [40] M.C. Villa-Uriol, I. Larrabide, J.M. Pozo, M. Kim, O. Camara, M.D. Craene, C. Zhang, A.J. Geers, H. Morales, H. Bogunovic, R. Cardenes, and A.F. Frangi. Toward integrated management of cerebral aneurysms. *Philosophical Transactions of the Royal Society A*, 368:2961–2982, 2010.
- [41] J.R. Cebral, M.A. Castro, T. Satoh, and J.E. Burgess. Evaluation of image-based CFD models of cerebral aneurysms using MRI. In *Proceedings of the ISMRM Flow Motion Workshop, Zurich, Switzerland, pp. 11-13*, 2004.
- [42] M.A. Castro, C.M. Putman, and J.R. Cebral. Computational fluid dynamics modeling of intracranial aneurysms: effects of parent artery segmentation on intra-aneurysmal haemodynamics. *American Journal of Neuroradiology*, 27(8):1703–1709, 2006. URL <http://www.ajnr.org/cgi/content/abstract/27/8/1703>.
- [43] V. Mihalef, R.I. Ionasec, P. Sharma, B. Gergescu, I. Voigt, M. Suehling, and D. Comaniciu. Patient-specific modelling of whole heart anatomy, dynamics and haemodynamics from four-dimensional cardiac CT images. *Royal Society Interface Focus*, 1:286–296, 2011.
- [44] A.D. Jeays, P.V. Lawford, R. Gillott, P. Spencer, D.C. Barber, K.D. Bardhan, and D.R. Hose. Characterisation of the haemodynamics of the Superior Mesenteric Artery. *Journal of Biomechanics*, 40:1916–1926, 2007.

- [45] C. Zhang, M.C. Villa-Uriol, M.D. Craene, J.M. Pozo, and A.F. Frangi. Morphodynamic analysis of cerebral aneurysm pulsation from time-resolved rotational angiography. *IEEE Transactions on Medical Imaging*, 28:1105–1116, 2009.
- [46] W.K. Purves, D. Sadava, G.H. Orians, and H.C. Heller. *Life: The science of biology*. Sirauer Associates, 7th edition, 2004.
- [47] W. Secomski, A. Nowicki, F. Guidi, P. Tortoli, and P.A. Lewin. Noninvasive in vivo measurements of Haematocrit. *Journal of Ultrasound in Medicine*, 22(4):375–384, 2003. URL <http://www.jultrasoundmed.org/cgi/content/abstract/22/4/375>.
- [48] T. Kenner. The measurement of blood density and its meaning. *Basic Research in Cardiology*, 84:111 – 124, 1989.
- [49] D.J. Hughes and B. Snyder. Speed of 10 MHz sound in canine aortic wall: Effects of temperature, storage and formalin soaking. *Medical and Biological Engineering and Computing*, 18:220 – 222, 1980.
- [50] R. L. Nasoni, T. Bowen, M.W. Dewhirst, H. B. Roth, and R. Premovich. The Speed of Sound as a Function of Temperature in Mammalian Tissue. In *Ultrasonics Symposium*, 1980.
- [51] A. F. Collings and N. Bajenov. Temperature dependence of the velocity of sound in human blood and blood components. *Australasian physical & engineering sciences in medicine*, 10(3):123–127, 1987.
- [52] D.J. Hughes, L.A. Geddes, C.F. Babbs, J.D. Bourland, and V.L. Newhouse. Attenuation and speed of 10 MHz ultrasound in canine blood of various packed-cell volumes at 37C. *Medical and Biological Engineering and Computing*, 17(5):619–622, 1979.
- [53] H. Hinghofer-Szalkay and J.E. Greenleaf. Continuous monitoring of blood volume changes in humans. *Journal of Applied Physiology*, 63:1003–1007, 1987.
- [54] T. Hassan, E. V. Timofeev, T. Saito, H. Shimizu, M. Ezura, T. Tominaga, A. Takahashi, and K. Takayama. Computational replicas: anatomic reconstructions of cerebral vessels as volume numerical grids at three-dimensional angiography. *American Journal of Neuroradiology*, 25(8):1356–1365, 2004. URL <http://www.ajnr.org/cgi/content/abstract/25/8/1356>.

- [55] B. Pirofsky. The determination of blood viscosity in man by a method based on Poiseuille's law. *Journal of Clinical Investigation*, 32(4):292–298, 1953.
- [56] R.S. Rosenson, A. McCormick, and E.F. Uretz. Distribution of blood viscosity values and biochemical correlates in healthy adults. *Clinical Chemistry*, 42(8):1189–1195, 1996. URL <http://www.clinchem.org/cgi/content/abstract/42/8/1189>.
- [57] D.M. Eckmann, S. Bowers, M. Stecker, and A. T. Cheung. Hematocrit, volume expander, temperature, and shear rate effects on blood viscosity. *Anesthesia and analgesia*, 91(3):539–543, 2000.
- [58] www.vilastic.com/tech10.html. Plasma viscosity and blood viscoelasticity. www, 2000. URL www.vilastic.com/tech10.html.
- [59] A.M. Artoli. *Mesosopic computational haemodynamics*. PhD thesis, University of Amsterdam, 2003.
- [60] A. R. Pries, D. Neuhaus, and P. Gaehtgens. Blood viscosity in tube flow: dependence on diameter and Haematocrit. *American Journal of Physiology - Heart and Circulatory Physiology*, 263:1770–1778, 1992. URL <http://ajpheart.physiology.org/cgi/content/abstract/263/6/H1770>.
- [61] M.D. Ford, N. Alperin, S.H. Lee, D. W. Holdsworth, and D.A. Steinman. Characterization of volumetric flow rate waveforms in the normal internal carotid and vertebral arteries. *Physiological Measurement*, 26:477–488, 2005.
- [62] S. Wetzels, S. Meckel, A. Frydrychowicz, L. Bonati, E.W. Radue, K. Scheffler, J. Hennig, and M. Markl. In vivo assessment and visualization of intracranial arterial hemodynamics with flow-sensitized 4D MR imaging at 3T. *American Journal of Neuroradiology*, 28(3):433–438, 2007. URL <http://www.ajnr.org/cgi/content/abstract/28/3/433>.
- [63] D.A. Steinman and B.K. Rutt. On the nature and reduction of plaque-mimicking flow artifacts in black blood MRI of the carotid bifurcation. *Magnetic Resonance in Medicine*, 39:635–641, 1998.

- [64] L. Jiang, C. Huang, P. Liu, B. Yan, J.Chen, H. Chen, R. Bai, and Y. Lu. Three dimensional rotational angiography for the treatment of spinal cord vascular malformations. *Surgical Neurology*, 69(4):369–73; discussion 373–4, Apr 2008. doi: 10.1016/j.surneu.2007.03.016. URL <http://dx.doi.org/10.1016/j.surneu.2007.03.016>.
- [65] K. Perktold, M. Hofer, G. Rappitsch, M. Loew, B.D. Kuban, and M.H. Friedman. Validated computation of physiologic flow in a realistic coronary artery branch. *Journal of Biomechanics*, 31:217–228, 1998.
- [66] R. Botnar, G. Rappitsch, M.B.Scheidegger, D. Liepsch, K.Perktold, and P. Boesiger. Haemodynamics in the carotid artery bifurcation: a comparison between numerical simulations and in vitro MRI measurements. *Journal of Biomechanics*, 33:137–144, 2000.
- [67] J.G. Myers, J.A. Moore, M. Ohja, K.W. Johnston, and C.R. Ethier. Factors influencing blood flow patterns in the human right coronary artery. *Annals of Biomedical Engineering*, 29:109–120, 2001.
- [68] R. Hose, A. Marzo, P. Singh, and P. Lawford. Aneurist: Integrated biomedical informatics for the management of cerebral aneurysms. Technical report, Pompeu Fabra University, Barcelona, 2009. URL www.aneurist.org.
- [69] J. Mazumdar. *Biofluid mechanics*. World Scientific, 1992.
- [70] S. Post. *Applied and computational fluid dynamics*. Jones and Bartlett, 2011.
- [71] A.G. Radaelli, T.S. Martinez, E.V. Diaz, X. Mellado, M.A. Castro, C.M. Putman, L. Guimaraens, J.R. Cebra, and A.F. Frangi. Combined clinical and computational inforamtion in complex cerebral aneurysms: application to mirror cerebral aneurysms. In *Proceedings of SPIE 6511, Medical Imaging: Physiology, Function and Structure from Medical Images*, 2007.
- [72] A.J. Geers, I. Larrabide, A.G. Radaelli, H. Bogunovic, H.A.F. Gratama van Andel, C.B. Majoie, and A.F. Frangi. Reproducibility of image-based computational haemodynamics in intracranial aneurysms: comparison of CTA and 3DRA. In *IEEE International Symposium of Biomedical Imaging*, pp. 610-613, 2009.

- [73] M.D. Ford, H.N. Nikolov, J.S. Milner, S.P. Lownie, E.M. DeMont, W. Kalata, and F. Loth. PIV-measured versus CFD-predicted flow dynamics in anatomically realistic cerebral aneurysm models. *Journal of Biomechanical Engineering*, 130:021015, 2008.
- [74] Y. Hoi, S.H. Woodward, M. Kim, and H. Meng. Validation of CFD simulations of cerebral aneurysms with implication of geometric variations. *Journal of Biomechanical Engineering*, 128:844–851, 2006.
- [75] J.M. Buick. *Lattice-Boltzmann methods in interfacial wave modelling*. PhD thesis, University of Edinburgh, 1997.
- [76] Y.C. Fung. *Biodynamics circulation*. Springer-Verlag, 1984.
- [77] K. Hayashi, H. Handa, A. Nagasawa, A. Okumura, and K. Moritake. Stiffness and elastic behaviour of human intracranial and extracranial arteries. *Journal of Biomechanics*, 13:175–184, 1980.
- [78] D.A. Vorp and J.P.V. Geest. Biomechanical determinants of abdominal aortic aneurysm rupture. *Arteriosclerosis, Thrombosis and Vascular Biology*, 25:1558–1566, 2005.
- [79] P.N. Watton and N.A. Hill. Evolving mechanical properties of a model of an abdominal aortic aneurysm. *Biomechanics and modelling in Mechanobiology*, 8:25–42, 2009.
- [80] P.N. Watton, Y. Ventikos, and G.A. Holzapfel. Modelling the growth and stabilisation of cerebral aneurysms. *Mathematical Medicine and Biology*, 26:133–164, 2009.
- [81] Y. Ventikos, E.C. Holland, T.J. Bowker, N.M.P. Kakalis, M. Megahed, F. Zhu, P.E. Summers, and J.V. Byrne. Computational modelling for cerebral aneurysms: Risk evaluation and interventional planning. *British Journal of Neuroradiology*, 82:S62–S71, 2009.
- [82] Y. Ventikos, T.J. Bowker, P.N. Watton, N.M.P. Kakalis, and J.V. Byrne. Risk evaluation and interventional planning for cerebral aneurysm: Computational models for growth, coiling and thrombosis. *International Journal of Computational Fluid Dynamics*, 23:595–607, 2009.

- [83] P.N. Watton, N.B. Raberger, G.A. Holzapfel, and Y. Ventikos. Coupling the haemodynamic environment to the evolution of cerebral aneurysms. *Journal of Biomechanical Engineering*, 131:101003, 2009.
- [84] S. Manos, S. Zasada, M.D. Mazzeo, G. Doctors, R. Haines, S. Brew, R. Pinning, J. Brooke, and P. V. Coveney. Patient-specific whole cerebral blood flow simulation: A future role in surgical treatment for neurovascular pathologies. In *Proceedings of the TeraGrid 2008 Conference, 9th–13th June, Las Vegas, USA*, 2008. URL www.teragrid.org/events/teragrid08/papers/28.pdf.
- [85] L. Axner. *High performance computational haemodynamics with the lattice-Boltzmann method*. PhD thesis, University of Amsterdam, 2007.
- [86] S.K. Sadiq, M.D. Mazzeo, S.J. Zasada, S. Manos, I Stoica, CV Gale, S.J. Watson, P. Kellam, S. Brew, and P.V. Coveney. Patient-specific simulation as a basis for clinical decision-making. *Philosophical Transactions of the Royal Society A, Mathematical Physical and Engineering Sciences*, 366:3199–3219, Jun 2008. doi: 10.1098/rsta.2008.0100. URL <http://dx.doi.org/10.1098/rsta.2008.0100>.
- [87] X. He, G. Duckwiler, and D.J. Valentino. Lattice-Boltzmann simulation of cerebral artery haemodynamics. *Computers and Fluids*, 38:789–796, 2009.
- [88] X. He and L. Luo. Lattice-Boltzmann model for the incompressible Navier-Stokes equations. *Journal of Statistical Physics*, 88:927–944, 1997.
- [89] Q. Zou, S. Hou, S. Chen, and G.D. Doolen. An improved incompressible lattice-Boltzmann model for time-independent flows. *Journal of Statistical Physics*, 81: 35–48, 1995.
- [90] Y. Chen, H. Ohashi, and M. Akiyama. Simulation of laminar flow over a backward-facing step using the lattice BGK method. *Japan Society of Mechanical Engineers International Journal*, 40(1):25–32, 1997.
- [91] A.C. Ladd. Numerical simulations of particulate suspensions via a discretized Boltzmann equation. Part 1. Theoretical foundation. *Journal of Fluid Mechanics*, 271: 285–309, 1994.

- [92] M. D. Mazzeo and P. V. Coveney. HemeLB: A high performance parallel lattice-Boltzmann code for large scale fluid flow in complex geometries. *Computer Physics Communications*, 178:894–914, June 2008. doi: 10.1016/j.cpc.2008.02.013.
- [93] M.D. Mazzeo, S. Manos, and P.V. Coveney. In-situ ray tracing and computational steering for interactive blood flow simulation. *Computer Physics Communications*, 181:355–370, 2010.
- [94] W.D. Gropp, D.K. Kaushik, D.E. Keyes, and B.F. Smith. High-performance parallel implicit CFD. *Parallel Computing*, 27(4):337 – 362, 2001. ISSN 0167-8191. doi: DOI: 10.1016/S0167-8191(00)00075-2. URL <http://www.sciencedirect.com/science/article/B6V12-42MFDG7-2/2/fd58d46aca108fa96977d7c1b4642d3f>.
- [95] P. M. A. Sloot and A. Hoekstra. Virtual vascular surgery on the Grid. *ERCIM News*, 59, 2004.
- [96] S. Melchionna, M. Bernaschi, S. Succi, E. Kaxiras, F.J. Rybicki, D. Mitsouras, A.U. Coskun, and C.L. Feldman. Hydrokinetic approach to large-scale cardiovascular blood flow. *Computer Physics Communications*, 181:462–472, 2010.
- [97] M. Bernaschi, S. Melchionna, S. Succi, M. Fyta, E. Kaxiras, and J.K. Sircar. MURPHY: A parallel MUlti PHYsics/scale code for high performance bio-fluidic simulations. *Computer Physics Communications*, 180:1495–1502, 2009.
- [98] S. Chen, Z Wang, X. Shan, and G.D. Doolen. Lattice-Boltzmann computational fluid dynamics in three dimensions. *Journal of Statistical Physics*, 68:379–399, 1992.
- [99] X. He and L.S. Luo. A priori derivation of the lattice-Boltzmann equation. *Physical Review E*, 55:6333–6336, June 1997. doi: 10.1103/PhysRevE.55.R6333.
- [100] X. He, Q. Zou, L.S. Luo, and M. Dembo. Analytic solutions of simple flows and analysis of nonslip boundary conditions for the lattice-Boltzmann BGK model. *Journal of Statistical Physics*, 87:115–136, April 1997. doi: 10.1007/BF02181482.
- [101] D.R. Noble, S. Chen, J.G. Georgiadis, and R.O. Buckius. A consistent hydrodynamic boundary condition for the lattice-Boltzmann method. *Physics of Fluids*, 7(1):203–209, 1995. doi: 10.1063/1.868767. URL <http://link.aip.org/link/?PHF/7/203/1>.

- [102] G. Zhao-Li, Z. Chu-Guang, and S. Bao-Chang. Nonequilibrium extrapolation method for velocity and pressure boundary conditions in the lattice-Boltzmann method. *Chinese Physics*, 11(4):366–374, 2002. URL <http://stacks.iop.org/1009-1963/11/366>.
- [103] D.P. Ziegler. Boundary conditions for lattice-Boltzmann simulations. *Journal of Statistical Physics*, 71:1171–1177, June 1993. doi: 10.1007/BF01049965.
- [104] T. Inamuro, M. Yoshino, and F. Ogino. A nonslip boundary condition for lattice-Boltzmann simulations. *Physics of Fluids*, 7:2928–2930, 1995.
- [105] X. He and Q. Zou. Analysis and boundary condition of the lattice-Boltzmann BGK model with two velocity components. *Los Alamos preprint LA UR 95 2293*, page 7002, July 1995.
- [106] M. Hecht and J. Harting. Implementation of on-site velocity boundary conditions for D3Q19 lattice-Boltzmann. *Journal of Statistical Mechanics*, page 01018, 2010. URL <http://www.citebase.org/abstract?id=oai:arXiv.org:0811.4593>.
- [107] O. Filippova and D. Hanel. Lattice-Boltzmann simulations of gas-particle flow in filters. *Computers and Fluids*, 26:697 – 712, 1997.
- [108] O. Filippova and D. Hanel. Grid Refinement for lattice-BGK models. *Journal of Computational Physics*, 147:219–227, 1998.
- [109] R. Mei, L. Luo, and W. Shyy. An accurate curved boundary treatment in the lattice Boltzmann method. *Journal of Computational Physics*, 155(2):307–330, 1999. ISSN 0021-9991. doi: <http://dx.doi.org/10.1006/jcph.1999.6334>.
- [110] S. Park and D. Lee. Experimental and numerical investigations of pressure drop in a rectangular duct with modified power law fluids. *Heat and Mass Transfer*, 39: 645–655, 2003.
- [111] S. Park and D. Lee. Anomalous predictions of pressure drop and heat transfer in ducts of arbitrary cross-section with modified power law fluids. *Heat and Mass Transfer*, 38:141–149, 2001.

-
- [112] S.P. Sullivan, L.F. Gladden, and M.L. Johns. Simulation of power-law fluid flow through porous media using lattice-Boltzmann techniques. *Journal of Non-Newtonian Fluid Mechanics*, 133:91–98, 2006.
- [113] D.J. Griffiths and H.J. Rollema. Urine flow curves of healthy males: a mathematical model of bladder and urethral function during micturition. *Medical and Biological Engineering and Computing*, 17:291 – 300, 1979. URL www.ucl.ac.uk/math/graduate/graduates.html.
- [114] L.A. Dimov and E.M. Bogushevskaya. Application of theory of beam analysis for arterial oil pipelines across swamps. *Soil Mechanics and Foundation Engineering*, 39:139–143, 2002.
- [115] L.G. Olson and D. Jamison. Application of a general-purpose finite-element method to elastic pipes conveying fluid. *Journal of Fluids and Structures*, 11:207–222, 1997.
- [116] G.M. Doctors, M.D. Mazzeo, and P.V. Coveney. A computationally efficient method for simulating fluid flow in elastic pipes in two and three dimensions. *Computer Physics Communications*, 181:1584–1592, 2010.
- [117] H. Fang, Z. Lin, and Z. Wang. Lattice-Boltzmann simulation of viscous fluid systems with elastic boundaries. *Physical Review E*, 57:R25–R28, 1998.
- [118] A.G. Hoekstra, J. van’t Hoff, A.M.M. Artoli, and P. M. A. Sloot. Unsteady flow in a 2D elastic tube with the LBGK method. *Future Generation Computer Systems*, 20:917–924, 2004.
- [119] G.A. Buxton, R. Verberg, D. Jasnow, and A.C. Balazs. Newtonian fluid meets an elastic solid: Coupling lattice-Boltzmann and lattice-spring models. *Physical Review E*, 71:056707, 2005.
- [120] D. Leitner, S. Wassertheurer, A. Hessinger, and A. Holzinger. A lattice-Boltzmann model for pulsative blood flow in elastic vessels. *Elektrotechnik und Informationstechnik*, 123(4):152–155, 2006.
- [121] L.D. Landau and E.M. Lifshitz. *Theory of Elasticity, 2nd edition*. Pergamon Press, 1970.

-
- [122] M. Hazewinkel. *Encyclopedia of mathematics, volume 1*. Kluwer academic publishers, 1995.
- [123] <http://openmp.org/wp>. The OpenMP API specification for parallel programming, 2008.
- [124] D.S. Bernstein. *Matrix mathematics*. Princeton University Press, 2005.
- [125] C.D. Bertram, C.J. Raymond, and T.J. Pedley. Mapping of instabilities for flow through collapsed tubes of differing length. *Journal of Fluids and Structures*, 4: 125–153, 1990.
- [126] M.P. Rast. Simultaneous solution of the Navier-Stokes and elastic membrane equation by a finite element method. *International Journal for Numerical Methods in Fluids*, 19:1115–1135, 1994.
- [127] M.E. Ralph and T.J. Pedley. Flow in a channel with a moving indentation. *Journal of Fluid Mechanics*, 190:87–112, 1988.
- [128] Discrete Fourier Transform for numpy. URL <http://docs.scipy.org/doc/numpy/reference/routines.fft.html>.